Imperial College London

Fundamental Study of Smouldering Combustion of Peat in Wildfires

A thesis submitted in partial satisfaction of the requirements for the degree

Doctor of Philosophy

in

Mechanical Engineering

by

Xinyan Huang

November 2015

Supervised by Dr Guillermo Rein

Declaration of Originality

I hereby declare that the material presented in this thesis is my own, except where otherwise acknowledged and appropriately referenced.

Xinyan Huang

November 2015

Copyright Declaration

DEDICATION

To *Yiyi Huang*

who brings so much pleasure and inspiration to my life

ABSTRACT

Fundamental Study of Smouldering Combustion of Peat in Wildfires

by

Xinyan Huang

Doctor of Philosophy in Mechanical Engineering

Imperial College London, November 2015

Supervised by Dr Guillermo Rein

Smouldering combustion is the slow, low-temperature, flameless burning of porous fuels and the most persistent type of combustion, different from flaming combustion. Smouldering is the dominant phenomena in fires of coal and natural deposits of peat which are the largest and longest burning fires on Earth. These megafires fires contribute considerably to annual greenhouse gas emissions roughly equivalent to 15% of the man-made emissions, and result in the widespread destruction of global ecosystems and regional haze events. Moreover, the atmospheric release of ancient carbon in soil and the sensitivity of peat ignition to higher temperatures and drier conditions create a positive feedback mechanism to climate change.

Compared to flaming combustion, smouldering combustion can be initiated with a much weaker ignition source, and provide a hazard shortcut to flaming. Once ignited, the persistent smouldering fires can consume a huge amount of earth biomass, and burn for very long periods of time (days, years and centuries) despite extensive firefighting efforts or climate changes. For the past few decades, there have been some experimental studies on smouldering peat fires of different scales. However, very few computational work has been done to systematically study such emerging fire phenomena before the research undertaken in this thesis.

This thesis is presented in a manuscript style: each chapter takes the form of an independent paper, which has been published or submitted to a journal publication. A final chapter summarizes the conclusions, and suggests potential areas of future research.

Chapter 1 first proposes a comprehensive 5-step kinetic model based on thermogravimetric analysis (TGA) to describe the heterogeneous reactions in smouldering combustion of peat. The corresponding kinetic parameters are inversely modelled using genetic algorithm (GA). This 5-step (including drying) kinetic model successfully explains the TG data of four different peat soils from different geographical locations. The chemical validity of the scheme is also investigated by incorporating it into a one-dimensional (1-D) plug-flow model. The reaction and species distributions of two most common fire spread modes, lateral and in-depth spread, are successfully simulated.

Chapter 2 presents a new comprehensive 1-D model of a reactive porous media to solve the conservation equations and the proposed 5-step heterogeneous chemical kinetics. This model is used to simulate several ignition experiments on bench-scale peat samples in the literature. The model first predicts the smouldering thresholds, relating to the critical moisture content (MC) and inert content (IC). The modelling results show a good agreement with experiments for a wide range of peat types and organic soils. The influences of the kinetic parameters, physical properties, and ignition protocol on initiating the peat fire are also investigated.

Chapter 3 continues to optimize this 1-D model to investigate the vertical in-depth spread of smouldering fires into peat columns 20-30 cm deep with heterogeneous profiles of MC, IC and density. Modelling results reveal that smouldering combustion can spread over peat layers with a very high MC ($\sim$ 250%) if the layer is thin and located below a thick and drier layer. It is also found that the critical MC for extinction can be much higher than the previously reported critical MC for ignition. Furthermore, depths of burn (DOB) in peat fire is successfully predicted, and shows a good agreement with experiments on 18 field peat samples in the literature.

Chapter 4 further looks into the kinetic schemes of different complexities to explain the TGA of two peat soils under various atmospheric oxygen concentration (X_{O_2}). Their best kinetic parameters are fast searched via Kissinger-genetic algorithm (K-GA) method, and the oxidation model is determined for the first time. Then, the kinetic model is applied into the 1-D model to simulate the peat experiment with fire propagation apparatus (FPA) in the literature. Try peat samples are used to minimize the influence of moisture, and ignited under both sub- and super-atmospheric oxygen concentration. Modelling results show a good agreement with experiment, and the stochastic sensitivity analysis is used to test the model sensitivity to multiple physico-chemical properties.

Chapter 5 investigates the interactions of atmospheric oxygen and fuel moisture in smouldering wildfires with the proposed 1-D model. Modelling results reveal a nonlinear

correlation existing between the critical fuel moisture and atmospheric oxygen as MC increases, a greater increase in oxygen concentration is required for both ignition and fire spread. Smouldering fires on dry fuel can survive at a substantially lower oxygen concentration ($X_{O_2} \sim 11\%$) than flaming fires, and fuel type and chemistry may play important roles especially in high MC. The predicted spread rate of smouldering peat fire is on the order of 1 mm/min, much slower than flaming fires. In addition, the rate of fire spread increases in an oxygen-richer atmosphere, while decreases over a wetter fuel.

Chapter 6 presents an experimental study on smouldering fires spreading over bench-scale peat samples under various moisture and wind conditions. The periodic "overhang" phenomenon is observed where the smouldering fire spreads beneath the top surface, and the overhang thickness is found to increase with peat MC and the wind speed. Experimental results show that the lateral spread rate decreases with MC, while increases with the wind speed. As peat MC increases, the fire spread behaviour becomes less sensitive to the wind condition and its depth. A simple heat transfer analysis is proposed to explain the influence of moisture and wind on the spread rate profile, and suggests that the overhang phenomena is caused by the spread rate difference between the top and the lower peat layers.

Chapter 7 summarizes the research of this thesis, and discuss the possible areas for future research.

ACKNOWLEDGEMENTS

First and foremost I would like to thank my teacher Dr Guillermo Rein. It has been an unexpected venture while a great fortune in my life to be your student. Your guidance, encouragement, and optimism has kept me conquering all those difficulties one after another in my research and toward life. I appreciate all your contributions of time, ideas, and guidance to make my academic experience productive, challenging, and exciting. I would love to learn more from you and have more collaboration with you in my future academic career.

I would like to express my deep gratitude to Profs. Michael Gollner (University of Maryland) and Forman Williams (University of California at San Diego), who brought me into the combustion and fire research at the first place, and continuously look after me from the other side of ocean. I am also especially grateful for all Haze Lab members, Elge, Izabella, Francesco, Nils, Virginia, Yuqi and Franz, who make me feel happy in campus. I had a really unforgettable time working with you, and it is my honour to be in the same academic family with all of you.

For this thesis, I would like to thank all my co-authors, Prof. Haixiang Chen (University of Science and Technology of China) for his advice on modelling as well as Francesco and Michela (University of Cambridge) for their help in experiment. I also wish to thank many research collaborators for their valuable advices, Prof. Kaiyuan Li, Prof. Naian Liu, Prof. Jie Ji, and Supan Wang (University of Science and Technology of China), Dr Chris Lautenberger (Reax Engineering), Dr Rory Hadden (University of Edinburgh), Dr Claire Belcher (University of Exeter), Dr Valérie Leroy-Cancellieri (University of Corsica), Dr Jon Yearsley, Nuria Prat-Guitart (University College Dublin), Dejian Wu (KU Leuven), Prof. Rajasekhar Bala, Dr Zhenggang Liu (National University of Singapore), Dr Long Shi (Victoria University), Yangkyun Kim (University of Ulster), and Zeyang Song (Nanjing Tech University).

I wish to thank Dr Salvador Navarro-Martinez (Imperial College) and Prof. Albert Simeoni (Exponent, Inc.) for serving as my examiners, and Prof. Peter Lindstedt for additional advice for my study. I also wish to thank Prof. Alex Taylor, Dr Stelios Rigopoulos, Dr Julia Varley and Dr Patrick Leevers (Imperial College) for offering me teaching assistant positions in the Department of Mechanical Engineering. It has been a great experience to study and work with them.

For the last three years, I have met many good friends here in London. It is hard to acknowledge all of them here. Some of them are Chao Zhang, Lianbo Li, Zhan Liu, Hongjing Yang, Ula Michlowicz, Hao Wang, Chengjian Ding, Martin Jurisch, Jin Jin,

Shija Wu, Fan Shi, and Tao Li. Their support and sharing parts of their lives kept with me has me grounded and helped me grow. I own special thanks to my old friends, Menglong Hao (US), Guangjie Gong, Yang Tao (China), Yixiong Xiang (Singapore), Jian Gao (Japan), and Wenli Zhu (France). Despite the distance between us, I am forever grateful for your time and encouragement.

I want to acknowledge the financial support from the Department of Mechanical Engineering at Imperial College, and travel support from Santander, Imperial Trust, Old Centralians' Trust, Association for Fire Ecology (AFE), Combustion Institute, International Association of Wildland fire (IAWF), and Institution of Physics (IOP).

I am deeply appreciated that my parents have created the best possible environment for me over my life. With their care and support, I feel very privilege to be able to fully devote myself to this intellectual journey.

At my final stage of PhD study, I have been deeply grateful for inspirations that Yiyi has brought to me. Your understanding and trust enabled me to be best of myself and go through the toughest time. I'd love to have you by my side for the rest of my life. This thesis is dedicated to you.

Xinyan Huang
London, UK
November 2015

TABLE OF CONTENTS

LIST OF FIGURES

LIST OF TABLES

NOMENCLATURE

c	heat capacity (J/kg-K)
d_p	characteristic pore size (m)
E	activation energy (kJ/mol)
h	enthalpy (J)
h_c	convective coefficient (W/m^2-K)
h_m	mass-transfer coefficient (kg/m^2-s)
ΔH	heat of reaction (MJ/kg)
k	thermal conductivity (W/m-K) or reaction constant
K	absolute permeability (m^2)
L	sample size (m)
m	normalized mass (-)
$\dot{m}''$	mass flux (kg/m^2-s)
n	reaction order (-)
P	pressure (Pa)
$\dot{q}''$	heat flux (kW/m^2)
$\dot{q}_e''$	environmental heat loss (kW/m^2)
R	universal gas constant (J/mol-K)
R_s	specific gas constant (J/kg-K)
S	particle surface area (m^2/g)
t	time (s)
T	temperature (K)
u	fire spread rate (cm/h)
U	wind speed (m/s)
X	volume fraction (-)
X_{O_2}	oxygen concentration, percentage by volume (%)
Y	mass fraction (-)
z	distance (m)
Δz	cell size (m)
Z	pre-exponential factor (s^{-1})

Greeks

α	diffusivity (m^2/s)
β	heating rate (K/min)
γ	radiative conductivity coefficient (m)
δ	thickness (m)
δ_o	overhang thickness (m)
ε	emissivity (-)
κ	radiation absorption coefficient (m^{-1})
ν	stoichiometric coefficient (kg/kg) or viscosity (m^2/s)
ρ	bulk density (kg/m^3)
ρ_s	solid density, $\rho/\rho_s = 1 - \psi$ (kg/m^3)
σ	Stefan-Boltzmann constant (kg/s^3-K^4)
χ	fraction factor (-)
ψ	porosity (-)
$\dot{\omega}$	reaction rate (kg/s)

Superscripts

$*$	critical or normalized

Subscripts

0	initial
∞	ambient
α	α-char
β	β-char
a	ash or air
c	cellulose or char
cl	clay
d	destruction
dr	drying
f	formation
ex	extinction
exp	experiment

g	gas
h	hemicellulose
i	condensed species number
ig	ignition
j	gaseous species number
k	reaction number
l	lignin
o	oxidation
O_2	oxygen
p	peat or pyrolysis
pre	prediction
sm	smouldering
t	top
w	water or wet

Abbreviations

0/1/2/3D	zero/one/two/three-dimensional
C	cellulose
DOB	depth of burn
DDTG	(2^{nd}) derivative of thermogravimetric
DTG	(1^{st}) derivative of thermogravimetric
GA	genetic algorithm
H	hemicellulose
IC	inorganic or inert content (wt.%)
L	lignin
MC	moisture content (wt.%)
MLR	mass-loss rate
OC	organic content
ODE	ordinary differential equations
OM	organic matter
PDE	partial differential equations
TG	thermogravimetric
TGA	thermogravimetric analysis

Preface

In this thesis, smouldering combustion of peat in wildfire has been systematically studied for (i) the *zero-dimensional* (0D) thermal analysis of microgram-scale peat degradation (Chapters 1 and 4), (ii) the *one-dimensional* (1D) in-depth spread of peat fires (Chapters 2-5), and (iii) the *two-dimensional* (2D) surface fire spread in bench-scale peat samples (Chapter 6). Smouldering combustion is the slow, low-temperature, flameless burning of porous fuels and the most persistent type of combustion. In particular, smouldering combustion of peat in wildfire are known as the largest and longest combustion phenomenon on Earth.

Compared to flaming fires, smouldering fires can be initiated by much weaker ignition sources. Once ignited, they become extremely difficult to control and suppress, despite extensive rains, weather changes, and fire-fighting attempts. For smouldering peat fires, there are two controlling mechanisms, *heat loss* and *oxygen supply*. Both mechanisms play different roles in ignition and extinction as well as in two dominating spread modes, *lateral* and *in-depth* spread, which are extensively studied throughout this thesis.

This thesis is written in manuscript format. As such each chapter is a standalone document suitable for journal publication. The material is presented as follows:

Chapter 1 proposes a sophisticate kinetic model to describe the smouldering combustion of peat, and the model is demonstrated in a 1D plug-flow model and for lateral and in-depth fire spread modes. The chapter is based on:

> X. Huang, G. Rein (2014) *Smouldering Combustion of Peat: Inverse Modelling of the Thermal and Oxidative Degradation Kinetics*, **Combustion and Flame** 161(6): 1633-44.

Chapter 2 presents a comprehensive 1D model of a reactive porous media to investigate smouldering threshold of peat fires, relating to the critical moisture and inert contents. The chapter is based on:

> X. Huang, G. Rein, H. Chen (2015) *Computational Smouldering Combustion: Predicting the Roles of Moisture and Inert Contents in Peat Wildfires*, **Proceedings of the Combustion Institute**, 35(3): 2673-81.

Chapter 3 studies the difference between critical moisture content for ignition and extinction in smouldering peat fires, and predict the depth of burn for peat samples in field. The chapter is based on:

> X. Huang, G. Rein (2015) *Computational Study of Critical Moisture and Depth of Burn in Peat Fires*, **International Journal of Wildland Fire**, 24: 798-808.

Chapter 4 investigates several kinetic scheme under different oxygen concentrations, and the kinetics are tested by modelling both the milligram thermogravimetric analysis (TGA) and bench-scale Fire Propagation Apparatus (FPA) experiments. The chapter is based on:

> X. Huang, G. Rein (2015) *Thermochemical Conversion of Biomass in Smouldering Combustion across Scales: the Roles of Heterogeneous Kinetics, Oxygen and Transport Phenomena*, **Bioresource Technology** (Accepted).

Chapter 5 studies the interactions of atmospheric oxygen and fuel moisture in smouldering wildfires, and find the corresponding critical conditions for both ignition and fire spread, which are compared with those for flaming wildfires. The chapter is based on:

> X. Huang, G. Rein (2016) *Interactions of Atmospheric Oxygen and Fuel Moisture in Smouldering Wildfires*, **Science of the Total Environment** (under minor revision).

Chapter 6 presents an experimental study on smouldering fires spreading over bench-scale peat samples. The lateral fire spread rate is measured, and the overhang phenomenon is observed and discussed. The chapter is based on:

> X. Huang, F. Restuccia, M. Gramola, G. Rein (2015) *Experimental Study of the Formation and Collapse of an Overhang in the Lateral Spread of Smouldering Peat Fires*, **Combustion and Flame** (Accepted).

Other Publications

The following publications are on combustion and fire related topics but not part of the thesis, co-authored during the course of this PhD.

∘ G. Rein, X. Huang, F. Restuccia, T. McArdle (2015) *O-Revealer: Novel technology for demining in peatlands by controlled smouldering combustion*, submitted to a journal for publication.

∘ S. Wang, X. Huang, H. Chen, N. Liu, G. Rein (2015) *Ignition of Low-density Expandable Polystyrene Foam by a Hot Particle*, **Combustion and Flame**, 162 (11): 4112-18.

∘ D. Wu, X. Huang, F. Norman, F. Verplaetsen, J. Berghmansa, E. Van den Bulcka (2015) *Experimental investigation on the self-ignition behavior of coal dust accumulations in oxy-fuel combustion system*, **Fuel**, 160: 245-54.

∘ K. Li, X. Huang, C.M. Fleischmann, G. Rein, J. Ji (2014) *Pyrolysis of Medium-Density Fiberboard: Optimized Search for Kinetic Scheme and Parameters via a Genetic Algorithm Driven by Kissinger's Method*, **Energy Fuels**, 28: 6130-9.

∘ X. Huang, M. J. Gollner (2014) *Correlations for Evaluation of Flame Spread over an Inclined Fuel Surface*, **Fire Safety Science**, 11: 222-33.

Chapter 1

Smouldering Combustion of Peat in Wildfires: Inverse Modelling of the Drying and the Thermal and Oxidative Decomposition Kinetics

Summary [1]

Smouldering combustion is the driving phenomenon of wildfires in peatlands, like those causing haze episodes in Southeast Asia and Northeast Europe. These are the largest fires on Earth and extensive sources of greenhouse gases, but poorly understood, becoming an emerging research topic in climate-change mitigation. In this chapter, a series of multistep heterogeneous kinetics are investigated to describe the drying and decomposition in smouldering combustion of peat. The decomposition schemes cover a range of complexity, including 2, 3 or 4-step schemes, and up to 4 solid pseudo-species. The schemes aim to describe the simultaneous pyrolysis and oxidation reactions of smouldering fires. A one-dimensional (0D) lumped model of mass loss is used to simulate thermogravimetric (TG) experiments in both nitrogen and air atmospheres. A genetic algorithm (GA) is applied to optimize the TG data from the literature, and to find the best kinetic parameters for four types of boreal peat from North China, Scotland and Siberia. The results show that all proposed schemes give a high degree of agreement with TG experiments. The validity of the schemes is then investigated outside the TG realm and incorporated into a 1-D plug-flow model to study the reaction profiles inside a smouldering front of peat. Both lateral and in-depth spread modes are considered. The results show that the drying sub-front is essential for peat fire, and that the best kinetics is 5-step with 5 condensed species (water, peat, α-char, β-char, and ash). This is the first time that the smouldering kinetics and the reaction-zone structure of a peat fire are explained and predicted, thus helping to understand this important natural and widespread phenomenon.

1. This chapter is based on "X. Huang, G. Rein (2014) *Smouldering Combustion of Peat: Inverse Modelling of the Thermal and Oxidative Degradation Kinetics*, **Combustion and Flame** 161: 1633-44."

1.1 Introduction

Smouldering combustion is the slow, low-temperature, flameless burning of porous fuels [1, 2] and the most persistent type of combustion phenomena [3]. It is sustained by the heat released when oxygen directly attacks the surface of a solid fuel [1]. It is different from the high-temperature homogenous flaming combustion, but especially common in solid fuels with a tendency to char. Many materials can sustain a smouldering fire, including synthetic fuels such as polyurethane foam or cellulosic insulation, and natural fuels like coal or soils rich in dead organic matter, like peat. Peatlands, made by the natural accumulation of partially decayed vegetation, are the most affected ecosystem by smouldering fires, both in frequency and size. Peat can form organic soil layers of carbon older than ten thousand years and of depths upon dozens of meters. They are the largest reserves of terrestrial carbon and the important ecosystem for a wide range of wildlife habitats, supporting biological diversity, and hydrological integrity [4].

Because of this vast accumulation of natural fuel, once ignited, smouldering peat fires burn for very long periods of time (*e.g.* months and years) despite extensive rains, weather changes, or fire-fighting attempts. These are the largest fires on Earth and large contributors of greenhouse gases [3–5]. Peat fires occur with some frequency worldwide in tropical, temperate and boreal regions (*e.g.* Indonesia, Canada, Florida, British Isles, and Siberia). During the 1997 extreme haze event in Southeast Asia, the greenhouse-gas emission from this single peatland fire was equivalent to 13-40% of the global man-made emissions of that year [4]. More recent figures estimate that the average emission from peat fires is roughly equivalent to 15% of the man-made emissions [6]. Moreover, the atmospheric release of ancient soil carbon and the sensitivity of peat ignition to higher temperatures and drier conditions create a positive feedback mechanism to climate change [3, 7].

For most smouldering fires and under typical conditions, two mechanisms control the rate of spread: the oxygen supply and heat loss [1]. At the micro scale, smouldering takes place on the surface of a solid fuel, and at the macro scale, it is a bulk phenomenon affecting a porous fuel bed at large. By reacting on the surface of the pores, the fire can penetrate deep into the bed of fuel if oxygen can be transported from a free surface (e.g. open atmosphere, crack or channel). Most peat fires are initiated on the top surface of the fuel bed [3]. The fire then spreads both laterally and in-depth, dominated by forward smouldering, as illustrated in Fig. 1.1. The lateral spread is enhanced by a direct supply of atmospheric oxygen so its rate is significantly faster than the in-depth spread. It leads to a void in the general shape of an ellipsoid or pan. When the uppermost layer is exposed to wind, the combustion is quenched by heat losses leaving a thin layer of charred material on the very top while smouldering continues just below it. As the fire propagates deeper, a layer of ash also builds up. These two layers, observed often in the field [8], act like an heat insulator to support the reaction front below.

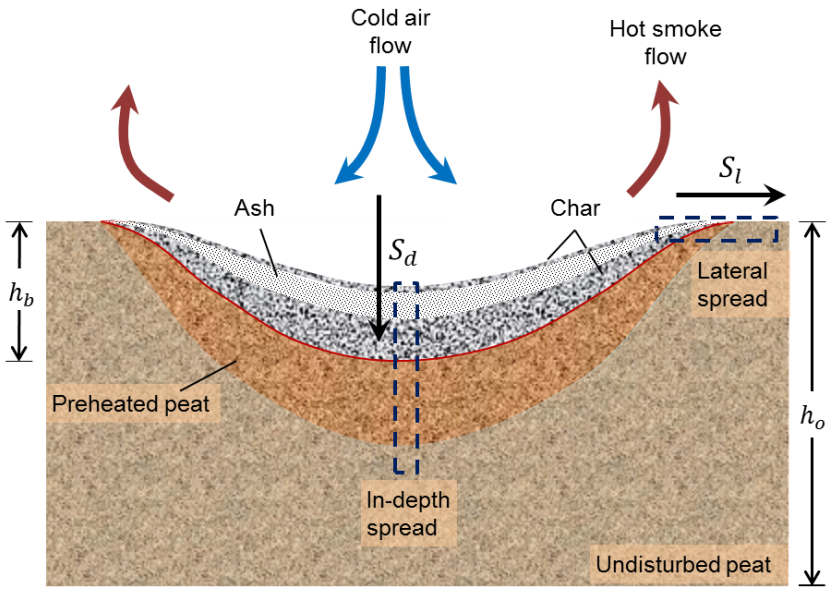

Figure 1.1: Schematic diagram of the lateral and in-depth spreads of a smouldering wildfire in a layer of peat.

The spread of smouldering fires is dominated by heat and mass transfer processes in a reactive porous media [1, 9, 10]. Among these mechanisms, the reactivity of peat in the form of a valid and quantified reaction scheme is currently missing. Knowledge of heterogeneous combustion reactions is less developed than homogenous gas-phase kinetics [9, 11]. One of the major reasons for this is that it is difficult to experimentally identify the various solid-phase species, especially for a complex organic mixture like peat [12]. Typically, kinetic schemes with just a few global steps and pseudo species are used. Current knowledge shows that smouldering combustion involves simultaneous and competing pyrolysis and oxidation reactions [1, 3, 10, 13].

Various kinetic schemes of different complexity have been proposed for smouldering combustion. Ohlemiller [1] proposed a 3-step and 3-species scheme, including one pyrolysis and two oxidations, as general scheme for any smoulder-prone fuel. Kashiwagi and Nambu [14] quantified the kinetic parameters of this scheme for cellulose using thermogravimetric analysis (TGA) on small samples (∼mg scale) under nitrogen and air atmospheres. Rein et al. [10] studied polyurethane foam, and extended Ohlemillers scheme to 5-step and 4-species kinetics (two pyrolysis and three oxidations). This extended scheme allows explaining the reaction structure of a smouldering front in both forward and opposed propagation. In doing so, Rein et al. [10] developed a methodology where a genetic algorithm is used to solve the corresponding inverse problem and find the best sets of kinetic and stoichiometric parameters of the scheme.

Because cellulose is an important component of biological matter, it should serve as foundation for the kinetics of peat. Hadden et al. [13] confirmed that the 3-step and 3-species scheme of Ohlemiller, and Kashiwagi and Nambu [14] qualitatively explained the

mass loss measurements taken during peat smouldering of large samples (∼100 g). Using TG data from Scottish and Siberian peat samples under air atmospheres, Cancellieri et al. [15] developed a 1-step and 2-species decomposition scheme and calculated analytically the corresponding set of kinetic parameters. Chen et al. [16] proposed and quantified two different schemes for the decomposition of a Chinese boreal peat based on TG data in both nitrogen and air atmospheres. In nitrogen, they proposed a 3-step and 3-species scheme whereas in air they proposed a 2-step and 3-species scheme. But the competition between pyrolysis and oxidation, key to smouldering spread, was not explicitly included or quantified. So far, no completing and quantified kinetic scheme including simultaneous pyrolysis and oxidation reactions has been proposed to explain smouldering peat fires.

In this chapter, TG data from the literature is used to propose, quantify and investigate a reaction scheme for smouldering of peat based on a 5-step (1-step drying plus 4-step decomposition) and 5-species kinetics scheme. Other simpler 3- and 2-step decomposition schemes are also investigated. Following the work of Rein et al. [10], a genetic algorithm is employed to find the best set of kinetic parameters for each of the schemes and for four different types of peat, from China (CH), Scotland (SC) and Siberia (SI-A and SI-B). The schemes are then applied to simulate the reaction-zone structure using a 1-D steady-state species model. This simple yet comprehensive model allows investigating the effect of the assumed reaction schemes on predicting the front structures in both lateral and in-depth spread modes.

1.2 Smouldering kinetics of peat

From the viewpoint of fire behaviour, the most important components of peat are the organic matter (OM), water and minerals [17, 18]. The left hand side of Fig. 1.2 shows the relative amounts of the different components found in typical peat samples, although the proportions can vary significantly with the ecosystem type (i.e. boreal, temperate or tropical), originating vegetation (e.g. sphagnum or feather) and depth (i.e. age and level of decomposition) [19]. Generally, carbon is one of the most abundant chemical elements and its fraction in peat is between 30 and 65% [19], similar to common biomass types [20] and most synthetic polymers [21].

1.2.1 Moisture content and drying

Peat can hold a wide range of moisture content [2] (MC) ranging from about 10% under drought conditions to well in excess of 300% under flooded conditions [8]. Thus, the drying process is crucial in determining the ignition and spread of smouldering peat

2. Moisture content (MC) is defined in dry basis as the mass of water divided by the mass of a dried soil sample. For a peat with a typical dry bulk density of 100 kg/m^2 and porosity of 0.9 [17], 10 vol% water results in a water bulk density of 100 kg/m^3, that is, MC = 100%.

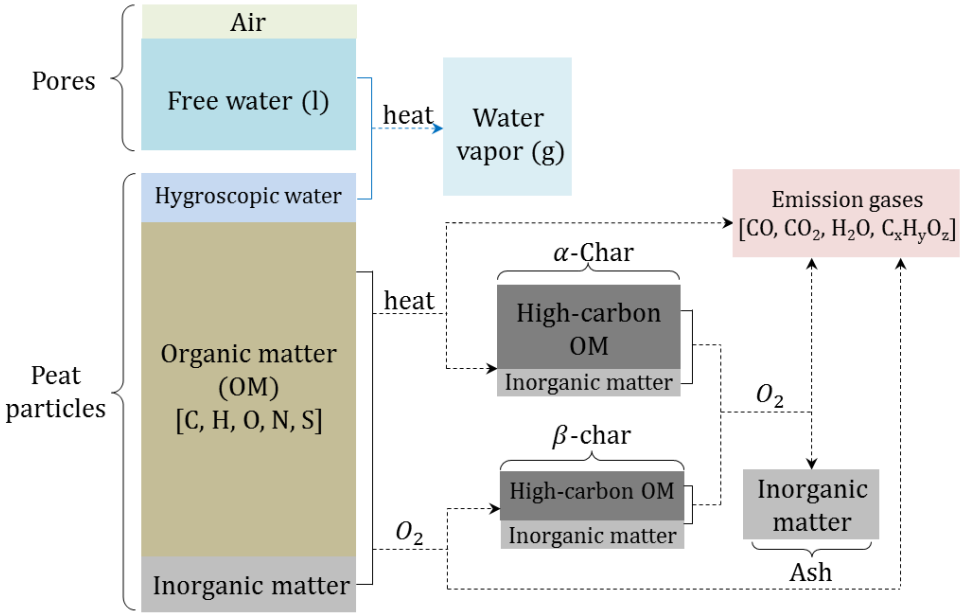

Figure 1.2: The composition of peat and a possible decomposition paths and products.

fires [3, 17, 18, 22]. The prominent role of moisture is such that natural or anthropogenic-induced droughts are the leading cause of smouldering megafires [3].

Condensed-phase water can exist within a porous media like peat in two different forms: hygroscopic (<10 vol% which is equivalent to MC < 100% [2]) and free (capillary and gravity, 10-40 vol%) [23] (see Fig. 1.2). The drying of peat is a multi-step physicochemical process that takes place at relatively low temperatures while the thermal decomposition is negligible. At high MC, water evaporation from porous media starts with the gravity free water in the large pores and then the capillary water in the small pores. As the water content decreases, the drying process finishes with the evaporation of the hygroscopic water bonded to the surface of peat particles [23]. Experimental studies [17, 18, 22] show that peat is not susceptible to fire ignition when the MC is above 115%. Therefore, the drying of free water is of low interest in peat fires and not studied here. Hygroscopic water in porous media is dominant at MC< 100% and can exist above the boiling temperature. In this form, the water is bonded to the solid surface within a thin film of 4-5 molecules thickness, so it cannot flow but only change to the vapour phase as temperature increases [24]. This allows modelling the drying as the dissociation step of peat-bound water as follows:

$$\text{Peat} \cdot \nu_w \text{H}_2\text{O} \rightarrow \text{Peat} + \nu_w \text{H}_2\text{O(g)}, \quad \text{(Drying)} \tag{1.1}$$

where ν_w = MC is the initial moisture content in the dry basis, and the dot in Eq. (1.1) means the water is bonded to the peat. The conversion of the mass fraction from dry basis ($[m_i]$) to the wet basis (m_i) is $m_i = [m_i](1 - m_{w0}) = [m_i]/(1+\text{MC})$. This drying step is mainly a chemical process, and can be modelled with a 1-step Arrhenius expression [25, 26].

1.2.2 Peat decomposition

As temperature increases, the decomposition of the organic soil becomes dominant. Despite of the complex composition and chemical process, experimental observations [13, 15, 16, 22] suggest that a few steps of global reactions can capture the most important behaviour of the thermal and oxidative degradation of peat. TG experiments in nitrogen atmosphere give information on the thermal decomposition and show that there is at least a 1-step pyrolysis process. Results in air atmosphere provide information on the simultaneous thermal and oxidative decomposition, and show that at least two additional steps are needed (to be presented later) .

The validity and accuracy of a proposed kinetic scheme reflects the understanding of the chemical process and the quantity and quality of the available experimental data, but little is known about the decomposition of peat. Further referring to the decomposition of biomasses [27, 28] and cellulose [14] and taking into account that smouldering involves the competition of pyrolysis and heterogeneous oxidations [3, 13], it is proposed here that the most complete yet simple global decomposition scheme for peat would be a 4-step, including peat pyrolysis, peat oxidation, β-char oxidation, and α-char oxidation with 4 solid pseudo-species (peat, α-char, β-char, and ash):

$$\text{Peat} \rightarrow \nu_{\alpha,pp}\alpha\text{-Char} + \nu_{g,pp}\text{Gas} \qquad \text{(Peat Pyrolysis)} \qquad (1.2)$$

$$\text{Peat} + \nu_{O_2,po}O_2 \rightarrow \nu_{\beta,po}\beta\text{-Char} + \nu_{g,po}\text{Gas} \qquad \text{(Peat Oxidation)} \qquad (1.3)$$

$$\beta\text{-Char} + \nu_{O_2,\beta o}O_2 \rightarrow \nu_{a,\beta o}\text{Ash} + \nu_{g,\beta o}\text{Gas} \qquad (\beta\text{-Char Oxidation}) \qquad (1.4)$$

$$\alpha\text{-Char} + \nu_{O_2,\alpha o}O_2 \rightarrow \nu_{a,\alpha o}\text{Ash} + \nu_{g,\alpha o}\text{Gas} \qquad (\alpha\text{-Char Oxidation}) \qquad (1.5)$$

where $\nu_{i,k}$ is the mass stoichiometric coefficient of species i ($= O_2$, g, p, α, β, a) in the reaction k ($= pp$, po, βo, αo). This scheme is also conceptually represented in Fig. 1.2. Overall, there are two possible parallel paths involved: (a) peat$\rightarrow$ α-char $\rightarrow$ash (Eqs. (1.2) and (1.5)), and (b) peat$\rightarrow$ β-char $\rightarrow$ash (Eqs. (1.3) and (1.4)).

Char is also called pyrogenic char or black carbon, and contains carbon in a porous structure but also other hydrocarbons and mineral species [12]. Due to the release of gaseous OM (e.g. volatiles and pyrolysate) in Eqs. (1.2) or (1.3), char has a lower organic content (OC) than the original peat (see Fig. 1.2). The α-char and β-char are yielded through different decomposing mechanisms, so in general they have different structures, compositions, and reactivities. The peak temperature in smouldering combustion of peat is about 800 K [13, 22], so the high-temperature pyrolysis of char and the decomposition of the minerals [16] are negligible and not included in the kinetics.

1.2.3 Reaction rate and mass evolution in TG experiment

Arrhenius-type reaction remains the most widely used expression to quantify and to simulate condensed-phase reactions [10, 11]. The reaction rate for each of the reactions

in Eqs. (1.1-1.5) is as follows:

$$\dot{\omega}_k(T, m_i, Y_{O_2}) = \left(m_{i\sum}\right) Z_i e^{-E_k/RT} \left(\frac{m_i}{m_{i\sum}}\right)^{n_k} Y_{O_2}^{n_{O_2,k}}, \tag{1.6}$$

where kinetic parameters Z_k, E_k, n_k and $n_{O_2,k}$ are the pre-exponential factor, activation energy, reaction-order of condensed species, and reaction-order of oxygen in the reaction k, respectively. The mass fraction of condensed species i, m_i, respects to the initial sample mass (i.e. in the wet basis). The cumulative mass is defined as

$$m_{i,\Sigma} = m_{i,0} + \int_0^t \dot{\omega}_{fi} d\tau$$

which remains constant or increases monotonically [29], avoiding zero in dominator for intermediate species ($m_{i0} = 0$) like chars. During the drying stage, the mass loss of the OM in peat is assumed to be negligible and that it does not interfere with the drying process. This is confirmed in the later sections of this chapter.

For each reaction, the kinetic and stoichiometric ($v_{i,k}$) parameters for peat are unknown, and difficult to be measured directly. TG experiments provide an ideal environment of controllable atmosphere and heating rate, and negligible thermal gradient and transport effects during the degradation of the small solid samples (∼mg). Therefore, the mass-loss rate measured during TG can be well simulated by a lumped zero-dimensional (0D) model, which for the 5-step kinetics above is as follows:

$$\begin{aligned}
\dot{m}_w &= -\dot{\omega}_{dr}, \\
\dot{m}_p &= -\dot{\omega}_{pp} - \dot{\omega}_{po}, \\
\dot{m}_\beta &= \nu_{\beta,po}\dot{\omega}_{po} - \dot{\omega}_{\beta o}, \\
\dot{m}_\alpha &= \nu_{\alpha,pp}\dot{\omega}_{pp} - \dot{\omega}_{\alpha o}, \\
\dot{m}_a &= \nu_{a,\beta o}\dot{\omega}_{\beta o} + \nu_{a,\alpha o}\dot{\omega}_{\alpha o}.
\end{aligned} \tag{1.7}$$

Thus, the total mass-loss rate of the sample is

$$\begin{aligned}
\dot{m} =& \dot{m}_w + \dot{m}_p + \dot{m}_\beta + \dot{m}_\alpha + \dot{m}_a \\
=& -\dot{\omega}_{dr} + (\nu_{\alpha,pp} - 1)\dot{\omega}_{pp} + (\nu_{\beta,po} - 1)\dot{\omega}_{po} \\
&+ (\nu_{a,\beta o} - 1)\dot{\omega}_{\beta o} + (\nu_{a,\alpha o} - 1)\dot{\omega}_{\alpha o}.
\end{aligned} \tag{1.8}$$

The initial conditions, rate of temperature increase, and atmosphere oxygen fraction are set to simulate the environment in the corresponding TG experiment as follows,

$$\begin{cases}
m_w(0) = m_{w0}, \\
m_p(0) = 1 - m_{w0}, \\
m_\alpha(0) = m_\beta(0) = m_a(0) = 0, \\
T(0) = T_0,
\end{cases} \tag{1.9}$$

$$\begin{cases} Y_{O_2} = 0 \ (N_2) \text{ or } Y_{O_2} = 0.232 \ (\text{air}), \\ \dfrac{dT}{dt} = \beta, \end{cases} \tag{1.10}$$

where the wet-basis moisture content (m_{w0}) can be converted to the dry-basis as MC $= m_{w0}/(1 - m_{w0})$; β is the heating-rate constant, i.e. the controlled temperature-increase rate inside the oven, converting the time-dependent problem into a temperature-dependent problem. Then, unknown parameters can be inversely modelled by matching the simulated mass losses with those in TG experiments.

TG data at various oxygen concentrations is needed to find the reaction-order for oxygen ($n_{O_2,k}$). As a first approximation, that $n_{O_2,i} = 1$ in oxidation and $n_{O_2,k} = 0$ in pyrolysis (i.e. oxygen independent) is assumed [10]. If a TG test is only performed in air (e.g. [15]), the scheme cannot distinguish the pyrolysis from the peat oxidation, and the accurate value for $n_{O_2,k}$ cannot be found.

Because the mass of inorganic matter (or minerals) is conserved during smouldering and becomes the ash after combustion (see Fig. 1.2), the stoichiometric parameters in consecutive reactions satisfy

$$\text{IC} = 1 - \text{OC} = \nu_{\alpha,pp}\nu_{a,\alpha o} = \nu_{\beta,po}\nu_{a,\beta o}, \tag{1.11}$$

where the initial inorganic content (IC) of peat relates to the initial MC and the mass of ash after combustion (m_a), as IC $= m_a/(1 - m_{w0}) = m_a(1+\text{MC})$.

Therefore, this system of ordinary differential equations contains a total of 18 unknown parameters: (Z_k, E_k, n_k) from the 5 reactions in the form of Eq. (1.6), plus m_{w0}, $\nu_{\alpha,pp}$ and $\nu_{\beta,po}$. The large number of unknowns produces a large search space and results in a complex landscape for the optimization, with numerous local maxima and minima. Solving it demands an efficient multi-dimensional optimization algorithm such as a Genetic Algorithm (GA) which has been used successfully in previous related work [10].

1.3 Inverse Kinetics Modelling

In the section, the smouldering kinetic and stoichiometric parameters for four peat soils (CH, SC, SI-A and SI-B) are first determined by optimization of the 0D TG experiments. Afterwards, in Section 1.4 these parameters will be further applied into a 1D plug flow model.

1.3.1 Genetic algorithm and optimization techniques

A Genetic Algorithm (GA) is a heuristic search method, imitating the principles of biological adaption based on Darwinian survival-of-the-fittest theory [30, 31]. In a GA, the candidate solutions represent the individuals in a population that evolves with time in a predetermined environment. It has been widely used in research of combustion science,

such as engine design [32], gas kinetics [33, 34], condensed-phase kinetics [10], and fire pyrolysis [35].

The search goal is to achieve a minimum overall error with all experimental TG data, defined as:

$$\Phi_i = \gamma \frac{\sum |\dot{m}_{pre,i} - \dot{m}_{exp,i}|}{\sum \dot{m}_{exp,i}} + (1-\gamma) \frac{\sum |m_{pre,i} - m_{exp,i}|}{\sum m_{exp,i}}, \tag{1.12}$$

which accounts for relative errors in both the total mass (m) and the mass-loss rate ($\dot{m}$), and γ is set to 0.5 [3], giving equal importance to each term. The summations in Eq. (1.12) are evaluated for each experiment data in the temperature range (from 300 to 900 K). In order to improve the uniqueness of solution, TG tests conducted in different atmospheres and heating rates can be optimized simultaneously. Then, the overall error is defined as the linear combination of the error in each test as

$$\Phi = \sum_{i=1}^{N} w_i \Phi_i, \qquad \left(\sum_{i=1}^{N} w_i = 1 \right) \tag{1.13}$$

where w_i is the weight coefficient. The GA code used here is GAOT [36]. Generally, good results are reached with a size population (the number of candidate solutions) between 100 and 500. The algorithm is stopped when little decrease in Φ ($\Delta\Phi < 0.1\%$) occurs after several hundred generations (iterations). Typically, convergence was achieved in less than 500 generations, requiring a total computer time of about 2 h with an Intel *i*7-3770 (3.40 GHz×8) CPU.

Table 1.1: Characteristics of four peat samples.

Name	CH [16]	SC [15]	SI-A [15]	SI-B [15]
Location	North China	Scotland	Siberia [19]	Siberia
Decomposition degree [a]	undecomposed [19]	42%	20%	10.5%
Organic content [b]	low (81.7%)	high (98.2%)	high (97.6%)	medium (87.9%)
Carbon fraction	low (∼ 30%)	high (53.32%)	medium (44.81%)	medium (43.09%)

a. Decomposition degree is defined by the fraction of structureless components observed in peat soil.
b. Organic content (OC) in dry basis is estimated in later sections.

1.3.2 Kinetic parameters of CH peat

The kinetic and stoichiometric parameters for an air-dried low-carbon Chinese (CH) peat (see Table 1.1) are first determined. The TG experiments were conducted by Chen et al. [16] at three heating rates, β = 7.5, 10, and 12.5 K/min, shown in Figs. 1.3 and

3. Simulations shows that the value of γ have little influence to optimization results.

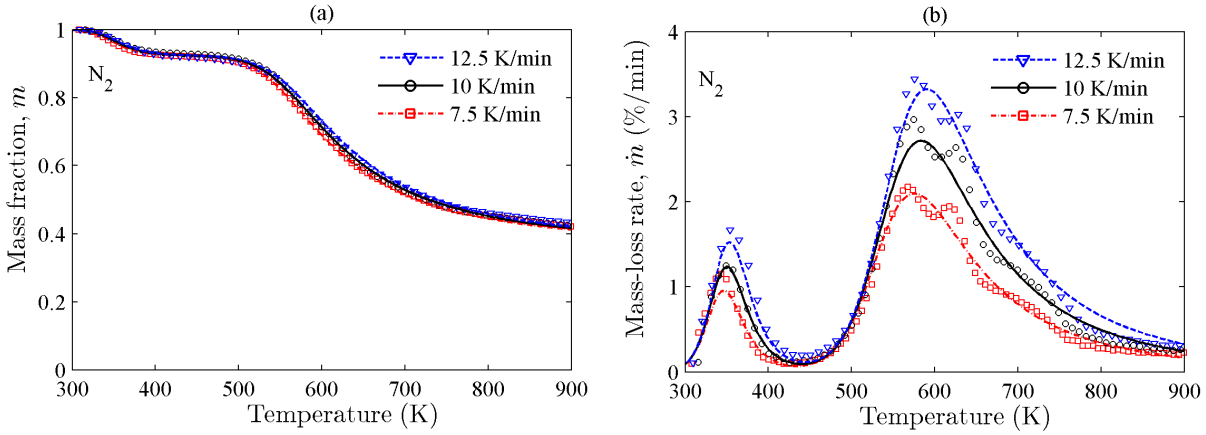

Figure 1.3: (a) mass, and (b) mass-loss rate of CH peat in nitrogen (wet basis) as a function of temperature for three heating rates. Marks: experimental data [16], and lines: simulations.

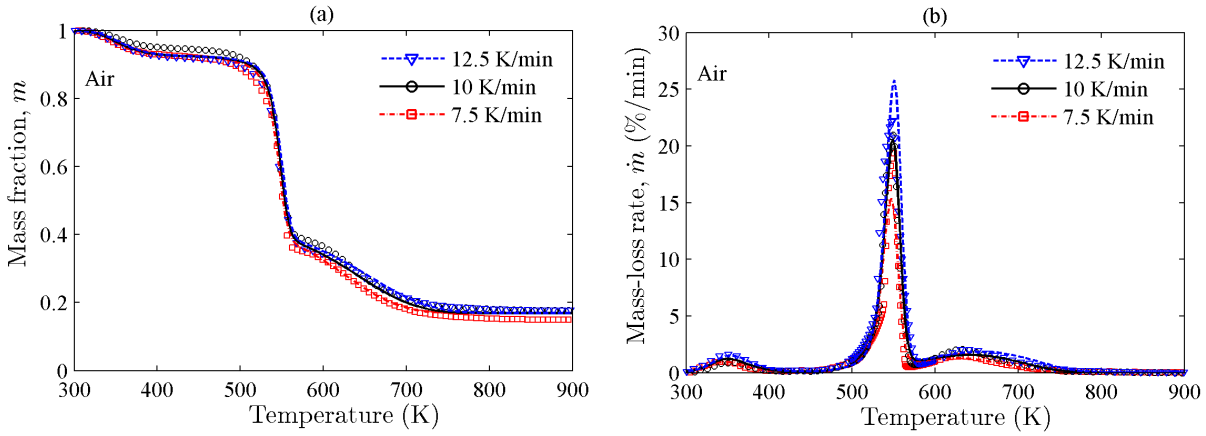

Figure 1.4: (a) mass, and (b) mass-loss rate of CH peat in air (wet basis) as a function of temperature for three heating rates. Marks: experimental data [16], and lines: simulations. Note that the scale in Fig. 1.3b is different from that in Fig. 1.4b.

1.4. For decomposition in nitrogen (Fig. 1.3), there are two peaks in the DTG curve: the low-temperature peak for drying and the high-temperature peak for peat decomposition. For decomposition in air (Fig. 1.4), one more peak is observed in the DTG curve at higher temperature (> 600 K), indicating the char oxidation. Moreover, the second peak for peat decomposition increases significantly, suggesting an important role of oxygen.

All six tests are modelled simultaneously with a same weight coefficient (w_i=1/6). The best value found for each parameter is listed in Table 1.2, together with the range of values of other good solutions (i.e. top individuals satisfying $\Delta\Phi = \Phi - \Phi_{min} < 0.3\%$). The experimental data and simulated TG curves are compared in Figs. 1.3 (nitrogen) and 1.4 (air).

In general, the proposed kinetics captures the position and magnitude of all TG data. The minimum value of the error is Φ_{min}=7.4%. The best value found for the initial

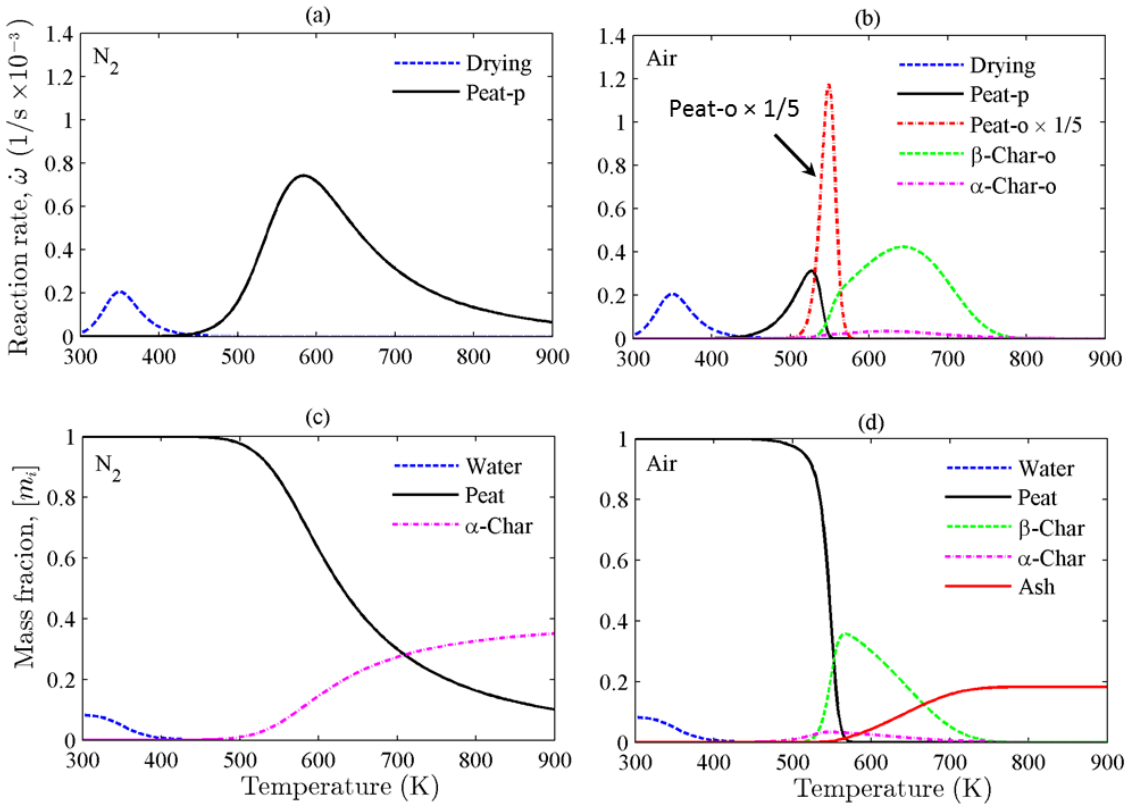

Figure 1.5: Simulation results of the TG experiment for CH peat at $k = 10$ K/min, (a) reaction rates, $\dot{\omega}_i$, and (b) dry-basis mass fractions, $[m_i]$, in nitrogen; (c) reaction rates, $\dot{\omega}_i$, and (d) dry-basis mass fractions, $[m_i]$, in air. The rate of peat oxidation is scaled down by 1/5 due to its exceptionally high peak.

moisture content, MC=8.4% is similar to the value of 9% found independently in [16] for the same peat sample. In nitrogen experiments (Fig. 1.3b), scrutiny reveals that the third (soft) peak in mass-loss rate just above 600 K cannot be simulated by the 1-step pyrolysis of Eq. (1.2). However, this second peak is of low intensity, taking place very close to the first higher peak between 580 and 620 K. Moreover, as it would be seen in Fig. 1.4b, above 550 K, the oxidation of peat or char is already dominant, and pyrolysis does not play an important role.

The simulated reaction rates, $\dot{\omega}_i$, and the dry-basis mass fractions, $[m_i]$, at $k = 10$ K/min are shown in Fig. 1.5. The first peak of mass-loss rate in both nitrogen (Fig. 1.3b) and air (Fig. 1.4b) between 300 and 400 K, is correctly simulated by Eq. (1.1) as the drying stage. In nitrogen (Fig. 1.3b), the subsequent peak is simulated by Eq. (1.2) as the peat pyrolysis. No clear overlapping between drying and pyrolysis is observed, which confirms the assumption of negligible peat decomposition during drying. In air (Fig. 1.5b), after drying, the simultaneous pyrolysis and oxidation reactions of peat as well as the subsequent β-char oxidation overlap in a narrow temperature range (500-570 K), producing the highest peak of mass-loss rate in Fig. 1.4b. Comparison between nitrogen and air simulations shows that in TG, the oxidation dominates the peat decomposition

($\dot{\omega}_{po}^{max}/\dot{\omega}_{pp}^{max} = 19$). Figure 1.5d shows that the production of β-char is larger than that of α-char ($m_{\beta}^{max}/m_{\alpha}^{max} = 11$). This also explains that above 500 K the oxidation rate of β-char is larger than that of α-char ($\dot{\omega}_{\beta o}^{max}/\dot{\omega}_{\alpha o}^{max} = 12$ in Fig. 1.5b). In other words, for this sample and under TG conditions (i.e. heating rate and ambient condition), the reaction path (b) (Peat→ β-char →ash) is about one order of magnitude faster than the alternative path (a) (Peat→ α-char →ash).

Table 1.2: Kinetic and stoichiometric parameters for the CH peat sample with the 5-step scheme.

Parameter	Best	Range	Unit
MC	8.4	[8.2, 9.3]	(%)
OC	81.7	-	(%)
$\lg Z_{dr}$	8.12	[6.05, 8.65]	$\lg(s^{-1})$
E_{dr}	67.8	[54.8, 71.3]	kJ/mol
n_{dr}	2.37	[1.77, 2.77]	-
$\lg Z_{pp}$	5.28	[4.28, 5.77]	$\lg(s^{-1})$
E_{pp}	86.0	[75.9, 91.1]	kJ/mol
n_{pp}	4.44	[3.58, 4.47]	-
$\nu_{\alpha,pp}$	0.39	[0.39, 0.43]	kg/kg
$\lg Z_{po}$	30.6	[28.3, 34.5]	$\lg(s^{-1})$
E_{po}	332	[309, 373]	kJ/mol
n_{po}	1.36	[1.24, 1.67]	-
$\nu_{\beta,po}$	0.43	[0.42, 0.45]	kg/kg
$\lg Z_{\beta o}$	1.86	[1.68, 2.19]	$\lg(s^{-1})$
$E_{\beta o}$	46.9	[45.0, 51.0]	kJ/mol
$n_{\beta o}$	0.93	[0.85, 0.93]	-
$\nu_{a,\beta o}$ [a]	0.43	-	kg/kg
$\lg Z_{\alpha o}$	2.57	[1.95, 2.57]	$\lg(s^{-1})$
$E_{\alpha o}$	54.1	[54.1, 60.4]	kJ/mol
$n_{\alpha o}$	1.53	[0.96, 1.57]	-
$\nu_{a,\alpha o}$ [a]	0.47	-	kg/kg
Φ	7.4	< 7.7	(%)

a. Calculated from Eq. (1.11).

In Table 1.2, the best values found for the kinetic triplet (Z_k, E_k, and n_k) fall in relatively wide ranges. However, their wide variations yield small differences in terms of error ($\Delta\Phi < 0.3\%$). Investigation of interdependence inside these ranges shows a clear linear compensation effect [11, 37] between $\lg Z_k$ and E_k. The sample data is plotted in

Fig. 1.6a and fitted as

$$\begin{cases} \lg Z_{dr} = -2.52 + 0.157E_{dr}, & (R^2_{dr} = 1.00) \\ \lg Z_{pp} = -3.21 + 0.099E_{pp}, & (R^2_{pp} = 1.00) \\ \lg Z_{po} = -1.58 + 0.097E_{po}, & (R^2_{po} = 1.00) \\ \lg Z_{\beta o} = -2.26 + 0.087E_{\beta o}, & (R^2_{\beta o} = 0.99) \\ \lg Z_{\alpha o} = 4.30 - 0.038E_{\alpha o}, & (R^2_{\alpha o} = 0.44) \end{cases} \tag{1.14}$$

showing a high linearity as measured by the R^2 coefficient, except for the α-char oxidation. The reaction order, n_k, also depends on E_k for all reactions, (see Fig. 1.6b). Except for $n_{\alpha o}$, all other n_k increases linearly with E_k, although the scatter of data is significant. Therefore, the kinetic triplet (Z_k, E_k and n_k) are interdependent. Such interdependence has recently been proved mathematically by [38]. For α-char oxidation, the most likely reason for the non-linear dependence of the triplet is that its very low reaction rate carries a low contribution to the total mass loss measured in TG. This is a limitation in the experimental data available that cannot provide sufficiently information to fix the temperature range and reaction rate of α-char oxidation accurately. Therefore, this serves as evidence that adding more reaction steps would not improve the interpretation of this TG data.

Finding the right level of complexity is a key question in kinetics modelling. In order to explore this issue, a reduced 3-step decomposition scheme with 3 solid pseudo-species for peat decomposition is obtained,

$$\begin{aligned} &\text{Peat} \rightarrow \nu_{\alpha,pp}\text{Char} + \nu_{g,pp}\text{Gas}, && \text{(Peat Pyrolysis)} \\ &\text{Peat} + \nu_{O_2,po}O_2 \rightarrow \nu_{c,po}\text{Char} + \nu_{g,po}\text{Gas}, && \text{(Peat Oxidation)} \\ &\text{Char} + \nu_{O_2,co}O_2 \rightarrow \nu_{a,co}\text{Ash} + \nu_{g,co}\text{Gas}, && \text{(Char Oxidation)} \end{aligned} \tag{1.15}$$

where only one type of char is considered. Chen et al. [16] proposed a more reduced 2-step scheme with 3 solid pseudo-species by neglecting the peat pyrolysis of Eq. (1.2) and lumping it into the peat oxidation of Eq. (1.3),

$$\begin{aligned} &\text{Peat} + \nu_{O_2,po}O_2 \rightarrow \nu_{c,po}\text{Char} + \nu_{g,po}\text{Gas}, && \text{(Peat Oxidation)} \\ &\text{Char} + \nu_{O_2,co}O_2 \rightarrow \nu_{a,co}\text{Ash} + \nu_{g,co}\text{Gas}. && \text{(Char Oxidation)} \end{aligned} \tag{1.16}$$

Figure 1.7 compares the results obtained with the different decomposition schemes plus drying, where only the mass-loss rate in air at 10 K/min is considered for the optimization and reported. No clear difference can be found between different schemes, and their degrees of fit are very similar: $\Phi_{min} = 7.7\%$ (2-step), 5.6% (3-step), and 5.4% (4-step). One major reason for such a good fit is that under TG conditions and air atmosphere, the reaction path (b) (Peat $\rightarrow$ β-char $\rightarrow$ ash) overwhelms the parallel path (a) (Peat $\rightarrow$ α-char $\rightarrow$ ash) so giving less importance to some of the reactions in the 4-step decomposition.

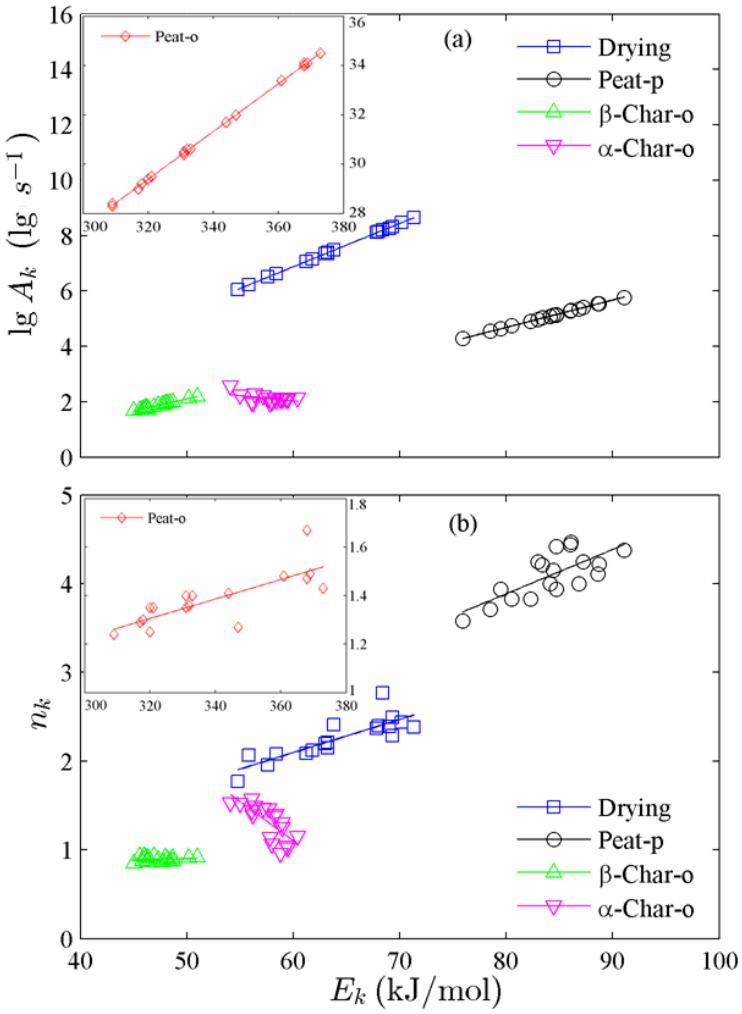

Figure 1.6: Interdependence among the kinetic parameters: (a) $\lg(Z_i)$ against E_i, and (b) n_i against E_i; data from good solutions satisfying $\Delta\Phi < 0.1\%$. The inserted sub-figures have different scales.

As the results show here, it is difficult to discern the relatively superiority of each schemes in the TG realm because the inverse modelling approach forces good results in all cases. However, in Section 1.4, this issue is further analyzed by applying these schemes and the kinetics parameters into a plug-flow model of a smouldering front.

1.3.3 Kinetic parameters of carbon-rich peat

The kinetic and stoichiometric parameters for another three oven-dried carbon-rich peat from Scotland (SC) and Siberia (SI-A and SI-B) have been found. The characteristics of the samples are listed in Table 1.1. The TG experiments were conducted by Cancellieri et al. [15] at three heating rates, $\beta = 10$, 20, and 30 K/min, in air only. The TG data is available at 500-900 K, so the drying process cannot be explored. Note that without TG results in a non-oxidizing atmosphere (e.g. nitrogen), the separation between the pyrolysis and oxidations reactions cannot be established thus leading to inaccuracies in

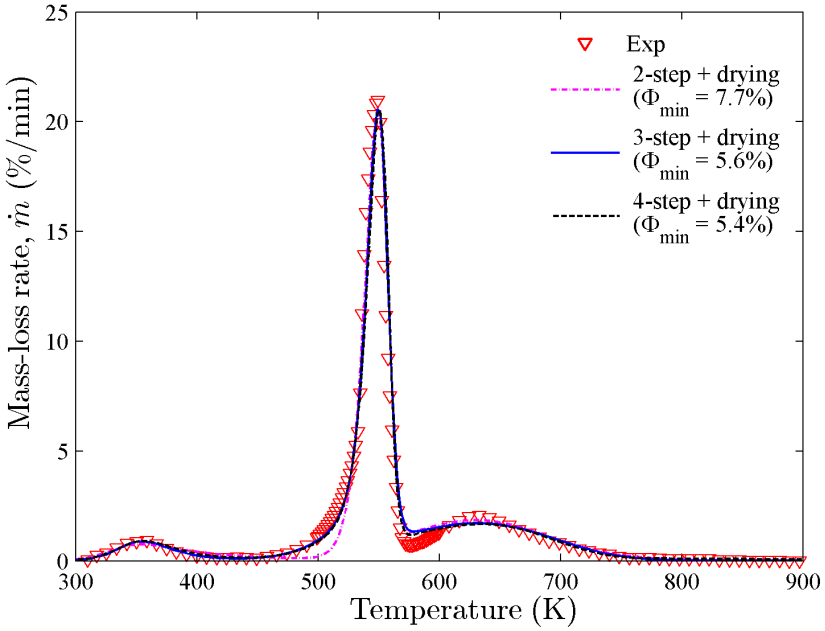

Figure 1.7: Mass-loss rate of CH peat in air (k = 10 K/min) simulated by chemical schemes with different number of steps. The number of steps in the legend includes the drying plus the peat decomposition steps.

the kinetics.

The highest heating rate of 30 K/min of this TG data is close to the range of heating rates observed experimentally in smouldering peat samples (between 30 and 50 K/min [39]). For this group of experimental data, the quality of inversely modelled kinetic parameters is investigated by optimizing with only the 20 K/min data, and using the other two heating rates (10 and 30 K/min) as blind predictions.

Due to the interdependence among three kinetics parameters, all reaction orders ($n_k = 1$) for the SI-A peat are fixed here. The values found for all kinetic and stoichiometric parameters are listed in Table 1.3. The minimum errors are Φ_{min}=1.5% (SC), 4.5% (SI-A), and 3.5% (SI-B). The experimental and simulated TG curves are compared in Fig. 1.8. In general, the proposed kinetics successfully captures the position and magnitude of all TG curves between 500 and 900 K at 20 K/min. The blind predictions for 10 and 30 K/min also show a good agreement, demonstrating the capabilities of the kinetic scheme when extrapolated to different heating rates. A strong linear compensation effect among $\lg Z_k$ and E_k is also observed for all reactions of 3 peat, similarly to the CH peat in Fig. 1.6.

The simulated reaction rates, $\dot{\omega}_k$, and the dry-basis mass fractions, m_i, at 20 K/min are explored in Fig. 1.9 (the results of 10 K/min and 30 K/min are very similar, not shown here). Similar to the results of CH samples, the rates of peat pyrolysis and oxidation peak at 550-600 K, and then rates of two char oxidations peak at about 700 K. But unlike the CH sample which has a large peat-oxidation rate and a small char-oxidation rate, these high-OC samples show that the maximum value of all reactions rates are in the

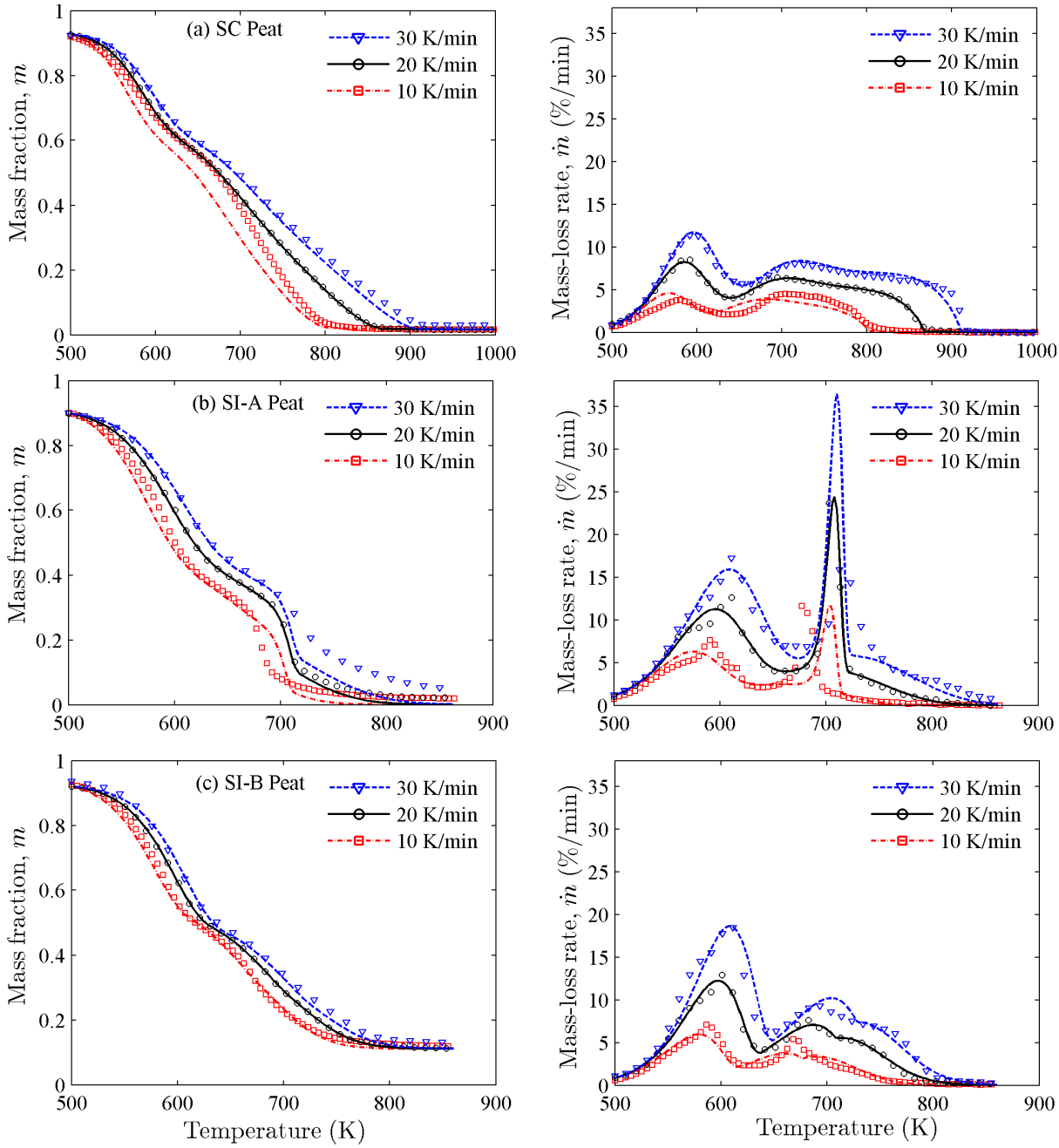

Figure 1.8: The wet-basis mass loss (up) and mass-loss rate (down) of (a) SC, (b) SI-A, and (c) SI-B samples in air for three heating rates. Marks: experimental data [15], and lines: simulations.

same order of magnitude. Also, α-char and β-char oxidations play a similarly important role at high temperature. These suggest that the differences in reactivity seen between CH and SC/SI samples are due to the different carbon contents which increase with decomposition degrees (see Table 1.1).

The influence of the number of reactions is also discussed here. Figure 1.10 compares the original 4-step decomposition scheme in Eqs. (1.2-1.5) with the 3-step scheme in Eq. (1.15) and the 2-step scheme in Eq. (1.16) by modelling the mass-loss rate at 20 K/min.

Table 1.3: Kinetic and stoichiometric parameters for Scottish and Siberian peat samples with the 4-step scheme of peat decomposition.

Peat type	SC		SI-A		SI-B		
Parameter	Best	Range	Best	Range	Best	Range	Unit
MC	8.1	[8.0, 8.2]	11.3	[11.2, 11.5]	8.8	[8.7, 8.9]	(%)
OC	98.2	-	97.6	-	87.9	-	(%)
$\lg Z_{pp}$	5.92	[5.75, 6.31]	4.81	[4.79, 5.99]	4.63	[3.58, 5.66]	$\lg(s^{-1})$
E_{pp}	93.3	[91.1, 97.6]	80.0	[80.0, 93.5]	74.3	[63.0, 84.6]	kJ/mol
n_{pp}	1.01	[0.96, 1.05]	1	-	1.64	[1.53, 1.91]	-
$\nu_{\alpha,pp}$	0.75	[0.70, 0.97]	0.55	[0.55, 0.68]	0.93	[0.92, 0.99]	kg/kg
$\lg Z_{po}$	6.51	[5.92, 6.69]	5.72	[4.26, 5.72]	7.62	[6.82, 8.80]	$\lg(s^{-1})$
E_{po}	89.8	[83.7, 91.6]	85.1	[68.4, 85.1]	104	[94.6, 116]	kJ/mol
n_{po}	1.03	[0.91, 1.03]	1	-	0.65	[0.63, 0.80]	-
$\nu_{\beta,po}$	0.65	[0.53, 0.68]	0.46	[0.35, 0.46]	0.30	[0.26, 0.32]	kg/kg
$\lg Z_{\beta o}$	1.65	[1.61, 1.73]	50.3	[49.6, 63.8]	5.06	[5.06, 5.83]	$\lg(s^{-1})$
$E_{\beta o}$	52.4	[51.8, 53.7]	689	[680, 872]	91.7	[91.7, 112]	kJ/mol
$n_{\beta o}$	0.54	[0.48, 0.57]	1	-	0.59	[0.50,0.63]	-
$\nu_{a,\beta o}$ [a]	0.03	-	0.05	-	0.40	-	kg/kg
$\lg Z_{\alpha o}$	7.04	[6.63, 7.75]	2.83	[2.16, 3.56]	4.69	[3.93, 4.91]	$\lg(s^{-1})$
$E_{\alpha o}$	112	[106, 120]	59.8	[51.0, 69.3]	80.8	[71.5, 83.4]	kJ/mol
$n_{\alpha o}$	1.85	[1.79, 2.14]	1	-	1.49	[1.34, 1.55]	-
$\nu_{a,\alpha o}$ [a]	0.02	-	0.04	-	0.13	-	kg/kg
Φ	1.5	<1.7	4.5	<4.8	3.5	<3.7	(%)

a. Calculated from Eq. (1.11)

Both the 3-step and 2-step schemes can roughly capture the two peaks of mass-loss rate, but the agreement is poor, especially for high-moor SC and SI-A peat. The difference in the degree of fit between 2-step and 3-step schemes is very tiny (difficult to discriminate for SC and SI-A samples in Fig. 1.10). Moreover, the simulation also reveals that with 3-step or 2-step kinetics the disagreement further increases in the blind prediction of other heating rates. Therefore, including two kinds of char (α-char and β-char) could be crucial to explain the smouldering combustion of peat with a high OC.

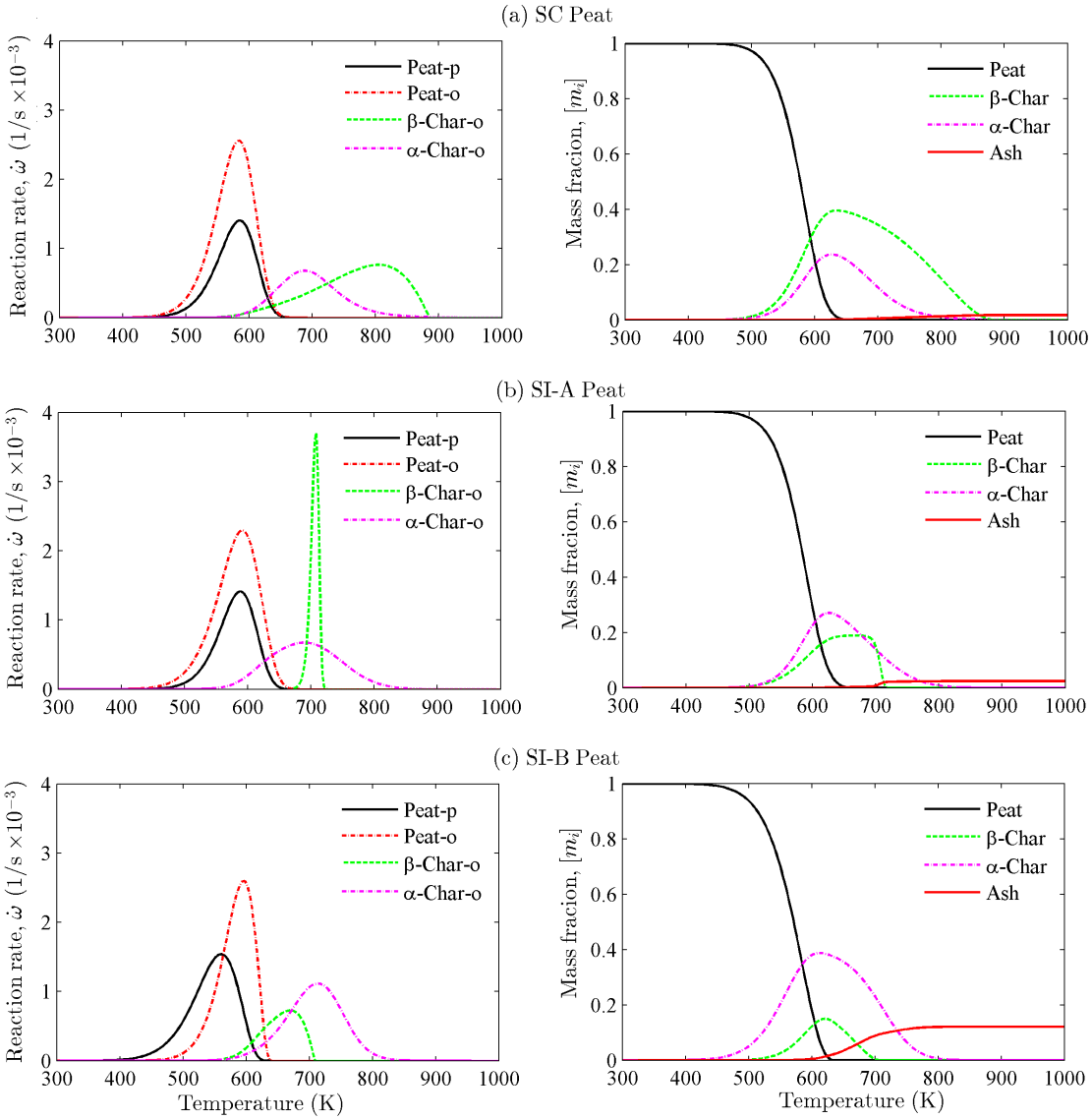

Figure 1.9: Modelled reaction rates, $\dot{\omega}_i$ (up) and species mass fraction, m_j (down) for (a) Sco-1, (b) Sib-2, and (c) Sib-3 peat in air ($k = 20$ K/min).

1.4 Application of the kinetics to smouldering front

1.4.1 1-D steady-state plug flow model

In this section, a 1-D species plug-flow model is used to explore the different chemical schemes and kinetic parameters, and study the reaction-zone structure of a smouldering front. The spread of a smouldering peat fire has two leading fronts that are significantly different (see Fig. 1.1: lateral and in-depth spreads). At the in-depth spread, a forward propagation configuration is assumed [3, 13], where the airflow by diffusion or convection and the smouldering front moves in the same direction. Both spread modes have been illustrated in more detailed Fig. 1.11 including the sub-fronts and their orders according to the literature [3, 22].

This plug flow model only solves species-conservation equations and is formulated

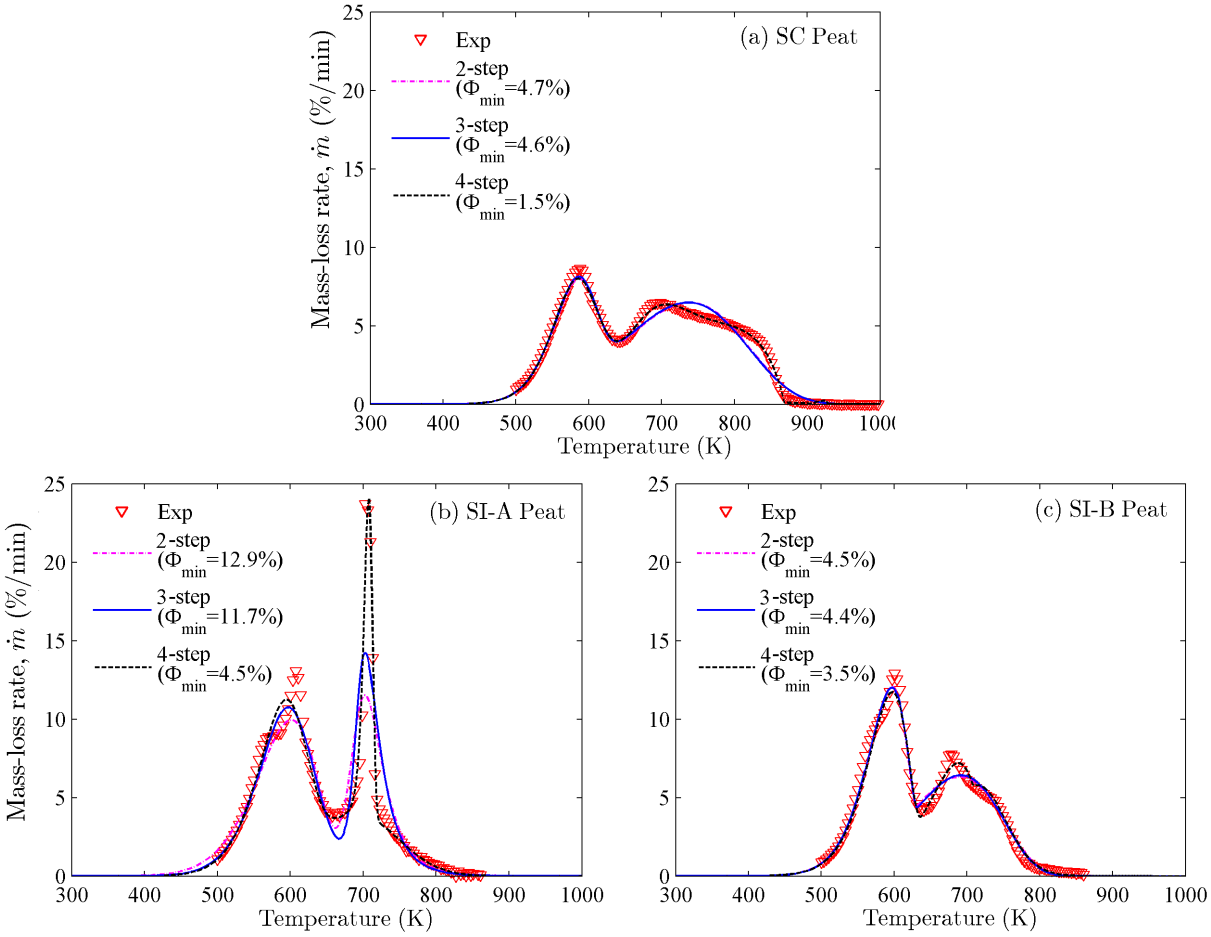

Figure 1.10: Mass-loss rate of (a) SC, (b) SI-A, and (c) SI-B peat in air (20 K/min) simulated by kinetics with different steps.

as a boundary-value problem [10]. It assumes a constant smouldering spread rate and a thermal equilibrium between gas and solid phases. Also, it does not solve the energy conservation but uses a prescribed temperature profile instead, converting the original partial differential equations (PDEs) into an ordinary differential equations (ODEs).

At the lateral spread (Fig. 1.11a), smoulder spreads along the top soil surface with an abundant oxygen supply, implying that the oxygen depletion in the reaction zone is negligible. So only species conservation for solid species is considered:

$$\frac{dm_i}{d\xi} = -Da_s \sum_k \nu_{i,k}\dot{\theta}_k, \tag{1.17}$$

where ξ is the non-dimensional spatial variable along the propagation direction (i.e. along the top surface) with respect to the characteristic smoulder-front thickness L; and the Damköhler number in solid phase is defined as Da_s = residence time/chemical time = $(L/S)/\tau$. According to Eq. (1.6), the non-dimensional reaction rate is scaled by a characteristic time τ as

$$\dot{\theta}_i = \tau\dot{\omega}_i = \tau Z_i e^{-E_i/RT} m_j^{n_i} Y_{O_2}^{\delta_i}, \tag{1.18}$$

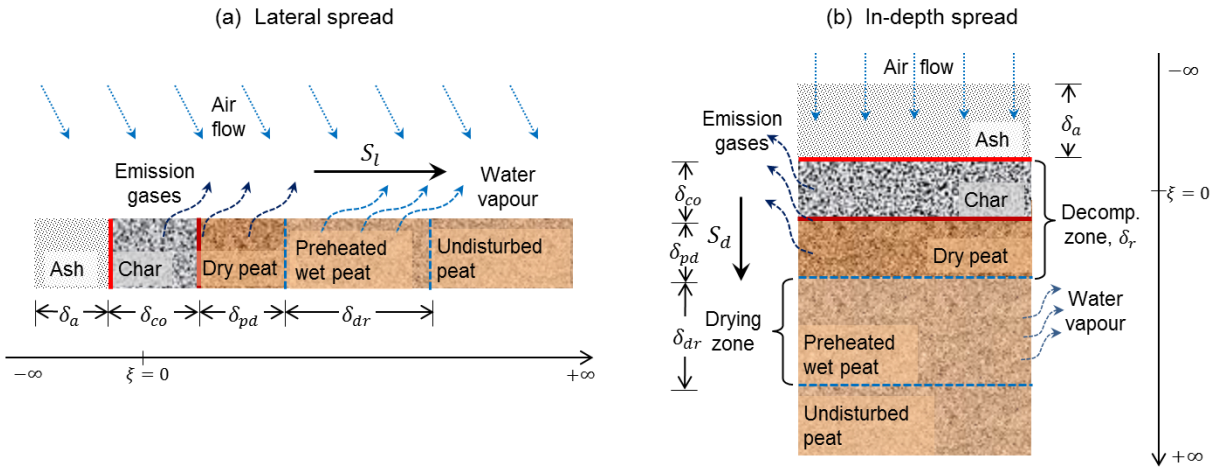

Figure 1.11: Spread modes of 1-D smouldering combustion: (a) lateral spread; and (b) in-depth spread. See Fig. 1.1 for a combined illustration of these fronts.

with $\dot{\theta}_i < 0$ for consumption and $\dot{\theta}_i > 0$ for generation. For simplicity, the density of the solid phase, ρ_s, is assumed to be constant and same for all species. Eq. (1.17) in the lateral spread (1-D in space) is equivalent to Eq. (1.8) in the TG (1-D in temperature), but their heating rates are different.

The boundary conditions for Eq. (1.17) are related to the species mass fractions ahead of the front (see in Fig. 1.11a), specified as

$$\begin{cases} m_w(\xi = +\infty) = m_{w0}, \\ m_p(\xi = +\infty) = 1 - m_{w0}, \\ m_c(\xi = +\infty) = m_\beta(\xi = +\infty) = m_a(\xi = +\infty) = 0. \end{cases} \tag{1.19}$$

The non-dimensional temperature profile is prescribed as

$$\Pi = \frac{T - T_\infty}{T_s - T_\infty} = \begin{cases} 1, & \xi \leq 0 \\ \exp(-\eta\xi), & \xi > 0 \end{cases} \tag{1.20}$$

where T_s is the peak smouldering temperature, and $\eta = SL/\alpha_s$ is estimated from non-dimensional analysis of the Fouriers law with the upstream solid-phase thermal diffusivity, α_s. That is, the temperature profile is steeper for a larger spread rate.

At the in-depth spread (Fig. 1.11b), smoulder spreads into the deep soil layers with a limited oxygen supply, so the oxygen conservation is also solved and coupled with solid species in heterogeneous reactions. By invoking mass conservation in the plug-flow model with a constant inlet airflow velocity, u_g, the mass fraction of oxygen in the gas phase varies as

$$\frac{dY_{O_2}}{d\xi} = -\frac{\rho_s}{\rho_g} Da_g \sum_k \nu_{O_2,k} \dot{\theta}_k. \tag{1.21}$$

At $\xi = -\infty$, it is assumed that

$$Y_{O_2}(\xi = -\infty) = y_{O_2,a}, \tag{1.22}$$

Table 1.4: Parameters used in plug flow model.

Parameter	Value	Unit	References/Notes
MC	50%	kg/kg	-
$\nu_{O_2,po}$	0.3	-	[13, 40]
$\nu_{O_2,co}$	1.0	-	[13, 40]
ρ_s	150	kg/m^3	[13]
α_s	10^{-7}	m^2/s	[41]
L	1	cm	scaling
τ	600	s	scaling (=10 min)
T_s	800	K	[22, 42] and Chapter 6
S_l	0.50	mm/min	[42] and Chapter 6
S_d	0.29/0.26	mm/min	calculated for CH/SC peat
u_g	0.80	mm/s	dimensional analysis
$Y_{O_2,a}$	0.12	-	assumed

where ξ is along the direction of in-depth spread; the Damköhler number in gas phase is defined as $Da_g = L/(u_g - S)/\tau$; the gas density, ρ_g, varies as the ideal-gas law; and the solid density. The inlet oxygen first diffuses through the ash layer before reaching the reaction zone, so an oxygen concentration lower than the atmospheric value is selected for $Y_{O_2,-\infty}$. A steady-state propagation is achieved when oxygen is completely consumed in the reaction zone. The temperature profile is also defined by Eq. (1.20). All parameters used in the model are summarized in Table 1.4. Note that the characteristic time, τ, is set to scale the non-dimensional reaction rates in the order of 1.

1.4.2 Results of lateral spread

The shallow-front spread is first modelled with the proposed 5-step kinetics (drying plus 4 decomposition reactions) and the corresponding kinetics parameters. Only the results of CH and SC samples are reported here, and the results of SI-A and SI-B samples are similar to those of SC sample. The drying parameters of the SC sample are assumed to be the same as that of the CH sample in Table 1.2.

Figure 1.12 shows the reaction rates and mass fractions at the lateral spread. These are qualitatively similar to those in Figs. 1.5 and 1.9a, as expected from the similarity between Eqs. (1.8) and (1.17). Three very distinct propagating sub-fronts are observed: drying, peat decomposition, and then followed by char oxidation, agreeing with experimental observations in [13, 22]. In particular, the role of the drying front is captured here for the first time. The thickness of each propagating sub-front is found when the non-dimensional reaction rate is dominant with a threshold value of 0.01: $\delta_{dr}/\delta_{pd}/\delta_{co}$ is 2.7/0.6/0.8 cm (CH sample), and 2.6/0.9/0.8 cm (SC sample). Similar relative positions are also observed for SI-A and SI-B samples, but not repeated here. The information is

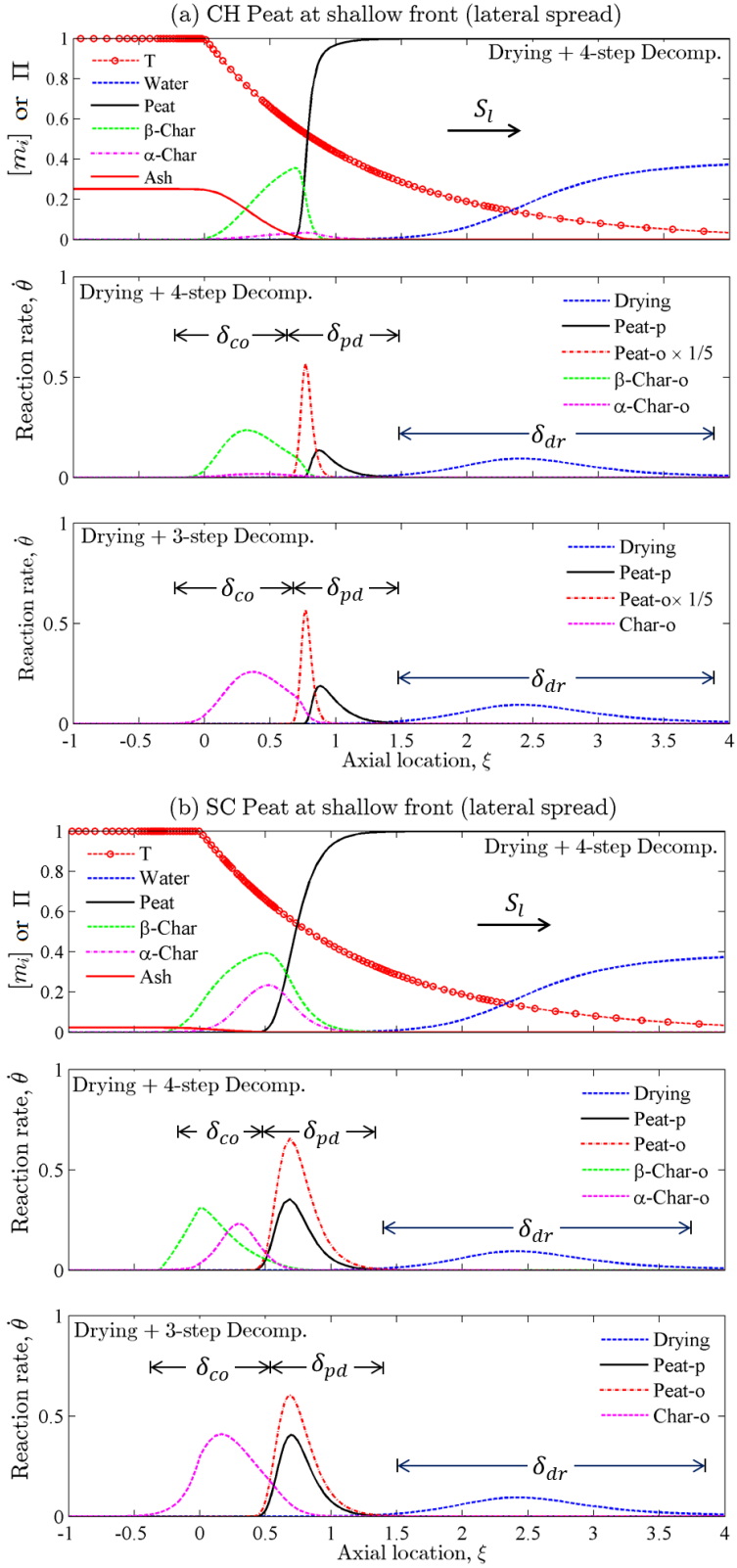

Figure 1.12: Reaction-zone structure of the lateral spread for (a) the CH peat; and (b) the SC peat.

clear: the drying front is long, and if moisture content increases, the drying front will become longer, so as to slower or forbid the fire spread.

For the CH sample (Fig. 1.12a) the peat-pyrolysis zone is longer than the peat-oxidation zone ($\delta_{pp}/\delta_{po} \approx 2$). But peat pyrolysis is much slower than peat oxidation ($\dot{\omega}_{po}^{max}/\dot{\omega}_{pp}^{max} = 21$), and the majority of the original peat (90%) is oxidized while only 10% is pyrolyzed. Consequently, the β-char oxidation dominates at high temperature. For the SC sample (Fig. 1.12b), both of the parallel paths (a and b) are important, but peat oxidation is still larger than pyrolysis ($\dot{\omega}_{po}^{max}/\dot{\omega}_{pp}^{max} = 2$), and up to 65% of peat is oxidized. In summary, at the lateral spread, peat oxidation and the corresponding reaction path of (Peat$\rightarrow$ β-char $\rightarrow$ash) are more important.

The validity and accuracy of the reaction-zone structure at the lateral spread is expected to be high because its environment is similar to that of the TG experiment in air, which can be viewed as a good reproduction of larger scales. For this reason, it is expected if a reduced kinetics can well explain the TG experiment in air, it can accurately capture the reaction-zone structure of the lateral spread. Figure 1.12 also shows the reaction-zone structure modelled from 3-step decomposition scheme plus drying, Eqs. (1.15) and (1.1). The comparison with the original 4-step decomposition scheme reveals a small difference because a close degree of fit is found in Figs. 1.7 and 1.10.

1.4.3 Results of in-depth spread

The same 5-step kinetics is applied to CH and SC samples at the in-depth spread. The oxygen stoichiometric coefficients for oxidations of peat ($\nu_{O_2,po}$), α-char ($\nu_{O_2,\alpha o}$), and β-char ($\nu_{O_2,\beta o}$) are obtained from carbon emission measurements [40] [4], and assumed to be proportional to the heat of oxidation as $\nu_{O_2,k} = \Delta H_k/(13.1\ \text{MJ/kg})$ [10, 43]. The heat of reaction can be estimated from the elemental composition [13, 15, 16], and assumed to be proportional to the mass loss of organic content in each step. The oxygen diffusion velocity is estimated from the dimensional analysis of Fick's law, $u_g \sim \sqrt{\alpha_g/\tau}$ where the gas thermal diffusivity α_g is in the same order of molecular diffusivity. Figure 1.13 shows the reaction rates and species distribution for in-depth spread.

The calculated in-depth spread rate is reported in Table 1.4, in the same order ($\sim$0.1 mm/min) of experimental observations in [3, 42] and Chapter 6. In general, the oxidation rate as well as the in-depth spread rate is lower than that of lateral spread because of the oxygen depletion. For the CH sample (Fig. 1.13a), a similar three-propagation-front structure is observed, but the dimension becomes larger where $\delta_{dr}/\delta_{pd}/\delta_{co}$ follows 3.6/1.5/1.1 cm. Compared to the lateral spread, the peat-decomposition zone is larger, but the peat-oxidation zone inside becomes even thinner ($\delta_{pp}/\delta_{po} = 10$). Thus, larger fraction of the original peat (36%) is pyrolyzed (only 10% at the lateral spread), and the oxidation rates of the two chars are comparable at high temperature. For the SC sample

4. The emission ratio of CO/CO_2 in bench-scale peat fire is measured to be 0.43 [40]. Thus, based on the carbon fraction in elementary analysis (see Table 1.1), the oxygen consumption can be estimated.

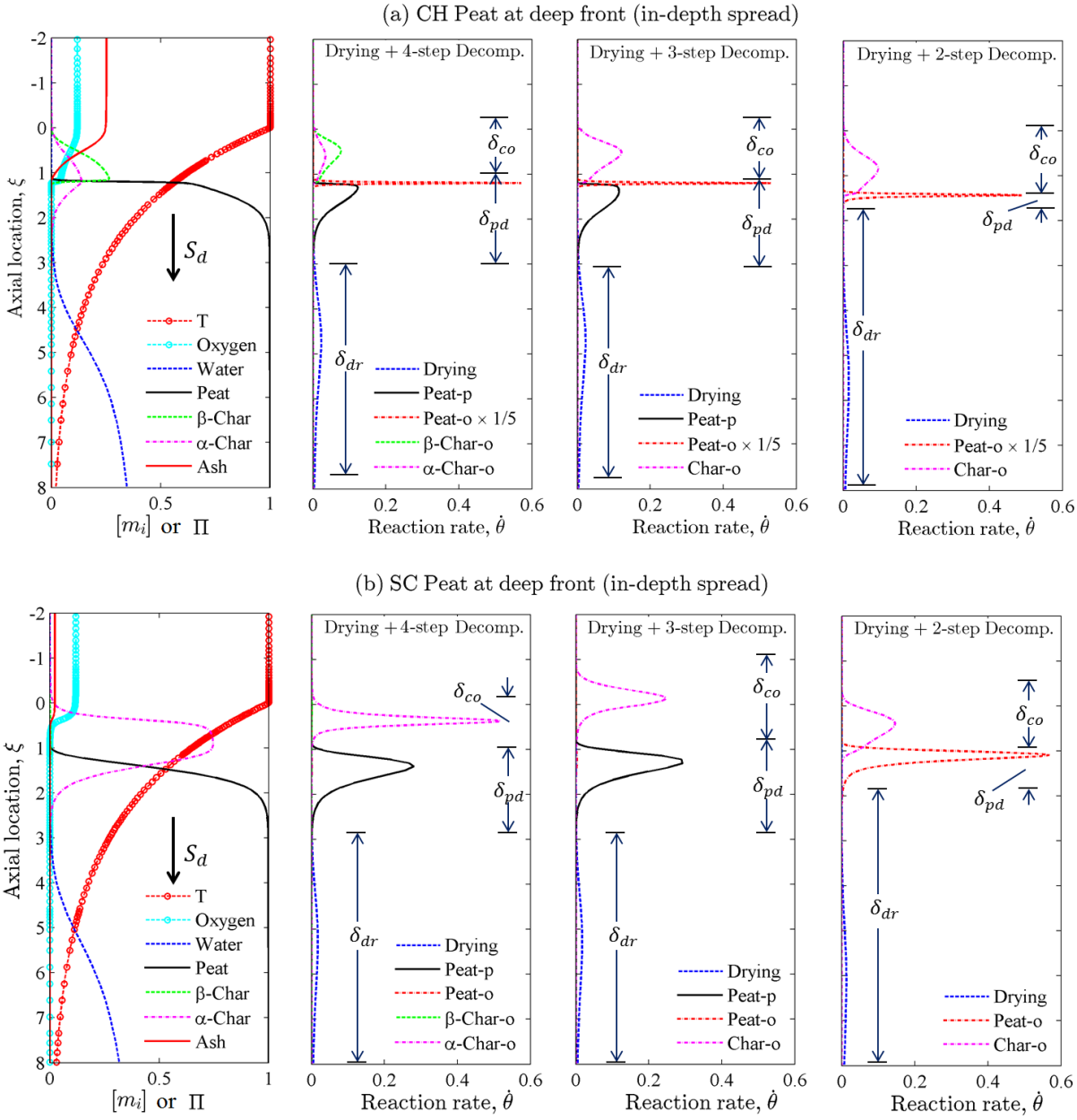

Figure 1.13: Reaction-zone structure of the in-depth spread for (a) the CH peat, and (b) the SC Peat.

(Fig. 1.13b), the propagation fronts also become larger: $\delta_{dr}/\delta_{pd}/\delta_{co}$ follows 4.0/1.9/1.0 cm. Pyrolysis becomes dominant, 98% of the peat is pyrolyzed, and so as the α-char oxidation at high temperature. In short, at the in-depth front the pyrolysis and the corresponding path of (peat $\rightarrow$ α-char $\rightarrow$ash) becomes more important or even dominant because the oxygen supply is limited upstream.

The validity and accuracy of reduced decomposition schemes (3-step and 2-step) plus drying are also explored in Fig. 1.13. For the CH sample, 3-step scheme, Eq. (1.15) including pyrolysis, gives a good agreement. Meanwhile, although 2-step scheme, Eq. (1.16), can give a good degree of fit to the TG curve in Fig. 1.7, the result for in-

depth spread is completely misleading, where the peat-decomposition zone becomes very thin and overlapping with the char-oxidation zone. The major reason is that the 2-step scheme does not include the oxygen-independent pyrolysis. Thus, it cannot capture the oxygen-limited character of in-depth spread.

Now, SC sample in Fig. 1.13b is discussed, although the reduced 3-step scheme gives a similar peat-decomposition zone, the thickness of char-oxidation zone becomes doubled and the char oxidation becomes much mild. For the 2-step scheme, similar misleading results are shown: the peat-decomposition zone becomes thinner and partially overlapping with the high-temperature ($T > 650$ K) char-oxidation zone, although in Fig. 1.10a these step-reduced schemes can give a comparable degree of fit as the 4-step decomposition.

In summary, a kinetic scheme, having good agreement with a limited number of TG experiments, is not necessarily beneficial for more accurately modelling smouldering combustion under various environmental conditions, unless it includes all the important dominant physics (e.g. under similar heating rate and oxygen concentration). In order to further improve the model accuracy, TG testing under various oxygen concentrations is necessary (see further study in Chapter 4).

1.5 Conclusions

In this chapter, a 5-step kinetics (1-step drying and 4-step decomposition) is proposed for smouldering combustion of peat. The scheme includes one pyrolysis, and three oxidations, plus 1-step drying with 5 condensed species (water, peat, α-char, β-char, and ash). The corresponding inverse problem on TG data from the literature is solved to find the best kinetic and stoichiometric parameters for four types of boreal peat. The interdependence among three kinetic parameters is shown. Reduced 3-step and 2-step decomposition schemes are found to give reasonable agreements with TG results as well. The results show that at the TG level, all proposed schemes seem to perform well, with a high degree of agreement resulting from the forced fitting in the inverse problem approach.

The validity of the schemes is then investigated outside the TG realm and incorporated into a 1-D plug-flow model to study the relative position of each reaction and the species distribution inside a peat smouldering front. Both lateral and in-depth spread modes are considered. The results show that the drying sub-front is essential, and the best kinetics is the 4-step decomposition. At the lateral spread, the structure is found to be similar to that in the TG experiment because of the analogy between time in TG and space in a 1-D moving framework. The path of (peat $\rightarrow$ β-char $\rightarrow$ ash) is dominant. At the in-depth spread, modelling results show that the oxygen consumption controls the thickness of the reaction front. Moreover, the pyrolysis as well as the path of (peat $\rightarrow$ α-char $\rightarrow$ ash) becomes more important. It is also found that the reduced kinetic scheme without pyrolysis (2-step) give misleading predictions of in-depth spread, despite the apparent agreement with TG data.

This is the first time that the smouldering kinetics and the reaction-zone structure of a peat fire are explained and predicted, thus helping to understand this important natural and widespread phenomenon.

Acknowledgements

I would like to thank Prof. Haixiang Chen (University of Science and Technology of China) and Dr Valérie Leroy-Cancellieri (University of Corsica) for providing the TG data. Valuable comments from Prof. Forman Williams (University of California at San Diego) and reviewers are also acknowledged.

References

[1] T. Ohlemiller, "Modeling of smoldering combustion propagation," *Progress in Energy and Combustion Science*, vol. 11, no. 4, pp. 277 – 310, 1985.

[2] D. Drysdale, *An Introduction to Fire Dynamics*. Wiley, 2011.

[3] G. Rein, "Smouldering Fires and Natural Fuels," in *Fire Phenomena and the Earth System* (C. Belcher, ed.), ch. 2, pp. 15–33, Wiley and Sons, 2013.

[4] S. E. Page, F. Siegert, J. O. Rieley, H.-D. V. Boehm, A. Jaya, and S. Limin, "The amount of carbon released from peat and forest fires in Indonesia during 1997," *Nature*, vol. 420, pp. 61–65, 2002.

[5] G. M. Davies, A. Gray, G. Rein, and C. J. Legg, "Peat consumption and carbon loss due to smouldering wildfire in a temperate peatland," *Forest Ecology and Management*, vol. 308, no. 0, pp. 169 – 177, 2013.

[6] B. Poulter, N. L. Christensen, and P. N. Halpin, "Carbon emissions from a temperate peat fire and its relevance to interannual variability of trace atmospheric greenhouse gases," *Journal of Geophysical Research*, vol. 111, 2006.

[7] M. R. Turetsky, B. Benscoter, S. Page, G. Rein, G. R. van der Werf, and A. Watts, "Global vulnerability of peatlands to fire and carbon loss," *Nature Geoscience*, vol. 8, pp. 11–14, 2015.

[8] L. Moreno, M.-E. Jimenez, H. Aguilera, P. Jimenez, and A. Losa, "The 2009 Smouldering Peat Fire in Las Tablas de Daimiel National Park (Spain)," *Fire Technology*, vol. 47, no. 2, pp. 519–538, 2011.

[9] C. Di Blasi, "Modeling chemical and physical processes of wood and biomass pyrolysis," *Progress in Energy and Combustion Science*, vol. 34, no. 1, pp. 47 – 90, 2008.

[10] G. Rein, C. Lautenberger, A. C. Fernandez-Pello, J. L. Torero, and D. L. Urban, "Application of genetic algorithms and thermogravimetry to determine the kinetics of polyurethane foam in smoldering combustion," *Combustion and Flame*, vol. 146, no. 1-2, pp. 95 – 108, 2006.

[11] S. Vyazovkin and C. A. Wight, "Kinetics in solids," *Annual Review of Physical Chemistry*, vol. 48, no. 1, pp. 125–149, 1997. PMID: 15012442.

[12] J. A. Gonzalez-Perez, F. J. Gonzalez-Vila, G. Almendros, and H. Knicker, "The effect of fire on soil organic matter: a review," *Environment International*, vol. 30, no. 6, pp. 855 – 870, 2004.

[13] R. M. Hadden, G. Rein, and C. M. Belcher, "Study of the competing chemical reactions in the initiation and spread of smouldering combustion in peat," *Proceedings of the Combustion Institute*, vol. 34, no. 2, pp. 2547 – 2553, 2013.

[14] T. Kashiwagi and H. Nambu, "Global kinetic constants for thermal oxidative degradation of a cellulosic paper," *Combustion and Flame*, vol. 88, no. 3-4, pp. 345 – 368, 1992.

[15] D. Cancellieri, V. Leroy-Cancellieri, E. Leoni, A. Simeoni, A. Y. Kuzin, A. I. Filkov, and G. Rein, "Kinetic investigation on the smouldering combustion of boreal peat," *Fuel*, vol. 93, no. 0, pp. 479 – 485, 2012.

[16] H. Chen, W. Zhao, and N. Liu, "Thermal Analysis and Decomposition Kinetics of Chinese Forest Peat under Nitrogen and Air Atmospheres," *Energy & Fuels*, vol. 25, no. 2, pp. 797–803, 2011.

[17] W. H. Frandsen, "The influence of moisture and mineral soil on the combustion limits of smoldering forest duff," *Canadian Journal of Forest Research*, vol. 17, no. 12, pp. 1540–1544, 1987.

[18] W. H. Frandsen, "Ignition probability of organic soils," *Canadian Journal of Forest Research*, vol. 27, no. 9, pp. 1471–1477, 1997.

[19] H. Grumpelt, "Peat," in *Ullmann's Encyclopedia of Industrial Chemistry* (F. Ullmann, ed.), Wiley-VCH, 2000.

[20] J. Koppejan and S. van van Loo, *The Handbook of Biomass Combustion and Co-firing*. Taylor & Francis, 2012.

[21] J. Brandrup, E. Immergut, and E. Grulke, *Polymer Handbook*. Polymer Handbook Series, John Wiley & Sons, 1999.

[22] G. Rein, N. Cleaver, C. Ashton, P. Pironi, and J. L. Torero, "The severity of smouldering peat fires and damage to the forest soil," *Catena*, vol. 74, no. 3, pp. 304 – 309, 2008.

[23] M. Pansu and J. Gautheyrou, *Handbook of Soil Analysis: Mineralogical, Organic and Inorganic Methods*. Springer, 2006.

[24] E. Plaster, *Soil Science and Management*. Texas Science Series, Delmar Cengage Learning, 2008.

[25] A. Chammari, B. Naon, F. Cherblanc, B. Cousin, and J. C. Bnet, "Interpreting the Drying Kinetics of a Soil Using a Macroscopic Thermodynamic Nonequilibrium of Water Between the Liquid and Vapor Phase," *Drying Technology*, vol. 26, no. 7, pp. 836–843, 2008.

[26] A. I. Filkov, A. Y. Kuzin, O. V. Sharypov, V. Leroy-Cancellieri, D. Cancellieri, E. Leoni, A. Simeoni, and G. Rein, "Comparative Study To Evaluate the Drying Kinetics of Boreal Peats from Micro to Macro Scales," *Energy & Fuels*, vol. 26, no. 1, pp. 349–356, 2012.

[27] F. He and F. Behrendt, "A new method for simulating the combustion of a large biomass particle - A combination of a volume reaction model and front reaction approximation," *Combustion and Flame*, vol. 158, no. 12, pp. 2500 – 2511, 2011.

[28] M. Amutio, G. Lopez, R. Aguado, M. Artetxe, J. Bilbao, and M. Olazar, "Kinetic study of lignocellulosic biomass oxidative pyrolysis," *Fuel*, vol. 95, no. 0, pp. 305 – 311, 2012.

[29] C. Lautenberger and C. Fernandez-Pello, "Generalized pyrolysis model for combustible solids," *Fire Safety Journal*, vol. 44, no. 6, pp. 819 – 839, 2009.

[30] J. A. Foster, "Evolutionary computation," *Nature Reviews Genetics*, vol. 2, no. 6, pp. 428–436, 2001.

[31] J. Arora, *Introduction to Optimum Design*. Elsevier Science, 2004.

[32] S. L. Kokjohn, R. M. Hanson, D. A. Splitter, and R. D. Reitz, "Fuel reactivity controlled compression ignition (RCCI): a pathway to controlled high-efficiency clean combustion," *International Journal of Engine Research*, vol. 12, no. 3, pp. 209–226, 2011.

[33] T.-Y. Park and G. F. Froment, "A hybrid genetic algorithm for the estimation of parameters in detailed kinetic models," *Computers & Chemical Engineering*, vol. 22, no. 0, pp. S103 – S110, 1998. European Symposium on Computer Aided Process Engineering-8.

[34] L. Elliott, D. Ingham, A. Kyne, N. Mera, M. Pourkashanian, and C. Wilson, "Genetic algorithms for optimisation of chemical kinetics reaction mechanisms," *Progress in Energy and Combustion Science*, vol. 30, no. 3, pp. 297 – 328, 2004.

[35] C. Lautenberger, G. Rein, and C. Fernandez-Pello, "The application of a genetic algorithm to estimate material properties for fire modeling from bench-scale fire test data," *Fire Safety Journal*, vol. 41, no. 3, pp. 204 – 214, 2006.

[36] C. Houck, J. Joines, and M. Kay, "GAOT: A Genetic Algorithm for Function Optimization: A Matlab Implementation," tech. rep., Report NCSU-IE TR 95-09 (1995).

[37] A. Lesnikovich and S. Levchik, "Isoparametric kinetic relations for chemical transformations in condensed substances (Analytical survey). II. Reactions involving the participation of solid substances," *Journal of thermal analysis*, vol. 30, pp. 677–702, 1985.

[38] D. M. Marquis, E. Guillaume, A. Camillo, T. Rogaume, and F. Richard, "Existence and uniqueness of solutions of a differential equation system modeling the thermal decomposition of polymer materials," *Combustion and Flame*, vol. 160, no. 4, pp. 818 – 829, 2013.

[39] R. M. Hadden, *Smouldering and Self-Sustaining Reactions in Solids: An Experimental Approach*. Phd thesis, University of Edinburgh, 2011.

[40] G. Rein, S. Cohen, and A. Simeoni, "Carbon emissions from smouldering peat in shallow and strong fronts," *Proceedings of the Combustion Institute*, vol. 32, no. 2, pp. 2489 – 2496, 2009.

[41] Y. Viswanadham and N. Jagan Mohana Rao, "The thermal diffusivity of soil at tropical stations in southern hemisphere," *Pure and Applied Geophysics*, vol. 101, pp. 247–260, 1972.

[42] N. Prat, C. Belcher, and J. Y. R. Hadden, G. Rein, "A laboratory study of the effect of moisture content on the spread of smouldering in peat fires," *FLAMMA*, vol. 6, no. 1, pp. 35–38, 2015.

[43] C. Huggett, "Estimation of rate of heat release by means of oxygen consumption measurements," *Fire and Materials*, vol. 4, no. 2, pp. 61–65, 1980.

Chapter 2

Computational Smouldering Combustion: Predicting the Roles of Moisture and Inert Contents in Peat Wildfires

Summary [1]

Smouldering combustion is the slow, low-temperature, flameless burning of porous fuels and the most persistent type of combustion. It is the driving phenomenon of wildfires in peatlands, like those causing haze episodes in Southeast Asia and Northeast Europe, but is poorly understood. In this chapter, a multi-physics 1-D model of a reactive porous media, using the open-source code Gpyro, is developed to investigate smouldering combustion of natural fuels with an emphasis on the role of the moisture and inert contents. The model solves the species, momentum, and energy conservation equations and includes heterogeneous chemical reactions. A previously developed 5-step reaction scheme for peat, including evaporation of water, is adopted to describe the drying, thermal and oxidative degradation during the smouldering combustion. The model predicts the transient temperature, species, and reaction profiles during ignition, spread, and extinction. The predicted smouldering thresholds related to the critical moisture and inorganic contents show a good agreement with the experimental results in the literature for a wide range of peat types and organic soils. The influences of the kinetic parameters, physical properties, and ignition protocol are investigated. This is the first time that a physics-based model of smouldering peat fires is developed, thus helping to understand this important natural and widespread phenomenon.

1. This chapter is based on "X. Huang, G. Rein, H. Chen (2015) *Computational Smoldering Combustion: Predicting the Roles of Moisture and Inert Contents in Peat Wildfires*, **Proceedings of the Combustion Institute**, 35 (3): 2673-81."

2.1 Introduction

Smouldering combustion is the slow, low-temperature, flameless burning of porous fuels and the most persistent type of combustion [1]. Smouldering is the dominant phenomenon in megafires in natural deposits of peat which are the largest and longest burning fires on Earth. These fires contribute considerably to global greenhouse gas emissions, and result in widespread destruction of ecosystems and regional haze events (e.g. recent megafires in Southeast Asia, North America and Northeast Europe) [2]. It is an emerging research topic in climate change mitigation but is poorly understood. For example, during the 1997 extreme haze event in Southeast Asia, peat fires emitted the equivalent to 13-40% of the global man-made greenhouse gas emissions of that year [3]. Rein [2] has pointed out that the atmospheric release of ancient carbon from the soil and the sensitivity of peat ignition to higher temperatures and drier soils could create a positive feedback mechanism for climate change.

Peat can hold a wide range of moisture contents [2] (MC), ranging from 10%, under drought conditions, to in excess of 300%, under flooded conditions [4]. Water represents a significant energy sink, and furthermore natural or anthropogenic-induced droughts are found to be the leading cause of smouldering megafires [2]. Therefore, soil moisture is the single most important property governing the ignition and spread of smouldering wildfires [5]. The critical moisture content (MC^*) for initiating smouldering of various boreal peat has been measured in the range 40-150% in dry basis [6, 7]. Drier than this threshold, peat becomes susceptible to smouldering. The second most important property is the soil inorganic content [2] (IC). As experimentally found by Frandsen [5, 6], there is a decreasing quasi-linear relationship between MC^* and IC^*: soil with a high IC can only be ignited at low MC. Mineral matter acts as a heat sink but also enhances the heat transfer via its higher heat conductivity. After moisture and inorganic contents, other important properties are bulk density, porosity and organic composition [2].

The spread of smouldering fires is controlled by heat and mass transfer processes in a reactive porous media. The computational studies on smouldering combustion in the literature have only included three fuels: cellulose [1, 8], polyurethane foam [1, 9] and char [10], simulated with chemical schemes of different complexity, including 1 [10], 3 [1] or 5 [9] steps. Ohlemiller [1] reviewed the early attempts on simulating smouldering combustion and provided the governing equations in general form. Rein et al. [9] numerically solved the 1-D smouldering combustion of polyurethane foam under forced flow with a 5-step kinetics, and the results were compared to microgravity experiments in both opposed and forward propagation modes. He et al. [10] developed a 1-D model to solve the in-depth spread of smouldering for char with 1-step chemistry and compared it to the experiments.

2. Moisture content (MC) is defined in dry basis as the mass of water divided by the mass of a dried soil sample, expressed as %. Inorganic content (IC<100%) is defined in dry basis as the mass of soil inorganic matter (minerals) divided by the mass of a dried soil sample, expressed as %.

Previous studies have not considered simulations of peat fires or the drying process.

In this chapter, a multi-physics 1-D model based on Gpyro [11] and the previously developed 5-step kinetics (including drying) is developed for peat kinetics in Chapter 1 to investigate the ignition and spread of smouldering in a bed of peat and other organic soils. Prediction of the smouldering thresholds related to MC^* and IC^* are the emphasis. The computational results are compared with experiments [5, 6]. The influences of the kinetic parameters, ignition protocol, and physical properties are investigated.

2.2 Computational model

Frandsen [5, 6] conducted two sets of pioneering experiments to determine the smouldering thresholds of multiple soil samples. In the first set of experiments [5], natural peat moss of negligible minerals (IC = 3.7%) was mixed with water (m_w) and mineral clay (m_{cl}) to produce modified soil samples of known MC = $m_w/(m_p+m_{cl})$ and IC = $m_c/(m_p+m_{cl})$. The modified samples were tested in an insulated box with the top open to the atmosphere, of a depth of 40 mm and a cross section of 90 × 90 mm (internal dimension). A coil heater was in contact with the top surface for 3 min to initiate the smouldering at least near the coil. In the second set of experiments [6], a large number of unmodified natural soil samples with different natural ICs at various sites of North America were tested to find MC^* and IC^*. The ignition protocol was different: an additional layer of dry peat of 10 mm was placed between the the coil heater and the soil sample (i.e. dry-peat ignition).

During smouldering, the peat is first dried and decomposed to char, and then char is oxidized to ash [2] and see Chapters 1 and 4. After the ignition of a vertical sample, a smouldering front starts to spread in-depth and a layer of ash is accumulated on the top, as illustrated in Fig. 2.1. Depending on both MC and IC, this smouldering front may become self-sustaining and consume most of the organic matter, or may not spread beyond the ignition zone. As a first approximation, Frandsen's experiments can be modelled as 1-D at the in-depth direction because buoyancy plays a negligible role in these relatively small samples (40 mm), i.e. vertical and horizontal samples behave the same way. The open-source code Gpyro [11] is used to implement a 1-D model and simulate the ignition and spread of smouldering combustion of peat.

2.2.1 1-D governing equations

The computational domain is a 40 mm deep sample with ignition at the top free surface and insulated at the bottom (Fig. 2.1). The model solves the 1-D transient equations for both solid and gas phases in the absence of gravity. The details are reported in [11]; only the essential conservation equations are presented here: (1) condensed-phase mass, (2) condensed-phase species, (3) condensed-phase energy, (4) gas-phase mass, (5) gas-phase species, and (6) gas-phase momentum (Darcy's law). Symbols are explained

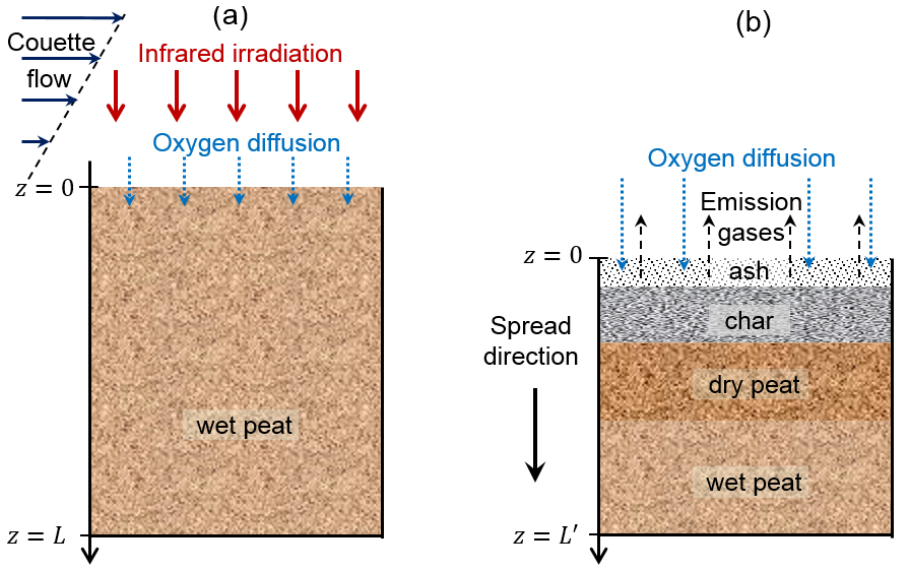

Figure 2.1: Illustration of the 1-D computational domain for in-depth spread of smouldering in a sample of peat (a) at the beginning of ignition, and (b) during sustained spread.

in the nomenclature, and subscripts i, j, and k refer to the number of condensed-phase species, gas-phase species, and reaction, respectively.

$$\frac{\partial \overline{\rho}}{\partial t} = -\dot{\omega}'''_{fg} \tag{2.1}$$

$$\frac{\partial \left(\overline{\rho} Y_i\right)}{\partial t} = \dot{\omega}'''_{fi} - \dot{\omega}'''_{di} \tag{2.2}$$

$$\frac{\partial (\overline{\rho}\overline{h})}{\partial t} + \frac{\partial \left(\dot{m}'' h_g\right)}{\partial z} = \frac{\partial}{\partial z}\left(\overline{k}\frac{\partial T}{\partial z}\right) + \sum_{k=1}^{K} \dot{\omega}'''_{di,k} \Delta H_k \tag{2.3}$$

$$\frac{\partial \left(\rho_g \overline{\psi}\right)}{\partial t} + \frac{\partial \dot{m}''}{\partial z} = \dot{\omega}'''_{fg} \tag{2.4}$$

$$\frac{\partial \left(\rho_g \overline{\psi} Y_i\right)}{\partial t} + \frac{\partial (\dot{m}'' Y_j)}{\partial z} = -\frac{\partial}{\partial z}\left(\overline{\psi}\rho_g D \frac{\partial Y_j}{\partial z}\right) + \dot{\omega}'''_{fj} - \dot{\omega}'''_{dj} \tag{2.5}$$

$$\dot{m}'' = -\frac{\overline{K}}{\nu}\frac{\partial P}{\partial z} \qquad (P = \rho_g R_s T) \tag{2.6}$$

The gas-phase temperature is assumed to be the same as the condensed-phase temperature (thermal equilibrium)[3]. The environmental pressure (P_∞) and temperature (T_∞) are assumed constant at 1 atm and 300 K, respectively. Within the first 3 min, a heat flux of $\dot{q}''_e = 30$ kW/m^2 without in-depth radiation is applied to simulate the heating of the coil heater (the effect of the heat flux level is explored in Section 2.4.2).

3. Simulations have also been conducted by solving additional gas-phase energy conservation equation (i.e. two-temperature mode). Because of very large heat transfer coefficient between gas and condensed phases, modelling results are similar to those with the assumption of thermal equilibrium.

The boundary conditions on the top free surface ($z = 0$) are

$$\begin{cases} -\overline{k}\dfrac{\partial T}{\partial z}\Big|_0 = \begin{cases} -h_{c0}\left(T_0 - T_\infty\right) + \overline{\varepsilon}\left[\dot{q}_e'' - \sigma\left(T_0^4 - T_\infty^4\right)\right] & (t \le 3 \text{ min}) \\ -h_{c0}\left(T_0 - T_\infty\right) - \overline{\varepsilon}\sigma\left(T_0^4 - T_\infty^4\right) & (t > 3 \text{ min}) \end{cases} \\ -\overline{\psi}\rho_g D\dfrac{\partial Y_j}{\partial z}\Big|_0 = h_{m0}\left(Y_{j\infty} - Y_{j0}\right) \\ P_0 = P_\infty \end{cases} \tag{2.7}$$

where an empirical convection coefficient for plate, $h_{c0} = 1.52\Delta T^{1/3} = 1.52(300)^{1/3} \approx 10$ W/m^2-K [12], is set for the energy conservation; and the heat-mass transfer analogy is used, $h_{m0} \approx 20$ g/m^2-s for gas species conservation, which uses the approximation of Couette flow [11] (see Fig. 2.1).

The boundary conditions on the back free surface ($z = L = 40$ mm) are

$$\begin{cases} -\overline{k}\dfrac{\partial T}{\partial z}\Big|_L = -h_{cL}\left(T_L - T_\infty\right) \\ -\overline{\psi}\rho_g D\dfrac{\partial Y_j}{\partial z}\Big|_L = h_{mL}\left(Y_{j\infty} - Y_{jL}\right) \\ \dot{m}_L'' = 0 \end{cases} \tag{2.8}$$

where $h_{cL} \approx k_w/\delta_w = 3$ W/m^2-K is assumed to simulate the small heat loss across the insulation wall, and $h_{mL} = 0$ g/m^2-s is assumed for the negligible gas diffusion.

A fully implicit formulation is adopted for solution of all equations. More details about the numerical solution are reported in [11]. Simulations were run with an initial cell size of $\Delta z = 0.1$ mm (400 cells per domain), and an initial time step of 0.01 s. Reducing the cell size and time step by a factor of 2 gives no significant difference in results, so the calculations are sufficiently resolved.

‘

2.2.2 Chemical kinetics

The heterogeneous reaction in mass basis is written as:

$$A_k + \sum_{j=1}^{N} \nu_{j,k}' \text{gas } j \rightarrow \nu_{B,k} B_k + \sum_{j=1}^{N} \nu_{j,k}'' \text{gas } j, \tag{2.9}$$

where $\nu_{B,k} = 1 + \left(\rho_B/\rho_A - 1\right)\chi_k$, and χ_k quantifies the shrinkage or intumescence of the cell size. The destruction rate of condensed species A in reaction k is expressed by the Arrhenius law

$$\dot{\omega}_{dA_k}''' = \frac{\left(\overline{\rho}Y_A\Delta z\right)_\Sigma}{\Delta z} Z_k e^{-E_k/RT}\left[\frac{\overline{\rho}Y_A\Delta z}{\left(\overline{\rho}Y_A\Delta z\right)_\Sigma}\right]^{n_k} Y_{O_2}^{n_{O_2,k}}, \tag{2.10}$$

$$\left(\overline{\rho}Y_A\Delta z\right)_\Sigma = \left(\overline{\rho}Y_A\Delta z\right)|_{t=0} + \int_0^t \dot{\omega}_{fi}'''\Delta z(\tau)d\tau, \tag{2.11}$$

where subscripts d and f represent destruction and formation. The formation rate of condensed species B and all gases from reaction k are $\dot{\omega}'''_{fB_k} = \nu_{B,k}\dot{\omega}'''_{dA_k}$ and $\dot{\omega}'''_{fg_k} = (1-\nu_{B,k})\dot{\omega}'''_{dA_k}$. The corresponding heat of reaction is $\dot{Q}'''_k = -\dot{\omega}'''_{dA_k}\Delta H_k$.

In Chapter 1, the decomposition schemes with different complexities were investigated using thermogravity (TG) data of four different peat samples from Scotland (SC), Siberia (SI-A and SI-B), and China (CH). The best kinetics scheme was found to be: (1) Drying (dr), (2) Peat pyrolysis (pp), (3) Peat oxidation (po), (4) β-Char oxidation (βo), and (5) α-Char oxidation (αo) as

$$\text{Peat} \cdot \nu_{w,dr}\text{H}_2\text{O} \rightarrow \text{Peat} + \nu_{w,dr}\text{H}_2\text{O(g)} \qquad (dr) \qquad (2.12)$$

$$\text{Peat} \rightarrow \nu_{\alpha,pp}\alpha\text{-Char} + \nu_{g,pp}\text{Gas} \qquad (pp) \qquad (2.13)$$

$$\text{Peat} + \nu_{O_2,po}O_2 \rightarrow \nu_{\beta,po}\beta\text{-Char} + \nu_{g,po}\text{Gas} \qquad (po) \qquad (2.14)$$

$$\beta\text{-Char} + \nu_{O_2,\beta o}O_2 \rightarrow \nu_{a,\beta o}\text{Ash} + \nu_{g,\beta o}\text{Gas} \qquad (\beta o) \qquad (2.15)$$

$$\alpha\text{-Char} + \nu_{O_2,\alpha o}O_2 \rightarrow \nu_{a,\alpha o}\text{Ash} + \nu_{g,\alpha o}\text{Gas} \qquad (\alpha o) \qquad (2.16)$$

where subscripts w, p, α, β, and a represent five condensed species (water, peat, α-char, β-char, and ash), in addition to four gaseous species: oxygen, nitrogen, water vapour, and emission gases.

2.3 Smouldering structure

2.3.1 Parameter selection

All gaseous species have the unit Schmidt number and equal diffusion coefficient and specific heat. Each condensed-phase species is assumed to have constant properties (e.g. bulk density, specific heat, and porosity). The averaged properties in each cell are calculated by weighting appropriate mass or volume fractions [11], for example,

$$\begin{aligned} \overline{c} &= \sum_{i=1}^{M} Y_i c_i, \quad \overline{h} = \sum_{i=1}^{M} Y_i h_i, \\ \overline{\rho} &= \sum_{i=1}^{M} X_i \rho_i, \quad \overline{k} = \sum_{i=1}^{M} X_i k_i, \end{aligned} \qquad (2.17)$$

and the conversion between the mass and volume fractions is

$$X_i = \overline{\rho}\frac{Y_i}{\rho_i} \qquad (2.18)$$

The physical properties of the condensed-phase species are listed in Table 2.1. The solid ($\psi = 0$) physical properties, $\rho_{s,i}$, $k_{s,i}$, c_i of peat, char, and clay are selected from [13]. The bulk densities of all species use the measurements from [14]. The properties of α-char and β-char are assumed to be the same.Then, porosity can be calculated as

$$\psi_i = 1 - \frac{\rho_i}{\rho_{s,i}} \qquad (2.19)$$

Table 2.1: The physical parameters of condensed-phase species before mixing where $\rho_{s,i}$, $k_{s,i}$, and c_i are from [13], and $\rho_{i,0}$ is from [5, 14].

Species (i)	$\rho_{s,i}$ (kg/m^3)	$\rho_{i,0}$ (kg/m^3)	$\psi_{i,0}$ (-)	$k_{s,i}$ (W/m-K)	c_i (J/kg-K)
water	1000	1000	-	0.6	4186
peat	1500	110	0.927	1.0	1840
α-char	1300	135	0.896	0.26	1260
β-char	1300	135	0.896	0.26	1260
ash	2500	20	0.992	0.8	880
clay	2500	1200	0.520	0.8	880

The effective thermal conductivity includes the radiation heat transfer across pores as

$$k_i = k_{s,i}(1-\psi_i) + \gamma_i \sigma T^3 \tag{2.20}$$

where $\gamma_i = 10^{-4} \sim 10^{-3}$ [4] m depends on the inter-particle pore size which is similar to the particle size ($\approx d_p$), i.e. $\gamma \sim d_p = 1/S_i\rho$. The particle surface area for soil and char is $S_p = S_c \sim 0.05$ m^2/g , and for ash is $S_a \sim 0.2$ m^2/g [15]. The absolute permeability of soil can be estimated from an empirical expression [16]

$$K_i = 10^4 \frac{\nu_w}{g} d_{p,i}^2 \approx 10^{-3} d_{p,i}^2 \sim \frac{1}{\rho_i^2} \tag{2.21}$$

which varies from 10^{-12} to 10^{-9} m^2, and decreases with the bulk density.

The sample volume expands after peat is mixed with clay, but for unsaturated samples, water occupies the pore space and does not expand the volume. Thus, the bulk density of mixed unsaturated soil is given as $\rho = (1+\text{MC})/[(1-\text{IC})/\rho_p + \text{IC}/\rho_{cl}]$. The properties of α-char and β-char are assumed to be the same, and so as natural minerals (ash) and clay. After combustion, the residue is a mixture of natural minerals and clay.

The Scotland (SC) peat sample with a high organic content (IC = 1.8%), studied in Chapter 1 is selected as the base case. Table 2.2 lists the kinetic and stoichiometric parameters. The heat of oxidation is related to the fraction of oxidized organic matter and assumed to be $\Delta H_k = \Delta H_{O_2}(1-\nu_k)$. By integrating the energy-flux curve of TG-DSC measurements of multiple peat samples [17, 18], $\Delta H_{O_2,po} = 10$ MJ/kg and $\Delta H_{O_2,\alpha o} = \Delta H_{O_2,\beta o} = 20$ MJ/kg are selected. Under TG conditions and a sufficient air supply, the total heat of combustion for a dry SC samples is calculated to be 15 MJ/kg, similar to measured values in [17, 19]. The oxygen consumption is related to the heat of

4. Although the overall porosity of solid species is large (~ 0.9), the actual inter-particle porosity is small because a single solid particle is also porous and has a large intra-particle porosity. Thus, the simplification for radiation in Eq. (2.20) is still reasonable under current large overall porosities.

Table 2.2: Reaction parameters and gaseous yields of 5-step reactions for SC peat sample (See Table 1.3 in Chapter 1).

Parameter/k	dr	pp	po	βo	αo
$\lg A_k$ ($\lg(s^{-1})$)	8.12	5.92	6.51	1.65	7.04
E_k (kJ/mol)	67.8	93.3	89.8	54.4	112
n_k (-)	2.37	1.01	1.03	0.54	1.85
$\nu_{B,k}$ (kg/kg)	0	0.75	0.65	0.03	0.02
ΔH_k (MJ/kg)	2.26	0.5	-3.54	-19.5	-19.5
$\nu_{O_2,k}$ (kg/kg)	0	0	0.27	1.48	1.49

oxidation by assuming a constant heat of combustion per unit of oxygen consumed as

$$\nu_{O_2,k} = \frac{\Delta H_k}{13.1 \text{ MJ/kg}} \tag{2.22}$$

where the value of 13.1 MJ/kg is found to be reasonable for many types of biomass [20].

2.3.2 Base case

A successful ignition and complete combustion of the sample is defined when most ($> 95\%$) of the organic matter is consumed, and only a small amount of char remains due to extinction near the deep boundary. If ignition succeeds, simulations show that the following spread in the 40 mm deep samples lasts for about 1 h, similar to the observed average spread rate of 30 mm/h in [5]. Computational results show that the spread rate decreases with MC.

Arbitrarily, a base case (SC sample, MC = 30% and IC = 40%) is chosen to investigate the combustion process in detail. Figure 2.2 shows the evolution of temperature profile. Right after ignition (3 min), the smouldering front reaches the peak temperature ($\sim$ 900°C), and then spreads downwards along with the free surface regression. In the middle of the sample ($10 < z < 30$ mm, $t < 25$ min), where drying and peat-decomposition stages are important, the peak temperature stabilizes at about 650°C, agreeing with the experimental observation in [7]. Near the deep boundary, char-oxidation dominates and the peak temperature increases upon 800°C. Combustion is quenched at the deep end due to heat loss and the lack of peat.

Figure 2.3a shows that water is vaporized within 20 min; peat is decomposed within 27 min; and char-oxidation dominates the rest of time. Figure 2.3b shows that the peak mass-loss rate occurs at the beginning of ignition heating, along with a quick regression of the fuel bed. Once the ignition source is removed, the mass-loss rate suddenly drops, and then slowly decreases during the peat-decomposition stage. The fuel bed continues to shrink rapidly due to both the mass loss and the density increase from peat to char. When the char-oxidation dominates, the mass-loss rate slightly decreases due to both the end

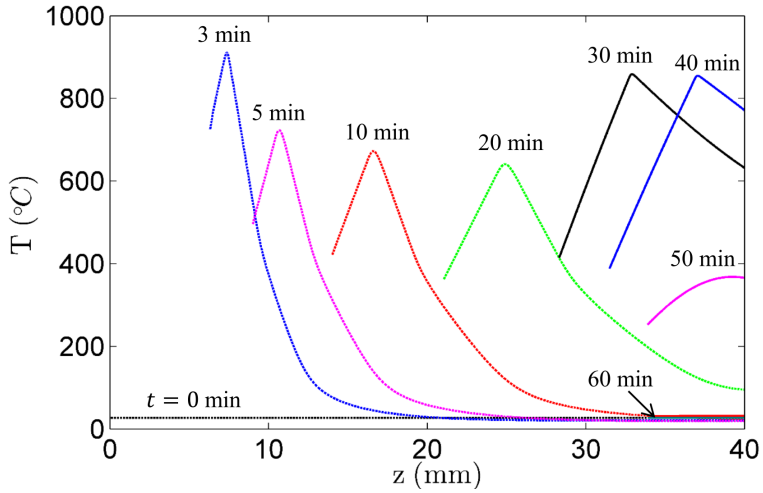

Figure 2.2: Predicted evolution of the temperature profile at different depths for SC peat with MC = 30% and IC = 40%.

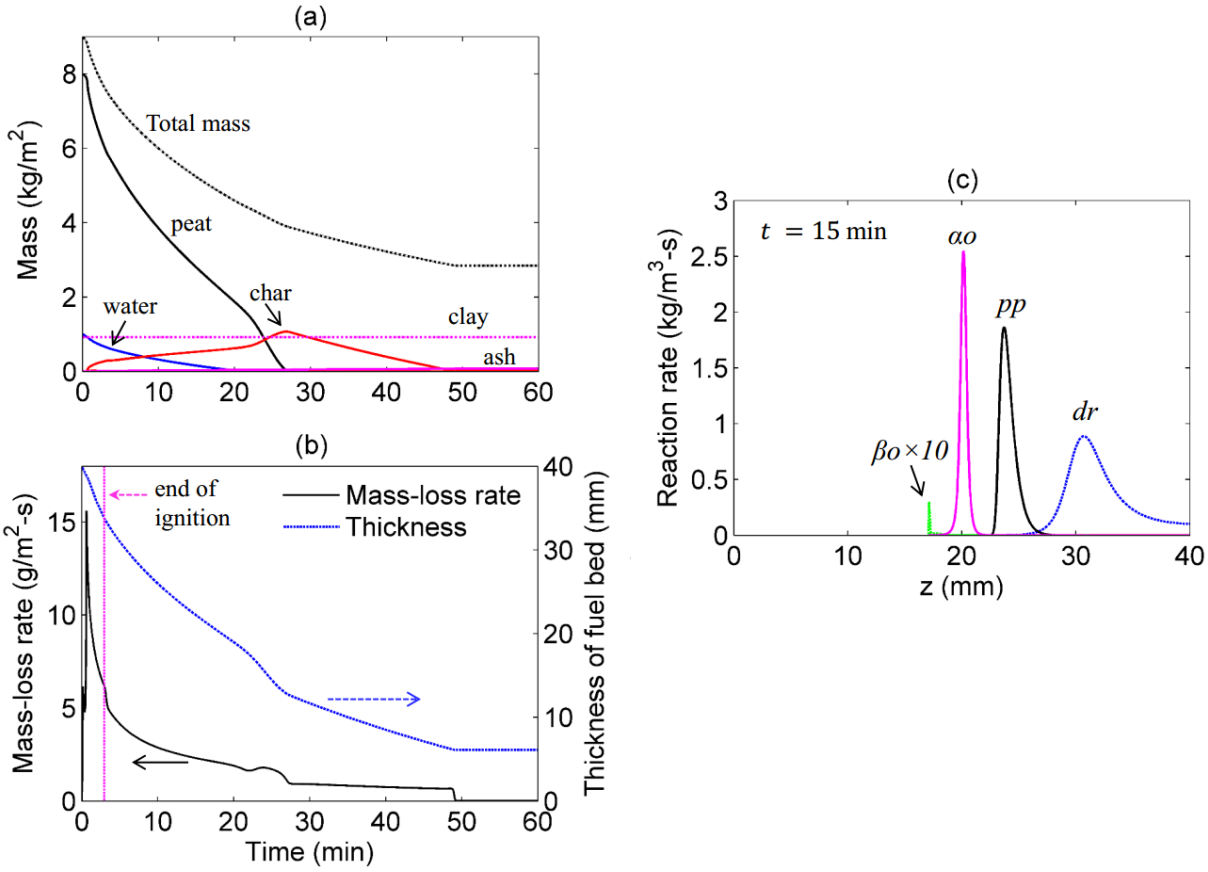

Figure 2.3: Predicted evolution of (a) mass of each species condensed species, (b) total mass-loss rate and thickness of fuel bed, and (c) reaction-rate profile at t = 15 min for SC peat with MC = 30% and IC = 40%.

heat loss and the limited oxygen supply with the accumulation of mineral residue. The regression becomes slower because the mass loss is compensated by the density decrease from char to ash.

Figure 2.3c shows the spread at $t = 15$ min. At this instant, the thickness of smouldering front is about 25 mm, and there are three sub-fronts (from deep to shallow): drying, peat decomposition, and char oxidation, and their reaction rates are on the same order of magnitude. The reaction rate of peat oxidation is two orders of magnitude smaller than peat pyrolysis (too small to be observed in Fig. 2.3c) because most of the oxygen is consumed in the char-oxidation sub-front and little oxygen diffuses through the deeper peat-decomposition sub-front. Consequently, very little of β-char is generated, and the β-char oxidation is small, agreeing with the prediction by a simplified plug-flow model previously studied in Chapter 1. Near the end of smouldering, only char is left, and the char-oxidation rate is high, thus increasing the temperatures in this region (see Fig. 2.2).

2.4 Smouldering thresholds

The MC* measured in experiments of modified samples is plotted against IC* in Fig. 2.4, and fitted by a linear correlation, MC$^* = 1.1 - 1.35$IC* as in [5]. The experimental data of natural samples in [6] is also plotted. In general, Frandsen's linear correlation provides a reasonable reference for smouldering thresholds, but experimental data shows that some soil samples can still burn some distance above the line. This is probably due to the differences in decomposition kinetics, ignition protocol, and physical properties. The influences of these factors are investigated here using the 1-D model.

2.4.1 Influence of kinetic parameters

By fixing IC* over a range of values, MC* can be found by increasing the moisture until the incomplete combustion occurs. On top of the SC peat, the smouldering threshold for another three peat types from Siberia (SI-A and SI-B) and China (CH) were also computed with the corresponding kinetic parameters found in Chapter 1. The SI-A peat also has a high organic content (IC = 2.4%), so a critical curve similar to that of SC peat is obtained. For the high-mineral samples of SI-B and CH peat (natural IC = 12.1% and 18.7%), only one critical point, MC*(natural IC), is included in Fig. 2.4.

Figure 2.4 shows that the computed critical curve for both SC and SI-A samples are nonlinear. For SC peat, the critical curve crosses the middle of the experimental data scatter. The critical curve of SI-A samples is much lower, i.e. requires a much lower MC to ignite. The MC* of SI-B and CH samples falls above and below the curve for SC. In short, the decomposition kinetics have a significant influence on smouldering thresholds.

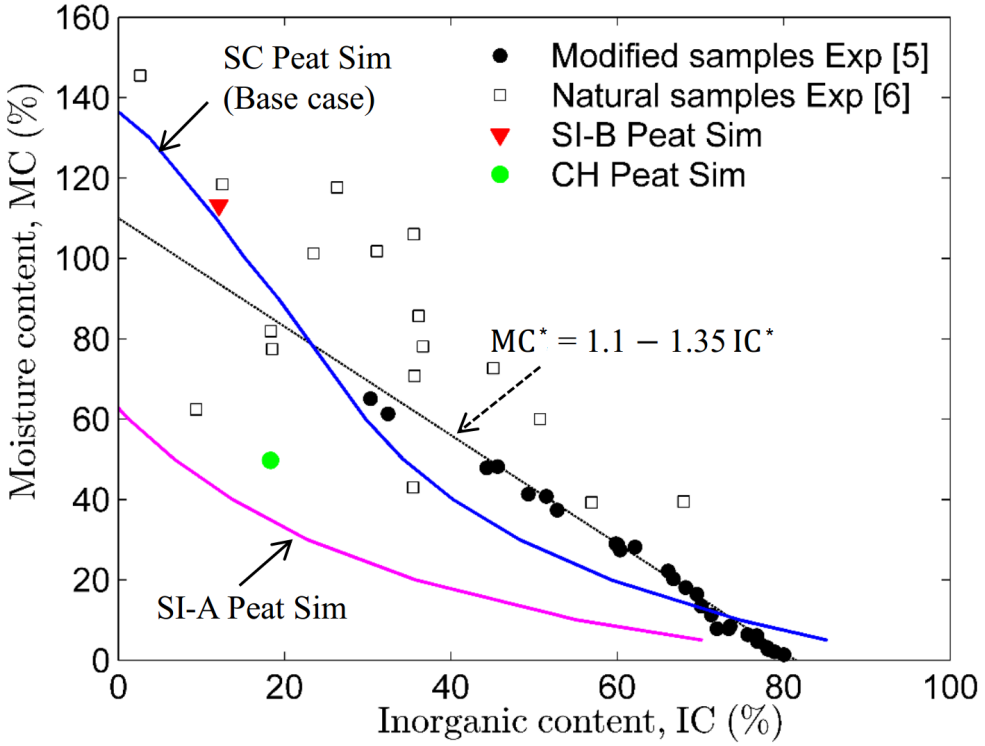

Figure 2.4: Predicted and measured critical curves MC* vs. IC* for the smouldering ignition thresholds of different soils. Above the critical curve, a soil sample cannot ignite.

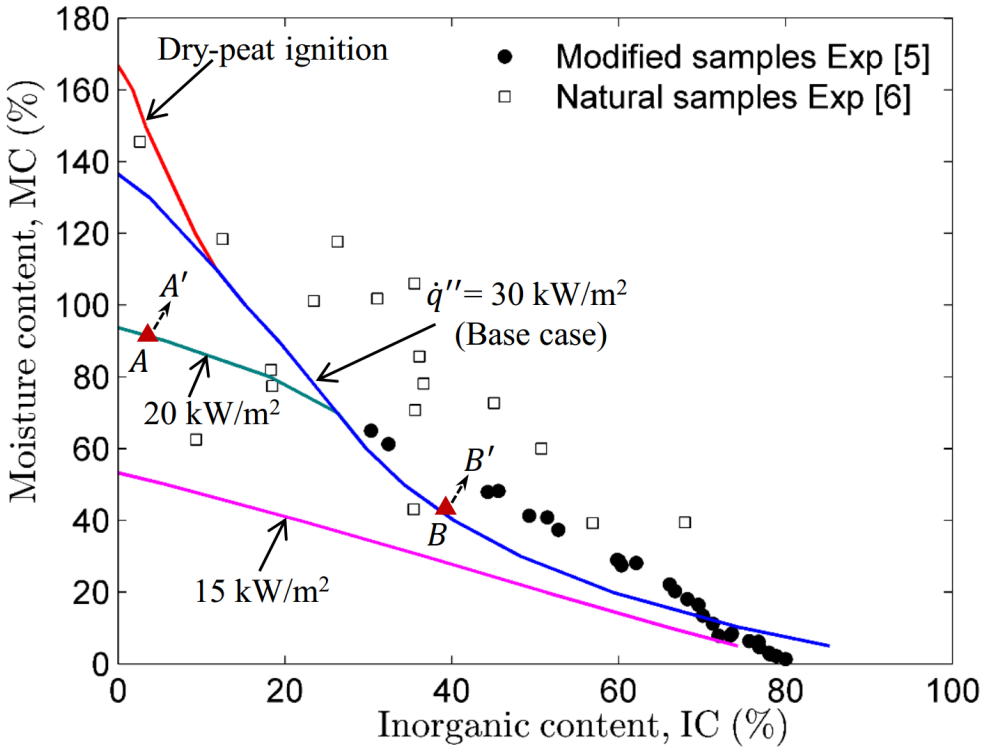

Figure 2.5: Predicted smouldering thresholds with different ignition protocols.

2.4.2 Influence of ignition protocol

The influence of ignition protocol on the smouldering thresholds is investigated by varying the external heat flux in the range from 15 to 30 kW/m^2. The results are shown in Fig. 2.5. The minimum heat flux to ignite a dry SC peat, whose MC is in equilibrium with the ambient (MC$_{dr}$ $\simeq$10% [17, 18]), is found to be 10.5 kW/m^2 for 3 min of heat, and 5.8 kW/m^2 for 30 min. This critical heat flux is much lower than the typical value for flaming fires ($\sim$30 kW/m^2) [21]. The dry-peat ignition protocol used in the second set of experiments of [6] is also simulated by adding 1 cm of dry peat on the top which is heated for the same 3 min under 30 kW/m^2.

For organic soils with IC $<$ 30%, increasing the heat flux extends the smouldering threshold because the drying of the whole sample bed induced by the ignition source increases. Slightly above the critical curve (e.g. point $A \rightarrow A'$), the reaction zone is quickly quenched ($<$ 5 min) near the top surface within the preheated zone. Therefore, for these cases, the threshold is defined as the critical moisture of ignition (MC$^*_{ig}$). For mineral soils with IC $>$ 30%, the influence of the ignition protocol becomes negligible. Slightly beyond the critical curve (e.g. $B \rightarrow B'$), the smouldering front is able to spread out of the preheated zone for a distance before extinction. These cases were recorded as "partial burn" in the experiments of [5, 6], therefore, the threshold is defined as the critical moisture of extinction (MC$^*_{ex}$) (see detailed discussions in Chapter 3).

The results show that the dry-peat ignition protocol is nearly equivalent to a heat flux of 55 kW/m^2 without the additional layer of dry peat. Once ignited, a sustained smouldering front is generated so that the threshold is for extinction. When the heat flux is very low ($\sim$ 15 kW/m^2), the whole critical curve declines, and the threshold is for ignition.

2.4.3 Sensitivity to properties and heat of combustion

The physical properties of peat are expected to vary somehow for different ecosystems. This might affect the smouldering thresholds. Here, the sensitivity of the thresholds is investigated with combinations of the three most important parameters varying over wide ranges of values found in the literature: bulk density of peat (ρ_p = 90$\sim$130 kg/m^3 [5]), solid thermal conductivity of peat ($k_{s,p}$ = 0.8$\sim$1.2 W/m-K [13]), and heat of char oxidation ($\Delta H_{O_2,\alpha o} = \Delta H_{O_2,\beta o}$ = 15$\sim$25 MJ/kg [17]). Figure 2.6 reveals that the range of predicted smouldering thresholds covers most of the experimental data.

Computational results show that MC* increases monotonously with the heat of combustion, but decreases with the bulk density and the thermal conductivity. Therefore, the case with maximum ΔH_{O_2} and minimum ρ_p and $k_{s,p}$ gives the upper boundary (see Fig. 2.6). As ΔH_{O_2} increases, the heat-generation rate increases, overcoming the heat-sink effect of water and minerals. The increase in $k_{s,p}$ is almost equivalent to the increase in IC regarding the threshold, thus lowering the critical curve (i.e. more difficult to smoulder),

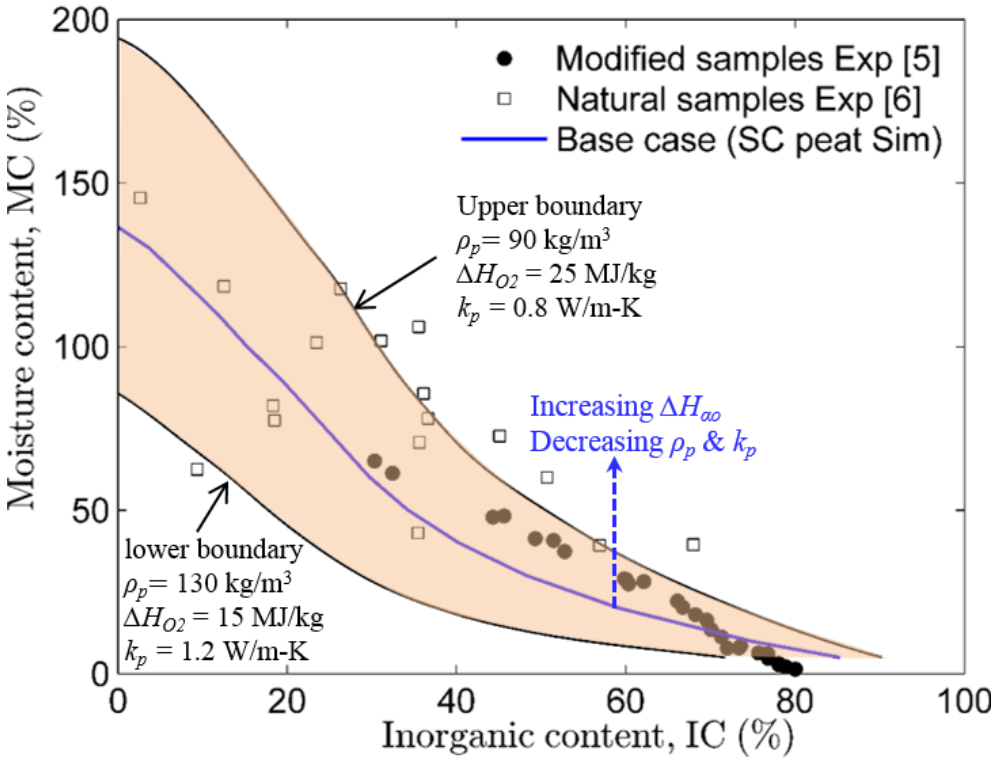

Figure 2.6: Predicted smouldering thresholds for a combination of ρ_p, $k_{s,p}$, and ΔH_{O_2}, varying in a wide range.

especially at low IC values. As ρ_p increases, the mass concentrations of water and clay also increase under the same MC and IC. Therefore, the increasing heat-sink effect moves the critical curve towards lower MC values, agreeing with experimental observations in [22].

2.5 Conclusions

In this chapter, a comprehensive 1-D model of a reactive porous media is implemented in the open-source code Gpyro to investigate the smouldering combustion of peat with a 5-step (including drying) heterogeneous kinetics. Two sets of small-scale experiments [5, 6] are simulated for the first time, and the transient temperature, species, reaction profiles, and surface regression of the fire are studied. The predicted smouldering thresholds related to the critical moisture and inorganic contents are nonlinear, as opposed to previously reported linear correlation, and show a better agreement with the experimental results for a wide range of soil types. The smouldering thresholds are found to depend on the decomposition kinetics, physical properties, and the ignition protocol. The results reveal that the threshold values found by Frandsen for organic soils are due to ignition, and for mineral soils are due to extinction. This is the first time that a physics-based model of smouldering peat fires is developed, thus helping to understand this important natural and widespread phenomenon.

Acknowledgements

I want to thank Professor Haixiang Chen (University of Science and Technology of China) for his valuable contribution to this chapter. I would also like to thank the support of Santander Overseas Research Scholarship and EPSRC. Valuable comments from Prof. Naian Liu (University of Science and Technology of China) and reviewers are acknowledged.

References

[1] T. Ohlemiller, "Modeling of smoldering combustion propagation," *Progress in Energy and Combustion Science*, vol. 11, no. 4, pp. 277 – 310, 1985.

[2] G. Rein, "Smouldering Fires and Natural Fuels," in *Fire Phenomena and the Earth System* (C. Belcher, ed.), ch. 2, pp. 15–33, Wiley and Sons, 2013.

[3] S. E. Page, F. Siegert, J. O. Rieley, H.-D. V. Boehm, A. Jaya, and S. Limin, "The amount of carbon released from peat and forest fires in Indonesia during 1997," *Nature*, vol. 420, pp. 61–65, 2002.

[4] L. Moreno, M.-E. Jimenez, H. Aguilera, P. Jimenez, and A. Losa, "The 2009 Smouldering Peat Fire in Las Tablas de Daimiel National Park (Spain)," *Fire Technology*, vol. 47, no. 2, pp. 519–538, 2011.

[5] W. H. Frandsen, "The influence of moisture and mineral soil on the combustion limits of smoldering forest duff," *Canadian Journal of Forest Research*, vol. 17, no. 12, pp. 1540–1544, 1987.

[6] W. H. Frandsen, "Ignition probability of organic soils," *Canadian Journal of Forest Research*, vol. 27, no. 9, pp. 1471–1477, 1997.

[7] G. Rein, N. Cleaver, C. Ashton, P. Pironi, and J. L. Torero, "The severity of smouldering peat fires and damage to the forest soil," *Catena*, vol. 74, no. 3, pp. 304 – 309, 2008.

[8] C. Di Blasi, "Mechanisms of Two-Dimensional Smoldering Propagation Through Packed Fuel Beds," *Combustion Science and Technology*, vol. 106, no. 1-3, pp. 103–124, 1995.

[9] G. Rein, A. C. Fernandez-Pello, and D. L. Urban, "Computational model of forward and opposed smoldering combustion in microgravity," *Proceedings of the Combustion Institute*, vol. 31, no. 2, pp. 2677 – 2684, 2007.

[10] F. He, N. Zobel, W. Zha, and F. Behrendt, "Effects of physical properties on one-dimensional downward smoldering of char: Numerical analysis," *Biomass and Bioenergy*, vol. 33, no. 8, pp. 1019 – 1029, 2009.

[11] C. Lautenberger and C. Fernandez-Pello, "Generalized pyrolysis model for combustible solids," *Fire Safety Journal*, vol. 44, no. 6, pp. 819 – 839, 2009.

[12] J. Holman, *Heat Transfer*. Mechanical engineering series, McGraw-Hill, 1989.

[13] R. Jacobsen, E. Lemmon, S. Penoncello, Z. Shan, and N. Wright, "Thermophysical Properties of Fluids and Materials," in *Heat Transfer Handbook* (A. Bejan and A. Kraus, eds.), ch. 2, pp. 43–159, John Wiley & Sons, 2003.

[14] R. M. Hadden, G. Rein, and C. M. Belcher, "Study of the competing chemical reactions in the initiation and spread of smouldering combustion in peat," *Proceedings of the Combustion Institute*, vol. 34, no. 2, pp. 2547 – 2553, 2013.

[15] H. de Jonge and M. C. Mittelmeijer-Hazeleger, "Adsorption of CO_2 and N_2 on Soil Organic Matter: Nature of Porosity, Surface Area, and Diffusion Mechanisms," *Environmental Science & Technology*, vol. 30, no. 2, pp. 408–413, 1996.

[16] B. Punmia and A. Jain, *Soil Mechanics and Foundations*. Laxmi Publications Pvt Limited, 2005.

[17] K. Bergner and C. Albano, "Thermal analysis of peat," *Analytical Chemistry*, vol. 65, no. 3, pp. 204–208, 1993.

[18] H. Chen, W. Zhao, and N. Liu, "Thermal Analysis and Decomposition Kinetics of Chinese Forest Peat under Nitrogen and Air Atmospheres," *Energy & Fuels*, vol. 25, no. 2, pp. 797–803, 2011.

[19] W. H. Frandsen, "Heat Evolved From Smoldering Peat," *International Journal of Wildland Fire*, vol. 1, p. 197204, 1991.

[20] C. Huggett, "Estimation of rate of heat release by means of oxygen consumption measurements," *Fire and Materials*, vol. 4, no. 2, pp. 61–65, 1980.

[21] D. Drysdale, *An Introduction to Fire Dynamics*. Wiley, 2011.

[22] R. Hartford, "Smoldering combustion limits in peat as influenced by moisture, mineral content, and organic bulk density," *Proceedings of the 10th Conference on Fire and Forest Meteorology*, pp. 282–286, 1989.

Chapter 3

Computational Study of the Depth of Burn and the Heterogeneous Moisture Profile in Smouldering Peat Fires

Summary [1]

Smouldering combustion is the slow, low-temperature, flameless burning of porous fuels and the driving phenomenon of wildfires in peatlands. Smouldering fires propagate horizontally and vertically through organic layers of the ground and can reach deep into the soil. In this chapter, a 1-D computational model of a reactive porous media, using the open-source code Gpyro, is established to investigate the in-depth spread of smouldering fires into peat samples with varying profiles of density, moisture, and inert contents. The model solves the species, momentum, and energy conservation equations with a heterogeneous reaction scheme, so as to predict the transient temperature, species, reaction profiles, and the depth of burn from ignition to extinction. Modelling results reveal that the critical moisture of extinction is higher than the previously found critical moisture of ignition, and it is not constant, but depends on conditions upstream of the column and the thickness of the moist layer. The influence of the upstream peat moisture, thickness and bulk density is investigated. The predicted depth of burn and critical moisture values are compared to all experimental measurements with natural organic soil samples in Benscoter et al. [1], showing a good agreement. This study improves the physical understanding on the role of moisture in ignition and extinction, and explains the phenomena of smouldering fire spreading over soils layers of extremely high moisture.

1. This chapter is based on "X. Huang, G. Rein (2015) *Computational Study of Critical Moisture and Depth of Burn in Peat Fires*, **International Journal of Wildland Fire**, 24: 798-808."

3.1 Introduction

Smouldering combustion is the slow, low-temperature, flameless burning of porous fuels and the most persistent type of combustion, different from flaming combustion [2]. Smouldering is the dominant phenomena in megafires in natural deposits of peat which are the largest and longest burning fires on Earth [3]. Locally, smouldering fires have a severe impact on the soil system by burning its organic content. The prolonged heating from the slowly propagating fire can kill roots, seeds and trees, increasing the likelihood of long term damage and erosion to local ecosystem [4–6]. Organic soils and peat may restore between 1/5 and 1/3 of plant's terrestrial organic carbon, approximately the same mass of carbon in atmosphere, despite peatlands occupying only 3% of earth surface [3, 7, 8]. Globally, these fires contribute considerably to greenhouse gas emissions, and result in widespread destruction of ecosystems and regional haze events (e.g. recent megafires in Southeast Asia, North America, and Northeast Europe) [9]. During the 1997 extreme haze event in Southeast Asia, peat fires emitted the equivalent to 13-40% of the global man-made greenhouse gas emissions of that year [10]. More recent figure estimate that the average emission from peat fires is roughly equivalent to 15% of the man-made emissions [11].

Peat can hold a wide range of moisture contents [2] (MC), ranging from about 10% under drought conditions to well in excess of 300% under flooded conditions [1, 9]. Water represents a significant energy sink to prevent smouldering fire, meanwhile natural or anthropogenic-induced droughts are found to be the leading causes of smoldering megafires [6, 9]. Therefore, soil moisture is the single most important property governing the ignition and spread of smoldering wildfires [6, 12, 13]. During the forced ignition, water needs to be first dried out, and then peat starts to decompose until initializing the exothermic char oxidation (i.e. a successful ignition). The critical moisture content of smouldering ignition (MC^*_{ig}) for various peat types has been measured in the range of 40-150% [6, 14, 15]. Drier than this threshold, peat becomes susceptible to smoldering. Secondary influence factors on the soil's susceptibility to smoldering includes the inorganic content [2] (IC), bulk density, porosity, and chemical composition. Frandsen's experiments [14, 15] showed there was a decreasing relationship between critical moisture and inorganic contents (MC^*_{ig} and IC^*_{ig}): a high-mineral soil can only be ignited at a low moisture. The influence of the bulk density has been studied experimentally in the literature [12, 16], but its specific impact to smouldering has not yet been conclusive. Hartford [16] found that a higher bulk density decreases the probability of soil smouldering at a given MC and IC. However, Garlough and Keyes [12] recently found that bulk density is not significant in the smouldering ignition of pine duff.

2. Moisture content (MC) is defined in dry basis as the mass of water divided by the mass of a dried soil sample, expressed as %. Inorganic content (IC) is defined in dry basis as the mass of soil inorganic matter (minerals) divided by the mass of a dried soil sample, expressed as %.

If the ignition is successful on the surface, a self-sustain smouldering front can spread both laterally and in-depth, dominated by the forward smouldering, as discussed in Chapter 1. The extinction occurs if a moist layer is wet and thick enough to quench the fire, defining a critical moisture of extinction (MC^*_{ex}). After extinction, the thickness of the burnt soil layer, i.e. the depth of burn (DOB), can be measured and further used to estimate the carbon release from soil [13, 17]. Wade et al. [18] reported an experiment that the upper organic layer can only be ignited at MC $< 65\%$, while once ignited, it can continue to burn a lower wetter layer up to 150%. Reardon et al. [19] found that after ignition, a 10-cm muck soil samples of MC$< 140\%$ can always be consumed while the depth of burn drops to 5.7 cm for MC $= 150-225\%$, and to 2.4 cm for MC $= 250-300\%$. Benscoter et al. [1] conducted a series of experiments of in-depth spread on several natural peat samples which reveal that no simple relationship exists among moisture, bulk density, and depth of burn. For most cases in [1], the smouldering front did not spread cross a peat layer with a MC over 150%, but for one particular case (Field Hol 1), a smouldering front was able to spread over a 3-cm layer of MC $= 295\%$ before extinction. Zaccone et al. [20] experimentally found that for a uniform Sphagnum peat, after a strong ignition, the depth of burn for MC $= 100\%$ and MC $= 200\%$ were 17 cm and 7 cm. All these experiments suggest that MC^*_{ex} differ from MC^*_{ig}, meanwhile, the depth of burn depend on both upstream and downstream conditions, which have not been well distinguished and studied before.

The computational studies on smouldering peat fire in the literature are limited. Benscoter et al. [1] adopted and modified Van Wagner's 0-D thermodynamic model [21], and by tuning a downward heat-transfer efficiency, the best prediction of depth of burn showed a fair agreement with experiments. In Chapter 2, a multi-physics 1-D model of a reactive porous media with an open-source code Gpyro is established to investigate the smouldering combustion of peat with a 5-step (including drying) heterogeneous kinetics. The model successfully reproduce Frandsen's experiments [14, 15] and reveal the sensitivity of smouldering threshold, regarding MC^* and IC^*, to the chemical kinetics and physical properties of soil as well as the ignition protocol.

In this chapter, multi-physics 1-D model is further applied, and further improve the model to solve peat samples with given profiles of moisture content and physical properties. With this model, the MC^*_{ex} and DOB in an in-depth spread of peat fire are investigated under different upstream conditions. The influences of layer thicknesses, physical properties, and ignition protocols are investigated. Afterward, this model is used to simulate the Benscoter et al.'s experiments [1], and the results of simulations and experiments are compared and discussed.

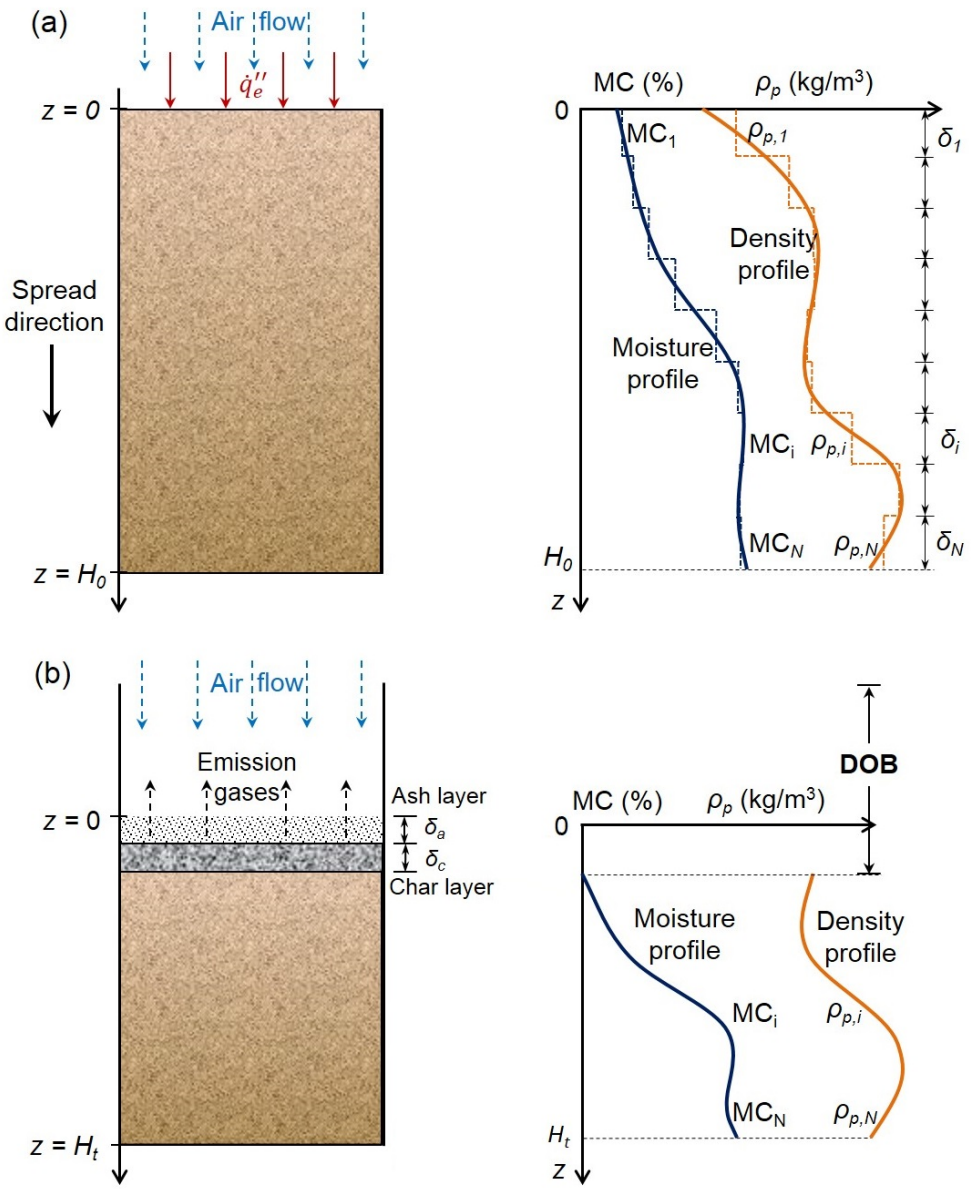

Figure 3.1: Illustrations of the 1-D computational domain of peat with moisture and density profiles for an in-depth spread of smouldering fire at (a) the beginning of ignition ($t = 0$), (b) the self-sustained spread.

3.2 Computational model of peat fire at in-depth spread

If the depth of peat column is larger than other dimensions (e.g in [1, 20]), in-depth spread can be approximated as 1-D at the direction of in-depth spread. Figure 3.1a shows the computational domain of a tall peat column and its moisture and density profiles. The ignition takes place on the top surface, and the forced ignition is simulated by a uniform heat flux. If the ignition source is weak or the moisture near the top is large, the smouldering front may not form or propagate. Once ignited, a smouldering front starts to spread in-depth, drying the peat downward, at the same time, a ash layer and a char layer start to accumulated on the top, as illustrated in Fig. 3.1b. The consumption

depth of original sample is defined as the depth of burn [1], which depends not only on the downstream MC and soil properties, but also the upstream burning condition. Similar to Chapter 2, the open-source code Gpyro [22] is used to develop this 1-D smouldering combustion of peat.

3.2.1 1-D governing equations

The model solves the 1-D transient equations for both solid and gas phases. The gas-phase temperature is assumed to be the same as the condensed-phase temperature (thermal equilibrium), and the Darcy's law is used to solved gas-phase momentum conservation equation. The details are reported in [22], only the essentials of the model are presented here: (1) condensed-phase mass conservation, (2) condensed-phase species conservation, (3) condensed-phase energy conservation, (4) gas-phase mass conservation, (5) gas-phase species conservation, and (6) gas-phase momentum conservation. All symbols are explained in the nomenclature, and subscripts i, j, and k refer to the number of condensed-phase species, gas-phase species, and reaction, respectively.

$$\frac{\partial \overline{\rho}}{\partial t} = -\dot{\omega}_{fg}^{'''} \tag{3.1}$$

$$\frac{\partial \left(\overline{\rho} Y_i\right)}{\partial t} = \dot{\omega}_{fi}^{'''} - \dot{\omega}_{di}^{'''} \tag{3.2}$$

$$\frac{\partial (\overline{\rho}\overline{h})}{\partial t} + \frac{\partial \left(\dot{m}^{''} h_g\right)}{\partial z} = \frac{\partial}{\partial z}\left(\overline{k}\frac{\partial T}{\partial z}\right) + \sum_{k=1}^{K} \dot{\omega}_{di,k}^{'''} \Delta H_k \tag{3.3}$$

$$\frac{\partial \left(\rho_g \overline{\psi}\right)}{\partial t} + \frac{\partial \dot{m}^{''}}{\partial z} = \dot{\omega}_{fg}^{'''} \tag{3.4}$$

$$\frac{\partial \left(\rho_g \overline{\psi} Y_i\right)}{\partial t} + \frac{\partial (\dot{m}^{''} Y_j)}{\partial z} = -\frac{\partial}{\partial z}\left(\overline{\psi}\rho_g D \frac{\partial Y_j}{\partial z}\right) + \dot{\omega}_{fj}^{'''} - \dot{\omega}_{dj}^{'''} \tag{3.5}$$

$$\dot{m}^{''} = -\frac{\overline{K}}{\nu}\frac{\partial P}{\partial z} \qquad (P = \rho_g R_s T) \tag{3.6}$$

Each condensed-phase species is assumed to have constant properties (e.g. bulk density, specific heat, and porosity). All gaseous species have unit Schmidt number, and equal diffusion coefficient and specific heat. The averaged properties in each cell are calculated by weighting the appropriate mass fraction (Y_i) or volume fraction (X_i) [22], for example,

$$\begin{aligned} \overline{c} &= \sum_{i=1}^{M} Y_i c_i, \quad \overline{h} = \sum_{i=1}^{M} Y_i h_i \\ \overline{\rho} &= \sum_{i=1}^{M} X_i \rho_i, \quad \overline{k} = \sum_{i=1}^{M} X_i k_i. \end{aligned} \tag{3.7}$$

and the conversion between the mass and volume fractions is

$$X_i = \overline{\rho}\frac{Y_i}{\rho_i} \tag{3.8}$$

At the free surface ($z = 0$), convective boundary condition is imposed: $h_{c,0} = 10$ W/m^2-K with surface reradiation ($\varepsilon = 0.95$) and $h_{m,0} = 0.02$ kg/m^2-s (approximation of Couette flow [22]). The environmental pressure and temperature are assumed to be atmospheric and 300 K. Within the first 5 min, an external heat flux ($\dot{q}_e''$) is applied as the ignition source, and the influence of ignition protocol is previously discussed in Chapter 2. At $z = L$, the mass flux is set to be zero, and heat loss is set with $h_{c,L} \approx k_{wall}/\delta_{wall} = 3$ W/m^2-K [1]. A fully implicit formulation is adopted for solution of all equations, and more details about numerical solution methodology are reported in [22]. Current simulations were run with an initial cell size of $\Delta z = 0.2$ mm, and initial time step of 0.02 s. Reducing the cell size and time step by a factor of 2 gives no significant difference in results, so the grid is sufficiently resolved.

3.2.2 Chemical kinetics

The heterogeneous reaction in mass basis is written as:

$$A_k + \sum_{j=1}^{N} \nu_{j,k}^{'} \text{gas } j \rightarrow \nu_{B,k} B_k + \sum_{j=1}^{N} \nu_{j,k}^{''} \text{gas } j, \tag{3.9}$$

where $\nu_{B,k} = 1 + (\rho_B/\rho_A - 1)\,\chi_k$, and χ_k quantifies the shrinkage or intumescence of the cell size. The destruction rate of a condensed species A in a reaction k is expressed by the Arrhenius law as

$$\dot{\omega}_{dA_k}''' = \frac{(\overline{\rho} Y_A \Delta z)_\Sigma}{\Delta z} A_k e^{-E_k/RT} \left[\frac{\overline{\rho} Y_A \Delta z}{(\overline{\rho} Y_A \Delta z)_\Sigma} \right]^{n_k} Y_{O_2}^{n_{O_2,k}}, \tag{3.10}$$

$$(\overline{\rho} Y_A \Delta z)_\Sigma = (\overline{\rho} Y_A \Delta z)\,|_{t=0} + \int_0^t \dot{\omega}_{fi}''' \Delta z(\tau) d\tau, \tag{3.11}$$

where subscripts d and f represent destruction and formation. The formation rate of the condensed species B and all gases from reaction k are $\dot{\omega}_{fB_k}''' = \nu_{B,k} \dot{\omega}_{dA_k}'''$ and $\dot{\omega}_{fg_k}''' = (1 - \nu_{B,k}) \dot{\omega}_{dA_k}'''$. The corresponding solid-phase heat of reaction is $\dot{Q}_{s,k}''' = -\dot{\omega}_{dA_k}''' \Delta H_k$.

In Chapter 1, various decomposition scheme were investigated using thermogravity (TG) data of four different peat samples from Scotland (SC), Siberia (SI-A and SI-B), and China (CH). The best kinetics scheme was found to be: (1) Drying (dr), (2) Peat pyrolysis (pp), (3) Peat oxidation (po), (4) β-Char oxidation (βo), and (5) α-Char oxidation (αo) as

$$\text{Peat} \cdot \nu_{w,dr} \text{H}_2\text{O} \rightarrow \text{Peat} + \nu_{w,dr} \text{H}_2\text{O(g)} \qquad (dr) \tag{3.12}$$

$$\text{Peat} \rightarrow \nu_{\alpha,pp} \alpha\text{-Char} + \nu_{g,pp} \text{Gas} \qquad (pp) \tag{3.13}$$

$$\text{Peat} + \nu_{O_2,po} O_2 \rightarrow \nu_{\beta,po} \beta\text{-Char} + \nu_{g,po} \text{Gas} \qquad (po) \tag{3.14}$$

$$\beta\text{-Char} + \nu_{O_2,\beta o} O_2 \rightarrow \nu_{a,\beta o} \text{Ash} + \nu_{g,\beta o} \text{Gas} \qquad (\beta o) \tag{3.15}$$

$$\alpha\text{-Char} + \nu_{O_2,\alpha o} O_2 \rightarrow \nu_{a,\alpha o} \text{Ash} + \nu_{g,\alpha o} \text{Gas} \qquad (\alpha o) \tag{3.16}$$

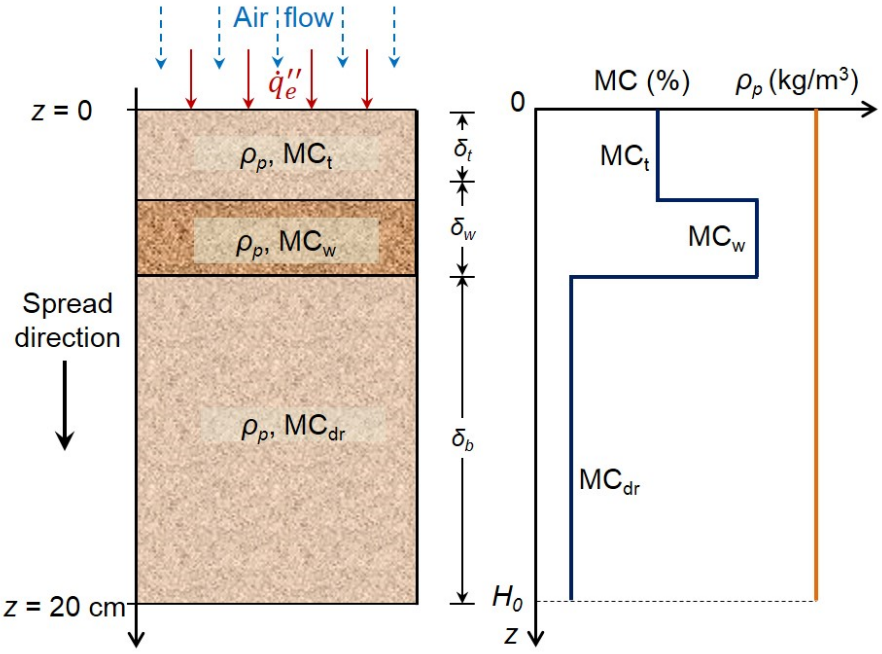

Figure 3.2: Illustrations of the 1-D computational domain of peat with moisture and density profiles for a simple 3-layer system.

where ν_w = MC, subscripts w, p, α, β, and a represent five condensed species (water, peat, α-char, β-char, and ash), and four gaseous species are considered: oxygen, nitrogen, water vapour, and emission gases. Essentially, there are two decomposition paths: (a) Peat $\rightarrow$ α-Char $\rightarrow$ Ash, and (b) Peat$\rightarrow$ β-Char $\rightarrow$Ash (see Chapter 1).

3.3 Smouldering process

In reality, it is impossible to obtain a continuous profile of soil property, while only the average value over a finite thickness (δ) can be experimentally measured, as illustrated in Fig. 3.1a. Each layer ($i = 1, 2, 3...N$) may have its own thickness (δ_i), moisture content (MC$_i$), physical properties (e.g. ρ_i, k_i, c_i), and decomposition chemistry. For the same reason, in order to input measured properties, the soil column in computational model also has to be differentiated into multiple layers. For example, in Benscoter et al.'s experiment [1], peat columns of 20-30 cm thickness were divided into multiple layers of 3 cm, while the measured moisture and density profiles were complex and random, discussed more in Section 3.5. Therefore, starting with simulating Benscoter et al.'s complex samples is difficult and not well-controlled.

In this section, a simple and well-controlled case in detail with the (both physically and chemically) same peat and three layers is studied: a top layer (δ_t), a middle wet layer (δ_w), and a bottom dry layer (δ_b). Figure 3.2 shows the computational domain, the length of which is fixed as $h_0 = \delta_t + \delta_w + \delta_b = 20$ cm while the thickness of each layer can be changed. The top layer has a moisture lower than the critical value of ignition

Table 3.1: The physical parameters of condensed-phase species where $\rho_{s,i}$, $k_{s,i}$, and c_i are from [23], and $\rho_{i,0}$ is from [1, 24].

Species (i)	$\rho_{s,i}$ (kg/m^3)	$\rho_{i,0}$ (kg/m^3)	$\psi_{i,0}$ (-)	$k_{s,i}$ (W/m-K)	c_i (J/kg-K)
water	1000	1000	0	0.6	4186
peat	1500	40	0.973	1.0	1840
α-char	1300	49	0.962	0.26	1260
β-char	1300	49	0.962	0.26	1260
ash	2500	7	0.997	1.2	880

(MC$_t$ <MC$^*_{ig}$), so it can be ignited after external heating. The middle wet layer can be much wetter. The bottom layer always uses the air-dried peat, in equilibrium with the ambient (MC$_{dr}$ = MC$_b \simeq 10\%$ (see TGA in Chapters 2 and 4). The major reason to add this bottom dry layer is to create a consistent bottom boundary condition and to avoid the possible influence on the extinction and depth of burn.

If the moisture of the middle wet layer (MC$_w$) is not very high, the ignited smouldering front in the top layer is able to propagate through it and further ignite the bottom layer, and eventually to consume all the fuel (i.e. DOB = h_0 = 20 cm). Hence, the extinction point as well as MC$^*_{ex}$ can be found by continuously increasing MC$_w$ until the combustion becomes incomplete. The influences of the moisture in the top layer (MC$_t$), the peat bulk density (ρ_p), and the strength of ignition source ($\dot{q}''_e$) are also investigated to better understand the characteristics of extinction and the depth of burn.

3.3.1 Parameter selection

The thermo-physical properties of each condensed-phase species (i) are assumed to be constant and temperature-independent, listed in Table 3.1. The solid ($\psi_i = 0$) thermo-physical properties, $\rho_{s,i}$, $k_{s,i}$, c_i of peat, char, and ash are selected from [23]. The porosity is calculated with the bulk density (ρ_i) as

$$\psi_i = 1 - \frac{\rho_i}{\rho_{s,i}} \tag{3.17}$$

The average bulk density of peat in [1] is around $\rho_p = 40$ kg/m^3 which is selected here. The bulk densities of char and ash are referred to the measurements in [24] by keeping the same ratio to the bulk density of peat.

The effective thermal conductivity includes the radiation heat transfer across pores as

$$k_i = k_{s,i}(1 - \psi_i) + \gamma_i \sigma T^3 \tag{3.18}$$

where $\gamma_i = 10^{-4} \sim 10^{-3}$ m depends on the pore size as $\gamma_i \approx 3d_{p,i}$ [25]. The average pore size relates to the particle surface area as $d_{p,i} = 1/S_i\rho_i$ where $S_p = S_c = 0.05$ m^2/g and

Table 3.2: Reaction parameters and gaseous yields of 5-step reactions for a (SC) Scotland subshrub and sphagnum high-moor peat sample (see Chapter 1).

Parameter/k	dr	pp	po	βo	αo
$\lg A_k$ ($\lg(s^{-1})$)	8.12	5.92	6.51	1.65	7.04
E_k (kJ/mol)	67.8	93.3	89.8	54.4	112
n_k (-)	2.37	1.01	1.03	0.54	1.85
$\nu_{B,k}$ (kg/kg)	0	0.75	0.65	0.03	0.02
ΔH_k (MJ/kg)	2.26	0.5	-2.66	-14.6	-14.6
$\nu_{O_2,k}$ (kg/kg)	0	0	0.20	1.11	1.12

$S_a = 0.2$ m^2/g [26]. The absolute permeability of soil can be estimated from an empirical expression [27]

$$K_i = 10^4 \frac{\nu_w}{g} d_{p,i}^2 \approx 10^{-3} d_{p,i}^2 \sim \frac{1}{\rho_i^2} \tag{3.19}$$

which varies from 10^{-12} to 10^{-9} m^2, and decreases with the bulk density. Because of a high porosity ($\psi_p = 0.973$) and the low volumetric water content, $VWC = 0.1$ at MC = 250∼400% [1], water is assumed to stay in the pores of peat without the volume expansion. Thus, the bulk density of a moist peat is $\rho = (1 + \text{MC})\rho_p$. The properties of α-char and β-char are assumed to be the same.

The decomposition chemistry of a Scotland (SC) peat, analyzed in Chapter 1, is selected for all peat layers, and Table 3.2 lists the kinetic and stoichiometric parameters. The heat of oxidation is related to the oxidized organic matter, assumed as $\Delta H_k = H_{O_2,k}(1 - \nu_{B,k})$. The surface peat in [1] has a low bulk density and is little decomposed, so the heat of combustion is expected to be lower than the high-density well-decomposed peat in [14, 15]. By integrating the energy-flux curve of TG-DSC measurements of multiple peat samples [28, 29], it is estimated that $H_{O_2,po} = 7.5$ MJ/kg and $H_{O_2,\alpha o} = H_{O_2,\beta o} = 15$ MJ/kg, leading to a heat of smouldering combustion of $\Delta H_{sm} = 11.7$ MJ/kg. The oxygen consumption is related to the heat of oxidation as $\nu_{O_2,k} = \Delta H_k/(13.1$ MJ/kg) [30].

3.3.2 Base case

A base case is arbitrarily chosen to investigate the combustion process and smouldering structure in detail: $\delta_t = 6$ cm, $\delta_w = 3$ cm, $\delta_b = 11$ cm. The peat sample has a uniform bulk density of 40 kg/m^3 and a wet layer with MC$_w$ = 180%. The top layer chooses the same air-dried peat as the bottom layer (MC$_t$ = MC$_{dr}$ = 10%) which is expected to have the strongest possible smouldering front after ignition. The minimum external heat flux to ignite the air-dried peat is found to be 8.3 kW/m^2 for 5 min and 5 kW/m^2 for 30

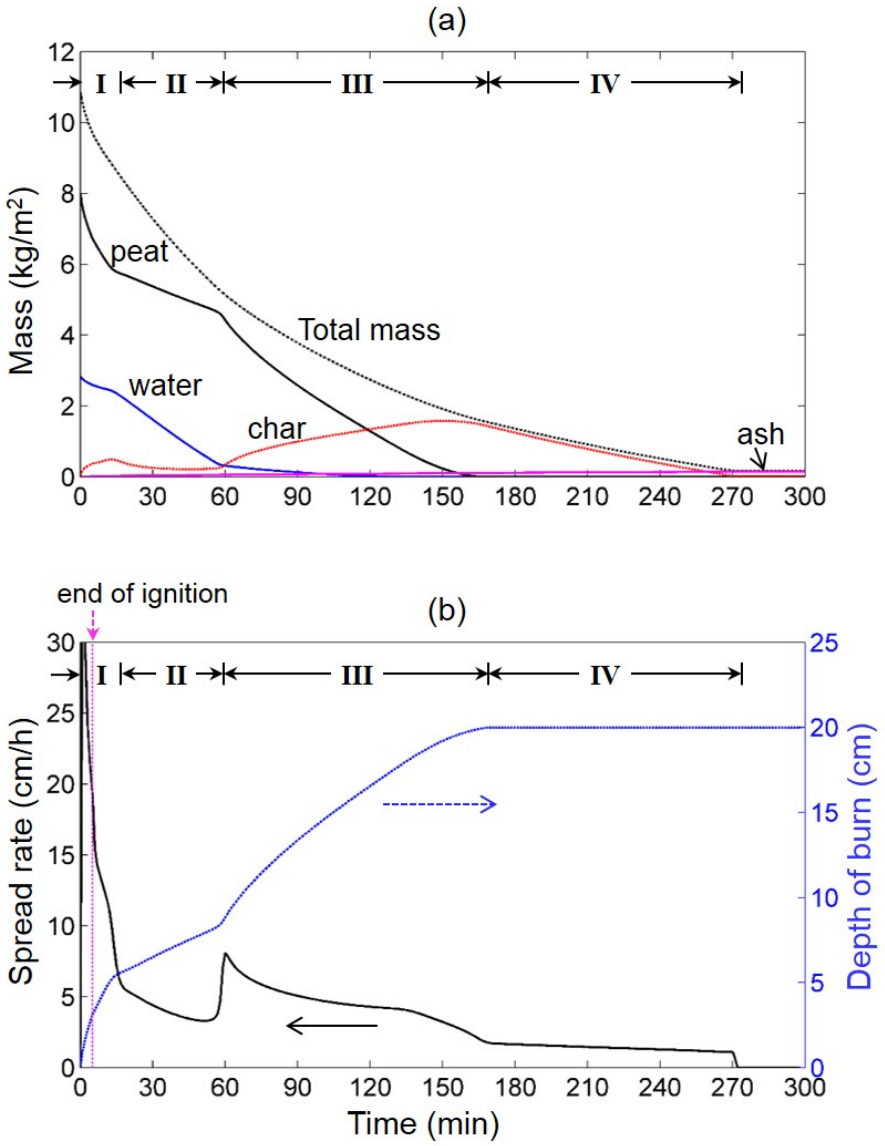

Figure 3.3: Predicted evolutions of (a) the species mass, m_i; and (b) depth of burning and spread rate for the base case: $\delta_t = 6$ cm ($\mathrm{MC}_t = 10\%$), $\delta_w = 3$ cm ($\mathrm{MC}_w = 180\%$), $\delta_b = 11$ cm ($\mathrm{MC}_b = 10\%$).

min, much lower than that for flaming fires (~ 30 kW/m^2 [31]). To ensure a uniform and successful ignition, $\dot{q}''_e = 30$ kW/m^2 for 5 min is selected as the ignition protocol. Figure 3.3 shows the predicted (a) mass evolution of each species, m_i, and (b) depth of burn and spread rate. Here, the depth of burn is defined by the position at which most of peat is decomposed (i.e. $Y_p < 5\%$). The spread rate is obtained by tracking the position of the peak temperature.

For the drying and decomposition of peat, three stages can be seen due to three lays with different MCs: (I) $t < 15$ min, (II) $15 < t < 60$ min, and (III) $60 < t < 170$ min. When smouldering front propagates through the middle wet layer (Stage II), drying becomes fast while the peat decomposition slows down. The spread rate decreases as

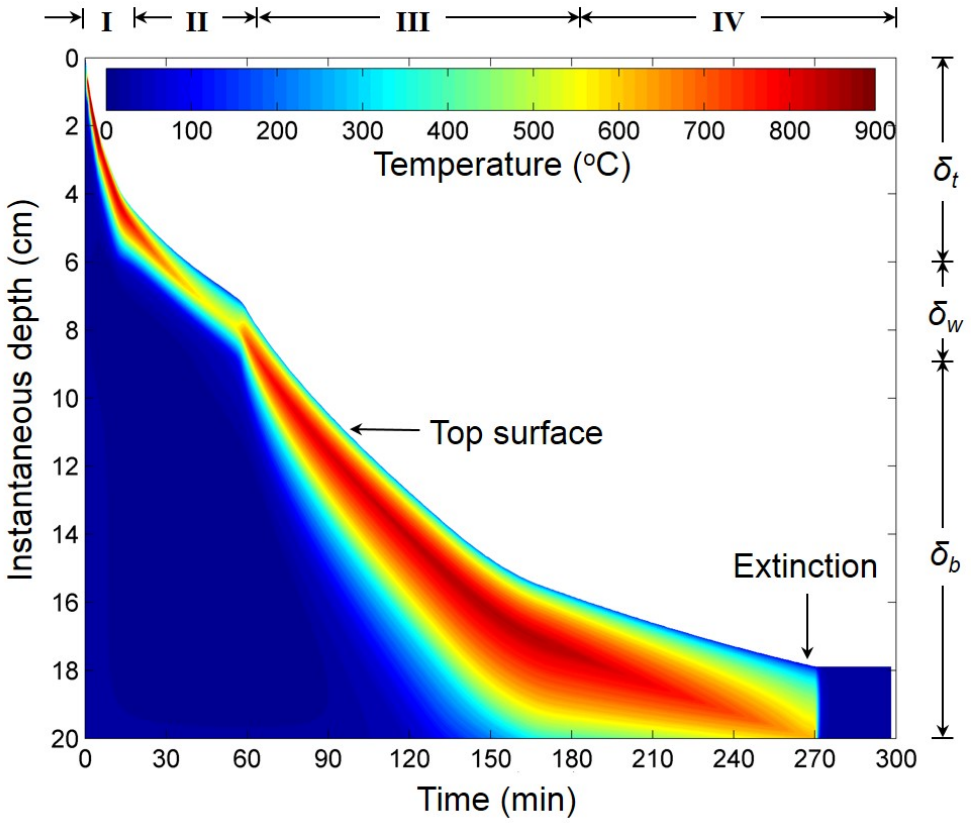

Figure 3.4: Predicted 2D contour of temperature varying with depth and time for the base case: δ_t = 6 cm (MC_t = 10%), δ_w = 3 cm (MC_w = 180%), δ_b = 11 cm (MC_b = 10%).

expected, leaving more residence time for the exothermic char oxidation to drive the smouldering front downward to the bottom layer. Once the bottom dry layer is ignited (Stage III), the spread rate increases rapidly and char starts to accumulate again. All peat are decomposed within 170 min, also denoted by the depth of burn in Fig. 3.3b. Afterward, the oxidation of char dominates (Stage IV).

The overall temperature evolution with both the depth and time is plotted by a 2D contour in Fig. 3.4 where the regression of the top surface can be visualized as well. After ignition, the peak temperature is found to always locate below the top surface, and to decrease appreciably in the wet layer. It also qualitatively shows the evolution of reaction zones. For example, the thickness of the high-temperature and exothermic oxidation zone increases in dry layers (Stage I & III), while decreasing in the wet layer (Stage II) as well as near the fuel depletion (Stage IV). The thickness of the lower-temperature drying zone follows a similar trend. Additionally, at about 130 min the smouldering front reaches ("sees") the bottom, and the bottom boundary starts to affect fire propagation until extinction.

More details of the predicted temperature (a), reaction (b), and species profiles (c-f) at several typical moments are summarized in Fig. 3.5. During ignition ($t \leq 5$

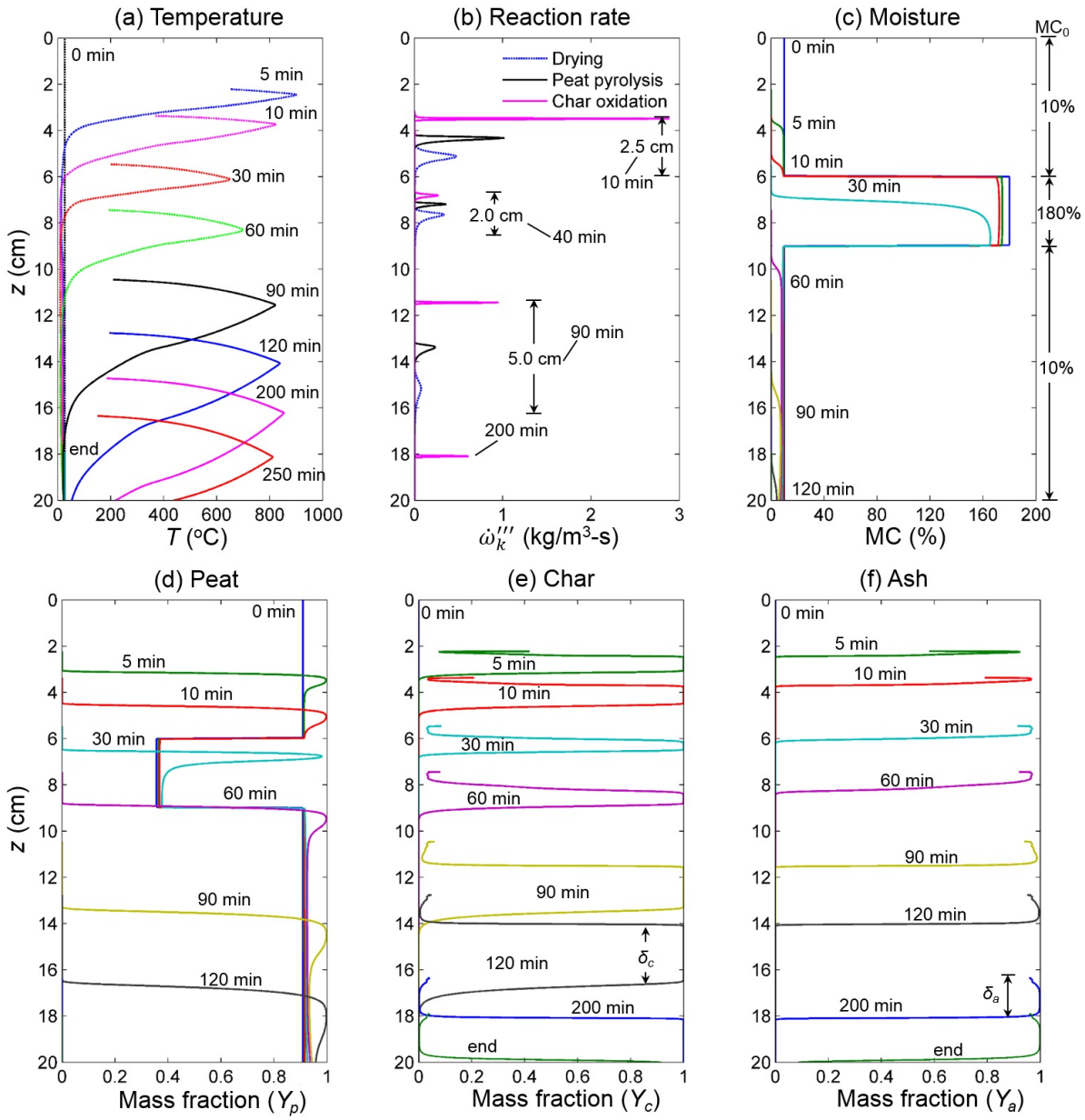

Figure 3.5: Predicted profiles of (a) temperature, T; (b) reaction rate, $\dot{\omega}_k$, (c) moisture content, MC $= Y_w/(1-Y_w)$, and species mass fraction, Y_i (d) peat; (e) char, and (f) ash for the base case: $\delta_t = 6$ cm (MC$_t$ = 10%), $\delta_w = 3$ cm (MC$_w$ = 180%), $\delta_b = 11$ cm (MC$_b$ = 10%).

min), under the strong external heat flux the temperature profile is high. Meanwhile, all reaction rates are also high because of the temperature-dependent Arrhenius expression in Eq. (5.8). After ignition, the peak temperature declines to about 550 °C at the wet layer during Stage II. The thickness of smouldering front is around 2.5 cm. Afterward, the peak temperature increases to about 800 °C during the decomposition of bottom dry layer (Stage III) and the later char oxidation (Stage IV), and eventually decreases near the end due to heat loss and the lack of fuel. At the same time, the thickness of

smouldering front first increases to 5 cm (Stage III) due to the increase of char layer (from 1 cm to 3 cm in seen Fig. 3.5e), and then decreases into a thin single-reaction zone. The thickness of ash layer (Fig. 3.5f) continues to increase up to $\delta_{a,max} \approx 2$ cm until the end of combustion. After extinction, the residue is a mixture of ash and a small portion of the unburnt char, as discovered in fields after smouldering wildfires [20, 32].

3.4 Discussions on critical moisture and depth of burn

3.4.1 Critical MC of extinction (MC^*_{ex}) and ignition (MC^*_{ig})

There are two controlling mechanisms in smouldering combustion: the oxygen supply and the heat loss [2]. Thus, extinction occurs not only due to the fuel burnout, but also if (1) the heat loss exceeds the heat generation (quenching), (2) the oxygen supply becomes insufficient (smothering), or (3) the combination of them. As MC increases, it requires a larger heat to dry the fuel downstream, thus slowing down the spread and char yield (see Fig. 3.3). As char gets depleted, the temperature profile declines to about 460°C, and then extinction occurs, defining a critical moisture content of extinction (MC^*_{ex}). However, the value of MC^*_{ex} cannot be a constant, but strongly depends on both upstream and downstream conditions. Figure 3.6 predicts how MC^*_w varying with the thickness of a top dry layer (δ_t, $MC_t = 10\%$) and the wet layer (δ_w): above the critical line, extinction

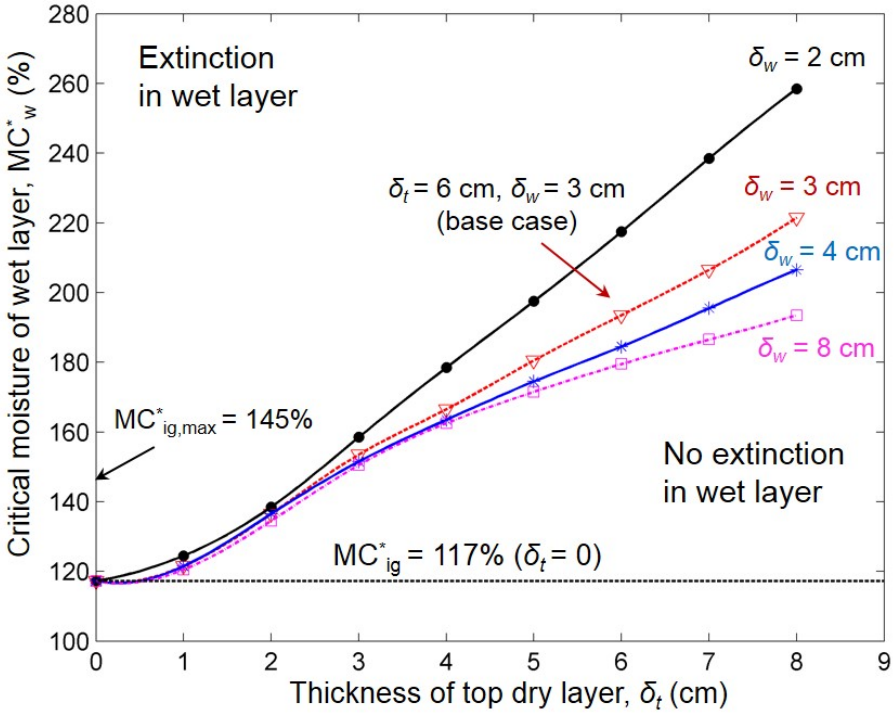

Figure 3.6: Predicted critical moisture content (MC^*_w) in the wet layer varies with thicknesses of the top dry layer (δ_t, $MC_t = 10\%$) and the wet layer (δ_m), where the peat bulk density is $\rho_p = 40$ kg/m^3.

occurs in the wet layer; below it, no extinction occurs before burnout.

If a drier top layer is ignited on the surface, part of its combustion heat will be transferred downward to dry and ignite the wet layer. As discussed above, a thicker top layer yields more char and facilitates a complete combustion of middle layer under a higher moisture. Figure 3.6 reveals smouldering fire is able to spread at an extremely wet layer above MC = 250% as the thickness of top layer δ_t increases. On the other hand, the heat sink effect of the wet layer increases with its thickness δ_w, thus reducing the value of MC^*_{ex}. For example, with $\delta_t = 8$ cm, the MC^*_{ex} decreases slightly from 256% to 195%, as δ_w increases 4 times from 2 to 8 cm. Also, note that as the thickness of dry layer further increases ($\geq$ 8 cm), the effect on wet peat layer does not increase linearly, but weaker than linearly, as seen for $\delta_w = 8$ cm.

If there is no top layer ($\delta_t = 0$), the problem becomes an ignition problem. Frandsen [14, 15] conducted a series of ignition experiments on multiple small peat samples of 4-5 cm thick. Those ignition experiments have been successfully predicted in Chapter 2. Under the current ignition protocol and peat properties, MC^*_{ig} is found to be 117%, much lower than the predicted MC^*_{ex}, plotted as the reference line in Fig. 3.6. This prediction is able to explain the experiment on the upper organic layer in [18] where $\mathrm{MC}^*_{ig} = 65\%$ is found to be much lower than $\mathrm{MC}^*_{ex} = 150\%$. Note that the MC^*_{ex} increases only mildly at $\delta_t < 1$ cm, implying the influence of the current ignition protocol (30 kW/m^2 for 5 min) is limited within the top 1 cm.

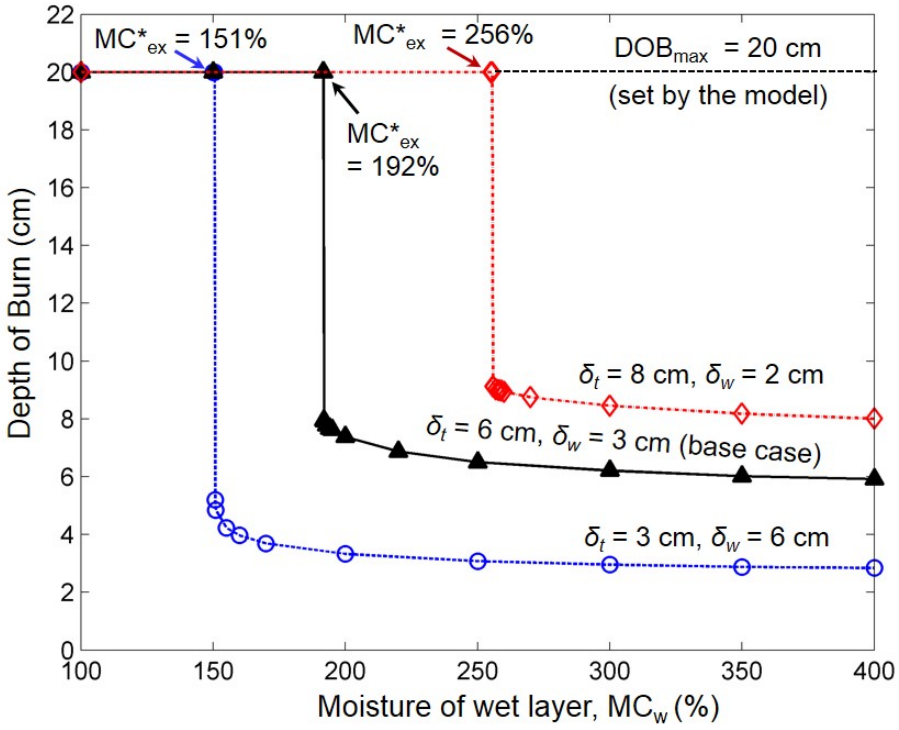

Figure 3.7: Predicted depth of burn varies with the moisture content of wet layer (MC_w), where the top layer is dry ($\mathrm{MC}_t = 10\%$) and the peat bulk density is $\rho_p = 40$ kg/m^3.

3.4.2 Depth of burn

After extinction, the final depth of burn can be obtained. Figure 3.7 plots the depth of burn for several typical cases. Clearly, MC^*_{ex} defines a jump point for the depth of burn: below it all peat column (20 cm) is burnout, while above it only 1-2 cm of the wet layer is consumed by the near extinct smouldering front upstream. Moreover, as the moist layer gets extremely wet (MC_w >300%), not even all the top dry layer can be consumed because the large conductivity in the wet layer creates a strong cooling boundary condition to quench the fire early. For example, in the base case at MC_w = 400%, DOB = 5.9 cm which is slightly less than the height of top layer (δ_t = 6 cm).

3.4.3 Sensitivity to moisture in the top layer (MC_t)

The moisture content of the top layer (MC_t) controls the possibility of ignition, and determines the upstream condition for the wet layer, thus affecting the critical moisture in the wet layer (MC^*_w). Figure 3.8 plots the predicted MC^*_w against MC_t for several typical cases. The value of MC^*_w slowly decreases with MC_t until near the critical value of ignition (MC^*_{ig}). Afterward, it quickly drops and converges to MC^*_{ig} = 117%. In addition, as the thickness of wet layer (δ_w) increases, the curve slope becomes flat, that is, MC^*_w starts to becomes less sensitive to the top moisture condition. For example, in the base case (δ_t = 6 cm, δ_w = 3 cm), when MC_t increases from 10% to 100%, MC^*_w only decreases from 192% to 173%.

Figure 3.8b shows the corresponding depth of burn in the base case, where several different zones (A-D) can be seen. If the top layer is very wet, Zone (A): MC_t >MC^*_{ig}, no ignition occurs. If the moisture of the whole soil bed is less than the ignition limit, Zone

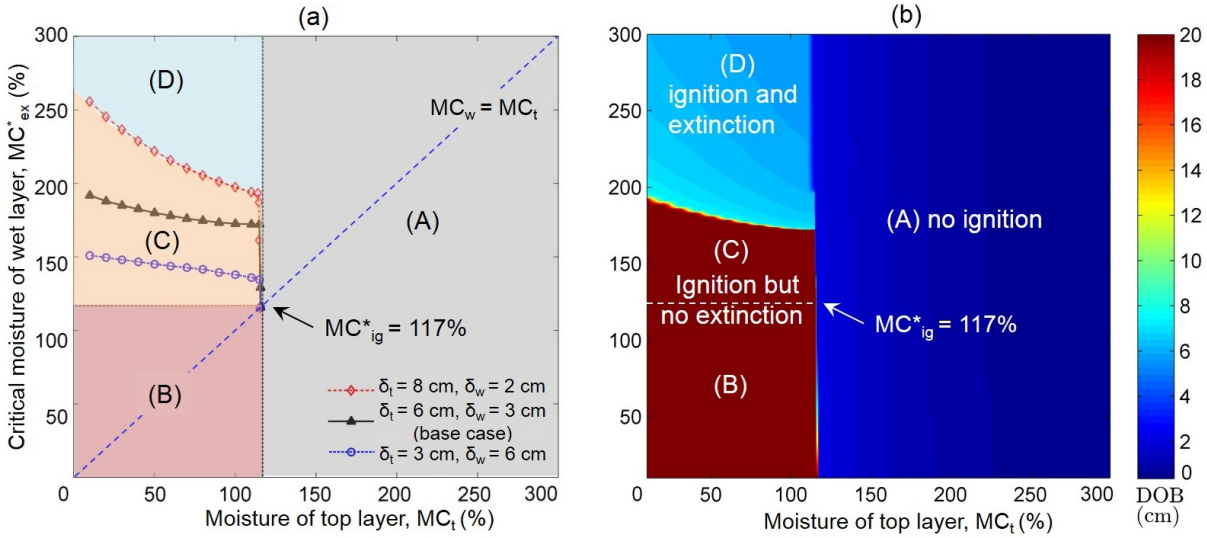

Figure 3.8: Predicted (a) critical moisture content of wet layer (MC^*_w), and (b) depth of burn (DOB) in the base case (δ_t = 6 cm, δ_w = 3 cm), varies with the moisture of top layer (MC_t), where the peat bulk density is ρ_p = 40 kg/m^3.

(B): $MC_i < MC^*_{ig}$, no extinction occurs before fuel burnout. These two zones were well understood in previous ignition experiments [14, 15] and simulations (Chapter 2). However, once ignited ($MC_t < MC^*_{ig}$), there is an additional wet Zone (C), $MC^*_{ig} < MC_w < MC^*_{ex}$, where all peat is also burnt out, and it has not been identified before. For Zone (D): $MC^*_{ex} < MC_w$, only the top layer and less than 1 cm of wet layer can be burnt.

3.4.4 Sensitivity to density

The bulk density of peat (ρ_p) can affect the ignition and extinction behaviors of smouldering meanwhile changing the MC*. Figure 3.9a plots the predicted MC^*_{ex} varying with the peat bulk density for two cases: $\delta_t = 2\delta_w = 6$ cm (base case), and $\delta_t = \delta_w = 3$ cm. These curves of MC^*_{ex} are found not to change with the external heat flux at $\dot{q}''_e < 40$ kW/m^2 as long as the top dry layer can be ignited. As implied from Fig. 3.6, the influence of the ignition source is limited in the top layer of a finite thickness ($\delta^*_{ig} < 1$ cm), below which the fire spread becomes independent of the ignition protocol.

Figure 3.9 shows MC^*_{ex} first increases rapidly with the peat bulk density until a turning point of $\rho_p \approx 100$ kg/m^3 and then slowly decreases. This result agrees with the fire-spread experiment on pine duff in [12] where the found MC^*_{ex} and depth of burn for low density upper-layer samples ($\overline{\rho_p} = 80$ kg/m^3) were in general smaller than high-density lower-layer samples ($\overline{\rho_p} = 150$ kg/m^3). The turning point implies that the peat bulk density has two competing mechanisms, one strong and one weak, controlling the

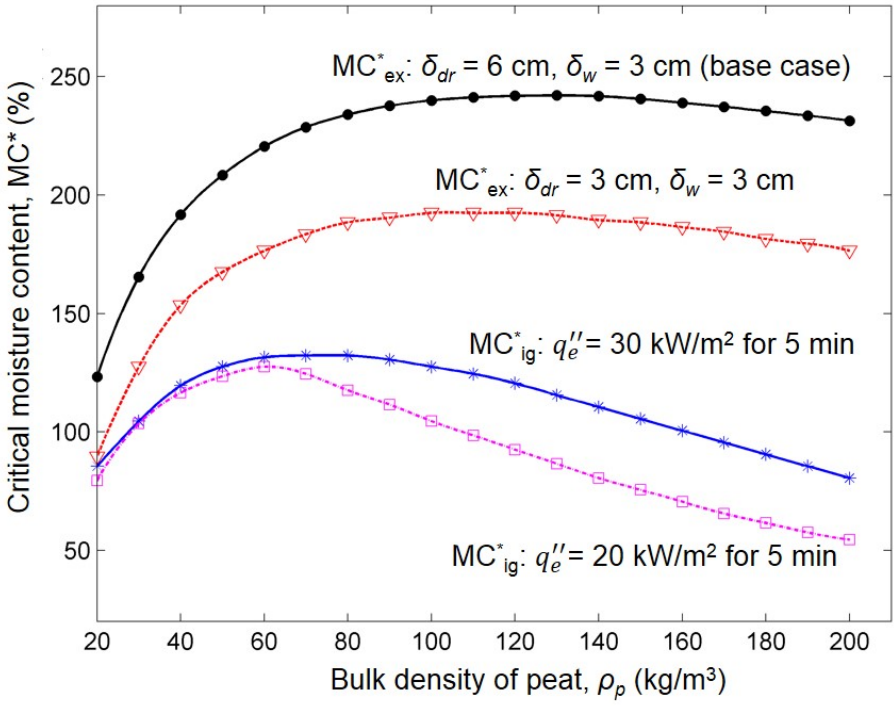

Figure 3.9: Predicted critical moisture content (MC*) varies with the peat bulk density, ρ_p, where the top layer is dry ($MC_t = 10\%$).

Table 3.3: Thermo-physical properties varies with the peat bulk density.

ρ_p	40	80	120	160	kg/m^3
$E_s = \rho_p \Delta H_{sm}$	468	936	1404	1872	MJ/m^3
d_p	0.50	0.25	0.17	0.13	mm
ψ_p	0.973	0.947	0.920	0.893	m^3/m^3
$k_{s,p}(1-\psi_p)$	0.027	0.053	0.080	0.107	W/m-K
$\gamma_p \sigma T^3$ [a]	0.067	0.033	0.022	0.017	W/m-K
k_p	0.094	0.086	0.102	0.124	W/m-K
K_a	5.09	1.27	0.57	0.31	m$^2 \times 10^{10}$

a. Assuming a typical smouldering temperature of 650°C.

extinction of smouldering.

Table 3.3 lists some physical properties under different bulk densities of peat. For a low-density peat (e.g. $\rho_p = 40$ kg/m^3), the energy density ($E_s \sim \rho_p$) as well as the heat release rate is low. Because of the large porosity (ψ_p) and pore size (d_p), the thermal conduction, $k_{s,p}(1-\psi_p)$ is small. On the contrary, the radiation heat transfer across pores, $\gamma_p \sigma T^3$, is dominant over conduction in Eq. (4.31) to control extinction. As the bulk density increases, the porosity and pore size decrease. Accordingly, the radiation heat loss as well as the effective heat transfer (k_p) decreases, thus increasing MC*.

Further increasing the density ($\rho_p > 100$ kg/m^3), radiation heat transfer becomes negligible, meanwhile, the linearly increased conduction becomes dominant (see Table 3.3). However, the conductive cooling effect is compensated by the same linearly increased energy density, resulting a very weak dependence on the bulk density. On the other hand, the permeability (K) decreases with the bulk density, reducing the oxygen supply through the ash layer to the reaction zone. However, this effect is expected to be weak because of a low-mineral peat and a thin ash layer.

The ignition probability and critical moisture of ignition (MC$^*_{ig}$) were also found to be affected by the peat bulk density and the ignition source, plotted in Fig. 3.9 for comparison. The MC$^*_{ig}$ is very different from MC$^*_{ex}$: having a much lower value, and increasing with the external heat flux. For the whole density range, the maximum MC for ignition varies from 50% to 125%, agreeing with the experimental range in [6, 12, 14, 15]. With increasing peat bulk density, the ignition curve follows a similar trend as the spread curve. However, the turning point takes place in a lower bulk density ($\rho_p \approx 60$ kg/m^3), and the following decline is faster.

For the forced ignition, the moist peat needs to be dried and reach a critical ignition temperature by the ignition source. Similar to extinction, the radiative cooling effect is dominant for the low-density peat ($\rho_p < 60$ kg/m^3), and is independent of the ignition source, as proved by the overlapping ascending curves for 20 and 30 kW/m^2. However,

further increasing the density, the radiative effect quickly fades away, meanwhile, both the thermal inertial and the overall heat transfer increase, weakening the heating effect from the ignition source. Thus, MC^*_{ig} quickly declines with increasing density and decreasing ignition source. These predictions agree with the experiment in [16] and the previous simulation ($\rho_p = 90 \sim 130$ kg/m^3) in Chapter 2. In short, the critical moisture of extinction can be much larger than the critical moisture of ignition ($MC^*_{ex} > MC^*_{ig}$), and they have different dependencies on peat properties.

3.5 Modelling of natural peat samples

The peat samples in the experiment of Benscoter et al. [1] were collected from Athabasca Bog, Alberta, Canada where the ground layer is dominated by Sphagnum fuscum and Pleurozium schreberi. Six different surface peat ranging from 20 to 30 cm in depth were extracted from the bog, and divided into several columns. Three moisture profiles for each peat were produced under two drying treatments: (1) field moisture (no drying); (2) 2-week air drying; and (3) 2-week air drying plus 48-h oven drying at 40 °C, i.e. 18 sample in total. The central portion of original column were extracted and placed into a burn box (top open) made by 1.3-cm ceramic fibreboard.

In order to measure the profiles of density, moisture and inorganic contents, the peat column were manually differentiated into several 3-cm layers, and then their average values of each layer were measured (see Fig. 3.1a). Note that the bulk density of peat samples ranges from 2 to 90 kg/m^3 with an average value of about 40 kg/m^3, much lower than the samples in [6, 14, 15]. The ignition source was a modified propane-fired radiator, placed above the top surface of column for 5 min. During ignition, a flaming fire may occur in some samples with a low surface density. Because the sample height is larger than the horizontal dimension and the ignition heat flux is almost uniform on the whole

Table 3.4: Measured property profiles of the *Oven Hol 2* sample [1].

z (cm)	ρ_p (kg/m^3)	MC (%)	IC (%)
0-3	18	52	6
3-6	36	32	8
6-9	36	80	6
9-12	43	229	10
12-15	52	373	10
15-18	48	579	10
18-21	41	915	4
Average	38.3	226	7.7

top surface, these experiments can be viewed as 1-D in depth, and described by the model in Section 3.2. The measured density and moisture profiles in [1] are input to the model. Other physical parameters choose the same in Tables 3.1, and assumed not to change with the depth and temperature. The ignition heat flux is chosen to be 30 kW/m^2 for 5 min, high enough to accommodate the impact of possible flaming fire.

3.5.1 Case study

One representative case, the oven-dried mixed-species hollow sample 2 (*Oven Hol 2*), is chosen to study the in-depth smouldering process. This sample is 21 cm thick, and Table 3.4 lists the measured profiles of bulk density, moisture, and inorganic content for seven 3-cm layers. The corresponding measurements of all 18 samples are available in the Accessory of [1]. In general, the bulk density of peat increases with the depth due to the higher pressure and the longer decomposition period. The MC also increases with the depth, and this trend becomes more obvious after drying. The average inorganic content of the column is relatively high ($\overline{\text{IC}} = 7.7\%$), thus, in the simulations decomposition chemistry of a Siberia scheuchzeria and sphagnum transition peat ($\text{IC}_{SI-B} \approx 8.8\%$ [33]), is used and its kinetic parameters have been found in Chapter 1.

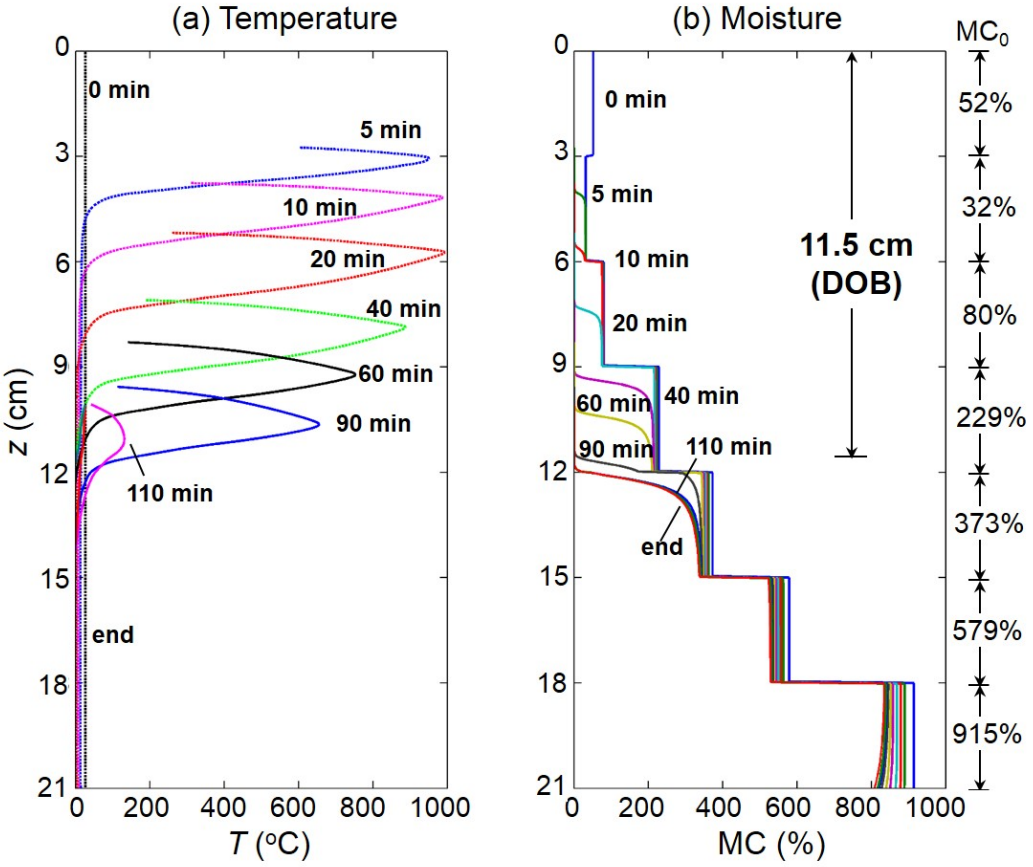

Figure 3.10: Predicted evolutions of (a) the temperature profile, T and (b) the profile of moisture, for the *Oven Hol 2* sample.

Figure 3.10 shows the predicted evolutions of the temperature and moisture profiles of the *Oven Hol 2* sample. The smouldering combustion lasts for about 2 h. Due to the extremely high moisture at $z > 9$ cm, the peat column cannot burn completely, as observed in the experiment. The predicted depth of burn is 11.5 cm, agreeing with the experimental measurement, 9 ± 3 cm. It can be seen that the temperature profile trends to decline with the depth as the moisture increases, and it starts to drop rapidly at about 90 min when the drying front hits the wet layer of MC = 373% at $z = 12$ cm where extinction occurs. Afterward, the high-temperature smouldering front continues to dry the peat below for another 40 min, and the MC of unburnt peat decreases about 50% until the reaction zone cools down completely.

3.5.2 Comparison of depth of burn

All 18 samples in [1] are modelled in the same manner. For the low-mineral peat ($\overline{\text{IC}} \leq 4\%$), the decomposition chemistry of a Scotland subshrub and sphagnum high-moor peat ($\text{IC}_{SC} \approx 1\%$ [33] and Chapter 1) is used (see Table 3.2). For the high-mineral peat ($\overline{\text{IC}} > 4\%$), the same Siberia (SI-B) peat as the *Oven Hol 2* sample is used. The obtained depth of burn are compared with the experimental measurements, illustrated

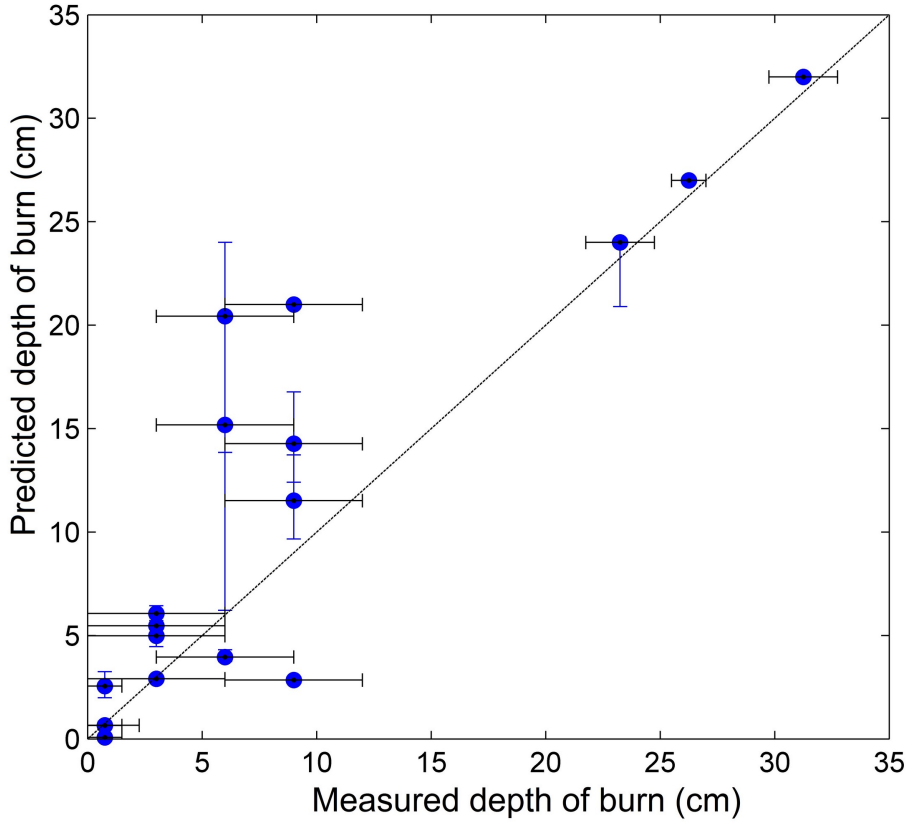

Figure 3.11: Comparison of depth of burn between simulations and experiments in [1]. The horizontal error bars come from experimental measurements in [1], and the vertical error bars come from the sensitivity analysis for modelling.

in Fig. 3.11.

The physical and chemical properties, e.g. the heat capacity, conductivity, and the heat of smouldering, may vary with the depth and from site to site. Modelling shows that both MC* and DOB increase with the heat of combustion, while decrease with the heat capacity and conductivity. In order to estimate the sensitivity of modelling results to these factors, the parameter range of $c_p = 1500 \sim 2000$ J/kg-K , $k_{s,p} = 0.8 \sim 1.2$ W/m-K [23], and $\Delta H_{sm} = 9.5 \sim 15$ MJ/kg [28, 34], are tested and plotted as the uncertainty of prediction for further comparison in Fig. 3.11. The degree of agreement between simulation and experiments is measured by the R^2 coefficient, the value of which is found to be 0.87. For a few samples with wet layers between 5 and 10 cm near the critical MC, the prediction becomes more sensitive to the selection of parameters (see large error bars in Fig. 3.11). Considering the complexity of the system, this model is able to give a good prediction to the depth of burn in the experiment on natural organic soil samples.

3.6 Conclusions

In this chapter, a comprehensive 1-D model of a reactive porous media is established in the open-source code Gpyro to investigate to the in-depth spread of smouldering fires into peat samples with varying profiles of density, moisture and inert contents. The critical moisture content and depth of burn are predicted. It is found that the smouldering peat fire can spread over an extremely high moisture (MC $> 250\%$) if the top burnt layer is thick and the wet layer below is thin. The critical MC of extinction is found to be very different from that of ignition: much higher value, insensitive to ignition protocol, and no tendency to decrease in high density. The model simulates the experiments of all 18 natural peat samples in Benscoter et al. [1], and the predicted depth of burn agrees well with experimental measurement. The sensitivity of predicted depth of burn to thermo-physical properties is also quantified. This is the first time to use a comprehensive physics-based model to simulate smoldering fires of natural fuel with heterogeneous moisture and property profiles, predict the depth of burn, and distinguish different critical moisture values between extinction and ignition, thus helping to understand this important natural and widespread phenomenon.

Acknowledgements

I would like to thank Prof. B. W. Benscoter (Florida Atlantic University), Prof. M. G. Davies (Ohio State University) and N. Prat (University College Dublin) for providing data and valuable discussions.

References

[1] B. W. Benscoter, D. K. Thompson, J. M. Waddington, M. D. Flannigan, B. M. Wotton, W. J. de Groot, and M. R. Turetsky, "Interactive effects of vegetation, soil moisture and bulk density on depth of burning of thick organic soils," *International Journal of Wildland Fire*, vol. 20, pp. 418–429, 2011.

[2] T. Ohlemiller, "Modeling of smoldering combustion propagation," *Progress in Energy and Combustion Science*, vol. 11, no. 4, pp. 277 – 310, 1985.

[3] M. R. Turetsky, B. Benscoter, S. Page, G. Rein, G. R. van der Werf, and A. Watts, "Global vulnerability of peatlands to fire and carbon loss," *Nature Geoscience*, vol. 8, pp. 11–14, 2015.

[4] K. C. Ryan and W. H. Frandsen, "Basal Injury From Smoldering Fires in Mature Pinus ponderosa Laws," *International Journal of Wildland Fire*, vol. 1, pp. 107–118, 1991.

[5] S. L. Stephens and M. A. Finney, "Prescribed fire mortality of Sierra Nevada mixed conifer tree species: effects of crown damage and forest floor combustion," *Forest Ecology and Management*, vol. 162, no. 2-3, pp. 261 – 271, 2002.

[6] G. Rein, N. Cleaver, C. Ashton, P. Pironi, and J. L. Torero, "The severity of smouldering peat fires and damage to the forest soil," *Catena*, vol. 74, no. 3, pp. 304 – 309, 2008.

[7] E. Gorham, "The future of research in canadian peatlands: A brief survey with particular reference to global change," *Wetlands*, vol. 14, no. 3, pp. 206–215, 1994.

[8] S. E. Page, J. O. Rieley, and C. J. Bands, "Global and regional importance of the tropical peatland carbon pool," *Global Change Biology*, vol. 17, no. 2, pp. 798–818, 2011.

[9] G. Rein, "Smouldering Fires and Natural Fuels," in *Fire Phenomena and the Earth System* (C. Belcher, ed.), ch. 2, pp. 15–33, Wiley and Sons, 2013.

[10] S. E. Page, F. Siegert, J. O. Rieley, H.-D. V. Boehm, A. Jaya, and S. Limin, "The amount of carbon released from peat and forest fires in Indonesia during 1997," *Nature*, vol. 420, pp. 61–65, 2002.

[11] B. Poulter, N. L. Christensen, and P. N. Halpin, "Carbon emissions from a temperate peat fire and its relevance to interannual variability of trace atmospheric greenhouse gases," *Journal of Geophysical Research*, vol. 111, 2006.

[12] E. C. Garlough and C. R. Keyes, "Influences of moisture content, mineral content and bulk density on smouldering combustion of ponderosa pine duff mounds," *International Journal of Wildland Fire*, vol. 20, pp. 589 – 596, 2011.

[13] A. C. Watts, "Organic soil combustion in cypress swamps: Moisture effects and landscape implications for carbon release," *Forest Ecology and Management*, vol. 294, pp. 178 – 187, 2013. The Mega-fire reality.

[14] W. H. Frandsen, "The influence of moisture and mineral soil on the combustion limits of smoldering forest duff," *Canadian Journal of Forest Research*, vol. 17, no. 12, pp. 1540–1544, 1987.

[15] W. H. Frandsen, "Ignition probability of organic soils," *Canadian Journal of Forest Research*, vol. 27, no. 9, pp. 1471–1477, 1997.

[16] R. Hartford, "Smoldering combustion limits in peat as influenced by moisture, mineral content, and organic bulk density," *Proceedings of the 10th Conference on Fire and Forest Meteorology*, pp. 282–286, 1989.

[17] G. M. Davies, A. Gray, G. Rein, and C. J. Legg, "Peat consumption and carbon loss due to smouldering wildfire in a temperate peatland," *Forest Ecology and Management*, vol. 308, no. 0, pp. 169 – 177, 2013.

[18] D. Wade, J. Ewel, and R. Hofstetter, "Fire in south Florida ecosystems," tech. rep., USDA Forest Service, Southeastern Forest Experiment Station General Technical Report SE-17.

[19] J. Reardon, R. Hungerford, and K. Ryan, "Factors affecting sustained smouldering in organic soils from pocosin and pond pine woodland wetlands," *International Journal of Wildland Fire*, vol. 16, pp. 107 – 118, 2007.

[20] C. Zaccone, G. Rein, V. DOrazio, R. M. Hadden, C. M. Belcher, and T. M. Miano, "Smouldering fire signatures in peat and their implications for palaeoenvironmental reconstructions," *Geochimica et Cosmochimica Acta*, vol. 137, no. 0, pp. 134 – 146, 2014.

[21] C. E. V. Wagner, "Duff Consumption by Fire in Eastern Pine Stands," *Canadian Journal of Forest Research*, vol. 2, no. 1, pp. 34–39, 1972.

[22] C. Lautenberger and C. Fernandez-Pello, "Generalized pyrolysis model for combustible solids," *Fire Safety Journal*, vol. 44, no. 6, pp. 819 – 839, 2009.

[23] R. Jacobsen, E. Lemmon, S. Penoncello, Z. Shan, and N. Wright, "Thermophysical Properties of Fluids and Materials," in *Heat Transfer Handbook* (A. Bejan and A. Kraus, eds.), ch. 2, pp. 43–159, John Wiley & Sons, 2003.

[24] R. M. Hadden, G. Rein, and C. M. Belcher, "Study of the competing chemical reactions in the initiation and spread of smouldering combustion in peat," *Proceedings of the Combustion Institute*, vol. 34, no. 2, pp. 2547 – 2553, 2013.

[25] F. Yu, G. Wei, X. Zhang, and K. Chen, "Two Effective Thermal Conductivity Models for Porous Media with Hollow Spherical Agglomerates," *International Journal of Thermophysics*, vol. 27, no. 1, pp. 293–303, 2006.

[26] H. de Jonge and M. C. Mittelmeijer-Hazeleger, "Adsorption of CO_2 and N_2 on Soil Organic Matter: Nature of Porosity, Surface Area, and Diffusion Mechanisms," *Environmental Science & Technology*, vol. 30, no. 2, pp. 408–413, 1996.

[27] B. Punmia and A. Jain, *Soil Mechanics and Foundations*. Laxmi Publications Pvt Limited, 2005.

[28] K. Bergner and C. Albano, "Thermal analysis of peat," *Analytical Chemistry*, vol. 65, no. 3, pp. 204–208, 1993.

[29] H. Chen, W. Zhao, and N. Liu, "Thermal Analysis and Decomposition Kinetics of Chinese Forest Peat under Nitrogen and Air Atmospheres," *Energy & Fuels*, vol. 25, no. 2, pp. 797–803, 2011.

[30] C. Huggett, "Estimation of rate of heat release by means of oxygen consumption measurements," *Fire and Materials*, vol. 4, no. 2, pp. 61–65, 1980.

[31] D. Drysdale, *An Introduction to Fire Dynamics*. Wiley, 2011.

[32] L. Moreno, M.-E. Jimenez, H. Aguilera, P. Jimenez, and A. Losa, "The 2009 Smouldering Peat Fire in Las Tablas de Daimiel National Park (Spain)," *Fire Technology*, vol. 47, no. 2, pp. 519–538, 2011.

[33] D. Cancellieri, V. Leroy-Cancellieri, E. Leoni, A. Simeoni, A. Y. Kuzin, A. I. Filkov, and G. Rein, "Kinetic investigation on the smouldering combustion of boreal peat," *Fuel*, vol. 93, no. 0, pp. 479 – 485, 2012.

[34] V. Leroy-Cancellieri, D. Cancellieri, E. Leoni, A. Simeoni, and A. I. Filkov, "Energetic potential and kinetic behavior of peats," *Journal of Thermal Analysis and Calorimetry*, vol. 117, no. 3, pp. 1497–1508, 2014.

Chapter 4

Smouldering Combustion across Scales: the Roles of Heterogeneous Kinetics, Oxygen and Transport Phenomena

Summary [1]

In this Chapter, the thermochemical conversion of biomass in smouldering combustion is investigated by combining experiments and modelling at two scales: matter (1 mg) and laboratory (100 g) scales. Emphasis is put on the effect of oxygen (0 to 33 vol.%) and oxidation reactions because these are poorly studied in the literature in comparison to pyrolysis. The results are obtained for peat as representative biomass supported by high-quality experimental data. Three kinetic schemes are explored, including various steps of drying, pyrolysis and oxidation. The kinetic parameters are found using the Kissinger-Genetic Algorithm method, and then implemented in a 1D model of heat and mass transfer. The predictions are validated in thermogravimetric and bench-scale experiments to unravel the role of heterogeneous reaction. This is the first time that the influence of oxygen on biomass smouldering is explained in terms of both chemistry and transport phenomena across scales.

1. This chapter is based on "X. Huang, G. Rein (2015) *Thermochemical Conversion of Biomass in Smouldering Combustion across Scales: the Roles of Heterogeneous Kinetics, Oxygen and Transport Phenomena*, **Bioresource Technology** (Accepted)."

4.1 Introduction

Biomass is a solid fuel of natural origin and can include high moisture and mineral contents [1]. Once heated, biomass dries and pyrolyzes [2], and if oxygen is present, it can ignite and support gas-phase homogenous combustion (flaming) or heterogeneous combustion (smouldering) [3, 4]. While most studies of biomass combustion have focused on flaming, this paper focuses on smouldering.

Smouldering combustion is the slow, low-temperature, flameless burning of porous fuels and the most persistent type of combustion [5]. The thermochemical process in smouldering includes drying, pyrolysis and oxidation steps [3] (also see Chapter 1). Therefore, compared to biomass pyrolysis [2, 6], smouldering is more complex and poorly studied. Particularly, biomass smouldering plays an important role in cooking fuels, biochar production, gasification of fossil fuels, incineration of biowastes, fire hazards and wildfires [7–9].

From a chemical point of view, biomass is a natural composite material, constituted by a mixture of three main components: hemicellulose (H), cellulose (C) and lignin (L) [2, 10, 11]. Neglecting the small amounts of extractives and other species, biomass composition can be approximated as:

$$\text{biomass} \approx Y_h\text{H} + Y_c\ \text{C} + Y_l\ \text{L} \tag{4.1}$$

where Y_i represents the mass fraction of component i. Figure 4.1 compares thermogravimetric (TG) data for a series of biomass types under both the inert and oxidative atmospheres [12–14]. A clear similarity in the decomposition process can be observed for pine needle, pine wood, forest peat and moss peat samples. Such similarity implies that there could be a general kinetic scheme to describe biomass thermochemical conversion in both inert and oxidative atmospheres.

Most studies in the literature investigate biomass kinetics via (∼1 mg) scale thermogravimetric (TG) experiment of dry samples under either inert ambient or air, e.g. Chapter 1 and [11]. Few studies conducted TG experiments under other oxygen concentrations (X_{O_2}, percentage by volume). For example, [14] found that as oxygen concentration decreased to sub-atmospheric level, the mass-loss rate of biomass in TG level decreased. [15] proposed a 6-step kinetics for the oxidative pyrolysis of lignocellulosic biomass. [16] proposed both 3- and 7-step kinetic schemes to explain the TG data of wood under several sub-atmospheric oxygen levels. However, studies at the TG scale alone do not provide in-sight about the changing role of chemistry at larger scales where heat and mass transfer processes are also important.

This paper chooses peat as a representative biomass because the literature offers high-quality experimental data in both TG and bench scales. Peat is an organic soil formed through incomplete humification processes of various plants. It is porous and charring biomass, thus prone to smouldering combustion [4]. Smouldering megafires of peatlands are a very important source of greenhouse gases, and result in the widespread

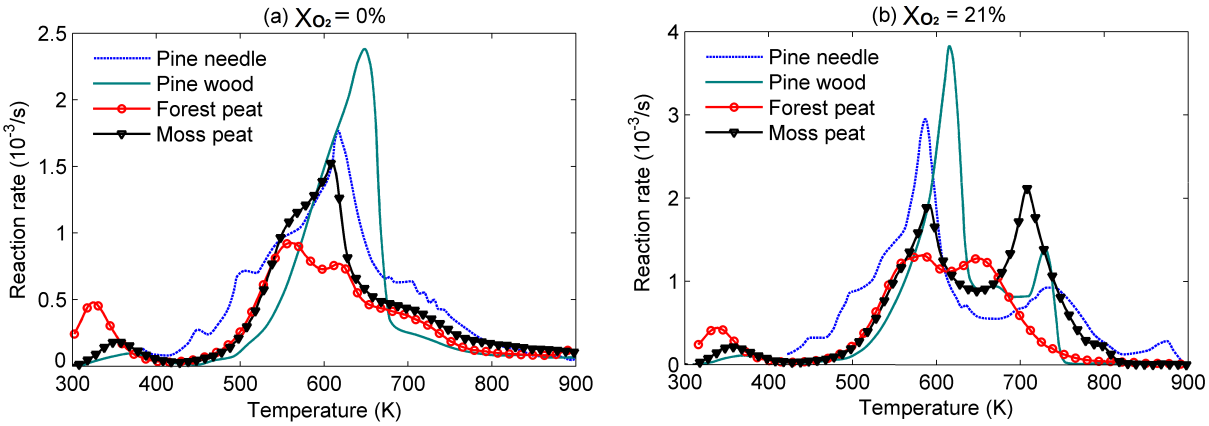

Figure 4.1: Comparison of DTG curves at 20 K/min for pine needle [12], pine wood [13], forest peat soil [14] and moss peat soil in this study under (a) inert ($X_{O_2} = 0\%$), and (b) air ($X_{O_2} = 21\%$) atmospheres.

destruction of valuable ecosystems and large regional haze events [9]. Several bench-scale (∼100 g) experiments studied the influence of oxygen on peat smouldering. [17] found that in laboratory scale experiments, smouldering could not be sustained for peat below a critical X_{O_2} of 16%. [18] found that smouldering of dry moss peat [2] (MC) could be initiated by an irradiation of 20 kW/m^2 within 1 minute under X_{O_2} as low as 11%. In Chapter 1, a 5-step kinetic scheme (including drying) is proposed and successfully explained all TG data of peat under both inert and air atmospheres, but did not address the effect of oxygen concentration at levels different than air. Then in Chapters 2 and 3, with a 1D multi-physical model, this kinetic model successfully predicted bench-scale experiments in air.

In this chapter, three kinetic schemes of different complexities for the thermochemical conversion of biomass in smouldering are studied. TG data of two peat is chosen, and their kinetic parameters are found via Kissinger-Genetic Algorithm (K-GA) method. Afterwards, a 1D model, including kinetics as well as heat and mass transfer, is developed to simulate a bench-scale experiments with dry peat samples under oxygen- or nitrogen-enriched atmospheres. Modelling results are compared with experiments in [19] and [18], and the model sensitivity to physico-chemical properties is investigated. So far, there is no computational study available in the literature investigating biomass smouldering under both sub- and super-atmospheric oxygen levels and in both TG and bench scales [3].

2. Moisture content (MC) is defined in dry basis as the mass of water divided by the mass of a dried soil sample, expressed as %. Inorganic content (IC) is defined in dry basis as the mass of soil inorganic matter (minerals) divided by the mass of a dried soil sample, expressed as %.

3. The interaction between oxygen concentration and moisture content in smouldering wildfires will be further discussed in Chapter 5

4.2 Kinetic model

4.2.1 Moisture content and drying

When the biomass is heated, water vaporizes below 400 K, denoted by the first peak in the curve of first derivative of TG (DTG curve), as seen in Fig. 4.1. If MC is low, there is no free or capillary water, while water molecules are only absorbed into large molecules by hydrogen bond, i.e. the bound water (< 10 vol.%) [20]. The drying of bound water in biomass may be described by a single dissociation step, as done in Chapter 1

$$\text{biomass} \cdot \nu_{w,dr}\text{H}_2\text{O} \rightarrow \text{biomass} + \nu_{w,dr}\text{H}_2\text{O(g)} \quad (dr) \tag{4.2}$$

where $\nu_{i,k}$ is the mass stoichiometric coefficient of species i in reaction k. In Eq. (4.2), $\nu_{w,dr} = \text{MC}_0$ is the initial moisture, and "$\cdot$" means that water is bonded to biomass.

4.2.2 Pyrolysis

Pyrolysis is the thermochemical degradation of a solid without consumption of oxygen, which produces gases (pyrolysate), liquids (tar) and solids (char) [10]. For the pyrolysis of most biomass in an inert atmosphere, there is a clear peak in DTG curves after the drying region ($T > 400$ K), as seen in Fig. 4.1(a). Accordingly, biomass pyrolysis is often represented by a global 1-step reaction [3, 21] as

$$\text{biomass} \rightarrow \nu_{\alpha,bp}\alpha\text{-char} + \nu_{g,bp}\text{gas} \quad (bp) \tag{4.3}$$

which has been widely used for wood, peat and biowaste [1, 6, 10, 22] (also see Chapter 1).

If biomass is viewed as a mixture of hemicellulose, cellulose and lignin as Eq. (4.1), its pyrolysis becomes a group of parallel reactions, each of which is a pyrolysis of one component. This kind of pyrolysis mechanism was proposed by [10] as

$$\begin{cases} \text{H} \rightarrow \nu_{\alpha,hp}\alpha\text{-char} + \nu_{g,hp}\text{gas} & (hp) \\ \text{C} \rightarrow \nu_{\alpha,cp}\alpha\text{-char} + \nu_{g,cp}\text{gas} & (cp) \\ \text{L} \rightarrow \nu_{\alpha,lp}\alpha\text{-char} + \nu_{g,lp}\text{gas} & (lp) \end{cases} \tag{4.4}$$

where the same α-chars is assumed to produced in each pyrolysis reaction.

4.2.3 Oxidation

For the biomass decomposing in oxidative atmosphere like air, there is another clear peak above the pyrolysis region in DTG curves, as shown in Fig. 4.1(b). Therefore, at least one oxidation reaction takes place at high temperature, *i.e.* char oxidation [5] as

$$\alpha\text{-char} + \nu_{O_2,\alpha o}\text{O}_2 \rightarrow \nu_{a,\alpha o}\text{ash} + \nu_{g,\alpha o}\text{gas} \quad (\alpha o) \tag{4.5}$$

[21] proposed using one pyrolysis plus one char oxidation (2-step) to simulate the smouldering process of cellulosic materials. It is so far the simplest scheme to describe the chemical process of smouldering, and has been used for many biomass [3, 10, 16] (also see Chapter 1).

The comparison between Fig. 4.1(a) and (b) shows that for each biomass, the second peak right after the drying region (400 K< T <650 K) is earlier and higher in air than in inert atmospheres. This shows that the presence of oxygen significantly alters the conversion. [3] first proposed a parallel fuel oxidation in smouldering as

$$\text{biomass} + \nu_{O_2,bo}\text{O}_2 \rightarrow \nu_{\beta,bo}\beta\text{-char} + \nu_{g,bo}\text{gas} \quad (bo) \tag{4.6}$$

where a different type of β-char is produced. Compared to α-char from pyrolysis in Eq. (4.3), this β-char is yielded through a different thermochemical process consuming oxygen, so in general they have different structures, compositions, and reactivities. In Chapter 1, it has been found that for peat a single char-oxidation is not sufficient to explain TG data at high temperature (T > 700 K). Therefore, β-char is assumed to go through a parallel oxidation into ash as

$$\beta\text{-char} + \nu_{O_2,\beta o}\text{O}_2 \rightarrow \nu_{a,\beta o}\text{ash} + \nu_{g,\beta o}\text{gas} \quad (\beta o) \tag{4.7}$$

This 5-step scheme (including drying and assuming first order oxidation) successfully explained TG data of four different peat types in Chapter 1.

On the other hand, TG experiments [15, 16] had shown that each component in biomass can go through a parallel oxidization simultaneously, same as the parallel pyrolysis. Thus, the biomass oxidation can be proposed as

$$\begin{cases} \text{H} + \nu_{O_2,ho}\text{O}_2 \rightarrow \nu_{\beta,ho}\beta\text{-char} + \nu_{g,ho}\text{gas} & (ho) \\ \text{C} + \nu_{O_2,co}\text{O}_2 \rightarrow \nu_{\beta,co}\beta\text{-char} + \nu_{g,co}\text{gas} & (co) \\ \text{L} + \nu_{O_2,lo}\text{O}_2 \rightarrow \nu_{\beta,lo}\beta\text{-char} + \nu_{g,lo}\text{gas} & (lo) \end{cases} \tag{4.8}$$

where the same β-char is assumed from all three oxidation reactions.

In summary, three kinetic schemes (including drying) are proposed for biomass smouldering as

(I) 3-step scheme

$$\begin{cases} \text{biomass} \cdot \nu_{w,dr}\text{H}_2\text{O} \rightarrow \text{biomass} + \nu_{w,dr}\text{H}_2\text{O(g)} & (dr) \\ \text{biomass} \rightarrow \nu_{\alpha,pp}\alpha\text{-char} + \nu_{g,pp}\text{gas} & (bp) \\ \alpha\text{-char} + \nu_{O_2,\alpha o}\text{O}_2 \rightarrow \nu_{a,\alpha o}\text{ash} + \nu_{g,\alpha o}\text{gas} & (\alpha o) \end{cases} \tag{4.9}$$

(II) 5-step scheme (same as that in Chapter 1)

$$\begin{cases} \text{biomass} \cdot \nu_{w,dr}\text{H}_2\text{O} \rightarrow \text{biomass} + \nu_{w,dr}\text{H}_2\text{O(g)} & (dr) \\ \text{biomass} \rightarrow \nu_{\alpha,pp}\alpha\text{-char} + \nu_{g,pp}\text{gas} & (bp) \\ \text{biomass} + \nu_{O_2,po}\text{O}_2 \rightarrow \nu_{\beta,po}\beta\text{-char} + \nu_{g,po}\text{gas} & (bo) \\ \beta\text{-char} + \nu_{O_2,\beta o}\text{O}_2 \rightarrow \nu_{a,\beta o}\text{ash} + \nu_{g,\beta o}\text{gas} & (\beta o) \\ \alpha\text{-char} + \nu_{O_2,\alpha o}\text{O}_2 \rightarrow \nu_{a,\alpha o}\text{ash} + \nu_{g,\alpha o}\text{gas} & (\alpha o) \end{cases} \tag{4.10}$$

(III) 9-step scheme

$$\begin{cases} \text{biomass} \cdot \nu_{w,dr}\text{H}_2\text{O} \rightarrow \text{biomass} + \nu_{w,dr}\text{H}_2\text{O(g)} & (dr) \\ \text{H} \rightarrow \nu_{\alpha,hp}\alpha\text{-char} + \nu_{g,hp}\text{gas} & (hp) \\ \text{C} \rightarrow \nu_{\alpha,cp}\alpha\text{-char} + \nu_{g,cp}\text{gas} & (cp) \\ \text{L} \rightarrow \nu_{\alpha,lp}\alpha\text{-char} + \nu_{g,lp}\text{gas} & (lp) \\ \text{H} + \nu_{O_2,ho}\text{O}_2 \rightarrow \nu_{\alpha,hp}\beta\text{-char} + \nu_{g,hp}\text{gas} & (ho) \\ \text{C} + \nu_{O_2,co}\text{O}_2 \rightarrow \nu_{\alpha,cp}\beta\text{-char} + \nu_{g,cp}\text{gas} & (co) \\ \text{L} + \nu_{O_2,lo}\text{O}_2 \rightarrow \nu_{\alpha,lp}\beta\text{-char} + \nu_{g,lp}\text{gas} & (lo) \\ \beta\text{-char} + \nu_{O_2,\beta o}\text{O}_2 \rightarrow \nu_{a,\beta o}\text{ash} + \nu_{g,\beta o}\text{gas} & (\beta o) \\ \alpha\text{-char} + \nu_{O_2,\alpha o}\text{O}_2 \rightarrow \nu_{a,\alpha o}\text{ash} + \nu_{g,\alpha o}\text{gas} & (\alpha o) \end{cases} \tag{4.11}$$

where for parallel reactions, e.g. $A \rightarrow \nu_B B \rightarrow \nu_a$ ash, and $A \rightarrow \nu_C C \rightarrow \nu_a$ash, the mass of ash or inorganic content [2] (IC) is conserved as

$$\nu_B \nu_a = \nu_C \nu_a = \text{IC}_A \tag{4.12}$$

4.2.4 Reaction rate

The general heterogeneous reaction, k, in the mass basis is written [23] as

$$A_k + \sum_{j=1}^{N} \nu'_{j,k}\text{gas } j \rightarrow \nu_{B,k}B_k + \sum_{j=1}^{N} \nu''_{j,k}\text{gas } j \tag{4.13}$$

For a small biomass particle sample of initial mass m_0 and uniform temperature T, the non-dimensional decomposition rate of species A ($\dot{\omega}^*_{dA_k} > 0$) is expressed by the Arrhenius-type reaction as

$$\dot{\omega}^*_{dA_k} = Z_k \exp\left(-\frac{E_k}{RT}\right) f\left(m^*_A\right) g\left(Y_{O_2}\right) \tag{4.14}$$

where Z_k and E_k are the pre-exponential factor and the activation energy, respectively; and $f(m^*_A)$ and $g(Y_{O_2})$ are the mass action functions of reactant A and oxygen, respectively.

Both $\dot{\omega}_k^*$ and $m_{dA_k}^*$ are non-dimensionalized to a characteristic mass of the cell. Here, m_A is non-dimensionalized to the source species for the reactant A as

$$m_A^* = \frac{m_A}{m_{sA0}} \tag{4.15}$$

where the subscript "$sA0$" represents the initial mass of source species for A. For example, the source species for water is water; and the source species for cellulose, char or ash is the original biomass. Non-dimensionalizing to the source species allows avoiding the interference among parallel reactions [4], and is especially suitable to model complex and heterogeneous mixtures like biomass (see conversions to other reaction-rate expressions in Appendix 4.A).

The n^{th}-order mass action function is chosen for reactant A as

$$f\left(m_A^*\right) = \left(m_A^*\right)^{n_k} = \left(\frac{m_A}{m_{sA0}}\right)^{n_k} \tag{4.16}$$

where n_k is called as the order of reaction k. The model for oxygen is chosen as

$$g(Y_{O_2}) = \begin{cases} 1 & \text{(inert atmosphere)} \\ \left(1 + Y_{O_2}\right)^{n_{O_2,k}} - 1 & \text{(oxidative atmosphere)} \end{cases} \tag{4.17}$$

where $n_{O_2,k}$ is the order of oxidation. In inert atmosphere ($Y_{O_2} = 0$), oxidation reaction rates are zero. Therefore, the dimensional expressions for the destruction rate of A, formation rate of B, and heat release rate for reaction k are

$$\dot{\omega}_{dA_k} = \dot{\omega}_{dA_k}^* m_{sA0}, \quad \dot{\omega}_{fB_k} = \dot{\omega}_{dA_k}^* \nu_{B,k} m_{sA0}, \quad \dot{Q}_k = \dot{\omega}_{dA_k} \Delta H_k \tag{4.18}$$

where subscripts "d" and "f" represent the destruction and the formation, respectively, and ΔH_k is the heat of reaction.

4.3 Results of modelling TG experiments

4.3.1 Thermogravimetric experiment

TG experiment is the most widely used technique to study solid-phase kinetics. It provides an environment of controlled atmosphere and heating rate, and small thermal gradient and transport effects during degradation of (∼mg) samples . Here, TG experiments of two peat types are studied. One sample is a commercial Shamrock moss peat (Bord na Móna Horticulture Ltd.) from Ireland. This low-mineral (IC ≈ 2%) moss peat is the same peat used in [17], [19] and [18], and details are presented here. The other peat sample is from the forest of Changpai Mountains in Northeast China. TG data of this

4. For example, if normalizing the species mass to the original mass of biomass ($m_0 = m_{b0} + m_{w0}$) for pyrolysis and oxidation reactions, once the initial moisture content changes, their reaction rates will changes accordingly. However, pyrolysis and oxidation reactions should be independent of the drying process. Note that the expression in Eq. (5.9) is slightly different from Eq. (1.6) in Chapter 1.

high-mineral (IC ≈ 22%) forest peat under 0-21% atmospheric X_{O_2} was reported in [14]. This forest peat is analyzed in the same way as the moss peat, and details are presented in Appendix 4.B.

The moss peat sample was pulverized into powders and dried at 90 °C for 48 h. A Shimadzu DTG-60H TG analyzer was used. The initial mass of peat was about 3.5 mg at three heating rates of 10, 20, and 30 K/min. Three atmospheric X_{O_2} were selected, 0% (helium), 10%, and 21% (air), under the flow rate of 50 mL/min. TG experiments were repeated twice for each case, showing a good repeatability (uncertainty ≈ 2%). Figure 4.2 shows the mass-loss rate (DTG) curves of this low-mineral moss peat soil.

4.3.2 K-GA method

The small sample in TG experiment can be assumed to be a lumped capacitance, and the normalized mass-loss rate can be modelled as

$$\frac{dm}{dT} = \frac{dt}{dT}\sum_{i=1}^{N}\frac{dm_i}{dt} = \frac{1}{\beta}\sum_{i=1}^{N}(\dot{\omega}_{f,i} - \dot{\omega}_{d,i}) \tag{4.19}$$

where $\beta = dT/dt$ is the heating rate.

The recent Kissinger-Genetic Algorithm (K-GA) method [22] is used here to quickly and accurately find good kinetic parameters to match the TG data as an inverse problem [5]. First, Kissinger's method is used with TG data of multiple heating rates to find approximate values of Z_k and E_k for 1-step drying and 1-step pyrolysis. For the 3-step pyrolysis, the local peak for each reaction can also be found from the zero point in the curve of the second derivative of TG (DDTG). Similar approach has been previously used to describe the pyrolysis of medium density fiberboard (MDF) in [22]. These approximate values are used to narrow the search range in Genetic Algorithm (GA). GA is a heuristic search method, imitating the principles of biological adaption based on Darwinian survival-of-the-fittest theory. GA is applied to couple with Eqs. (5.8), (4.18) and (4.19) to search for all kinetic and stoichiometric parameters.

In this chapter, the searched parameters include the initial mass fractions (Y_{i0}) of each species, the kinetic triplets (Z_k, E_k, and n_k), yields ($\nu_{i,k}$), and the order of oxidation ($n_{O_2,k}$). The number of optmized parameters for 3-, 5- and 9-step schemes are 13, 22 and 40, respectively. In order to accelerate the optimization, parameters for drying and pyrolysis are optimized first with only TG data at inert atmosphere. Then, the remaining parameters of oxidation reactions are optimized with TG data at oxidative atmospheres.

The optimization target is to minimize the prediction error with respect to TG data, defined as

$$\Phi = \gamma\frac{\sum|\dot{m}_{pre,i} - \dot{m}_{exp,i}|}{\sum\dot{m}_{exp,i}} + (1-\gamma)\frac{\sum|m_{pre,i} - m_{exp,i}|}{\sum m_{exp,i}} \tag{4.20}$$

where summations means evaluating all TG data points; subscripts "*exp*" and "*pre*" denote the experimental and predicted results; and $\gamma = 0.5$ as used previously in [5] and

Chapter 1. In general, the population size in GA is set around 200, and the convergence ($\Delta\Phi < 0.1\%$) occurred less than 1000 generations. To improve the validity of parameters, a wide range of TG experiments conducted under various heating rates and oxygen concentrations are optimized simultaneously. The GA module in MATLAB is used.

4.3.3 Predicted TG data and kinetic parameters

For the low-mineral moss peat, 9 sets of TG data are available: 3 oxygen concentrations × 3 heating rates. Seven sets are first chosen for optimization. Then, these optimized parameters are used to predict another 2 sets of TG data: $X_{O_2} = 0\%$ at 10 K/min and (2) $X_{O_2} = 21\%$ at 30 K/min (i.e. blind predictions). The best values found for parameters are listed in Tables 4.1 (3- and 5-step) and 4.B1 (9-step in appendix). Table 4.2 summarizes the overall errors in both optimization and blind prediction for each kinetic scheme. All experimental and predicted TG curves as well as the predicted reaction rates at 20 K/min in $X_{O_2} = 0\%$ and 21% are compared in Fig. 4.2.

Figure 4.2 show that all three kinetics schemes are able to produce three major DTG peaks in all heating rates and oxygen concentrations for the moss peat [5]. More importantly, based on this extensive TG data set under various oxygen concentrations, the order of oxidation ($n_{O_2,k}$) is determined here, instead of assuming its value, e.g. assuming first order ($n_{O_2,k} = 1$) in [23], [15] and Chapter 1. Tables 4.1 and 4.B1 show that for both peat samples $n_{O_2,k} < 1$ is found for all oxidation reactions in all three kinetic schemes, similar to found values for wood [16] and coal [24, 25]. This shows that the influence of oxygen in biomass smouldering is weaker than the widely assumed first order.

Comparison between 3-step and 5-step schemes shows that there is a large improvement in both optimized and blind predictions. Specifically, Table 4.2 shows that for both peat samples the minimum error for the optimization (Φ_{opt}) decreases from about 8% to 5.5%, and for the blind prediction (Φ_{pre}) decreases from 17% to 11%. Although the 9-step scheme improves TG prediction in inert atmosphere, there is only 0.5-2% reduction of the error for predicting the oxidative TG data. Table 4.2 shows that the overall difference in predicting TG data between 5-step and 9-step schemes is smaller than the expected uncertainty of TG experiment (2%). Therefore, it becomes questionable whether this 9-step scheme has the appropriate level of complexity in modelling [26].

Figure 4.2(c) also shows three things for 9-step scheme: (1) there is significant overlapping of reaction-rate profiles between 550 and 650 K for six reactions (*hp*, *cp*, *lp*, *ho*, *co*, and *lo*); (2) the rate of hemicellulose oxidation ($\dot{\omega}''_{ho}$) is negligible; and (3) values of the found kinetic parameters vary widely (Table 4.B1). Similar results are also found for the forest peat in Fig. 4.B1(c) where significant overlapping of four reactions takes place between 600 and 700 K. These observations further suggest that the optimization of TG

5. The exceptionally high second peak in DTG curve ($X_{O_2} = 21\%$) is probably due to the uncertainty of TG experiment which cannot be reproduced by any of three schemes.

Table 4.1: Kinetic parameters for the low-mineral moss peat and high-mineral forest peat samples with the 3- and 5-step schemes (including 1-step drying). $\Delta H > 0$ (endothermic); $\Delta H < 0$ (exothermic).

Parameter		Moss peat	Range	Forest peat	Range	Unit
	MC	4.1	[2.9, 4.2]	9.0	[7.8, 9.2]	%
	IC	2.1	[2.1, 2.3]	22.2	[21.8, 22.5]	%
3-step	$\lg A_{dr}$	6.91	[6.62, 7.35]	7.27	[7.10, 8.79]	$\lg(s^{-1})$
	E_{dr}	58.7	[56.9, 61.5]	58.6	[57.8, 67.9]	kJ/mol
	n_{dr}	2.37	[2.25, 2.53]	2.60	[2.56, 2.72]	-
	ΔH_{dr}	-2.26	-	-2.26	-	MJ/kg
	$\lg A_{pp}$	8.18	[6.01, 8.18]	6.85	[6.61, 7.13]	$\lg(s^{-1})$
	E_{pp}	112	[89.9, 112]	99.2	[97.2, 101]	kJ/mol
	n_{pp}	5.31	[3.12, 5.31]	5.67	[5.19, 5.67]	-
	$\nu_{\alpha,pp}$	0.28	[0.28, 0.36]	0.40	[0.38, 0.40]	kg/kg
	ΔH_{pp}	-0.5	-	-0.5	-	MJ/kg
	$\lg A_{\alpha o}$	10.2	[0.17, 11.4]	3.99	[3.99, 6.84]	$\lg(s^{-1})$
	$E_{\alpha o}$	160	[139, 170]	67.8	[67.8, 93.7]	kJ/mol
	$n_{\alpha o}$	0.51	[0.51, 1.21]	0.47	[0.39, 1.92]	-
	$n_{O_2,\alpha o}$	0.86	[0.80, 0.96]	0.59	[0.38, 0.91]	-
	$\nu_{a,\alpha o}$	0.01	[0.009,0.01]	0.24	[0.24, 0.41]	kg/kg
	$\Delta H_{\alpha o}$	29.7	-	15.1	-	MJ/kg
5-step [b]	$\lg A_{po}$	16.8	[12.0, 16.8]	6.63	[6.35, 7.38]	$\lg(s^{-1})$
	E_{po}	195	[142, 195]	89.2	[86.0, 96.7]	kJ/mol
	n_{po}	2.33	[1.68, 2.40]	1.86	[1.63, 2.00]	-
	$n_{O_2,po}$	0.24	[0.23, 0.26]	0.55	[0.50, 0.58]	-
	$\nu_{\beta,po}$ [a]	0.61	[0.61, 0.63]	0.39	[0.36, 0.44]	kg/kg
	ΔH_{po}	11.6	-	12.3	-	MJ/kg
	$\lg A_{\beta o}$	7.38	[7.28, 8.27]	14.4	[9.87, 15.3]	$\lg(s^{-1})$
	$E_{\beta o}$	117	[113, 124]	181	[136, 190]	kJ/mol
	$n_{\beta o}$	1.32	[1.19, 1.32]	2.26	[1.42, 2.45]	-
	$n_{O_2,\beta o}$	0.52	[0.47, 0.62]	0.54	[0.51, 0.72]	-
	$\nu_{a,\beta o}$	0.04	[0.03, 0.04]	0.62	[0.55, 0.65]	-
	$\Delta H_{\beta o}$	28.9	-	7.6	-	MJ/kg
	$\lg A_{\alpha o}$	13.3	[12.0, 13.7]	10.1	[9.97, 14.2]	$\lg(s^{-1})$
	$E_{\alpha o}$	172	[158, 175]	143	[142, 176]	kJ/mol
	$n_{\alpha o}$	2.58	[2.38, 2.83]	1.31	[1.23, 3.44]	-
	$n_{O_2,\alpha o}$	0.86	[0.85, 0.96]	0.86	[0.81, 1.09]	-
	$\nu_{a,\alpha o}$	0.07	[0.07, 0.08]	0.59	[0.59, 0.61]	kg/kg
	$\Delta H_{\alpha o}$	27.8	-	8.1	-	MJ/kg

a. Calculated from Eq. (4.12).

b. Drying and pyrolysis parameters of 5-step scheme are the same as 3-step scheme.

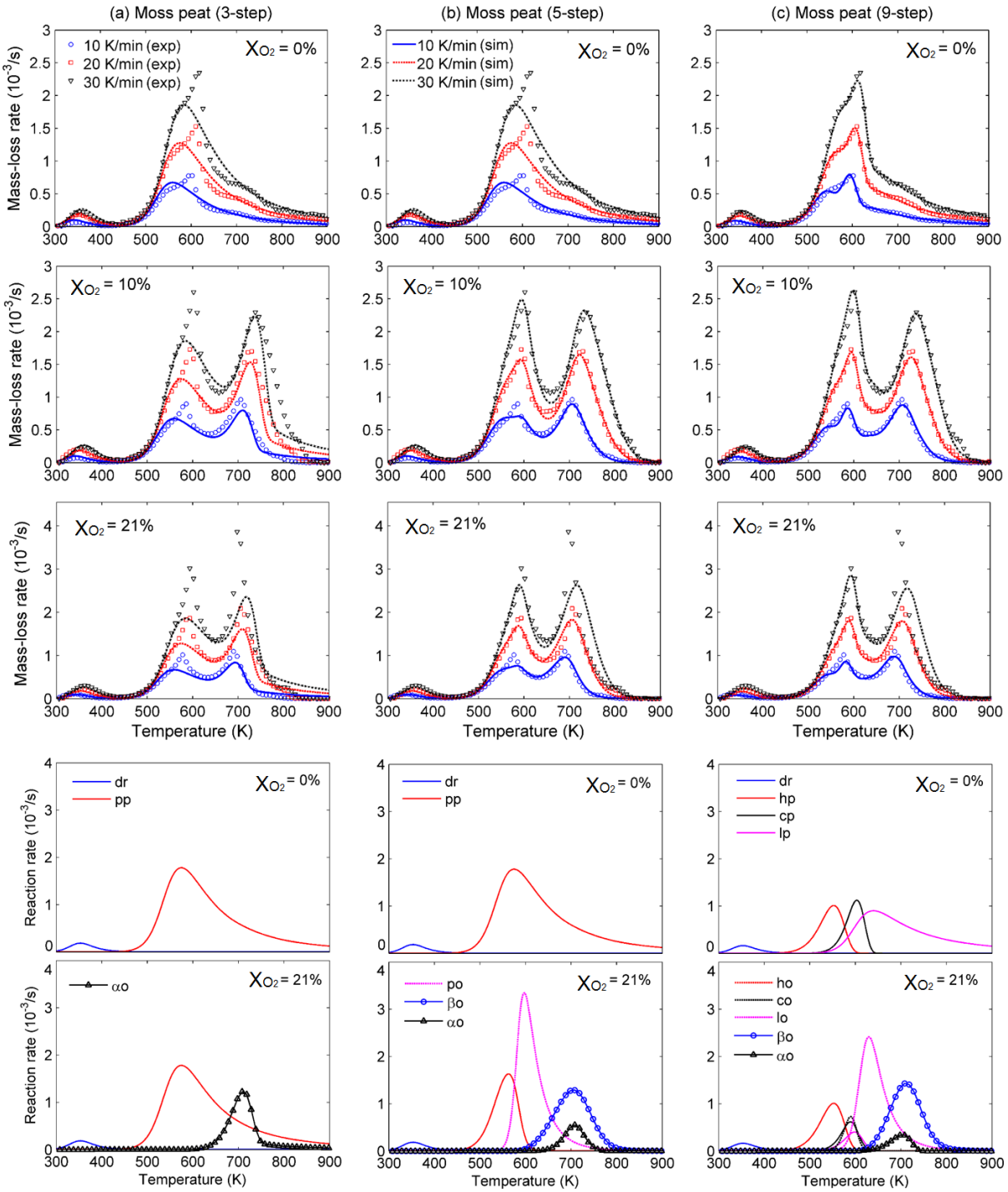

Figure 4.2: Measured and predicted DTG curves as well as predicted reaction rates of the low-mineral moss peat under different oxygen concentrations (X_{O_2}), modelled by (a) 3-step, (b) 5-step, and (c) 9-step kinetic schemes.

Table 4.2: The minimum error (Φ) after optimization and blind prediction of TG data for forest and moss peat.

error	3-step		5-step		9-step	
(%)	Forest	Moss	Forest	Moss	Forest	Moss
Φ_{opt}	7.9	8.7	5.5	5.5	5.0	4.2
Φ_{pre}	16.7	16.5	10.5	11.0	10.0	9.0

data based on the 9-step scheme is over-determined [26]. The necessity and redundancy of these kinetic schemes are further investigated in the next section.

4.4 Modelling bench-scale smouldering experiments

The chemical validity of the schemes are investigated outside the TG realm in this section. They are incorporated into a 1-D heat and mass transfer model to study the reaction and the species distribution inside a peat smouldering front.

In order to isolate the effect of biomass moisture and focus on the effect of atmospheric oxygen, [19] used the oven-dried peat (MC $\approx$ 10%) which is same moss peat for TG experiment in Fig. 4.2. Experiments were conducted under various atmospheric X_{O_2} (0$\sim$35%) within a bench-scale smouldering reactor (125 mm diameter and 30 mm height with 80 ± 3 g peat), as shown in Fig. 4.3a. The reactor walls were porous to allow gas diffusing into the sample. Ignition was on the top surface by infrared irradiation at flux levels of 7.5, 10 and 20 kW/m^2 for 1 min, 10 min and the entire experiment. More details about these experiments can be found in [19]. Note that unlike ($\sim$1 mg) TG experiment, inside this ($\sim$100 g) thick sample, the heat and mass transfer can no longer be neglected.

4.4.1 Governing equations

The horizonal dimension of the sample is much larger than the vertical dimension, and both irradiation and gas flow are uniform in the top and bottom surfaces. Therefore, the smouldering spread can be approximated as 1D spread along the vertical direction (Fig. 4.3a). If the top ignition source is too weak or the atmospheric oxygen concentration is too low, the smouldering front may not ignite or spread. If ignited, a smouldering front starts to spread downward vertically.

In Chapters 2 and 3, the influence of MC on ignition and spread in normal air ($X_{O_2} = 21\%$) had been studied with a 1D model established in the open-source code Gpyro [23]. Such model is improved with non-first-order oxidation and in-depth irradiation to simulate current bench-scale experiments, and for the first time simulate the effect of oxygen on biomass smouldering. The model solves transient equations for both the condensed and gas phases. The governing equations include Eq. (4.21) for condensed-phase mass conservation, Eq. (4.25) for condensed-phase species conservation, Eq. (4.23) for

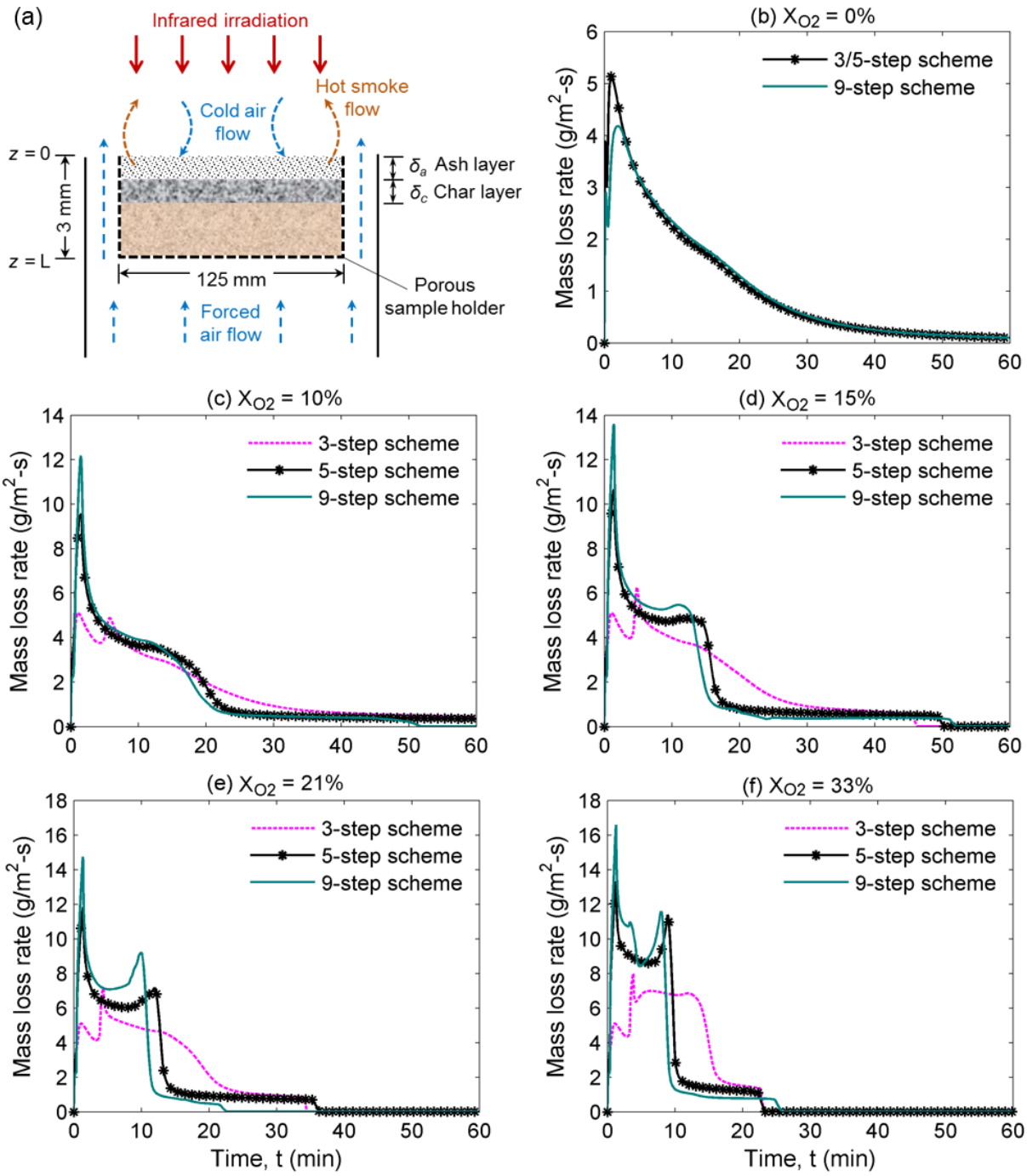

Figure 4.3: (a) sketch of bench-scale (∼100 g) experimental setup in [19] and [18] and the corresponding computational domain; predicted bench-scale mass-loss rate by 3-, 5- and 9-step schemes for moss peat under atmospheres of (b) N_2 ($X_{O_2} = 0\%$), (c) $X_{O_2} = 10\%$, (d) $X_{O_2} = 15\%$, (e) air ($X_{O_2} = 21\%$), and (f) $X_{O_2} = 33\%$ under an irradiation $\dot{q}''_e = 20$ kW/m^2 during the entire experiment.

energy conservation (assuming thermal equilibrium between condensed and gas phases), Eq. (4.24) for gas-phase mass conservation, Eq. (4.25) for gas-phase species conservation and Eq. (4.26) for gas-phase momentum conservation:

$$\frac{\partial \overline{\rho}}{\partial t} = -\dot{\omega}_{fg}^{'''} \tag{4.21}$$

$$\frac{\partial \left(\overline{\rho} Y_i\right)}{\partial t} = \dot{\omega}_{fi}^{'''} - \dot{\omega}_{di}^{'''} \tag{4.22}$$

$$\frac{\partial(\overline{\rho}\overline{h})}{\partial t} + \frac{\partial \left(\dot{m}^{''} h_g\right)}{\partial z} = \frac{\partial}{\partial z}\left(\overline{k}\frac{\partial T}{\partial z}\right) + \sum_{k=1}^{K} \dot{\omega}_{di,k}^{'''} \Delta H_k - \frac{\partial \dot{q}_r^{''}}{\partial z} \tag{4.23}$$

$$\frac{\partial \left(\rho_g \overline{\psi}\right)}{\partial t} + \frac{\partial \dot{m}^{''}}{\partial z} = \dot{\omega}_{fg}^{'''} \tag{4.24}$$

$$\frac{\partial \left(\rho_g \overline{\psi} Y_i\right)}{\partial t} + \frac{\partial(\dot{m}^{''} Y_j)}{\partial z} = -\frac{\partial}{\partial z}\left(\overline{\psi}\rho_g D \frac{\partial Y_j}{\partial z}\right) + \dot{\omega}_{fj}^{'''} - \dot{\omega}_{dj}^{'''} \tag{4.25}$$

$$\dot{m}^{''} = -\frac{\overline{K}}{\nu}\frac{\partial P}{\partial z} \qquad (P = \rho_g R_s T) \tag{4.26}$$

A constant irradiation ($\dot{q}_e^{''}$) of variable intensity and duration is applied as the ignition source. The in-depth radiation in Eq. (4.23) is considered as

$$\dot{q}_r^{''}(z) = \overline{\varepsilon}\dot{q}_e^{''} exp\left(-z/\kappa\right) \tag{4.27}$$

where $\kappa = 1000$ m is assumed in [26]. The boundary conditions on the top free surface ($z = 0$) are

$$\begin{cases} -\overline{k}\dfrac{\partial T}{\partial z}\bigg|_0 = -h_{c0}\left(T_0 - T_\infty\right) - \overline{\varepsilon}\sigma\left(T_L^4 - T_\infty^4\right) \\ -\overline{\psi}\rho_g D\dfrac{\partial Y_j}{\partial z}\bigg|_0 = h_{m0}\left(Y_{j\infty} - Y_{j0}\right) \\ P_0 = P_\infty \end{cases} \tag{4.28}$$

where an empirical convection coefficient is used, $h_{c0} = 1.52\Delta T^{1/3} = 1.52(300)^{1/3} \approx 10$ W/m^2-K [27]; and the heat-mass transfer analogy is used, $h_{m0} \sim h_{c0}/c_g \approx 10$ g/m^2-s. The environmental pressure (P_∞) and temperature (T_∞) are constant at 1 atm and 300 K, respectively.

Similar convective boundary conditions are imposed on the back free surface ($z = L$) as

$$\begin{cases} -\overline{k}\dfrac{\partial T}{\partial z}\bigg|_L = -h_{cL}\left(T_L - T_\infty\right) - \overline{\varepsilon}\sigma\left(T_L^4 - T_\infty^4\right) \\ -\overline{\psi}\rho_g D\dfrac{\partial Y_j}{\partial z}\bigg|_L = h_{mL}\left(Y_{j\infty} - Y_{jL}\right) \\ P_L = P_\infty \end{cases} \tag{4.29}$$

Table 4.3: Physical properties of condensed-phase species: ρ_{si}, k_{si}, and c_i are from [28], and ρ_{i0} is from [19] and [18].

Species (i)	ρ_{si} (kg/m^3)	ρ_{i0} (kg/m^3)	ψ_{i0} (-)	k_{si} (W/m-K)	c_i (J/kg-K)
water	1000	1000	0	0.6	4186
peat	1500	200 [a]	0.867	1.0	1840
α-char	1300	185	0.962	0.26	1260
β-char	1300	185	0.962	0.26	1260
ash	2500	35	0.997	1.2	1380

a. Bulk density of oven-dried peat (MC = 10%) is 200(1+MC) = 220 kg/m^3.

where $h_{cL} = h_{c,0} = 10$ W/m^2-K with surface radiation ($\varepsilon = 0.95$) because the bottom wall is not insulated, and $h_{mL} = 2$ g/m^2-s because the bottom wall is porous (mesh porosity = 0.26, reduced oxygen supply).

A fully implicit method is adopted to solve all equations. Details about numerical solution methodology are reported in [23]. The sample height during spread is equal to the sum of the height of each cell, $H_t = \sum_{n=1}^{N} \Delta z_n$, which depends on the mass conservation and density, capturing the surface regression during experiment. Simulations were run with an initial cell size of $\Delta z = 0.1$ mm, and initial time step of 0.02 s. Reducing the cell size and time step by a factor of 2 gives little difference in results, so this discretisation is acceptable.

4.4.2 Parameter selection and stochastic sensitivity analysis

Each condensed-phase species is assumed to have constant and temperature-independent properties (e.g. bulk density, specific heat, and porosity) for the sake of simplicity and the lack of data in the literature. All gaseous species have unity Schmidt number, and equal diffusion coefficient and specific heat. The averaged properties in each cell are calculated by weighting the appropriate mass fraction (Y_i) or volume fraction (X_i) [23].

The bulk densities of all species for this moss peat were measured in [19]. The properties of α-char and β-char are assumed to be the same. The solid ($\psi_i = 0$) thermophysical properties, $\rho_{s,i}$, $k_{s,i}$, c_i of peat, char, and ash are selected from [28], all listed in Table 4.3. Then, porosity can be calculated as

$$\psi_i = 1 - \frac{\rho_i}{\rho_{s,i}} \tag{4.30}$$

which is found to be high for peat ($\psi_p = 0.867$). Also, the peat sample is dried, so the small amount of bound water (MC $\leq$ 10%) is assumed to stay in the pores of peat without volume expansion and the wet peat bulk density is estimated as $\rho = (1 + \text{MC})\rho_p$.

Table 4.4: Physicochemical parameters studied in sensitivity analysis, and corresponding ranges for stochastic sampling. 4 parameters are selected and 40 stochastic sampling are conducted at a time.

Parameter	k_{sp} (W/m-K)	k_{sc} (W/m-K)	c_p $(J/kg-K)$	ΔH_{pp} (MJ/kg)	ΔH_{O_2} (MJ/kg)	$h_{m,0}$ (g/m^2-s)
Initial value	1.0	0.26	1840	-0.5	30	10
Sampling range	[0.5, 1.5]	[0.15, 0.4]	[1500, 2200]	[-1, -0.2]	[25, 35]	[5, 15]

The effective thermal conductivity includes the radiation across pores as

$$k_i = k_{s,i}(1-\psi_i) + \gamma_i \sigma T^3 \tag{4.31}$$

where $\gamma_i = 10^{-4} \sim 10^{-3}$ m depends on the pore size as $\gamma_i \approx 3d_{p,i}$ [6] [29]. The average pore size relates to the particle surface area as $d_{p,i} = 1/S_i\rho_i$ where $S_p = S_c = 0.05$ m^2/g and $S_a = 0.2$ m^2/g [30]. The absolute permeability of soil is independent of permeating fluid, and can be estimated [20] as

$$K_i = 10^4 \frac{\nu_w}{g} d_{p,i}^2 \approx 10^{-3} d_{p,i}^2 \sim 1/\rho_i^2 \tag{4.32}$$

which varies from 10^{-12} to 10^{-9} m^2, and decreases as the bulk density increases.

The three proposed kinetic schemes (3-, 5- and 9-step) for biomass smouldering are examined with this sophisticated 1D model. The heat of pyrolysis is chosen as $\Delta H_{pp} = -0.5$ MJ/kg (endothermic); the heat of oxidation is assumed to relate to the oxidized organic matter as $\Delta H_k = \Delta H_{O_2}(1-\nu_{B,k})$ as Chapter 2. According to differential scanning calorimetry (DSC) of multiple peat samples [31], $\Delta H_{O_2} = 30$ MJ/kg is estimated for the low-mineral moss peat, and $\Delta H_{O_2} = 20$ MJ/kg for high-mineral forest peat. The heat of reactions are listed in Table 4.1 and 4.B1, with overall smouldering heats of $\Delta H_{sm} = 18.7$ MJ/kg (moss peat) and $\Delta H_{sm} = 10.2$ MJ/kg (forest peat) in TG environment with air. The oxygen consumption is related to the heat of oxidation as $\nu_{O_2,k} = \Delta H_k/(13.1$ MJ/kg) [32].

Figure 4.3(b-f) compares the predicted moss-loss rates in bench-scale experiment by 3-, 5-, and 9-step schemes for moss peat under different oxygen concentrations. In inert atmosphere (Fig. 4.3b), the single pyrolysis reaction (Eqs. (4.3)) in 3- and 5-step schemes gives a very similar prediction to three pyrolysis reactions (Eq. (4.4)) in 9-step scheme, despite small differences in the peak.

In the oxidative atmosphere cases (Fig. 4.3c-f), 3-step scheme predicts a relatively low mass-loss rate, different from 5- and 9-step predictions. This shows the prediction

6. Although the overall porosity of solid species is large (~ 0.9), the actual inter-particle porosity is small because a single solid particle is also porous and has a large intra-particle porosity. Thus, the simplification for radiation in Eq. (4.31) is still reasonable under current large overall porosities.

error at TG scale can be significantly amplified at bench scale. Meanwhile, the prediction difference between 5- and 9-step scheme is found to be small (average correlation value of 0.96) under various oxygen concentrations. Therefore, the simulation of bench-scale experiments further suggests (1) 3-step scheme results in a significant inaccuracy; (2) 9-step scheme is over-complex; and (3) 5-step scheme is the best: relatively simple but still adequate to accurately reproduce experiments, so it is used in all following simulations.

Since the species conductivity (k_i), heat capacity (c_i), and heat of reactions (h_k) are selected from the literature, appreciable uncertainties exist in these parameters. In order to study the sensitivity of these input parameters, their variation ranges are selected from the literature (see Table 4.4), and an stochastic sensitivity analysis is conducted. Six parameters, k_{sp}, k_{sc}, c_p, ΔH_{pp}, ΔH_{O_2}, and $h_{m,0}$, are sampled randomly and combined to conduct many simulations and study their sensitivity to possible range from [28].

4.4.3 Modelling results

Figure 4.4 shows the predicted evolution of the temperature and reaction-rate profiles for the experiment under irradiation of 20 kW/m^2 for the entire experiment. The modelling results show that the peak temperature quickly increases to 550°C within 1 min (Fig. 4.4a) because oven-dried peat only has a small amount of water (MC $\approx$ 10%) and thus a weak endothermic contribution from drying (Fig. 4.4b). This shows that a successful ignition can be simulated with 1 min irradiation, agreeing with the experiment in [19]. Then, the temperature continues to increase as the rate of char oxidation increases, while the rate of pyrolysis weakens and widens.

By about 12 min, both the thermal front (Fig. 4.4a) and the multi-layer smouldering front (Fig. 4.4b-d) reach the bottom. At this moment, a second forward char oxidation front is started fed by oxygen diffusion through the porous bottom wall (Fig. 4.4d), which increases the temperature profile and results in a second peak in mass-loss rate curve (Figs. 4.3 and 4.4b). Same as the experimental observation in [19], all organic content is consumed by the end, and only mineral ash is left.

Figure 4.4a and b compares the mass-loss rate between experiment and numerical simulation at both N_2 (X_{O_2}= 0%) and air (X_{O_2} = 21%) atmospheres. In N_2 (Fig. 4.4a), the predicted mass-loss rate shows only one peak, and gives an excellent agreement with experiment. In order to test the modelling sensitivity to physico-chemical properties, 40 runs of stochastic sampling for four parameters (k_{sp}, k_{sc}, c_p, and ΔH_{pp}) are conducted. Then, 40 stochastic mass-loss rate curves are shown by a shadow region in Fig. 4.4a. Clearly, most of experimental date is included in the shadow region, suggesting that the prediction has a high accuracy, and the modelling result in the inert atmosphere is not sensitive to these four parameters.

In air (Fig. 4.4b), the model predicts the same two-peaks mass-loss rate curve as experiment, although the overall matching is not as high as the N_2 case. Modelling reveals that when the thermal and oxidation waves reach the bottom, the second peak

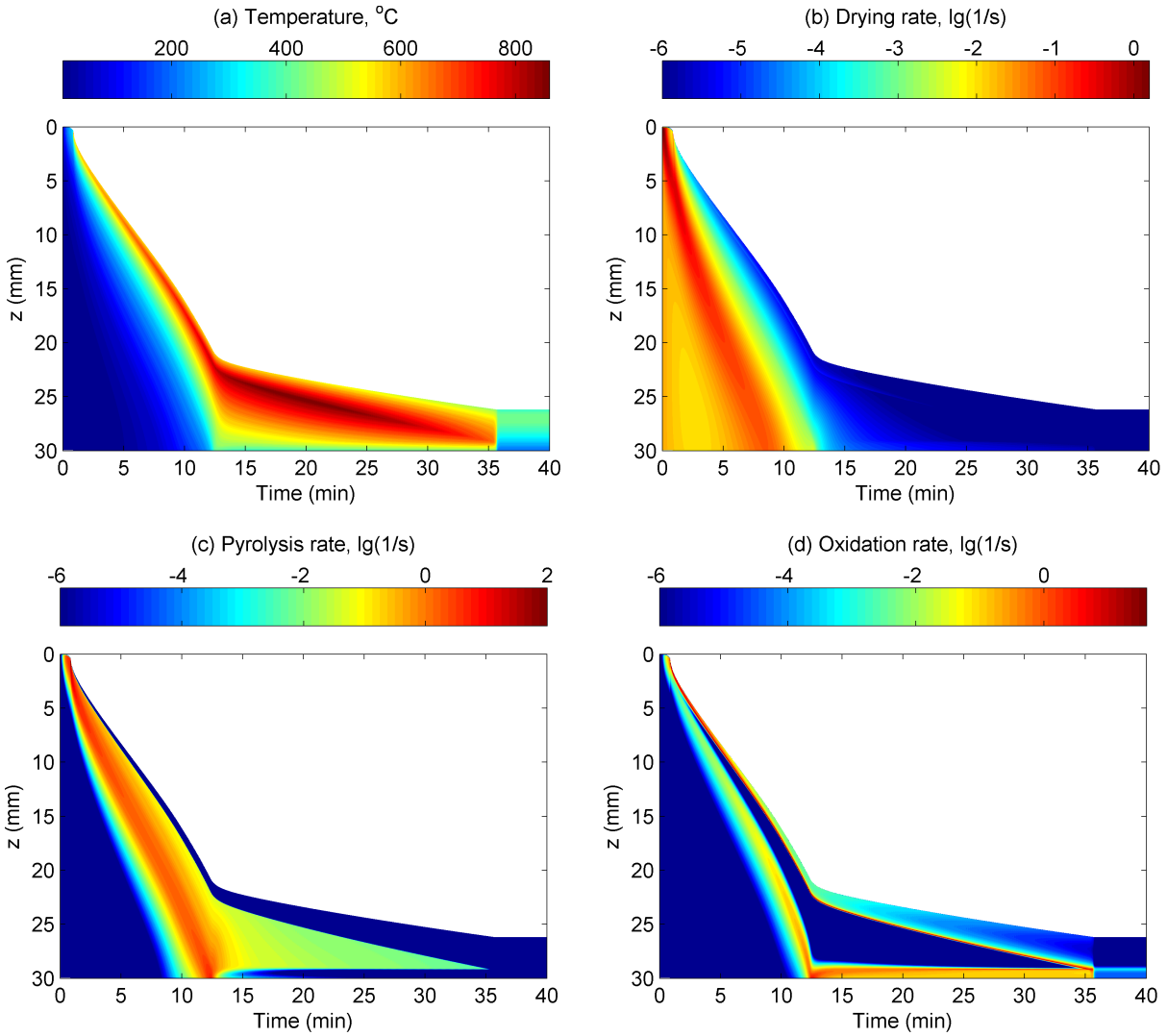

Figure 4.4: Predicted 2D contours of depth vs. time, (a) temperature, (b) drying rate, (c) pyrolysis rate, and (d) oxidation rate, for the bench-scale peat experiment in air under an irradiation $\dot{q}''_e = 20$ kW/m^2 during the entire experiment.

occurs because of the initiation of a second forward char oxidation front (Fig. **??**b). Another group of four parameters (k_{sp} c_p, ΔH_{O_2} and h_{m0}) are selected for a similar stochastic sensitivity analysis. Modelling generates a similar shadow region, which also covers most of experimental data points, implying the a good predictability of the overall model setup. The shadow region is much larger than the N_2 case, showing the prediction in the oxidative atmosphere is more sensitive to variations of the selected parameters. Particularly, values of h_{m0} (relating to oxygen supply) and ΔH_{O_2} (relating to overall heat of smouldering) are found to strongly affect modelling results, especially changing the peak of mass-loss rate and smouldering duration.

With the same experimental setup, [18] further conducted experiments with the irradiation of 20 kW/m^2 for a short pulse of 1 min under different oxygen concentrations, and the mass-loss rates are plotted in Fig. 4.4c. After 1 min irradiation, there is a clear

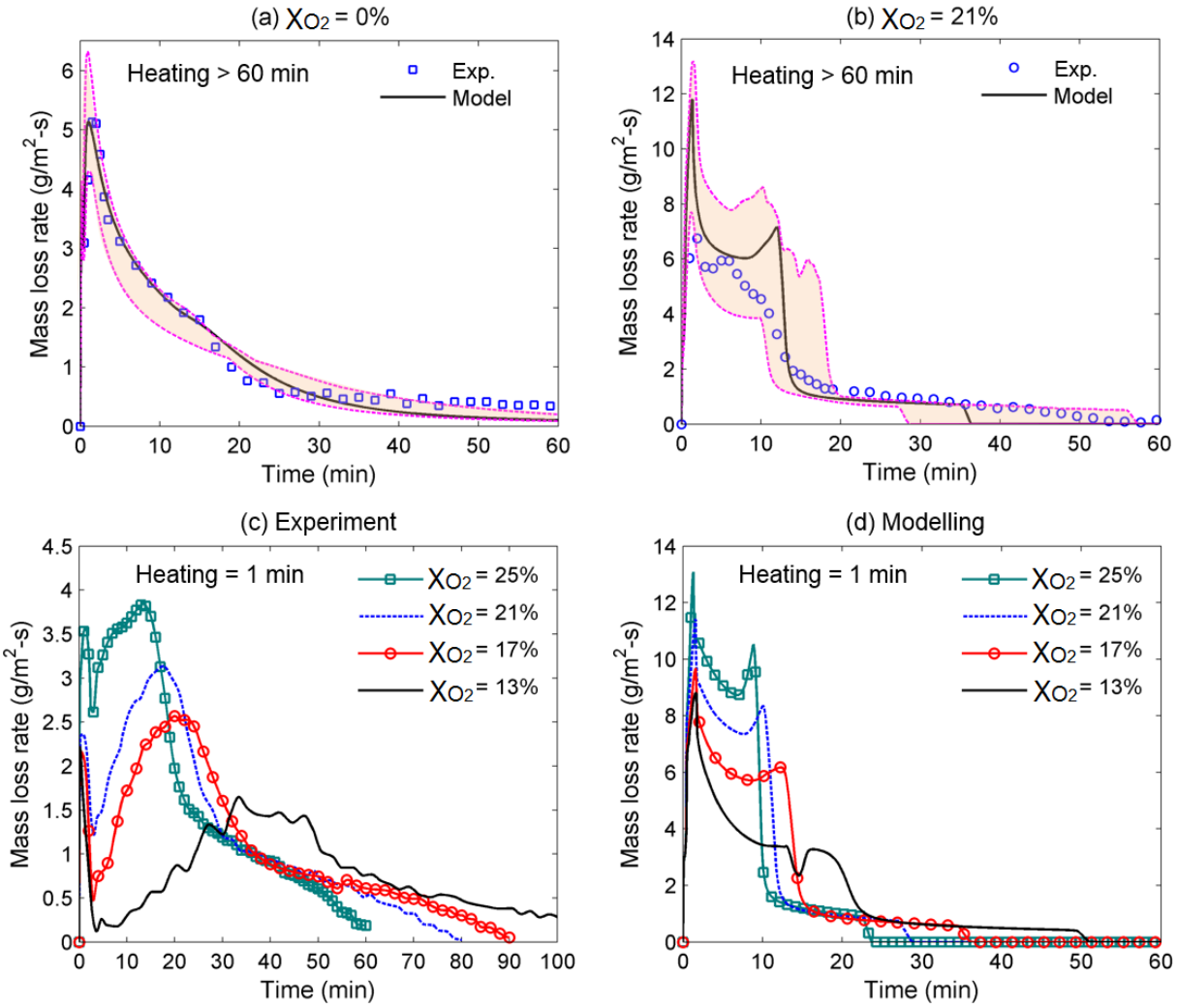

Figure 4.5: Comparison of bench-scale mass-loss rate between measurements in [19] and predictions at (a) N_2 ($X_{O_2} = 0\%$), and (b) air ($X_{O_2} = 21\%$) under $\dot{q}''_e = 20$ kW/m^2 during entire experiment. The shadow shows sensitivity from stochastic sampling. Qualitative comparison for the ignition protocol of $\dot{q}''_e = 20$ kW/m^2 for 1 min, between (c) measurements [18], and (d) predictions.

decrease in mass-loss rate. However, as observed from their experiments, for 1 min irradiation on the top surface, only several small spots were successfully ignited, rather than uniformly igniting the whole surface at once, which is a 2D or 3D spread. Therefore, a long duration is found to reach the bottom and produce the second peak of mass-loss rate. Such a high-dimensional smouldering spread cannot be quantitatively represented by the current simplified 1D model, so only qualitative comparison can be conducted for the short pulse cases.

Figure 4.4d shows the modelled mass-loss rate for these 1-min ignition experiments. In order to ensure a successful ignition under low oxygen concentration, a larger oxygen supply ($h_{m,0} = 20$ g/m^2-s) is set for the boundary condition on the top surface. Comparison shows that the model successfully predicts two peaks of all mass-loss rate curves, in

agreement with experiment. Modelling also shows three things as X_{O_2} increases: (1) the overall mass-loss rate increases, (2) the second peak occurs earlier; and (3) smouldering duration decreases. All three findings agree with the experimental curves in Fig. 4.4c. Therefore, the proposed 5-step scheme and the multi-physical 1D model show a good capability to simulate the smouldering combustion of peat at various oxygen concentrations.

4.5 Conclusions

The thermochemical conversion of peat in smouldering combustion has been investigated by combining experiments and modelling at both TG and bench scales under various oxygen concentrations. Three kinetic schemes are explored. Excellent balance between accuracy and complexity is found in the 5-step scheme which includes drying, one pyrolysis and three oxidations. We found that the influence of oxygen is weaker than the first order as assumed in the literature. This is the first time that the influence of oxygen on biomass smouldering is explained in terms of both chemistry and transport phenomena across scales.

Acknowledgements

The authors thank Prof. Haixiang Chen (University of Science and Technology of China) for valuable discussions and providing TG data. Valuable comments from Dr Rory Hadden (University of Edinburgh) and Francesco Restuccia (Imperial College London) are acknowledged.

References

[1] P. McKendry, "Energy production from biomass (part 1): overview of biomass," *Bioresource Technology*, vol. 83, no. 1, pp. 37 – 46, 2002. Reviews Issue.

[2] A. Anca-Couce, "Reaction mechanisms and multi-scale modelling of lignocellulosic biomass pyrolysis," *Progress in Energy and Combustion Science*, vol. 53, pp. 41 – 79, 2016.

[3] T. Ohlemiller, "Modeling of smoldering combustion propagation," *Progress in Energy and Combustion Science*, vol. 11, no. 4, pp. 277 – 310, 1985.

[4] G. Rein, "Smoldering Combustion," in *SFPE Handbook of Fire Protection Engineering* (M. J. Hurley, D. T. Gottuk, J. R. Hall Jr., K. Harada, E. D. Kuligowski, M. Puchovsky, J. L. Torero, J. M. Watts Jr., and C. J. WIECZOREK, eds.), pp. 581–603, Springer New York, 2016.

[5] G. Rein, C. Lautenberger, A. C. Fernandez-Pello, J. L. Torero, and D. L. Urban, "Application of genetic algorithms and thermogravimetry to determine the kinetics of polyurethane foam in smoldering combustion," *Combustion and Flame*, vol. 146, no. 1-2, pp. 95 – 108, 2006.

[6] C. Di Blasi, "Modeling chemical and physical processes of wood and biomass pyrolysis," *Progress in Energy and Combustion Science*, vol. 34, no. 1, pp. 47 – 90, 2008.

[7] E. R. Carvalho, C. A. G. Veras, and J. A. CarvalhoJr, "Experimental investigation of smouldering in biomass," *Biomass and Bioenergy*, vol. 22, no. 4, pp. 283 – 294, 2002.

[8] C. Di Blasi, C. Branca, and B. Teislev, "Development of a novel reactor for the oxidative degradation of straw," *Bioresource Technology*, vol. 91, no. 3, pp. 263 – 271, 2004.

[9] G. Rein, "Smouldering Fires and Natural Fuels," in *Fire Phenomena and the Earth System* (C. Belcher, ed.), ch. 2, pp. 15–33, Wiley and Sons, 2013.

[10] C. Di Blasi, "Modeling and simulation of combustion processes of charring and non-charring solid fuels," *Progress in Energy and Combustion Science*, vol. 19, no. 1, pp. 71 – 104, 1993.

[11] Y. Ding, C. Wang, M. Chaos, R. Chen, and S. Lu, "Estimation of beech pyrolysis kinetic parameters by Shuffled Complex Evolution," *Bioresource Technology*, vol. 200, pp. 658 – 665, 2016.

[12] H. Niu, *Pyrolysis Kinetics and Flammability Study of Forest Fuels*. PhD thesis, Unversity of Science and Technology of China, 2014.

[13] Y. Su, Y. Luo, W. Wu, Y. Zhang, and S. Zhao, "Characteristics of pine wood oxidative pyrolysis: Degradation behavior, carbon oxide production and heat properties," *Journal of Analytical and Applied Pyrolysis*, vol. 98, no. 0, pp. 137 – 143, 2012.

[14] W. Zhao, H. Chen, N. Liu, and J. Zhou, "Thermogravimetric analysis of peat decomposition under different oxygen concentrations," *Journal of Thermal Analysis and Calorimetry*, vol. 117, no. 1, pp. 489–497, 2014.

[15] M. Amutio, G. Lopez, R. Aguado, M. Artetxe, J. Bilbao, and M. Olazar, "Kinetic study of lignocellulosic biomass oxidative pyrolysis," *Fuel*, vol. 95, no. 0, pp. 305 – 311, 2012.

[16] A. Anca-Couce, N. Zobel, A. Berger, and F. Behrendt, "Smouldering of pine wood: Kinetics and reaction heats," *Combustion and Flame*, vol. 159, no. 4, pp. 1708 – 1719, 2012.

[17] C. M. Belcher, J. M. Yearsley, R. M. Hadden, J. C. McElwain, and G. Rein, "Baseline intrinsic flammability of Earths ecosystems estimated from paleoatmospheric oxygen over the past 350 million years," *Proceedings of the National Academy of Sciences*, vol. 107, no. 52, pp. 22448–22453, 2010.

[18] R. M. Hadden, G. Rein, and C. M. Belcher, "Study of the competing chemical reactions in the initiation and spread of smouldering combustion in peat," *Proceedings of the Combustion Institute*, vol. 34, no. 2, pp. 2547 – 2553, 2013.

[19] R. M. Hadden, *Smouldering and Self-Sustaining Reactions in Solids: An Experimental Approach*. Phd thesis, University of Edinburgh, 2011.

[20] B. Punmia and A. Jain, *Soil Mechanics and Foundations*. Laxmi Publications Pvt Limited, 2005.

[21] N. Moussa, T. Toong, and C. Garris, "Mechanism of smoldering of cellulosic materials," *Symposium (International) on Combustion*, vol. 16, no. 1, pp. 1447 – 1457, 1977.

[22] K.-Y. Li, X. Huang, C. Fleischmann, G. Rein, and J. Ji, "Pyrolysis of Medium-Density Fiberboard: Optimized Search for Kinetics Scheme and Parameters via a Genetic Algorithm Driven by Kissingers Method," *Energy & Fuels*, vol. 28, no. 9, pp. 6130–6139, 2014.

[23] C. Lautenberger and C. Fernandez-Pello, "Generalized pyrolysis model for combustible solids," *Fire Safety Journal*, vol. 44, no. 6, pp. 819 – 839, 2009.

[24] V. Cozzani, "Reactivity in Oxygen and Carbon Dioxide of Char Formed in the Pyrolysis of Refuse-Derived Fuel," *Industrial & Engineering Chemistry Research*, vol. 39, no. 4, pp. 864–872, 2000.

[25] D. Wu, X. Huang, F. Norman, F. Verplaetsen, J. Berghmans, and E. V. den Bulck, "Experimental investigation on the self-ignition behaviour of coal dust accumulations in oxy-fuel combustion system," *Fuel*, vol. 160, pp. 245 – 254, 2015.

[26] N. Bal and G. Rein, "Relevant model complexity for non-charring polymer pyrolysis," *Fire Safety Journal*, vol. 61, no. 0, pp. 36 – 44, 2013.

[27] J. Holman, *Heat Transfer*. Mechanical engineering series, McGraw-Hill, 1989.

[28] R. Jacobsen, E. Lemmon, S. Penoncello, Z. Shan, and N. Wright, "Thermophysical Properties of Fluids and Materials," in *Heat Transfer Handbook* (A. Bejan and A. Kraus, eds.), ch. 2, pp. 43–159, John Wiley & Sons, 2003.

[29] F. Yu, G. Wei, X. Zhang, and K. Chen, "Two Effective Thermal Conductivity Models for Porous Media with Hollow Spherical Agglomerates," *International Journal of Thermophysics*, vol. 27, no. 1, pp. 293–303, 2006.

[30] H. de Jonge and M. C. Mittelmeijer-Hazeleger, "Adsorption of CO_2 and N_2 on Soil Organic Matter: Nature of Porosity, Surface Area, and Diffusion Mechanisms," *Environmental Science & Technology*, vol. 30, no. 2, pp. 408–413, 1996.

[31] K. Bergner and C. Albano, "Thermal analysis of peat," *Analytical Chemistry*, vol. 65, no. 3, pp. 204–208, 1993.

[32] C. Huggett, "Estimation of rate of heat release by means of oxygen consumption measurements," *Fire and Materials*, vol. 4, no. 2, pp. 61–65, 1980.

Appendices

4.A Conversion of kinetic parameters

In this section, we show the conversion of kinetic parameters when choosing different reactant mode, i.e. $f(m_A^*)$ in Eq. (5.9). The reactant mode quantifies the conversion degree of A using the virtual peak mass of the reactant as characteristic. Both $\dot{\omega}_k$ and m_A could be normalized to a different characteristic mass, for example, FDS [7], ThermaKin [8], and [5] normalize to the initial cell mass (m_0) as

$$\begin{cases} (\dot{\omega}_k^*)' = Z_k' e^{-E_k/RT} \left[(m_A^*)'\right]^{n_k} f(Y_{O_2}) \\ (m_A^*)' = \dfrac{m_A}{m_0} \end{cases} \tag{4.33}$$

7. www.nist.gov/el/fire_research/fds_smokeview.cfm
8. www.fire.tc.faa.gov/pdf/TN08-17.pdf

Since the actual destruction rate of A in Eq. (4.29) is always the same regardless the selection of reactant mode, $\dot{\omega}_{dA_k} = m_{sA,0}\dot{\omega}_k^* = m_0(\dot{\omega}_k^*)'$, E_k and n_k are independent of the chosen characteristic mass, and a simple conversion exists between their pre-exponential factor as

$$Z_k' = Z_k \left(\frac{m_{sA,0}}{m_0}\right)^{1-n_k} = Z_k \left(Y_{sA,0}\right)^{1-n_k}. \tag{4.34}$$

where $Y_{sA,0} = m_{sA,0}/m_0$ is the initial mass fraction of source species for A in the cell. Similar simple conversion may also exist when normalized to some other characteristic mass.

4.B Predicting TG data of peat sample with high mineral content

The second soil sample was collected from the wild forest of Changpai Mountains in Northeast China (forest peat soil) with a high mineral content (IC $\approx$ 22%). The sample was pulverized into powders and dried at 80 °C for 24 h. A SDT Q600 TG-DSC thermal analyzer was used to record both the mass-loss (previously reported in [14]) and heat-flow curves. The initial mass of peat was about 5 mg for all experiments. In each experiment, the TG temperature was increased from 298 K to 1100 K at three heating rates of 10, 20, 30 K/min. Five atmospheric oxygen concentrations were selected, 0% (nitrogen), 5%, 10%, 15% and 21% (air). Therefore, in total 15 sets of TG data are available: 5 oxygen concentrations $\times$ 3 heating rates. The designed atmosphere flow rate was 50 mL/min at the atmospheric pressure and the room temperature. The uncertainty of two repeating TG tests is within 2%, showing a good repeatability.

We choose 12 sets for optimization, and another 3 sets: (1)$X_{O_2} = 0\%$ at 10 K/min, (2) $X_{O_2} = 10\%$ at 20 K/min, and (3) $X_{O_2} = 21\%$ at 30 K/min for blind predictions. The best values found for the parameters are listed in Tables 4.1 (3- and 5-step) and 4.B1 (9-step), respectively. The overall errors in both the optimization and blind prediction for each kinetic scheme can be found in Table 4.2. The measured and predicted TG curves of all mass-loss rates and reaction rates (20 K/min) in $X_{O_2} = 0\%$ and 21% are shown in Fig. 4.B1. Similar to the low-mineral peat samples of Fig. 4.2, 5- and 9-step kinetic schemes give a better prediction than the 3-step kinetic scheme. Note that the exceptionally high second peak in DTG curve ($X_{O_2} = 21\%$) is probably due to the uncertainty of TG experiment.

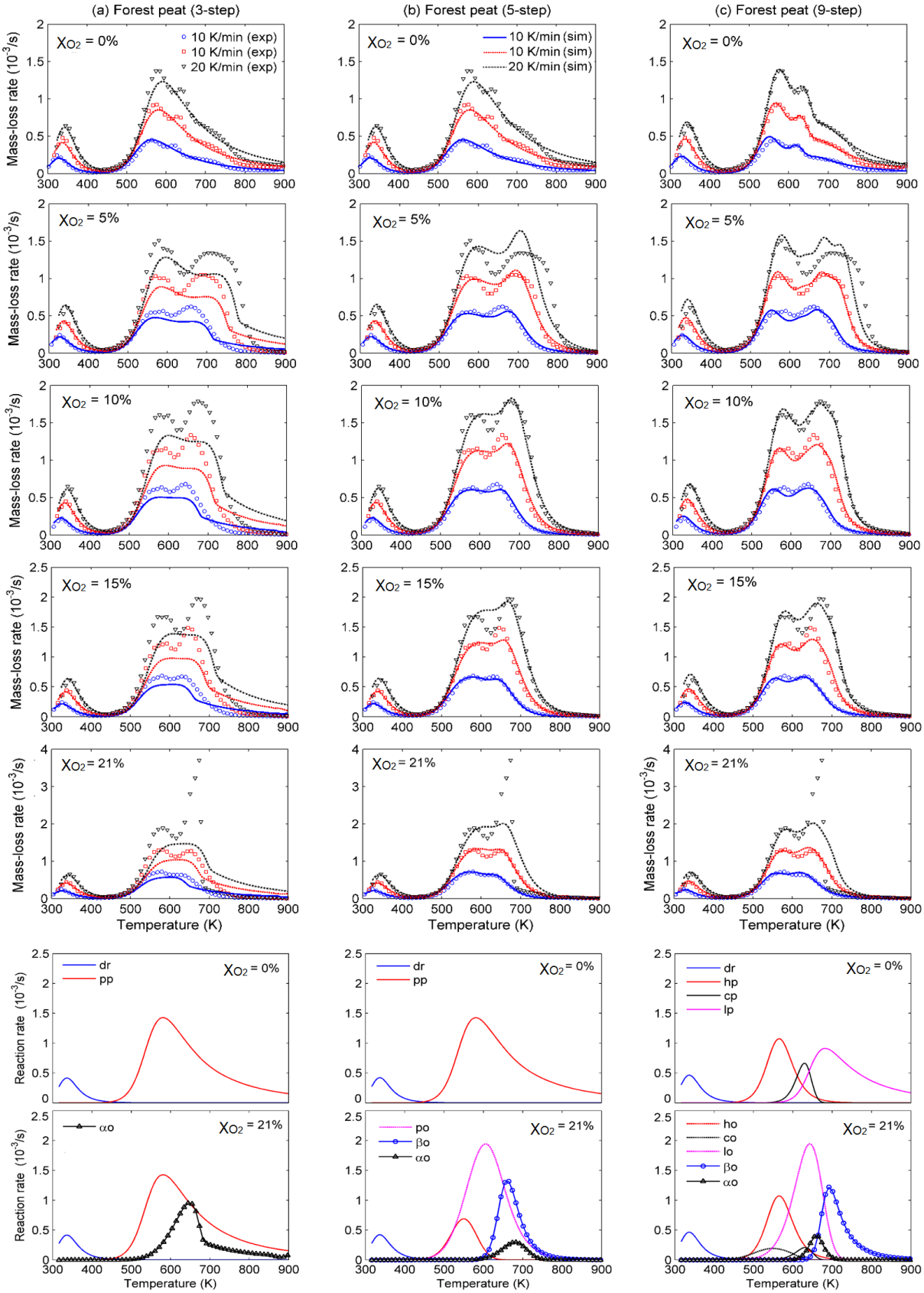

Figure 4.B1: Measured and predicted DTG curves as well as predicted reaction rates of the high-mineral forest peat under different oxygen concentrations (X_{O_2}) [14], modelled by (a) 3-step, (b) 5-step, and (c) 9-step kinetic schemes.

.

Table 4.B1: Kinetic parameters for the low-mineral moss peat and high-mineral forest peat samples with the 9-step scheme. $\Delta H > 0$ (endothermic); $\Delta H < 0$ (exothermic). The parameters for drying are listed in Table 4.1.

	Moss peat	Range	Forest peat	Range	Unit
Y_{h0}	20.1	[19.9, 22.6]	30.9	[17.8, 31.5]	
Y_{c0}	17.4	[17.3, 24.6]	10.8	[9.8, 15.8]	%
Y_{l0}	61.7	[54.9, 62.1]	58.3	[57.1, 68.7]	
$\lg A_{hp}$	6.95	[5.29, 7.20]	8.91	[8.91, 15.6]	$\lg(s^{-1})$
E_{hp}	93.8	[78.5, 96.5]	111	[111, 170]	kJ/mol
n_{hp}	0.98	[0.74, 1.00]	1.98	[0.98, 2.37]	-
$\nu_{\alpha,hp}$	0.16	[0.15, 0.25]	0.14	[0.13, 0.68]	kg/kg
ΔH_{hp}	-0.5	-	-0.5	-	MJ/kg
$\lg A_{cp}$	11.7	[9.43, 12.9]	13.6	[11.7, 14.9]	$\lg(s^{-1})$
E_{cp}	156	[131, 168]	183	[159, 199]	kJ/mol
n_{cp}	1.00	[0.88, 1.13]	1.61	[0.99, 1.28]	-
$\nu_{\alpha,cp}$	0.03	[0.03, 0.04]	0.39	[0.25, 0.43]	kg/kg
ΔH_{cp}	-0.5	-	-0.5	-	MJ/kg
$\lg A_{lp}$	10.9	[10.1, 12.5]	12.7	[11.6, 14.7]	$\lg(s^{-1})$
E_{lp}	142	[135, 158]	174	[161, 185]	kJ/mol
n_{lp}	7.07	[6.20, 8.10]	6.64	[6.22, 7.34]	-
$\nu_{\alpha,lp}$	0.37	[0.37, 0.41]	0.55	[0.36, 0.57]	kg/kg
ΔH_{lp}	-0.5	-	-0.5	-	MJ/kg
$\lg A_{ho}$	20.2	[15.0, 20.2]	4.17	[4.17, 5.75]	$\lg(s^{-1})$
E_{ho}	294	[228, 295]	86.1	[69.8, 87.6]	kJ/mol
n_{ho}	0.47	[0.40, 1.60]	2.75	[1.71, 2.75]	-
$n_{O_2,ho}$	0.11	[0.10, 0.13]	0.95	[0.90, 1.30]	-
$\nu_{\beta,ho}$ [a]	0.30	[0.30, 0.56]	0.12	[0.10, 0.14]	kg/kg
ΔH_{ho}	20.9	-	26.2	-	MJ/kg
$\lg A_{co}$	24.2	[20.4, 25.4]	7.17	[6.15, 7.47]	$\lg(s^{-1})$
E_{co}	278	[236, 297]	70.6	[66.3, 91.6]	kJ/mol
n_{co}	1.73	[1.00, 1.97]	3.07	[2.15, 3.12]	-
$n_{O_2,co}$	0.74	[0.72, 0.91]	0.98	[0.91, 1.21]	-
$\nu_{\beta,co}$ [a]	0.06	[0.72, 0.91]	0.34	[0.31, 0.51]	kg/kg
ΔH_{co}	28.2	-	19.8	-	MJ/kg
$\lg A_{lo}$	23.9	[20.6, 24.5]	6.59	[5.30, 6.58]	$\lg(s^{-1})$
E_{lo}	289	[254, 299]	97.5	[79.9, 97.5]	kJ/mol
n_{lo}	4.01	[2.79, 4.16]	1.09	[0.93, 1.38]	-
$n_{O_2,lo}$	0.93	[0.91, 1.08]	0.93	[0.82, 1.01]	-
$\nu_{\beta,lo}$ [a]	0.70	[0.68, 0.77]	0.48	[0.44, 0.56]	kg/kg
ΔH_{lo}	9.7	-	15.5	-	MJ/kg
$\lg A_{\beta o}$	7.64	[6.89, 8.2]	17.8	[17.0, 21.0]	$\lg(s^{-1})$
$E_{\beta o}$	120	[110, 127]	231	[203, 269]	kJ/mol
$n_{\beta o}$	1.25	[1.08, 1.45]	3.58	[3.53, 4.64]	-
$n_{O_2,\beta o}$	0.89	[0.74, 0.95]	0.87	[0.53, 0.87]	-
$\nu_{a,\beta o}$	0.04	[0.03, 0.04]	0.67	[0.59, 0.75]	-
$\Delta H_{\beta o}$	28.8	-	9.8	-	MJ/kg
$\lg A_{\alpha o}$	12.2	[10.6, 12.8]	19.0	[15.3, 19.9]	$\lg(s^{-1})$
$E_{\alpha o}$	177	[159, 186]	243	[202, 253]	kJ/mol
$n_{\alpha o}$	0.93	[0.75, 0.99]	1.59	[1.26, 1.82]	-
$n_{O_2,\alpha o}$	0.52	[0.50, 0.64]	0.92	[0.87, 1.04]	-
$\nu_{a,\alpha o}$	0.08	[0.07, 0.08]	0.59	[0.57, 0.64]	kg/kg
$\Delta H_{\alpha o}$	27.8	-	12.4	-	MJ/kg

a. Calculated from Eq. (4.12).

Chapter 5

Interactions of Atmospheric Oxygen and Fuel Moisture in Smouldering Wildfires

Summary [1]

Vegetation, wildfire and atmospheric oxygen on Earth have changed throughout geological times, and are dependent to each other, determining the evolution of ecosystems, the carbon cycle, and the climate, as found in the fossil record. Previous work in the literature has only studied flaming wildfires, but smouldering is the most persistent type of fire phenomena, consuming large amounts of soil biomass and burning for very long periods of time (years or centuries). In this study, the dependence of smouldering fires in peatlands, the largest and longest wildfires on Earth, with atmospheric oxygen is investigated. A novel physics-based computational model of reactive porous media is developed which previously validated against experiments. Simulations are conducted for different values of atmospheric oxygen concentration and fuel moisture content to find thresholds for ignition and extinction. The predicted rate of spread increases in oxygen-richer atmospheres, while decreasing over wetter fuels. A novel nonlinear relationship between critical oxygen and moisture is reported. More importantly, compared to flaming fires in the literature, smouldering fires can be ignited and sustained at a substantially higher moisture content ($> 100\%$), and at a substantially lower oxygen concentration ($\sim 12\%$). This defines lower oxygen thresholds to help explain the char remains and historical fire activities seen in the fossil record.

1. This chapter is based on "X. Huang, G. Rein (2016) *Interactions of Atmospheric Oxygen and Fuel Moisture in Smouldering Wildfires*, **Science of the Total Environment** (under minor revision)."

5.1 Introduction

Vegetation, wildfire and atmospheric oxygen on Earth have changed throughout geological times [1, 2], and are dependent to each other, determining the evolution of ecosystems, the carbon cycle, and the climate, as found in the fossil record [3–5]. Increasing the oxygen concentration (X_{O_2}, percentage by volume) above the present-day level of 21%, the ignition probability of vegetation on the land surface becomes higher, and mega-fires can consume biomass of all ecosystems on a global scale in most ecosystems [2, 6]. Several studies have investigated the influence of atmospheric oxygen on the flammability of Earth ecosystems [3, 4, 7, 8]. Most of these studies considered flaming wildfires, and their results suggested that below a critical X_{O_2} of 12-16%, fire activity will be suppressed or entirely switched off. Compared to flaming, smouldering wildfires are the most persistent type of fire phenomena on Earth, consuming large amounts of soil biomass and burning for very long periods of time (years or centuries) [9]. However, the interdependence of atmospheric oxygen and fuel moisture on smouldering wildfire has not yet been well studied.

Smouldering combustion is the slow, low-temperature, flameless burning of porous fuels and the most persistent type of combustion, different from flaming combustion [9, 10]. Smouldering is the dominant phenomena in megafires in natural deposits of peat which are the largest and longest burning fires on Earth. Compared to flaming fires, smouldering fires can be initiated by much weaker ignition sources, and are much more difficult to suppress despite of extensive rains and climate changes [9]. Therefore, understanding the dependence of smouldering wildfires with atmospheric oxygen is crucial to estimate the burning threshold of Earth's vegetation throughout geological times. In the literature [3, 7, 8], two critical oxygen values have been studied for flaming fires: (1) critical oxygen for ignition, below which fire cannot be initiated by an ignition source, and (2) critical oxygen for fire spread (or extinction), below which an existing fire cannot be sustained or extinction occurs. So far, such critical oxygen values have not been well studied for smouldering wildfires.

For wildfires, similar critical values have also been found for fuel moisture [8, 11–14]. Therefore, atmospheric oxygen and fuel moisture are two of the most crucial factors governing the ignition and spread of wildfires throughout Earth's history, more important than other properties like mineral content, chemical composition, and bulk density. Organic soils like peat are porous and have a higher carbon content, thus they are prone to smouldering, and are able to hold a wider range of moisture contents [2] (MC), ranging from about 10% under drought conditions to well in excess of 300% under flooded conditions [9, 13]. Similar to flaming fires, the fuel moisture represents a significant energy sink to prevent smouldering fires.

2. Moisture content (MC) is defined in dry basis as the mass of water divided by the mass of a dried soil sample, expressed as %.

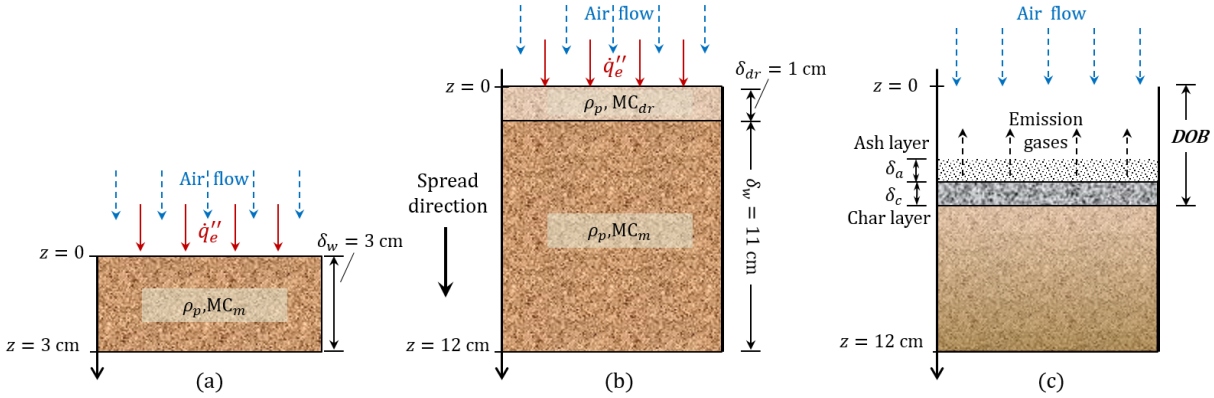

Figure 5.1: Diagrams of computational domain for (a) igniting a 3-cm thick peat sample, (b) fire spread over a 12-cm thick peat column, and (c) burning peat during smouldering spread with the associated depth of burn (DOB) .

Watson and Lovelock [8] experimentally studied the probability of flaming ignition and rate of flaming spread of cellulosic paper with varying MC and oxygen concentration. Their results showed that there could be a linear correlation between MC and oxygen concentration for the spread of flaming fires, and the rate of fire spread as well as the probability of ignition increased with oxygen concentration while decreased with MC. Several studies have investigated the critical MC under current atmosphere ($X_{O_2} \sim 21\%$) for smouldering peat fires through both experimental [11–13] and computational approaches (Chapters 2 and 3). Their results confirmed that under a fixed atmosphere, MC dominated the fire dynamics in smouldering wildfires, and different critical MCs existed for ignition (MC^*_{ig}) and extinction (MC^*_{ex}) . Some other studies looked into the influence of oxygen on smouldering fuels with fixed MC [4, 15, 16]. Belcher et al. [4] found that the smouldering fire could not be sustained for relatively dry moss peat below a critical X_{O_2} of 16%. Hadden et al. [15] found that oven-dried moss peat (MC $\leq$10%) could be ignited by an irradiation of 20 kW/m^2 for 1 minute under a X_{O_2} as low as 11%. So far, there is no study, especially no computational study, available in the literature investigating the interaction of atmospheric oxygen and fuel moisture on smouldering wildfires.

In this chapter, a model of smouldering is developed to simulate peat fires under varying oxygen concentration and moisture content. The critical oxygen concentration and MC for smouldering wildfire are found, which will help explain the char remains and historical fire activities seen in the fossil record.

5.2 Computational model

In order to find the critical oxygen concentration ($X^*_{O_2}$) to ignite Earth biomass and sustain the fire spread, Watson and Lovelock [8, 17] had conducted a series of pioneering experiments with paper as fuel under various oxygen concentration and MC. For their experiments of flaming ignition, the paper tape was enclosed inside a volume of bell jar

and subject to the application of an energetic electric discharge (7.5 kV and 0.12 A). The critical duration of discharge (minimum ignition energy) for ignition was measured for various combination of oxygen concentration and MC.

For their experiments of flame spread and extinction, thin shredded paper of ∼2.5 mm wide and MC from 0 to 150% was laid out in a stainless-steel wire mesh (5 cm wide, 2 cm deep, and 12 cm long), and was placed inside a bell jar, flushed by air enriched in oxygen or nitrogen. The ignition was achieved by a miniature methane gas burner directly (regular ignition) or by the ignited dry paper (high ignition). The critical oxygen concentration and MC to suppress flame spread and the spread rate were found [8]. Based on these experiments, they proposed a linear correlation, $\mathrm{MC}^* = 8X^*_{O_2} - 128$, for Earth's wildfire threshold. However, so far no related research, either experimental and computational, has been conducted to study the critical oxygen concentration and MC for smouldering wildfires, the most resistant type of fire.

5.2.1 Modelling setup

In order to extend the critical atmospheric oxygen to the domain of smouldering wildfire, both the smouldering ignition and spread of peat fire are modelled in a one-dimensional (1D) domain. For ignition, a homogeneous 3-cm thick peat sample is modelled, similar to the bench-scale experiment in [15]. This small sample is heated by a constant and strong external irradiation (30 $\mathrm{kW/m^2}$), and the heating duration is varied to find the critical value for successful ignition under various oxygen concentration and peat MC. For fire spread, a heterogenous 12-cm thick peat sample is used with 1-cm dry peat on the top and 11-cm wet peat on the bottom. The dry fuel is used to guarantee a successful ignition, in agreement with the flaming spread experiment of [8].

Previously, through a 1D model, the influence of varying MC on smouldering peat fires had been studied at the fixed atmosphere ($X_{O_2} \approx 21\%$) in Chapters 2 and 3. In addition, the influence of varying oxygen concentration on smouldering peat fires had been studied with fixed MC (dry peat at MC $\approx 10\%$) in Chapter 4. This 1D model, established in the open-source code Gpyro, is also adopted for this study, and the details of Gpyro can be found in [18]. The proposed model solves transient equations for both the condensed and gas phases. The governing equations include Eq. (5.1) for condensed-phase mass conservation, Eq. (5.5) for condensed-phase species conservation (assuming thermal equilibrium with the gas phase), Eq. (5.3) for condensed-phase energy conservation, Eq. (5.4) for gas-phase mass conservation, Eq. (5.5) for gas-phase species conservation and

Eq. (5.6) for gas-phase momentum conservation (Darcys law):

$$\frac{\partial \overline{\rho}}{\partial t} = -\dot{\omega}_{fg}^{'''} \tag{5.1}$$

$$\frac{\partial \left(\overline{\rho} Y_i\right)}{\partial t} = \dot{\omega}_{fi}^{'''} - \dot{\omega}_{di}^{'''} \tag{5.2}$$

$$\frac{\partial(\overline{\rho}\overline{h})}{\partial t} + \frac{\partial \left(\dot{m}^{''} h_g\right)}{\partial z} = \frac{\partial}{\partial z}\left(\overline{k}\frac{\partial T}{\partial z}\right) + \sum_{k=1}^{K} \dot{\omega}_{di,k}^{'''} \Delta H_k \tag{5.3}$$

$$\frac{\partial \left(\rho_g \overline{\psi}\right)}{\partial t} + \frac{\partial \dot{m}^{''}}{\partial z} = \dot{\omega}_{fg}^{'''} \tag{5.4}$$

$$\frac{\partial \left(\rho_g \overline{\psi} Y_i\right)}{\partial t} + \frac{\partial(\dot{m}^{''} Y_j)}{\partial z} = -\frac{\partial}{\partial z}\left(\overline{\psi}\rho_g D \frac{\partial Y_j}{\partial z}\right) + \dot{\omega}_{fj}^{'''} - \dot{\omega}_{dj}^{'''} \tag{5.5}$$

$$\dot{m}^{''} = -\frac{\overline{K}}{\nu}\frac{\partial P}{\partial z} \qquad (P = \rho_g R_s T) \tag{5.6}$$

Each condensed-phase species is assumed to have constant and temperature-independent properties (e.g. bulk density, specific heat, and porosity). All gaseous species have unit Schmidt number, and equal diffusion coefficient and specific heat. The averaged properties in each cell are calculated by weighting the appropriate mass fraction or volume fraction.

At the top free surface ($z = 0$), an empirical convection coefficient h_c considers the effect of blowing using the Couette flow approximation with $h_{c,0} = 10$ W/m^2-K [18], which varies during the burning process. Also, surface reradiation ($\varepsilon = 0.95$) is considered in the energy conservation. The heat-mass transfer analogy is used, $h_{m,0} \approx 20$ g/m^2-s in the gas species conservation to ensure a good oxygen supply.

The environmental pressure and temperature are assumed to be 1 atm and 300 K. An constant external irradiation ($\dot{q}_e^{''}$) is applied as the ignition source. On the bottom boundary layer ($z = L$), a small heat loss is set, $h_{c,L} = 3$ W/m^2-K; and there is no gas mass flux $\dot{m}^{''} = 0$ kg/m^2-s, same as Chapter 2.

A fully implicit formulation is adopted for the solution of all equations, and more details about numerical solution methodology are reported in [18]. The sample height during spread is equal to the sum of the heights of each cell, $H_t = \sum_{n=1}^{N} \Delta z_n$, which depends on the mass conservation and density. Simulations were run with an initial cell size of $\Delta z = 0.1$ mm, and initial time step of 0.02 s. Reducing the cell size and time step by a factor of 2 gives little difference in results, so this discretisation is acceptable.

5.2.2 Chemical kinetics

The general heterogeneous reaction, k, in the mass basis is written as

$$A_k + \sum_{j=1}^{N} \nu_{j,k}^{'} \text{gas } j \rightarrow \nu_{B,k} B_k + \sum_{j=1}^{N} \nu_{j,k}^{''} \text{gas } j. \tag{5.7}$$

For a small cell of a uniform temperature of T, the non-dimensional conversion rate ($\dot{\omega}_k^*$) from species A to B can be expressed by the Arrhenius law as

$$\dot{\omega}_k^* = Z_k e^{-E_k/RT} f\left(m_A^*\right) g\left(Y_{O_2}\right), \tag{5.8}$$

where Z_k and E_k are the pre-exponential factor and the activation energy, respectively.

Here, $f(m_A^*)$ and $g(Y_{O_2})$ are the reaction model for the reactant A and oxygen:

$$f\left(m_A^*\right) = \left(m_A^*\right)^{n_k} = \left(\frac{m_A}{m_{sA,0}}\right)^{n_k} \tag{5.9}$$

$$g(Y_{O_2}) = \begin{cases} 1 & \text{(inert atmosphere)} \\ \left(1 + Y_{O_2}\right)^{n_{O_2,k}} - 1 & \text{(oxidative atmosphere)} \end{cases} \tag{5.10}$$

where n_k and $n_{O_2,k}$ are the order of reaction and oxygen, respectively.

Both $\dot{\omega}_k^*$ and m_A^* are normalized to a characteristic mass of the cell, $m_A^* = m_A/m_{sA,0}$, where the subscript "$sA, 0$" represents the initial mass of source species for A, discussed in Chapter 4. Therefore, the (dimensional) destruction rate of A, formation rate of B, and corresponding heat of reaction in the reaction k are $\dot{\omega}_{dA_k} = \dot{\omega}_k^* m_{sA,0}$, $\dot{\omega}_{fB_k} = \dot{\omega}_k^* \nu_{B,k} m_{sA,0}$, and $\dot{Q}_k = \dot{\omega}_{dA_k} \Delta H_k$ where subscripts "d" and "f" represent the destruction and the formation, and ΔH_k is the heat of reaction.

In Chapters 1 and 4, the decomposition schemes of different complexities were investigated using thermogravity (TG) data of six different peat samples from Scotland, Siberia, Ireland, and China. The best kinetics scheme was found to be 5-step: (1) Drying (dr), (2) Peat pyrolysis (pp), (3) Peat oxidation (po), (4) β-Char oxidation (βo), and (5) α-Char oxidation (αo) as

$$\begin{cases} \text{Peat} \cdot \nu_{w,dr}\text{H}_2\text{O} \rightarrow \text{Peat} + \nu_{w,dr}\text{H}_2\text{O(g)} & (dr) \\ \text{Peat} \rightarrow \nu_{\alpha,pp}\alpha\text{-Char} + \nu_{g,pp}\text{Gas} & (pp) \\ \text{Peat} + \nu_{O_2,po}\text{O}_2 \rightarrow \nu_{\beta,po}\beta\text{-Char} + \nu_{g,po}\text{Gas} & (po) \\ \beta\text{-Char} + \nu_{O_2,\beta o}\text{O}_2 \rightarrow \nu_{a,\beta o}\text{Ash} + \nu_{g,\beta o}\text{Gas} & (\beta o) \\ \alpha\text{-Char} + \nu_{O_2,\alpha o}\text{O}_2 \rightarrow \nu_{a,\alpha o}\text{Ash} + \nu_{g,\alpha o}\text{Gas} & (\alpha o) \end{cases} \tag{5.11}$$

where subscripts w, p, α, β, and a represent five condensed species (water, peat, α-char, β-char, and ash), in addition to four gaseous species: oxygen, nitrogen, water vapour, and emission gases.

5.2.3 Parameter selection

The solid ($\psi_i = 0$) thermo-physical properties, $\rho_{s,i}$, $k_{s,i}$, c_i of peat, char, and ash are selected from [19]. The porosity is calculated from the bulk and solid densities (ρ_i & $\rho_{s,i}$) as

$$\psi_i = 1 - \frac{\rho_i}{\rho_{s,i}} \tag{5.12}$$

where the bulk densities of all species for this moss peat were measured in [15], all listed in Table 5.1.

Table 5.1: The physical parameters of condensed-phase species where $\rho_{s,i}$, $k_{s,i}$, and c_i are from [19], and $\rho_{i,0}$ is from [15].

Species (i)	$\rho_{s,i}$ (kg/m^3)	$\rho_{i,0}$ (kg/m^3)	$\psi_{i,0}$ (-)	$k_{s,i}$ (W/m-K)	c_i (J/kg-K)
water	1000	1000	0	0.6	4186
peat	1500	200 [a]	0.867	1.0	1840
α-char	1300	185	0.962	0.26	1260
β-char	1300	185	0.962	0.26	1260
ash	2500	35	0.997	1.2	1380

a. Bulk density of oven-dried peat (MC = 10%) is 200(1+MC) = 220 kg/m^3.

The effective thermal conductivity includes the radiation heat transfer across pores as

$$k_i = k_{s,i}(1 - \psi_i) + \gamma_i \sigma T^3 \tag{5.13}$$

where $\gamma_i = 10^{-4} \sim 10^{-3}$ m, dependent on pore size as $\gamma_i \approx 3d_{p,i}$ [20]. The average pore size relates to the particle surface area as $d_{p,i} = 1/S_i\rho_i$ where $S_p = S_c = 0.05$ m^2/g and $S_a = 0.2$ m^2/g [21]. The absolute permeability of soil can be estimated from an empirical expression [22]

$$K_i = 10^{-3} d_{p,i}^2 \sim 1/\rho_i^2 \tag{5.14}$$

which varies from 10^{-12} to 10^{-9} m^2, and decreases with the bulk density.

Because of a high porosity ($\psi_p = 0.867$) and the low volumetric water content, water is assumed to stay in the pores of peat without volume expansion. Thus, the wet peat bulk density is calculated as $\rho = (1 + \text{MC})\rho_p$. The properties of α-char and β-char are assumed to be the same.

The kinetic parameters of a low-mineral (IC $\approx 2\%$) moss peat sample from Ireland, found in Chapter 4, is selected for a case study, listed in Table 5.2. This same moss peat has been used for bench-scale smouldering experiments in [4, 15] and Chapter 6. The heat of pyrolysis chooses $\Delta H_{pp} = -0.5$ MJ/kg (endothermic); the heat of oxidation is assumed to relate to the oxidized organic matter, assumed as $\Delta H_k = \Delta H_{O_2}(1 - \nu_{B,k})$. According to the DSC analysis of multiple peat samples in [23], $\Delta H_{O_2} = 30$ MJ/kg is estimated for this low-mineral moss peat. The oxygen consumption is related to the heat of oxidation as $\nu_{O_2,k} = \Delta H_k/(13.1$ MJ/kg) [24].

Table 5.2: Reaction parameters and gaseous yields of 5-step reactions for the Irish peat sample (see Chapter 4).

Parameter/k	dr	pp	po	βo	αo
$\lg A_k$ ($\lg(s^{-1})$)	6.91	8.18	16.8	7.38	13.3
E_k (kJ/mol)	58.7	112	195	117	172
n_k (-)	2.37	5.31	2.33	1.32	2.58
n_{k,O_2} (-)	-	-	0.24	0.52	0.86
$\nu_{B,k}$ (kg/kg)	0	0.28	0.61	0.04	0.07
ΔH_k (MJ/kg)	2.26	0.5	-11.6	-28.9	-27.8
$\nu_{O_2,k}$ (kg/kg)	0	0	0.89	2.21	2.12

5.3 Ignition of smouldering

For igniting this 3-cm peat sample (Fig. 5.1a), the successful ignition is defined as: after heating, the smouldering front is formed, consuming all organic matter. Figure 5.2 shows the predicted evolution of the temperature profile for an unsuccessful ignition and a successful ignition with the same peat MC = 80% and oxygen concentration of X_{O_2} = 28%. For the no-ignition case (external heating time t_{ig} = 72 s), at the end of heating the peak temperature reaches just 310 °C which is not high enough to form a

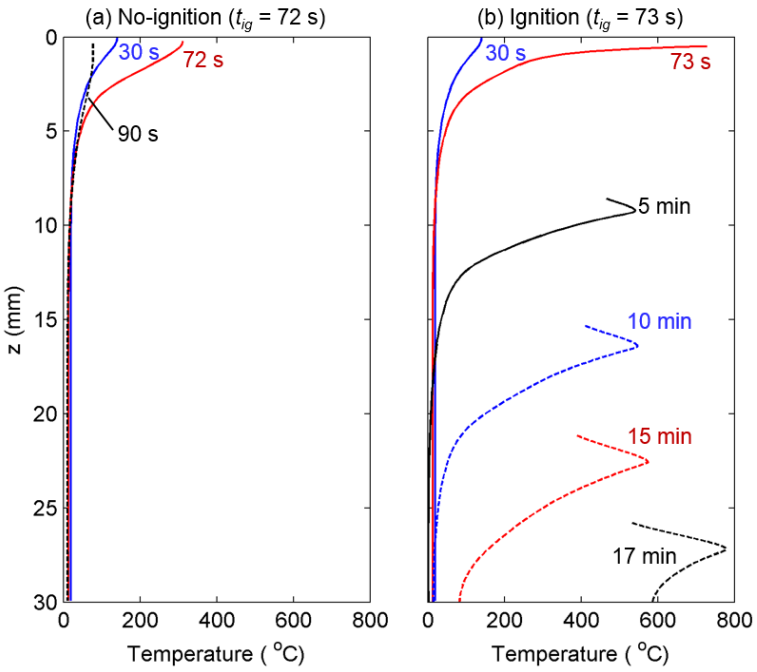

Figure 5.2: The predicted evolution of temperature profile in the case of (a) no-ignition (t_{ig} = 72 s), and (b) ignition (t_{ig} = 73 s), where peat moisture content is MC = 80%, and oxygen concentration is X_{O_2} = 28%.

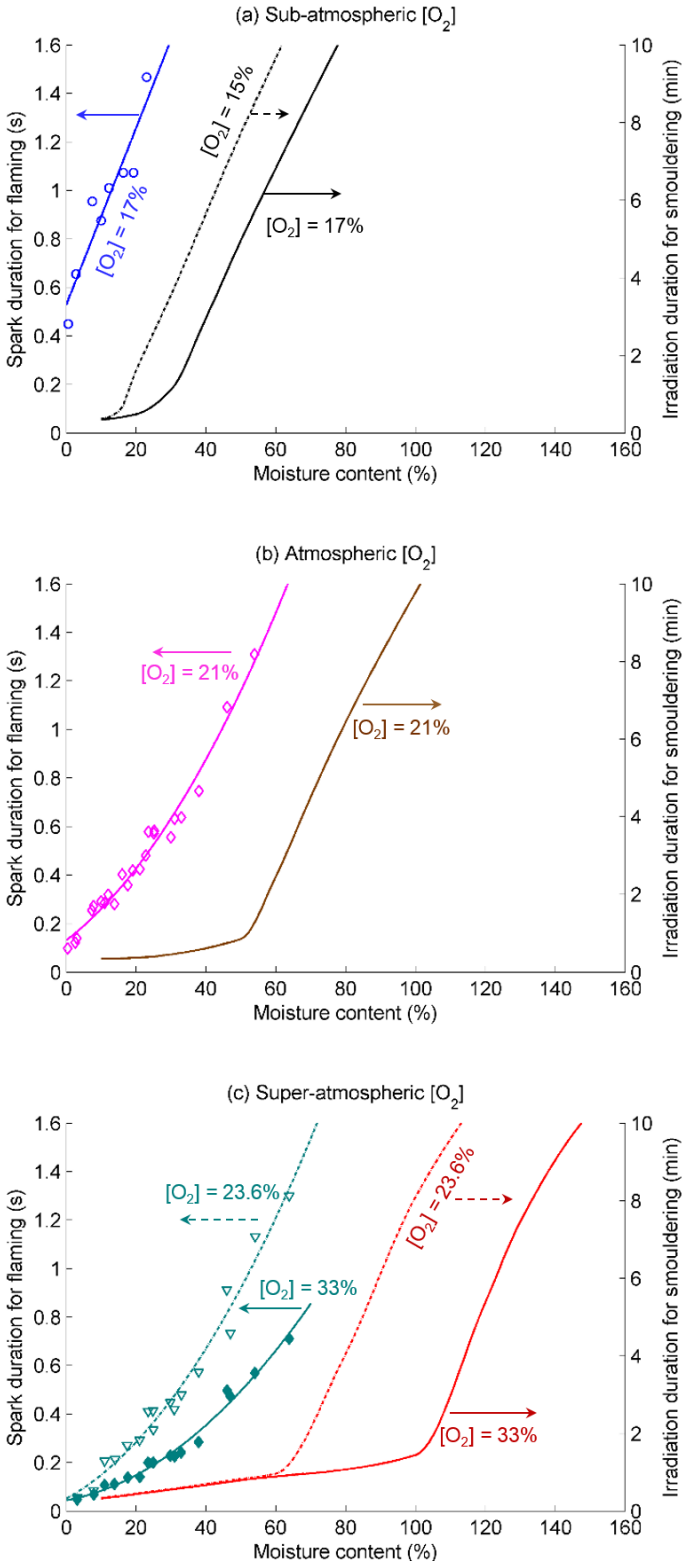

Figure 5.3: Comparison of critical ignition time versus fuel moisture between spark ignition for paper flaming experiments of [8] (points and fitting curves) and infrared irradiation for peat smouldering by current simulations (curves) at (a) sub-atmospheric $X_{O_2} < 21\%$, (b) atmospheric $X_{O_2} = 21\%$, and (c) super-atmospheric $X_{O_2} > 21\%$. Note that time scales are different for flaming and smouldering.

smouldering front. Afterwards, the temperature profile quickly decreases to the room temperature. For the ignition case (external heating time t_{ig} = 73 s), at the end of heating the peak temperature exceeds 600°C, high enough to generate a smouldering front [9, 12]. Afterwards, smouldering consumes all the fuel within 20 min, showing a clear difference to the no-ignition case.

Figure 5.3 shows the predicted heating duration versus fuel moisture for smouldering, compared with the spark ignition of flaming [8]. As expected, in order to ignite a wetter fuel or at a lower-oxygen atmosphere, a longer heating duration is required for both flaming and smouldering. The comparison shows that under the same atmospheric oxygen, smouldering can be initiated in a fuel of MC > 100%, substantially higher than flaming. More importantly, smouldering can be ignited in a low oxygen environment where flaming ignition is not possible. For example, dry paper was found not to flame in $X_{O_2} < 17\%$, while peat with MC = 30% and 10% can still be ignited at $X_{O_2} = 15\%$ and 13%, respectively. These predictions agree with the experiments by [15], where dry peat (MC ≈ 10%) can be ignited at $X_{O_2} = 13\%$ under a 1-min heating. Therefore, compared to flaming fires, smouldering fires have a much lower threshold in a lower oxygen atmosphere and in a more humid environment.

It is also found that for both flaming and smouldering ignition, the required heating duration increases greater than a fixed linear correlation with MC. Modelling results show that as peat MC increases up to a transition point, the required heating duration increases significantly, and the MC^*_{ig} at the transition point also increases with oxygen concentration. For this new region with relatively high MC^*, if the heating duration is slightly below the curve, a smouldering front can be formed and spread for a small distance, rather than a sudden extinction as Fig. 5.3(a). Such transient smouldering spread becomes sensitive to the sample thickness and bottom boundary condition. On the other hand, once a smouldering front is generated, the effectiveness of external heating is found to be weak, also shown in the experiment of [15]. Therefore, the critical moisture there is for fire spread (or extinction) as MC^*_{ex} (introduced in Chapter 3), which will be further discussed and compared with MC^*_{ig} in the following section.

5.4 Spread and extinction of smouldering wildfires

For the 12-cm thick peat sample, a strong ignition protocol, 30 kW/m^2 for 3 min, is selected in all cases to ensure the ignition of top 1-cm dried peat layer (MC = 10%). It can be seen in Fig. 5.4, after 3 min irradiation, the temperature profile exceeds 600 °C, similar to Fig. 5.2b, showing smouldering ignition is successful. Afterwards, if the atmospheric oxygen is too low or the 11-cm bottom layer is too wet, smouldering spread cannot be sustained, and fire extinguishes after spreading for a short distance (Fig. 5.4a), different from the sudden cooling in no-ignition case (Fig. 5.2a). Otherwise, smouldering will spread along the wet peat layer up to the end of the sample (Fig. 5.4b). Therefore,

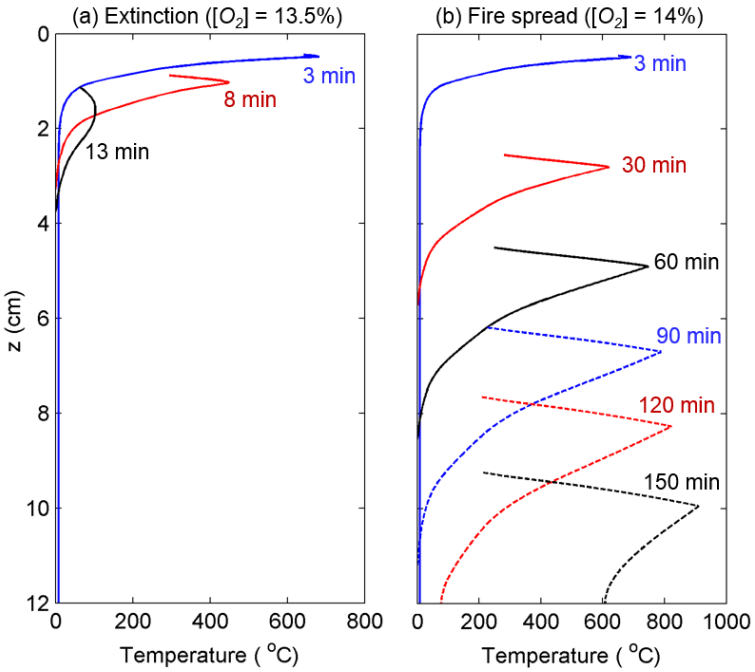

Figure 5.4: The predicted temperature-profile evolution in the case of (a) extinction ($X_{O_2} = 13.5\%$), and (b) fire spread ($X_{O_2} = 14\%$), where wet bottom peat moisture content is MC = 40%.

the critical peat moisture (MC^*_{ex}) and oxygen concentration ($X^*_{O_2}$) for extinction are determined just before the fire cannot consume the whole peat sample.

For in-depth fire spread, the spread rate is not a constant, but monotonically decreases with the depth due to decreasing oxygen supply from the free surface, as shown in Fig. 3.3 of Chapter 3. Therefore, for an easy comparison, the average fire spread rate between 3 and 6 cm deep, in which the spread rate does not vary much, is selected as the characteristic fire spread rate. Figure 5.5 shows the predicted characteristic spread rate for smouldering as a function of oxygen concentration and MC, where the interaction between oxygen concentration and MC is manifested. A combination of critical conditions ($X^*_{O_2}$ vs. MC*) defines a critical curve for smouldering spread, similar to flaming fire in [8]. Outside the critical curve, fire spread cannot be sustained, and the fire spread rate quickly drops to zero from about 0.5 mm/min. The modelled spread rate of smouldering peat fire is on the order of 1 mm/min, similar to experimental measurements in Chapter 6, and is at least 2 orders of magnitude slower than flaming fires [25].

Figure 5.6 shows critical moisture content (MC*) vs. critical oxygen concentration ($X^*_{O_2}$) found in current simulations, compared with those found in experiments of flaming paper fires [8] and smouldering peat fires [4, 15]. For modelling smouldering ignition, a fixed ignition protocol (30 kW/m^2 for 90 s) is selected. Clearly, for both flaming and smouldering, MC* increases with $X^*_{O_2}$, indicating that fire risk increases significantly in an oxygen-enriched environment.

Each of the smouldering ignition experiment in [15] and smouldering spread exper-

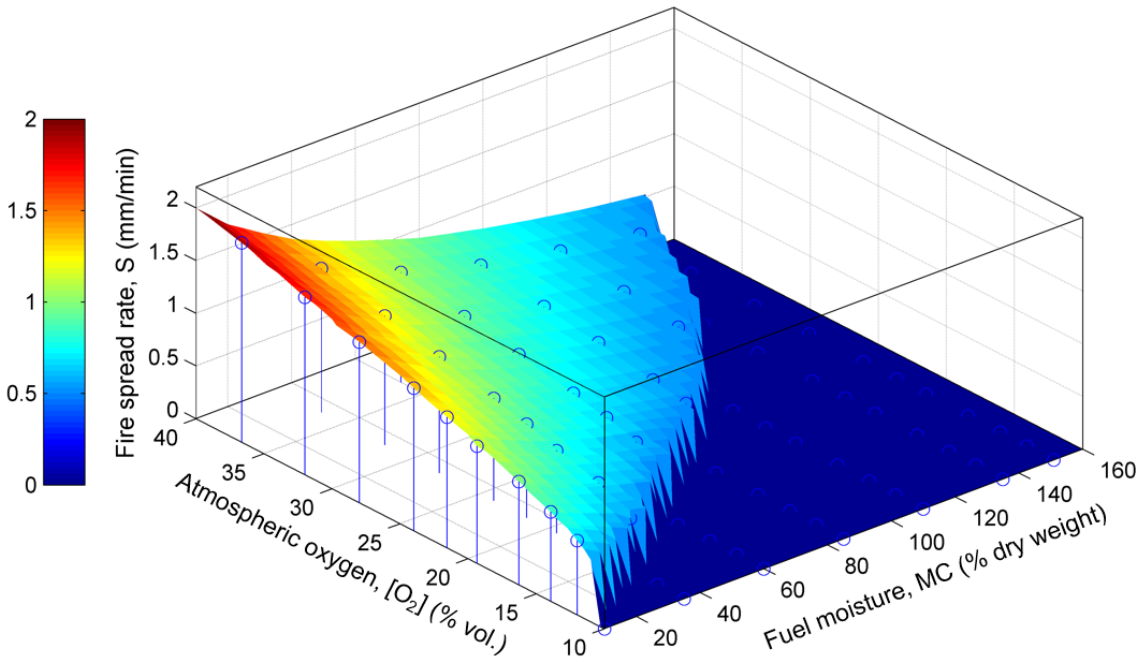

Figure 5.5: Fire spread rate as a function of atmospheric oxygen concentration (X_{O_2}) and fuel moisture content (MC). The color also helps visually indicate the rate of smouldering spread, which increases from blue to red.

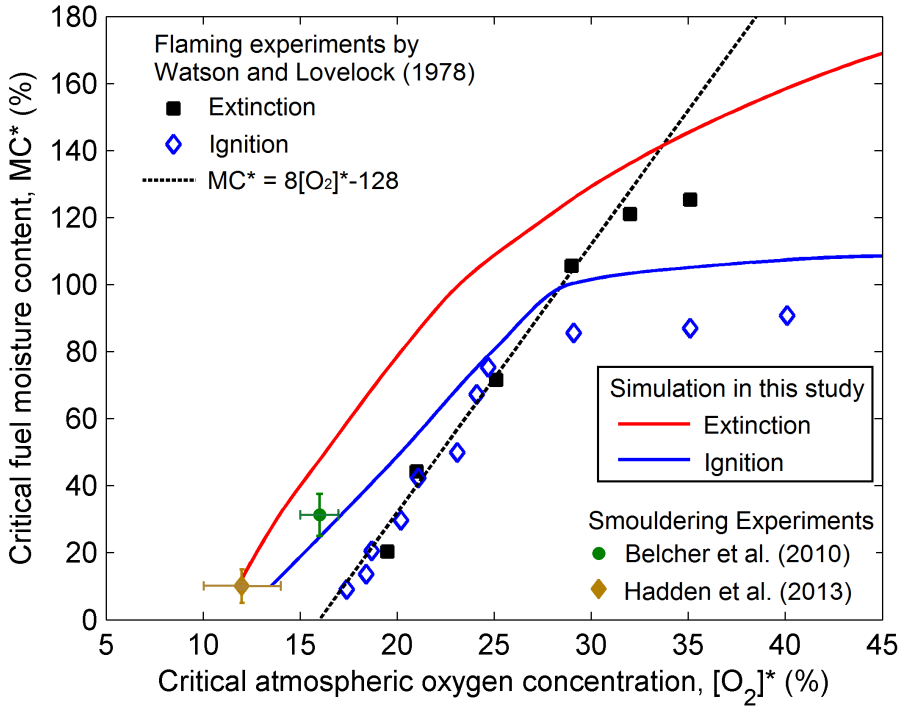

Figure 5.6: Critical moisture content (MC*) vs. critical ambient oxygen concentration ($X^*_{O_2}$) found in experiments of flaming combustion on paper [8], experiments of smouldering combustion on peat [4, 15], and our predictions.

iment in [4] with fixed peat MC (relatively dry) provides one point [3] in Fig. 5.6. Note that these two experiments used the same moss peat, and physico-chemical parameters of this peat are input into the model. It can been seen that both points are within the model prediction, suggesting a high reliability of modelling results at least in the low MC range. It is also observed that for both flaming and smouldering, the MC^*_{ig} is lower than MC^*_{ex}, and their difference increases at high MC and X_{O_2}. Modelling results also show that for smouldering, the MC^*_{ig} curve beyond the transition point is sensitive to the ignition protocol and back boundary condition, while the initial linear part is not. More discussions on MC^*_{ig} and MC^*_{ex} can be found in Chapter 3.

More importantly, it is revealed that compared to flaming spread, smouldering spread can be sustained in a substantially lower oxygen concentration (X_{O_2} as low as 12%), and in a substantially higher MC ($> 100\%$). Therefore, it is the smouldering, rather than flaming, defining the lower fire threshold and upper vegetation-consumption limit in wildfires on Earth throughout geological times. In addition, at both high fuel moisture and atmospheric oxygen, there is a clear nonlinear correlation for fire threshold: the required oxygen concentration increases greater than the increase in MC. This nonlinear critical curve are observed in both flaming and flaming experiments. Therefore, the linear correlation, $MC^* = 8X^*_{O_2} - 128$, presented in [8] and re-plotted in Fig. 5.6, may become inappropriate for smouldering and for flaming at high MC and oxygen concentration.

5.5 Conclusions

In this study, fires on peatlands, the largest and most common smouldering wildfires, are investigated with a novel 1D model of a reactive porous media. The interdependence of atmospheric oxygen and fuel moisture on smouldering peat fires is investigated. Modelling results reveal a novel nonlinear correlation between the critical oxygen concentration and moisture content: as moisture content increases, a greater increase in oxygen concentration is required for both ignition and fire spread. More importantly, compared to flaming fires in the literature, smouldering fires can be ignited in a substantially higher fuel moisture content ($> 100\%$), and at a substantially lower oxygen concentration ($\sim 12\%$), defining a much lower wildfire threshold in Earth history.

For smouldering fires, it is also found that (1) the critical curve of MC^* and $X^*_{O_2}$ for extinction is higher than that for ignition; and (2) the rate of fire spread increases in oxygen-richer atmospheres, while decreasing over wetter fuels, both in agreement with flaming fires. The predicted spread rate of smouldering peat fire is on the order of 1 mm/min, much slower than flaming fires. This is the first time a sophisticated physics-based model is used to study interactions among atmospheric oxygen, fuel moisture and

3. For smouldering experiments in [4, 15], the uncertainty of peat MC is estimated from the bound water ($MC = 3 \sim 10\%$) remained after drying and the potential absorption of atmospheric moisture. The uncertainty in $X^*_{O_2}$ comes from various criteria to judge successful ignition or fire spread.

smouldering wildfires, and to compare with flaming fires. Thus, it helps understand the char remains and historical fire activities seen in the fossil record.

Acknowledgements

I would like to thank Dr Claire Belcher (University of Exeter) and Dr Rory Hadden (University of Edinburgh) for fruitful discussions on Earth oxygen and fires.

References

[1] J. Lovelock, *Gaia, a new look at life on earth*. Oxford paperbacks, Oxford University Press, 1979.

[2] T. M. Lenton and A. J. Watson, "Redfield revisited: 2. What regulates the oxygen content of the atmosphere?," *Global Biogeochemical Cycles*, vol. 14, no. 1, pp. 249–268, 2000.

[3] C. M. Belcher and J. C. McElwain, "Limits for Combustion in Low O_2 Redefine Paleoatmospheric Predictions for the Mesozoic," *Science*, vol. 321, no. 5893, pp. 1197–1200, 2008.

[4] C. M. Belcher, J. M. Yearsley, R. M. Hadden, J. C. McElwain, and G. Rein, "Baseline intrinsic flammability of Earths ecosystems estimated from paleoatmospheric oxygen over the past 350 million years," *Proceedings of the National Academy of Sciences*, vol. 107, no. 52, pp. 22448–22453, 2010.

[5] T. M. Lenton, "Fire Feedbacks on Atmospheric Oxygen," in *Fire Phenomena and the Earth System* (C. Belcher, ed.), pp. 289–308, John Wiley & Sons, 2013.

[6] J. E. Lovelock and J. P. Lodge, "Oxygen in the contemporary atmosphere," *Atmospheric Environment*, vol. 6, no. 8, pp. 575 – 578, 1972.

[7] R. A. Wildman, L. J. Hickey, M. B. Dickinson, R. A. Berner, J. M. Robinson, M. Dietrich, R. H. Essenhigh, and C. B. Wildman, "Burning of forest materials under late Paleozoic high atmospheric oxygen levels," *Geology*, vol. 32, no. 5, pp. 457–460, 2004.

[8] A. J. Watson and J. E. Lovelock, "The Dependence of Flame Spread and Probability of Ignition on Atmospheric Oxygen," in *Fire Phenomena and the Earth System* (C. Belcher, ed.), pp. 273–287, John Wiley & Sons, 2013.

[9] G. Rein, "Smouldering Fires and Natural Fuels," in *Fire Phenomena and the Earth System* (C. Belcher, ed.), ch. 2, pp. 15–33, Wiley and Sons, 2013.

[10] T. Ohlemiller, "Modeling of smoldering combustion propagation," *Progress in Energy and Combustion Science*, vol. 11, no. 4, pp. 277 – 310, 1985.

[11] W. H. Frandsen, "Ignition probability of organic soils," *Canadian Journal of Forest Research*, vol. 27, no. 9, pp. 1471–1477, 1997.

[12] G. Rein, N. Cleaver, C. Ashton, P. Pironi, and J. L. Torero, "The severity of smouldering peat fires and damage to the forest soil," *Catena*, vol. 74, no. 3, pp. 304 – 309, 2008.

[13] B. W. Benscoter, D. K. Thompson, J. M. Waddington, M. D. Flannigan, B. M. Wotton, W. J. de Groot, and M. R. Turetsky, "Interactive effects of vegetation, soil moisture and bulk density on depth of burning of thick organic soils," *International Journal of Wildland Fire*, vol. 20, pp. 418–429, 2011.

[14] A. C. Watts, "Organic soil combustion in cypress swamps: Moisture effects and landscape implications for carbon release," *Forest Ecology and Management*, vol. 294, pp. 178 – 187, 2013. The Mega-fire reality.

[15] R. M. Hadden, G. Rein, and C. M. Belcher, "Study of the competing chemical reactions in the initiation and spread of smouldering combustion in peat," *Proceedings of the Combustion Institute*, vol. 34, no. 2, pp. 2547 – 2553, 2013.

[16] D. Wu, X. Huang, F. Norman, F. Verplaetsen, J. Berghmans, and E. V. den Bulck, "Experimental investigation on the self-ignition behaviour of coal dust accumulations in oxy-fuel combustion system," *Fuel*, vol. 160, pp. 245 – 254, 2015.

[17] A. Watson, J. E. Lovelock, and L. Margulis, "Methanogenesis, fires and the regulation of atmospheric oxygen," *Biosystems*, vol. 10, no. 4, pp. 293 – 298, 1978.

[18] C. Lautenberger and C. Fernandez-Pello, "Generalized pyrolysis model for combustible solids," *Fire Safety Journal*, vol. 44, no. 6, pp. 819 – 839, 2009.

[19] R. Jacobsen, E. Lemmon, S. Penoncello, Z. Shan, and N. Wright, "Thermophysical Properties of Fluids and Materials," in *Heat Transfer Handbook* (A. Bejan and A. Kraus, eds.), ch. 2, pp. 43–159, John Wiley & Sons, 2003.

[20] F. Yu, G. Wei, X. Zhang, and K. Chen, "Two Effective Thermal Conductivity Models for Porous Media with Hollow Spherical Agglomerates," *International Journal of Thermophysics*, vol. 27, no. 1, pp. 293–303, 2006.

[21] H. de Jonge and M. C. Mittelmeijer-Hazeleger, "Adsorption of CO_2 and N_2 on Soil Organic Matter: Nature of Porosity, Surface Area, and Diffusion Mechanisms," *Environmental Science & Technology*, vol. 30, no. 2, pp. 408–413, 1996.

[22] B. Punmia and A. Jain, *Soil Mechanics and Foundations*. Laxmi Publications Pvt Limited, 2005.

[23] K. Bergner and C. Albano, "Thermal analysis of peat," *Analytical Chemistry*, vol. 65, no. 3, pp. 204–208, 1993.

[24] C. Huggett, "Estimation of rate of heat release by means of oxygen consumption measurements," *Fire and Materials*, vol. 4, no. 2, pp. 61–65, 1980.

[25] D. Drysdale, *An Introduction to Fire Dynamics*. Wiley, 2011.

Chapter 6

Experimental Study of the Formation and Collapse of an Overhang in the Lateral Spread of Smouldering Peat Fires

Summary [1]

Smouldering combustion is the driving phenomenon of wildfires in peatlands, and is responsible for large amounts of carbon emissions and haze episodes in Southeast Asia and Northeast Europe. Compared to flaming fires, smouldering is slow, low-temperature, flameless, and most persistent, yet it is poorly understood. Peat, as a typical organic soil, is a porous and charring natural fuel, thus prone to smouldering. The spread of smouldering peat fire is a multidimensional phenomenon, including two main components: in-depth vertical and surface spread. In this study, the lateral spread of peat fire under various moisture and wind conditions is explored. Visual and infrared cameras as well as a thermocouple array are used to measure the temperature profile and the spread rate. For the first time the overhang, where smouldering spreads fastest beneath the free surface, is observed in the laboratory, which helps understand the interaction between oxygen supply and heat losses. The periodic formation and collapse of overhangs is observed. The overhang thickness is found to increase with moisture and wind speed, while the spread rate decreases with moisture and increases with wind speed. A simple theoretical analysis is proposed and shows that the formation of overhang is caused by the spread rate difference between the top and lower peat layers as well as the competition between oxygen supply and heat losses.

1. This chapter is based on "X. Huang, F. Restuccia, M. Gramola, G. Rein (2015) *Experimental Study of the Formation and Collapse of an Overhang in the Lateral Spread of Smouldering Peat Fires*, **Combustion and Flame** (Accepted)."

6.1 Introduction

Smouldering wildfires in peatlands are the largest combustion phenomenon on Earth, and contribute considerably to annual greenhouse gas emissions [1]. Peatlands cover 2-3% of the Earth's land surface, and are most abundant in boreal and tropical regions. They are important ecosystems for a wide range of wildlife habitats supporting biological diversity, hydrological integrity and storing 25% of the world's soil carbon [2]. Annually, peat fires release large amounts of ancient carbon roughly equivalent to 15% of the man-made emissions [3, 4], and result in the widespread destruction of ecosystems and regional haze events, *e.g.* recent megafires in Southeast Asia, North America, and Northeast Europe [1, 3]. Moreover, climate change might dry peatlands and increase the extend and depth of smouldering fire, creating a positive feedback to the climate system [5].

Peat is an important organic soil. It is a porous and charring natural fuel, thus prone to smouldering [1, 6]. Smouldering combustion is the slow, low-temperature, flameless burning of porous fuels, and the most persistent type of combustion phenomena [6–8]. Smouldering involves heterogeneous reactions, and is sustained by the heat released when oxygen directly attacks the fuel surface. It is especially common in solid fuels like polymers, coal and organic soils with tendency to charring [6], differing from the high-temperature homogenous flaming combustion. Once ignited, natural smouldering fires can burn for very long periods of time (*e.g.* months and years) despite extensive rains, weather changes, or fire-fighting attempts [1].

Two mechanisms control the spread of smouldering combustion: oxygen supply and heat losses [6, 8]. Peat fires can be initiated by flaming fires, lightning strikes or embers. The probability of ignition depends on moisture content [2] (MC), inert content [2] (IC), and other chemico-physical properties, as discussed in Chapters 1-3. Afterwards, smouldering spreads laterally along the free surface and vertically in-depth, as shown in Fig. 6.1, both dominated by forward smouldering (see Chapter 1).

Compared to flaming wildfires, the fundamental chemistry and dynamics of smouldering wildfires are not as well understood, with only a limited number of studies found in the literature. Palmer [9] conducted a series of pioneering experiments on the smouldering combustion of dust and fibrous materials. Ohlemiller [10] studied the two-dimensional (2D) profiles for smouldering spread of dry wood fibres. Various thermal analysis at mg-scale [11, 12] has investigated the smouldering chemistry and found the existence of a multi-front (drying, pyrolysis and oxidation fronts) structure (see more discussions in Chapter 1). Frandsen [13] studied the ignition thresholds for various bench-scale soil samples, and found a correlation between critical MC and IC, verified computationally in Chapter 2. Hadden *et al.* performed a bench-scale peat experiment, and revealed

2. Moisture content (MC) is defined here in dry basis as the mass of water divided by the mass of a dried soil sample, expressed as %. Inorganic content (IC) is defined here in dry basis as the mass of soil inorganic matter (minerals) divided by the mass of a dried soil sample, expressed as %.

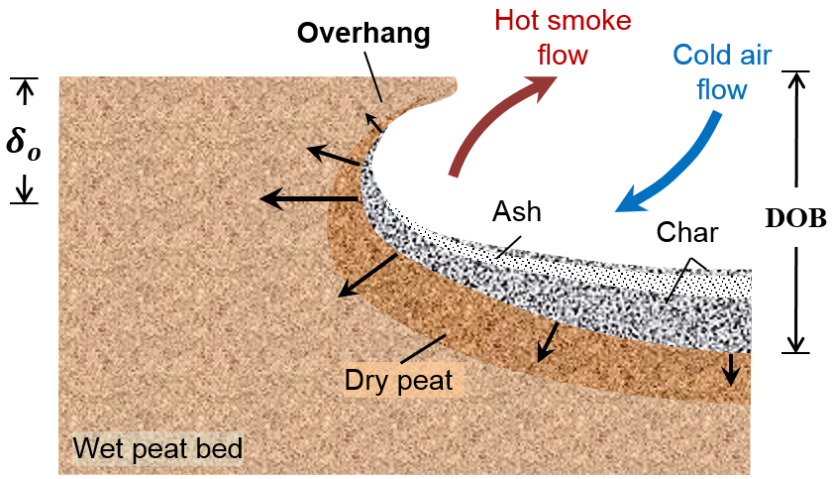

Figure 6.1: Schematic diagram of smouldering spread along the surface and in-depth with overhang and depth of burn (DOB).

the competing roles of the pyrolysis and oxidation reactions in the formation and consumption of char [14]. In actual field peat fires, smouldering has been found to consume peat up to depths in excess of several meters [3, 4, 15]. The depth of burn (DOB) and critical MC for extinction have been investigated experimentally [16–18] and numerically in Chapter 3. The lateral spread of the fire has been found not to spread on the free surface but at a depth below ("overhang" phenomenon, see Fig. 6.1) [19–21], which has not been well explained or studied until now.

In this chapter, lateral fire spread over bench-scale moss peat samples are investigated in the laboratory under different moisture and wind conditions. This experimental study focused on the lateral spread and the periodic formation and collapse of the overhang. The influence of MC and environmental wind are measured, and analyzed through a simple heat transfer model.

6.2 Experimental method

Figure 6.2(a) shows the schematic diagram of the experimental setup. A top-open reactor with internal dimensions of $20 \times 20 \times 10$ cm^3, and a 1.27 cm thick insulation board was used to contain the peat sample, similar to the design in [15, 22]. Additional experiments were conducted with a taller ($20 \times 20 \times 20$ cm^3) reactor. A 20-cm coil heater was buried in the sample attached to one side 5 cm below the top free surface, and used to initiate a uniform smouldering front spreading laterally and vertically. The ignition protocol was 100 W for 30 min [15], which is strong enough to initiate a smouldering spread with MC $< 150\%$. In order to study the influence of environmental wind, a small fan was used after ignition to generate forward wind along the direction of lateral fire spread. The average wind speed was measured by a hot-wire anemometer at multiple locations 1-cm above the peat free surface, and two wind speeds were used: 0.5 (low) and

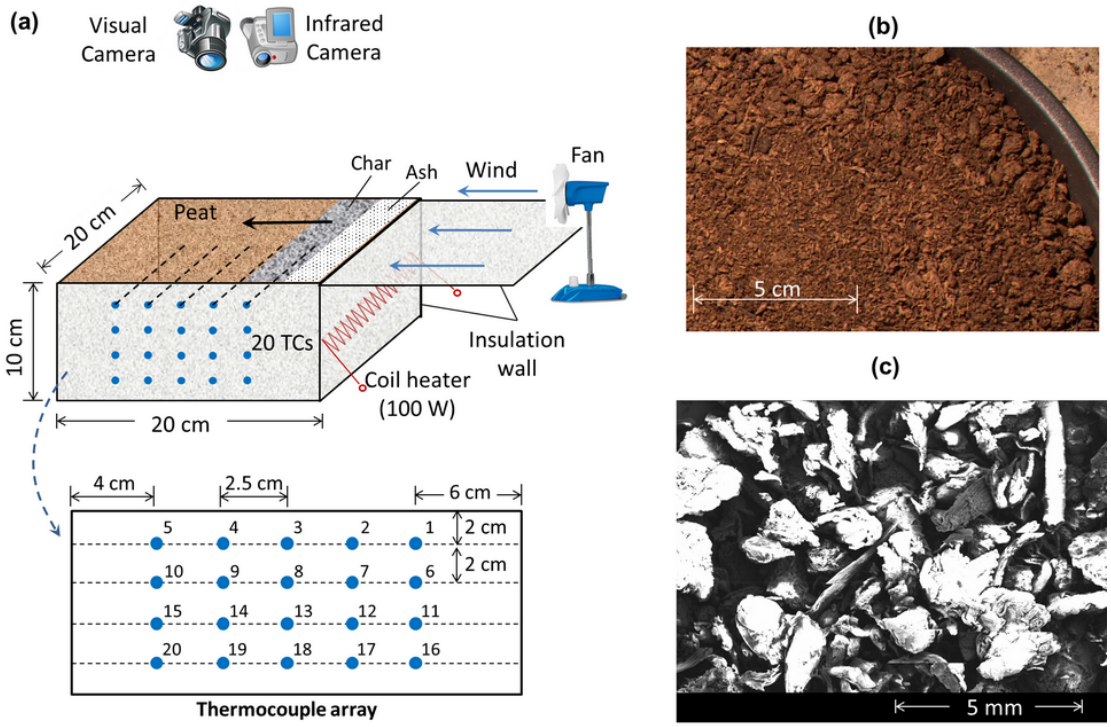

Figure 6.2: (a) Diagram of the experimental setup and the arrangement of thermocouples array; (b) visual image of peat sample; and (c) scanning electron microscopy imaging of peat particles.

1.2 (high) (±0.1) m/s.

The peat used in the experiment is a commercial Irish moss peat (Shamrock Irish Moss Peat, Bord na Mona Horticulture Ltd.), as shown in Fig. 6.2(b) and (c). It is used instead of naturally sourced peat because it is readily available in large quantities, has homogeneous properties and constant composition, and had been used in previous work [14, 22]. Peat samples have a dry density of 136 ±5 kg/m^3 and a low mineral content ($\sim$ 2%). The element analysis for the organic matter is 53.8/5.5/38.4/1.9/0.5 [% in mass] mass fraction for C/H/O/N/S, respectively.

In order to obtain a desired MC in peat samples, peat was first dried at 95 °C for 48 h [23], and then mixed with the corresponding amount of water. Then, sample was left to equilibrate inside a sealed container, without compression, for another 48 h. Once the dry peat comes in contact with air, it quickly absorbs the ambient moisture and reach an equilibrium with a MC of 5-10%, so studying completely dry peat with 0% MC is not possible. Targeted MCs for peat were 5%, 50%, 100%, 130%, and 150%. After mixing, the experimental uncertainty of the actual MC is ±5%. Figure 3 shows that the measured density of wet peat increases with MC, while the density of dry peat decreases with MC because of expansion with water addition.

Both a visual and an infrared (IR) imaging were captured above the sample to monitor the process on the top surface. A typical smouldering experiment in the $20 \times 20 \times 10$

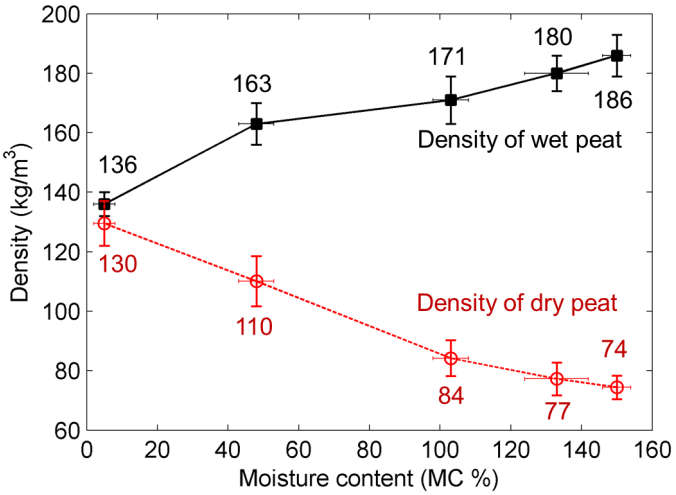

Figure 6.3: Density of wet peat (i.e. mass of peat and water/total volume) and density of dry peat (i.e. mass of peat/total volume) vs. moisture content (MC) with experimental uncertainty.

cm^3 reactor would last between 3 and 15 h, depending on the density, MC, and wind speed, so both cameras were set at a low capture frequency of one image per minute. 20 thermocouples (TCs) were placed as an array of 4 rows $\times$ 5 columns and inserted through one side into the central plane of the sample (10 cm away from the side wall) to measure the temperature evolution, as shown in Fig. 6.2(a). At least 3 experiments on spread rate measurement were conducted at each condition for repeatability. In some experiments, the mass loss of the sample was measured.

6.3 Experimental results

6.3.1 Imaging and overhangs

Figure 6.4 shows the visual and IR imaging for smouldering spread over peat samples with 50% and 100% MC. The IR camera was used to track the movement of the smouldering front (high emssion region) on the top surface. It can be seen in Fig. 6.4 that for MC = 50%, 4 h after ignition, the smouldering fire had spread laterally for 20 cm and reached the other side of the reactor. For MC = 100%, fire only spread for half of the distance (10 cm). As the MC increases, the lateral spread rate and the overall burning rate decreases significantly. MC is known to be the most important peat property to control the fire spread [1, 15].

For wet peat samples (MC $\geq$ 50%), overhang could be visually observed in experiments. The smouldering fire tended to spread at some depth (δ_o) below the top surface, as illustrated in Fig. 6.5(II). Peat within the overhang does not degrade into char, while, for peat below the overhang, charring and burning process are observed.

This overhang is unstable because as in-depth peat is burnt underneath, the produced

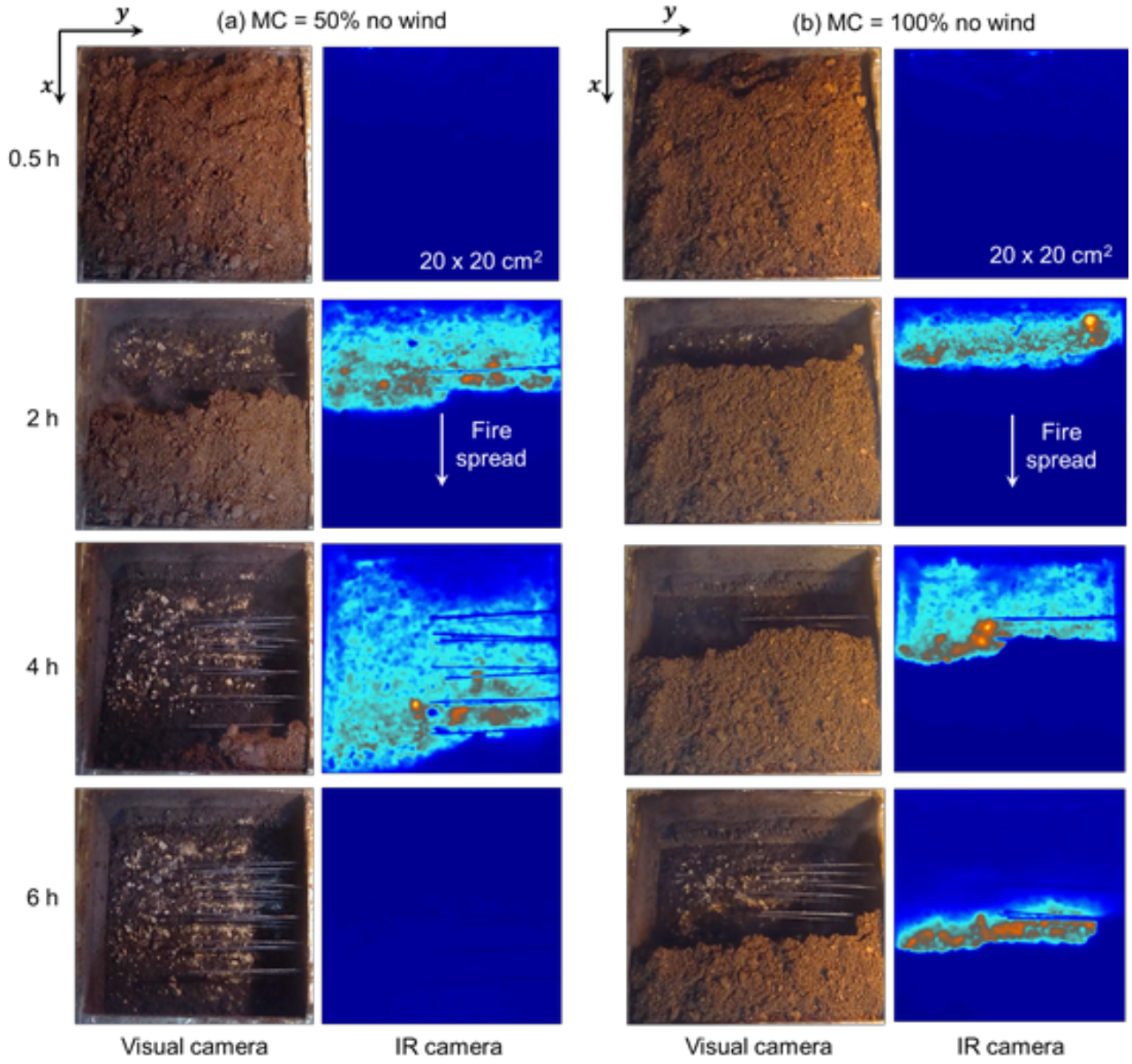

Figure 6.4: Imaging by visual and IR camera from the top view for smouldering fire spread in peat samples with (a) MC = 50% without wind, and (b) MC = 100% without wind. Time lapses at 0.5, 2, 4 and 6 h after ignition.

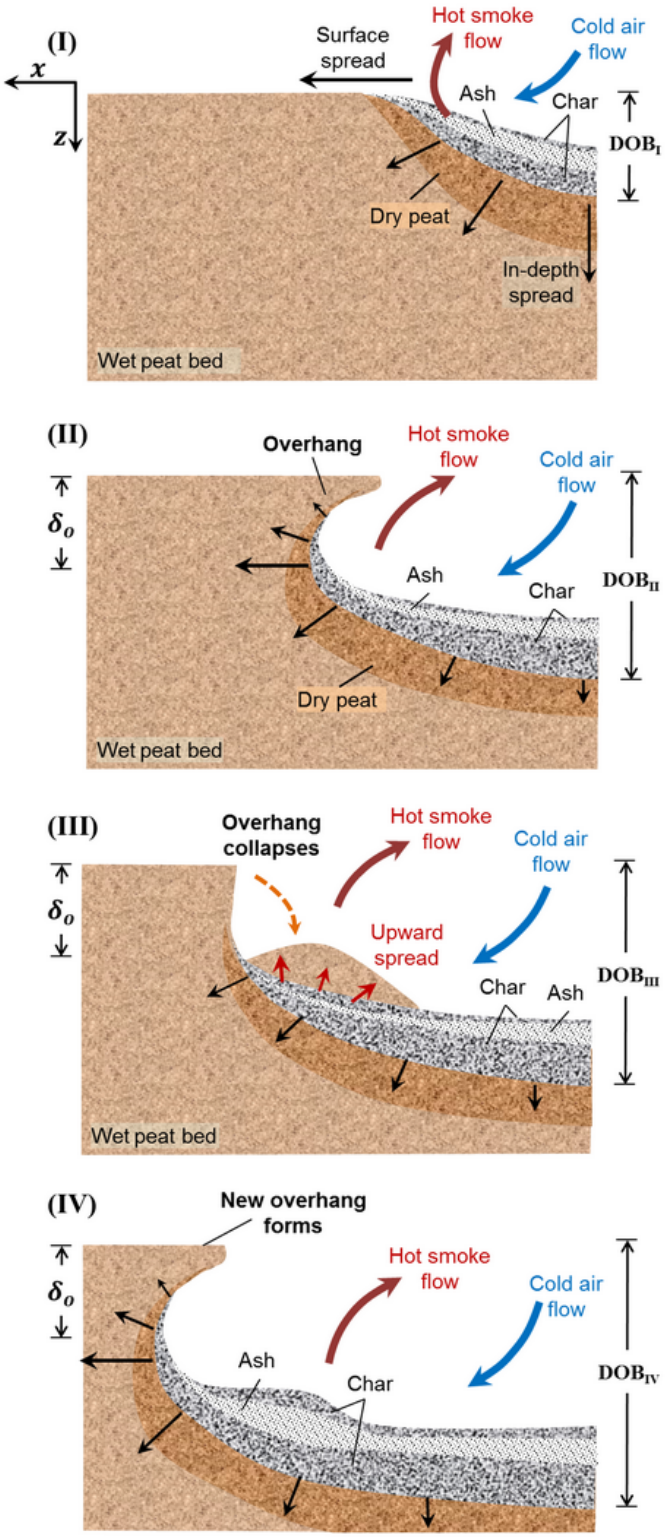

Figure 6.5: Schematic diagram for the periodic formation and collapse of overhang in smouldering spread over wet peat: (I) soon after ignition, (II) formation of the overhang, (III) collapse and consumption of the overhang, (IV) formation of a new overhang.

char and ash were not strong enough to support the peat above. Therefore, the overhang collapses. The collapsed overhang falls on the top of the burning char, as illustrated in Fig. 6.5(III), and then ignited and consumed. At the same time, fire continues to spread in-depth vertically, increasing the depth of burn (DOB), and laterally, generating a new overhang (Fig. 6.5(IV)). Therefore, a cycle of overhang formation and collapse is created until the entire peat bed is burnt.

6.3.2 Temperature profiles and overhang thickness

Figures 6.6 and 6.7 show a set of thermocouple measurements for 5%, 50%, and 100% MC without wind, and with wind of 1.2 m/s, respectively. Each subfigure shows the measurements of five thermocouples under the same depth (z = 2, 4, 6, 8 cm). For the dry peat (5% MC) in Fig. 6.6(a), all 20 thermocouples manifest negligible drying process below 100°C, as expected. It is found that as the depth increases from 2 to 8 cm, (i) the peak temperature increases from 500°C to 570°, and (ii) the burning duration significantly increases. This can be explained as the deeper layers are better insulated but have lower oxygen supply [1, 6].

For 50% MC in Fig. 6.6(b), there is a clear heating and drying process where it took several hours for each thermocouple to increase from room temperature to 100°C. Compared to 5% MC in Fig. 6.6(a), peak temperatures at z = 6 and 8 cm are similar, and they also increase with the depth. For the first row (2 cm depth), three thermocouples away from the ignition source ($x \geq 11$ cm) did not reach 200°C which is a typical temperature for the onset of peat pyrolysis (see TGA in Chapters 1 and 4). In other words, the pyrolysis front did not affect this shallow layer. Therefore, in addition to the visual observation, the temperature measurements also indicate the formation of the overhang. At 4 cm depth, the measured peak temperature ranges from 450 to 550°C, indicating a burning smouldering front. Therefore, the overhang thickness in this case is estimated as $\delta_o = 3 \pm 1$ cm for 50% MC. Moreover, the ignition and burning of the collapsed overhang were seen by multiple small peaks 1 h after the major peak at z = 4 cm.

Similar measurements were found for 100% MC in Fig. 6.6(c): the thermocouple at z = 6 cm did not reach 200°C. Meanwhile, at z = 8 cm, the maximum temperature exceeded 200°C where the observed multiple peaks indicate the burning of the collapsed overhang. Therefore, for peat MC of 100% the overhang thickness is ≥ 7 cm. Additional experiments were conducted in a taller reactor ($20 \times 20 \times 20$ cm^3) to find the overhang thickness for peat MC > 50%. Figure 6.8 summarizes all measurements: the overhang thickness (δ_o) rapidly increases from 0.5 cm to 12 cm as the MC increases from 5% to 130% before reaching the ignition limit at 150% MC.

For fire spread with wind, Fig. 6.7(a) shows that for the dry peat the measured peak temperatures were about 50°C higher than the corresponding no-wind case (see Fig. 6.6(a)). As the wind speed increases, the enhanced oxygen supply results in a higher

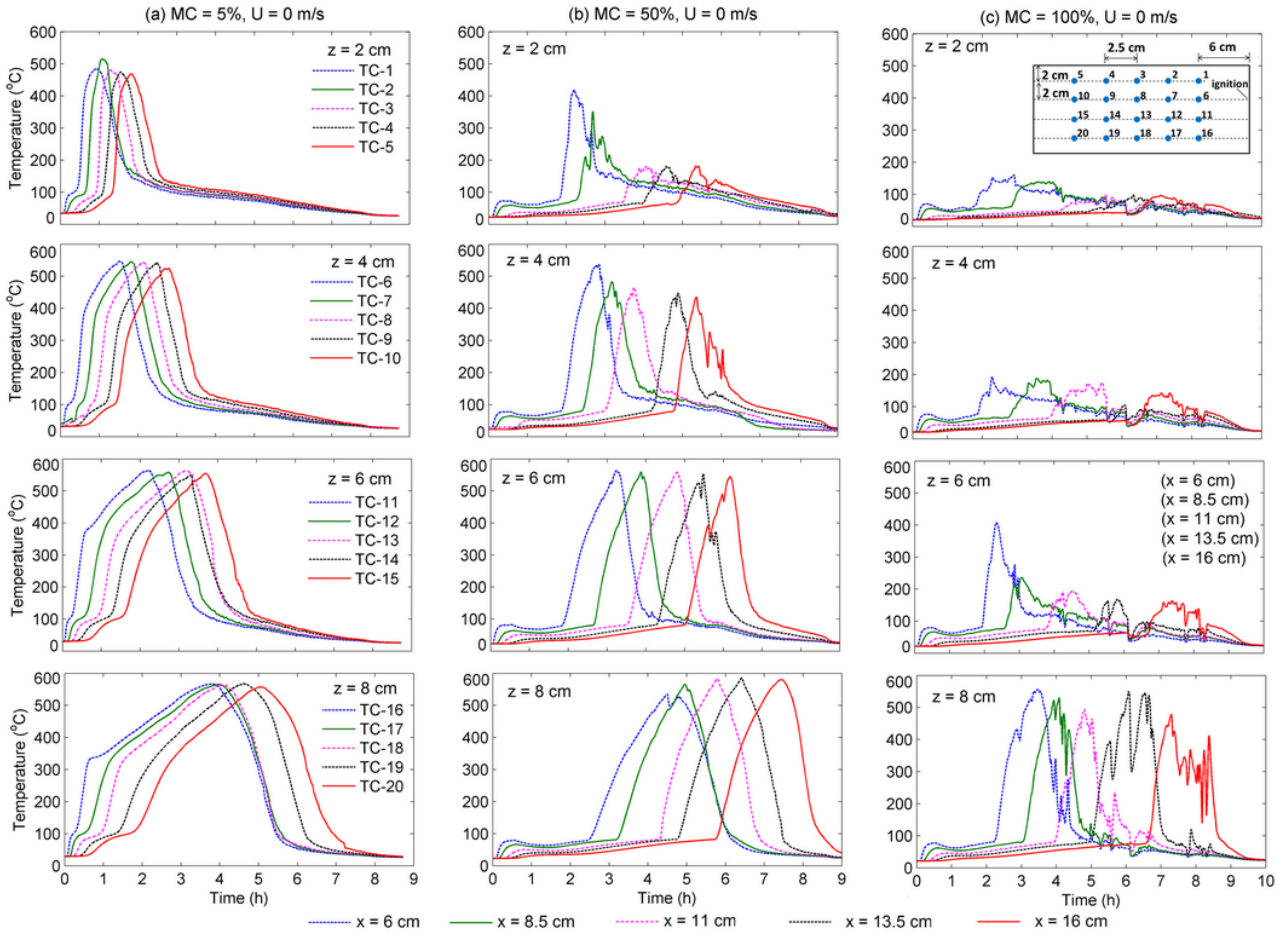

Figure 6.6: Temperature measurements of 20 thermocouples without wind for peat of (a) MC = 5% (dry); (b) MC = 50%; and (c) MC = 100%. The overhang region is indicated by temperature lower than the onset of pyrolysis at 200°C.

heat release rate [1, 8], and overwhelms the increased convective heat loss due to wind.

Figure 6.7(b) shows that for 50% MC, some thermocouples at $z = 6$ cm did not reach 200°C. In other words, the overhang thickness increases from 3 ±1 cm (no wind) to 7 ±1 cm (1.2 m/s wind). For 100% MC in Fig. 6.7(c), the overhang thickness is showed to be $\geq$ 8 cm, higher than the no-wind case. All measurements of overhang thickness are compared in Fig. 6.8. In general, δ_o increases as both MC and wind. Because wind becomes weaker with depth, its effect tends to decrease as the overhang thickness increases.

6.3.3 Spread rate profile

Using visual and IR imaging at the top view (see Fig. 6.3), the lateral spread rate on the free surface can be measured. Due to the formation and collapse of the overhang, peat on the free surface does not burn in situ (see Fig. 6.5), so the visual and IR cameras actually measured the rate of disappearance (collapse) on the free surface and the spread rate of the high-temperature region in a lower layer, respectively.

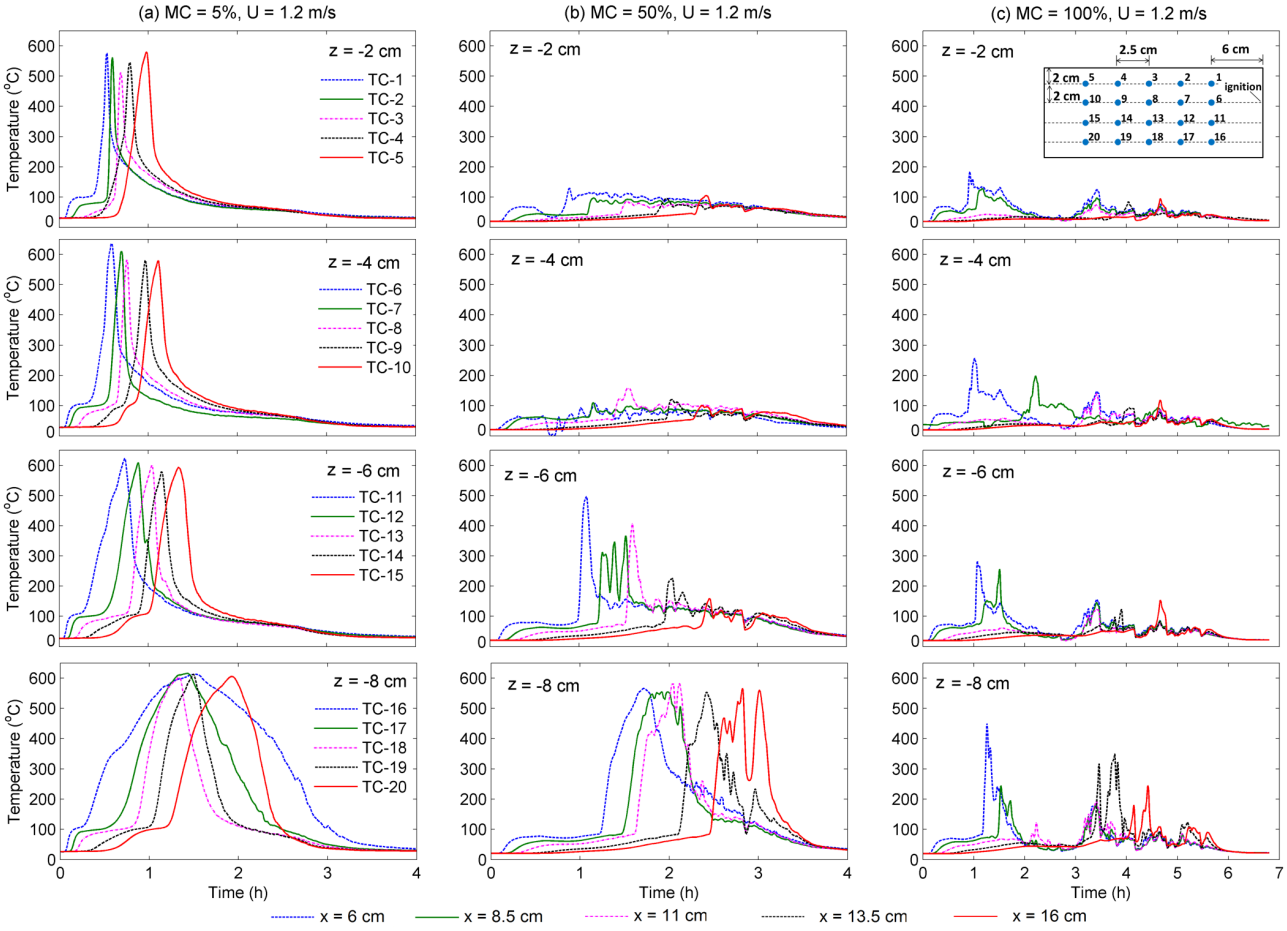

Figure 6.7: Temperature measurements of 20 thermocouples under wind speed of 1.2 m/s for peat of (a) MC = 5% (dry); (b) MC = 50%; and (c) MC = 100%. The overhang region is indicated by temperature lower than the onset of pyrolysis at 200°C.

The lateral spread rate below the free surface can be estimated by tracking thermocouple measurements, *e.g.* in Figs. 6.6 and 6.7. Data processing showed that tracking the peak temperature (as proxy for oxidation front), pyrolysis front (200°C), and drying front (100°C) gave similar values for the spread rate. The spread rate was found to be relatively uniform within 10 cm (over 5 thermocouples) at each depth. Therefore, if all thermocouples in each row are below the overhang region, their peak temperatures were tracked to estimate the mean spread rate. Within the overhang layer, the drying front (100°C) was tracked. Figure 6.9 shows the depth profile of the mean spread rate, $u(z)$, as a function of MC and without wind.

As expected, the overall spread rate reduces remarkably as the MC increases. For the dry peat (5% MC), the spread rate decreases appreciably from 12 to 7 cm/h with increasing depth. Similar decreasing $u(z)$ was found in the smouldering experiment of dry wood-based fibres [10]. This is because as the depth increases, the ambient oxygen supply is reduced [1].

Figure 6.10 shows the depth profile of the spread rate under different wind speeds.

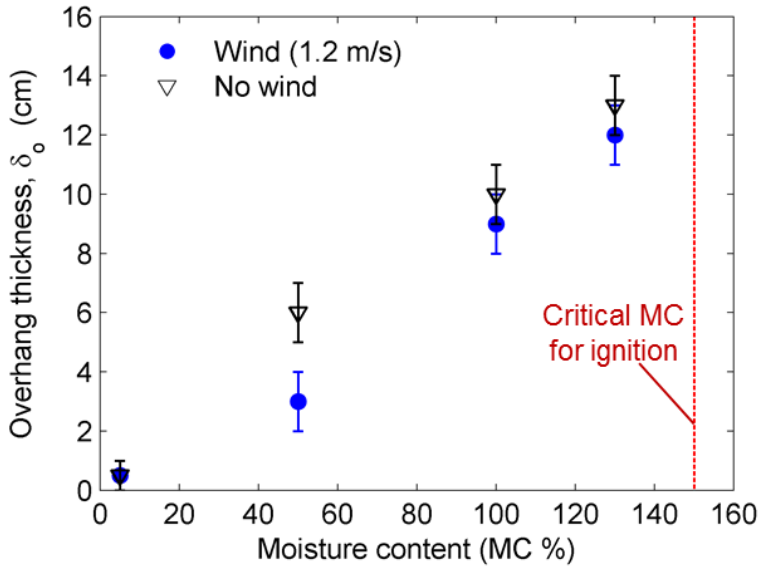

Figure 6.8: Measurement of the overhang thickness (δ_o) vs. moisture content (MC) and wind speed.

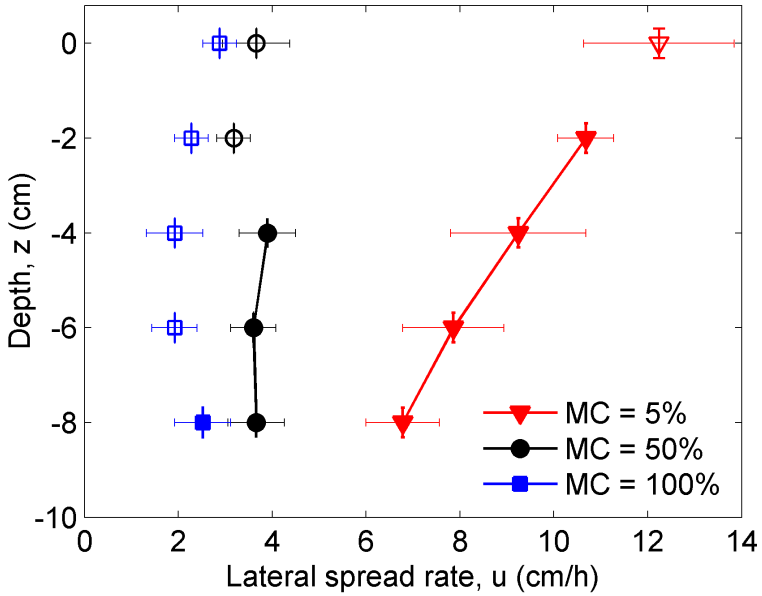

Figure 6.9: Depth profile of the mean lateral spread rate, $u(z)$ for different moisture contents (MC) without wind. Solid symbols are measurements of the peak temperature below the overhang, and hollow symbols are measurements of 100° within the overhang.

For each MC, the overall spread rate increases with wind speed. The wind promotes the oxygen supply while it also increases convective heat losses. Moreover, the wind also provides preheating of the fuel ahead by driving hot gas products downstream [6]. Both effect act to increase the fire spread rate and the peak temperature. As discussed above, the promotion in oxygen supply is seen to be dominant, indicated by a higher peak temperature under wind for example as seen in Fig. 6.7(a). As the depth increases, the wind effects on the fire spread become weak.

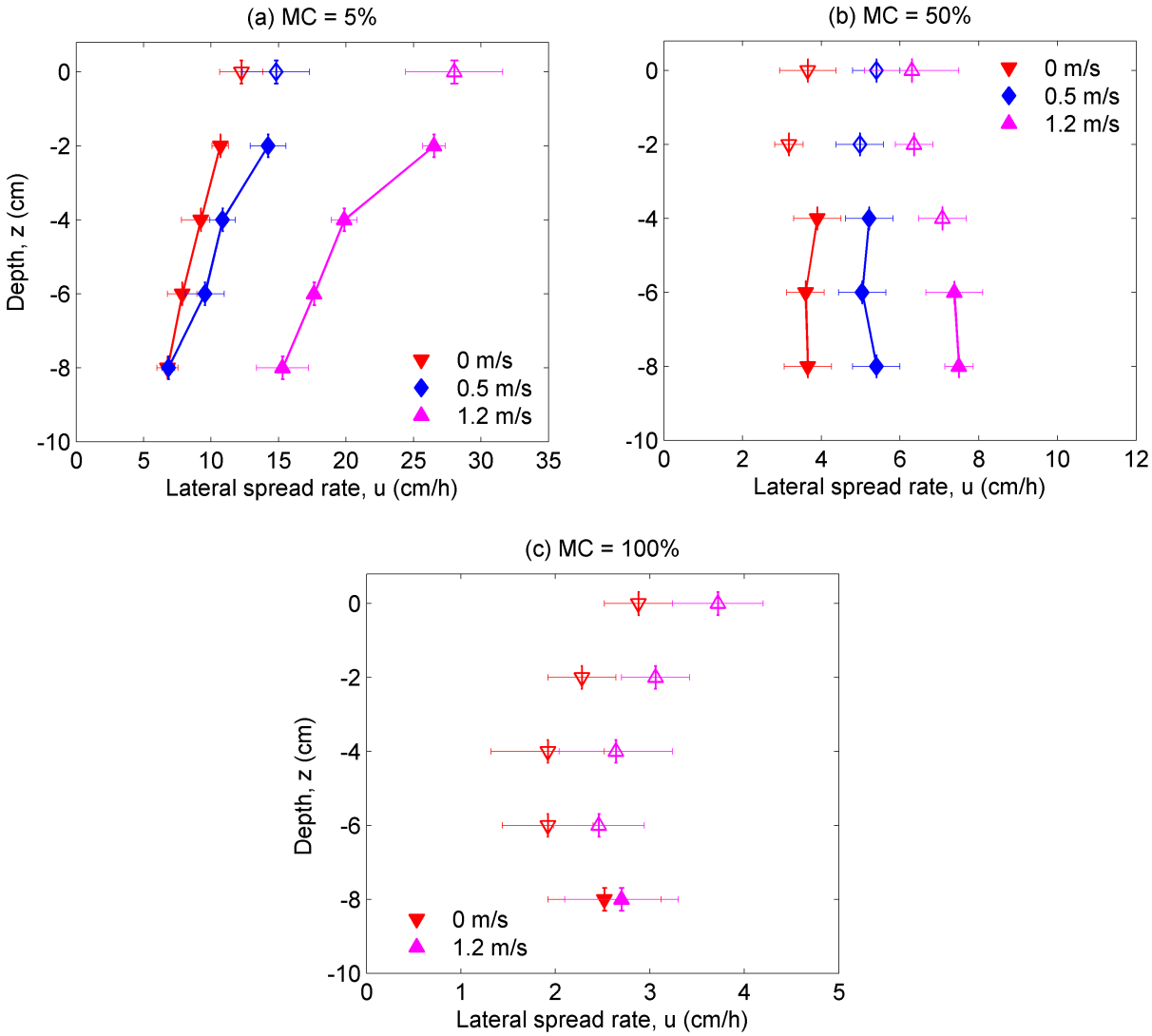

Figure 6.10: Depth profile of the lateral spread rate, $u(z)$ under different wind speeds with peat moisture content (MC) of (a) 5%, (b) 50%, and (c) 100%. Solid symbols are measurements of the peak temperature below the overhang, and hollow symbols are measurements of 100° within the overhang. Note that the x-axis scales are different in each plot.

On the other hand, the wind effect tends to decrease with MC. This result was also found in the experiments with smouldering pine needles [24]. Such observation suggests that for wet peat samples, it is the moisture or heat loss, rather than the oxygen supply, dominating in smouldering spread. Note that for peat sample of 100% MC (as well as 130% MC), the spread rate near the bottom (8 cm below top surface) was slightly higher than the upper layer, probably because of the insulating effect of the bottom wall.

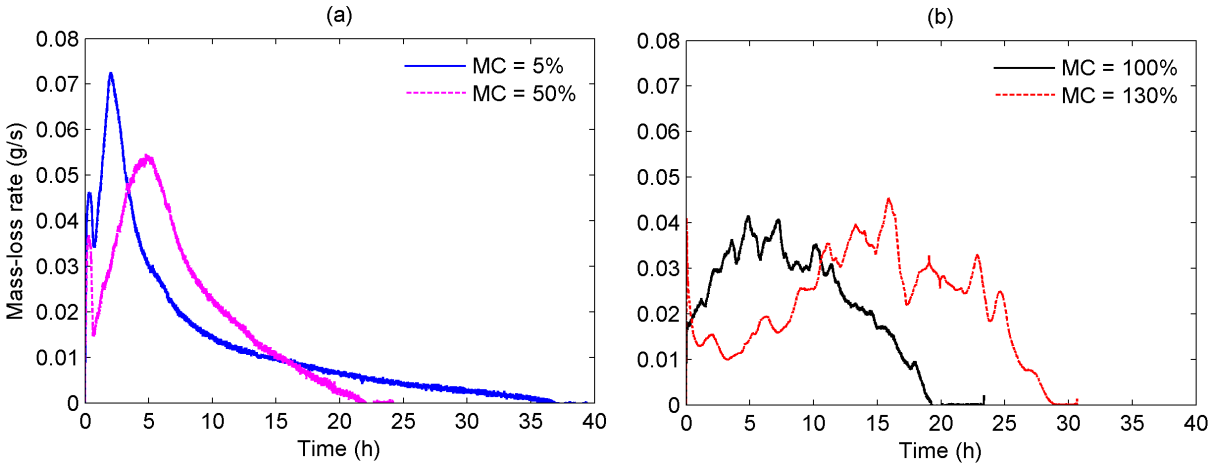

Figure 6.11: Measured mass-loss (burning) rates in the tall reactor ($20 \times 20 \times 20$ cm^3) for (a) dryer peat samples (MC = 5% and 50%), and (b) wetter peat samples (MC = 100% and 130%).

6.3.4 Burning rate

Figure 6.11 shows the measured mass-loss (burning) rate in the large reactor ($20 \times 20 \times 20$ cm^3) for different MCs. For dryer peat samples (5% and 50% MC in Fig. 6.11a), there are two clear peaks: the first one occurs within the first 30 min from ignition; the second one occurred when the smouldering front on the top surface reached the opposite side of the reactor. Afterwards, the mass-loss rate decreased. The burning duration for 50% MC was shorter than that for 5% MC partly because the density of dry peat actually decreases by 15% as MC increase from 5 to 50% (see Fig. 6.3).

For wetter peat samples (100% and 130% MC in Fig. 6.11b), multiple peaks of mass-loss rate are found. They are the result of the periodic formation and collapse of overhang (see Fig. 6.5). The frequency of local peaks agrees with the frequency of overhang collapse, which is confirmed from video. Such frequency is controlled by the interaction between solid mechanics and combustion, which deserves a separate study in the future. The burning duration increases when MC goes from 100% to 130%, while both cases still gave shorter burning durations than the 5% MC case because of the lower densities of dry peat.

6.4 Analysis of overhang formation

The overhang phenomenon in peat fires has been observed in the field, but it has not been studied in-depth before. Overhang has been explained by the possible heterogeneous soil profile, i.e. the MC or IC of surface layer too high to support combustion [19], or by the convective heat losses due to wind [20]. These field overhangs were also found to have relatively large thickness, $O(10)$ cm $\sim O(1)$ m. However, this well-controlled laboratory experiments show that overhang can be observed in small homogeneous samples and in

a wind-free environment as well, and the collapsed overhang can still burn out. In order to explain the overhang formation, the depth profile of lateral spread, $u(z)$ is the key.

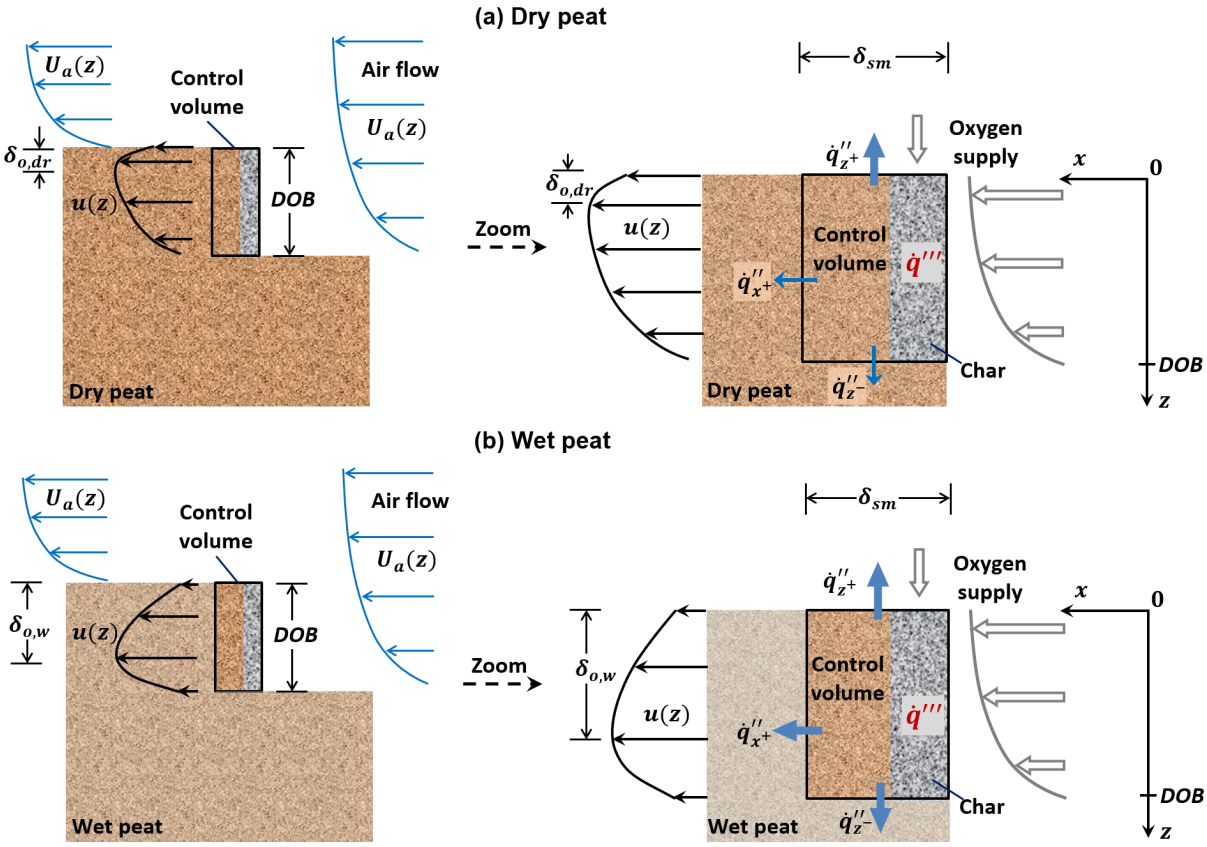

Figure 6.12: Schematic diagram of heat balance for surface spread of a smouldering fire for (a) dry peat, and (b) wet peat. Right image is an augmented version of the control volume.

Let's approximate that the lateral spread of peat fire is controlled by the heat diffusion in the porous bed (see [6, 8] and Chapter 1). The energy-conservation equation for the 2D steady-state spread is

$$\dot{q}'''_{sm} + \frac{\partial}{\partial x}\left(\lambda \frac{\partial T}{\partial x}\right) + \frac{\partial}{\partial z}\left(\lambda \frac{\partial T}{\partial z}\right) + \dot{q}'''_{e} = \rho c u \frac{\partial T}{\partial x} \tag{6.1}$$

where $\dot{q}'''_{sm}$ is the volumetric heat release from smouldering; λ is the thermal conductivity; T is the temperature; $\dot{q}'''_{e}$ is the volumetric heat losses to environment; x and z are the lateral and vertical spread directions, respectively. On the right hand side, the advective term neglects the small motion in the vertical direction due to a uniform vertical temperature profile after a uniform ignition, ρ, c, and u are the peat density, heat capacity, and the lateral spread rate, respectively.

Figure 6.12 illustrates the mechanism in surface spread of smouldering over (a) dry and (b) wet peat samples. The smouldering front inside width δ_p and a height equal to the depth of burn (DOB) is chosen as the control volume. For both dry and wet samples, the smouldering front includes the same pyrolysis and char layers, and is under the same

wind condition. Within the control volume, the dried peat increases from $T_{dr} \approx 100°C$ to a characteristic peak smouldering temperature $T_{sm} \approx 550°C$ along the x direction, and the in-depth spread is much slower than lateral spread, $u_z \ll u_x$. The fire spread is oxygen limited, and integrating along x over the pyrolysis and oxidation fronts (δ_{sm}) as

$$\int_0^{\delta_{sm}} \dot{q}'''_{sm} dx + \int_0^{\delta_{sm}} \left[\frac{\partial}{\partial x}\left(\lambda \frac{\partial T}{\partial x}\right) + \frac{\partial}{\partial z}\left(\lambda \frac{\partial T}{\partial z}\right) \right] dx + \int_0^{\delta_{sm}} \dot{q}'''_e dx = \int_0^{\delta_{sm}} \rho c u \frac{\partial T}{\partial x} dx \quad (6.2)$$

and reorganizing the energy-conservation equation as

$$\rho_a Y_{O_2} U_a(z) \Delta H + \dot{q}''_{MC}(z) + \dot{q}''_e(z) = \rho c u(z) \Delta T \quad (6.3)$$

where the first term comes from $\dot{q}'''_{sm}$; ρ_a is the air density; Y_{O_2} is the oxygen mass fraction in air; U_a is the air velocity; $\Delta H \approx 13.1$ MJ/kg is the heat of oxidation [25]; $\dot{q}''_{MC}$ is the overall heat conduction to dry the moisture (cooling, $\dot{q}'' < 0$); $\Delta T = T_{sm} - T_{dr}$. Therefore, the spread rate profile, $u(z)$ is determined by the profiles of $U_a(z)$, $\dot{q}''_{MC}(z)$ and $\dot{q}''_e(z)$.

Figure 6.13 illustrates the qualitative depth profiles of each terms in Eq. (6.3). The air velocity profile, $U_a(z)$, does not change with MC. Direct measurements by the hot-wire anemometer show that $U_a(z)$ decreases with depth. For the heat loss, because of moisture, $\dot{q}''_{MC}(z)$ increases with MC but does not change with wind. As the depth increase, $\dot{q}''_{MC}(z)$ has a nearly uniform profile until close to $z =$ DOB, where additional heat loss appears to the wet peat below (see Fig. 6.12b). Note that peat is a porous media where heat transfer includes not only conduction, but also convection and radiation across pores. The heat loss to environment, $\dot{q}''_e(z)$, does not change with MC, but increases with wind speed especially near the free surface. Meanwhile, $\dot{q}''_e(z)$ drops significantly with depth. Therefore, by combining all three terms, there is an optimal depth to sustain the fastest fire spread, i.e. the overhang thickness (δ_o) [6].

Figure 6.13a shows that without wind, $\dot{q}''_{MC}(z)$ is very small for the dry peat (solid line). Thus, the oxygen supply, indicated by $U_a(z)$, dominates the left hand side of Eq. (6.3). Because the heat loss to the environment close to the free surface $\dot{q}''_e(z \to 0)$ is large and it rapidly decreases with depth, the optimal depth for smouldering is not on the free surface, but at a small distance below it (a thin overhang layer).

As the MC increases (dashed line in Fig. 6.13a), the enhanced cooling of $\dot{q}''_{MC}(z)$ becomes dominant on left hand side of Eq. (6.3), reducing the spread rate. It slows the spread rate near the free surface and pushes the optimal location deeper. Thus, the overhang thickness becomes larger with MC, agreeing with the experimental measurement in Fig. 6.8.

Figure 6.13b shows that as the wind speed increases, both $U_a(z)$ and $\dot{q}''_e(z)$ increases significantly, especially near the free surface. Comparatively, the increase in oxygen supply is more manifest than the increase in environmental heat loss, as measured peak temperatures under wind (Fig. 6.7) are higher than those without wind (Fig. 6.6). The rate of smouldering increases exponentially with temperature, thus, the forward wind leads to a faster overall smouldering spread.

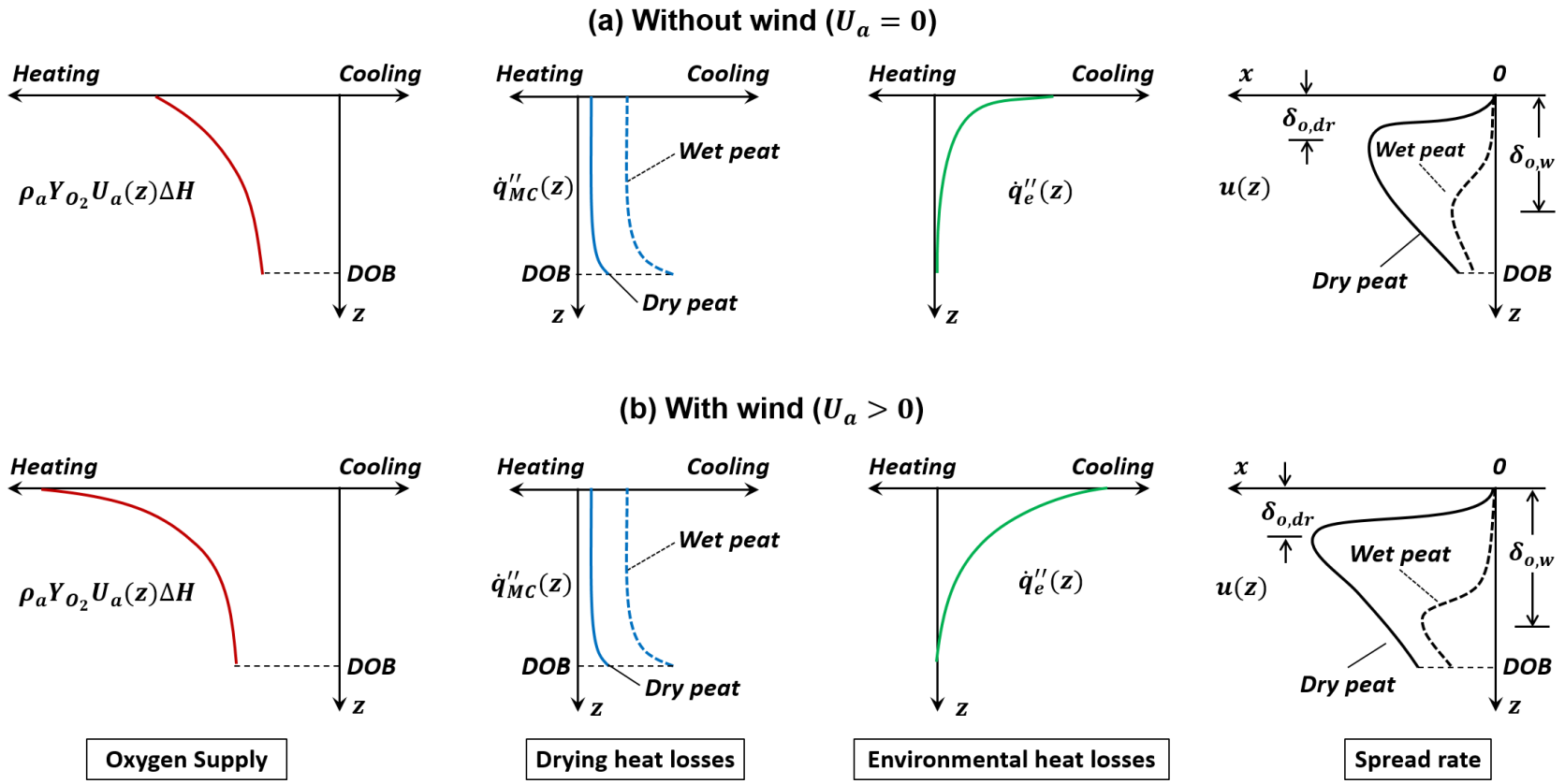

Figure 6.13: Depth profiles of terms in Eq. (6.3) for the surface spread of a smouldering fire (a) without wind, and (b) with wind.

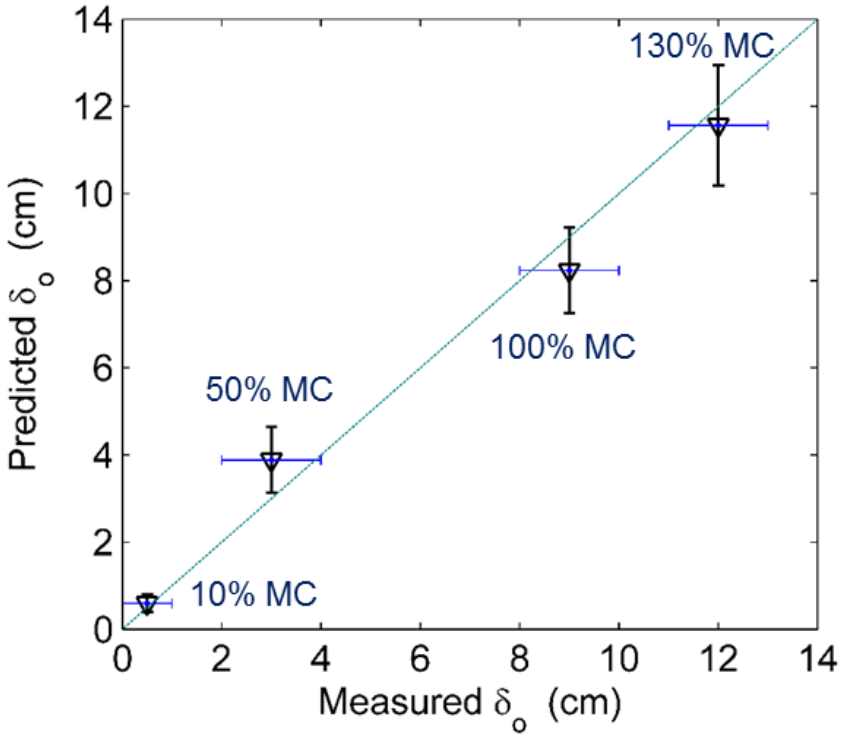

Figure 6.14: Comparison between experimental and predicted overhang thickness (δ_o) without wind at various peat moisture contents (MC). The horizontal error bar comes from direct experimental measurements of δ_o, and the vertical error bar comes from the uncertainty of measured spread rate.

For the dry peat, the oxygen supply becomes more dominant over $\dot{q}''_{MC}(z)$ with increasing wind. Below the thin overhang, the spread rate profile $u(z)$ mimics the wind speed profile of $U_a(z)$. As the MC increases, $\dot{q}''_{MC}(z)$ becomes more important, which can dominate over the competition between $U_a(z)$ and $\dot{q}''_e(z)$. As a result, smouldering tends to spread at a deeper layer (i.e. a larger overhang thickness), where cooling is smaller.

According to the definition of overhang thickness (δ_o): the optimal depth at which the fastest burning is achieved, and the simple heat transfer framework in Eq. (6.3) as well as the illustration in Fig. 6.13, a non-dimensional analysis[3] is used to estimate the overhang thickness. The overhang thickness, as a characteristic length scale in solid phase, should relate to the spread rate difference between the top and lower layers, and the thermal property of the peat bed as

$$\delta_o \sim \frac{\alpha_p}{\Delta u} \tag{6.4}$$

where the α is the thermal diffusivity of dry peat ($\sim 4.5 \times 10^{-7}$ m^2/s [11, 35]); Δu is the difference between the maximum spread rate at δ_o ($u_{max} = u_{z=\delta_o}$) and the spread rate at

3. This non-dimensional analysis is a phenomenological description, rather than a strictly derivation from Eq. (6.1).

the top surface ($u_{z=0} \to 0$) because of quenching [6]. Here, u_{max} has been measured (the first solid point in Fig. 6.9).

Figure 6.14 compares the predicted overhang thickness with the experimental measurement without wind in Fig. 6.8. In general, a good agreement is shown, supporting the critical role of spread-rate profile $u(z)$ in the formation of overhang. In order to compute the spread rate profile and the overhang thickness, a comprehensive 2D numerical model is required to solve Eq. (6.1).

6.5 Conclusions

In this work, the lateral spread of smouldering peat fire has been investigated under various moisture and wind conditions. For the first time the overhang phenomenon, i.e. fire spreading fastest below the free surface, is observed with bench-scale tests using homogeneous peat samples in the laboratory. In addition, the formation and collapse of overhang is found to be periodical, and the thickness of overhang is found to increase with both moisture and wind speed. The depth profile of lateral spread rate is successfully measured by visual and infrared imaging as well as by a thermocouple array.

Experimental results show that the lateral spread rate decreases with moisture content, while increases with wind speed. The proposed simple analysis shows that the oxygen supply is the dominant mechanism for dry peat samples, so the spread rate decreases with depth. As the moisture content increases, the spread rate becomes less sensitive to depth and wind speed because moisture becomes the dominant mechanism. The analysis further suggests that for surface peat fire spread, formation of overhang is caused by the spread rate difference between the top and lower peat layers as well as the competition between oxygen supply and heat losses. This experimental study provides a physical understanding of the surface spread and overhang phenomenon in peat wildfires, and explains the role of moisture and oxygen supply, thus helping to understand this important natural and widespread phenomenon.

Acknowledgements

I want to acknowledge Francesco Restuccia (Imperial College London) and Michela Gramola (University of Cambridge) for important assistance in conducting experiments. I would also like to thank the support from EPSRC, and the travel grant from Imperial College Trust, International Association of Wildland Fire (IAWF), and Association for Fire Ecology (AFE). Valuable discussion with Ms Nuria Prat (University College Dublin) is also acknowledged.

References

[1] G. Rein, "Smouldering Fires and Natural Fuels," in *Fire Phenomena and the Earth System* (C. Belcher, ed.), ch. 2, pp. 15–33, Wiley and Sons, 2013.

[2] S. E. Page, J. O. Rieley, and C. J. Bands, "Global and regional importance of the tropical peatland carbon pool," *Global Change Biology*, vol. 17, no. 2, pp. 798–818, 2011.

[3] S. E. Page, F. Siegert, J. O. Rieley, H.-D. V. Boehm, A. Jaya, and S. Limin, "The amount of carbon released from peat and forest fires in Indonesia during 1997," *Nature*, vol. 420, pp. 61–65, 2002.

[4] U. Ballhorn, F. Siegert, M. Mason, and S. Limin, "Derivation of burn scar depths and estimation of carbon emissions with LIDAR in Indonesian peatlands," *Proceedings of the National Academy of Sciences*, vol. 106, no. 50, pp. 21213–21218, 2009.

[5] M. R. Turetsky, B. Benscoter, S. Page, G. Rein, G. R. van der Werf, and A. Watts, "Global vulnerability of peatlands to fire and carbon loss," *Nature Geoscience*, vol. 8, pp. 11–14, 2015.

[6] G. Rein, "Smoldering Combustion," in *SFPE Handbook of Fire Protection Engineering* (M. J. Hurley, D. T. Gottuk, J. R. Hall Jr., K. Harada, E. D. Kuligowski, M. Puchovsky, J. L. Torero, J. M. Watts Jr., and C. J. WIECZOREK, eds.), pp. 581–603, Springer New York, 2016.

[7] D. Drysdale, *An Introduction to Fire Dynamics*. Wiley, 2011.

[8] T. Ohlemiller, "Modeling of smoldering combustion propagation," *Progress in Energy and Combustion Science*, vol. 11, no. 4, pp. 277 – 310, 1985.

[9] K. Palmer, "Smouldering combustion in dusts and fibrous materials," *Combustion and Flame*, vol. 1, no. 2, pp. 129 – 154, 1957.

[10] T. J. Ohlemiller, "Smoldering combustion propagation through a permeable horizontal fuel layer," *Combustion and Flame*, vol. 81, no. 3, pp. 341 – 353, 1990.

[11] H. Chen, W. Zhao, and N. Liu, "Thermal Analysis and Decomposition Kinetics of Chinese Forest Peat under Nitrogen and Air Atmospheres," *Energy & Fuels*, vol. 25, no. 2, pp. 797–803, 2011.

[12] V. Leroy-Cancellieri, D. Cancellieri, E. Leoni, A. Simeoni, and A. I. Filkov, "Energetic potential and kinetic behavior of peats," *Journal of Thermal Analysis and Calorimetry*, vol. 117, no. 3, pp. 1497–1508, 2014.

[13] W. H. Frandsen, "The influence of moisture and mineral soil on the combustion limits of smoldering forest duff," *Canadian Journal of Forest Research*, vol. 17, no. 12, pp. 1540–1544, 1987.

[14] R. M. Hadden, G. Rein, and C. M. Belcher, "Study of the competing chemical reactions in the initiation and spread of smouldering combustion in peat," *Proceedings of the Combustion Institute*, vol. 34, no. 2, pp. 2547 – 2553, 2013.

[15] G. Rein, N. Cleaver, C. Ashton, P. Pironi, and J. L. Torero, "The severity of smouldering peat fires and damage to the forest soil," *Catena*, vol. 74, no. 3, pp. 304 – 309, 2008.

[16] B. W. Benscoter, D. K. Thompson, J. M. Waddington, M. D. Flannigan, B. M. Wotton, W. J. de Groot, and M. R. Turetsky, "Interactive effects of vegetation, soil moisture and bulk density on depth of burning of thick organic soils," *International Journal of Wildland Fire*, vol. 20, pp. 418–429, 2011.

[17] G. M. Davies, A. Gray, G. Rein, and C. J. Legg, "Peat consumption and carbon loss due to smouldering wildfire in a temperate peatland," *Forest Ecology and Management*, vol. 308, no. 0, pp. 169 – 177, 2013.

[18] A. C. Watts, "Organic soil combustion in cypress swamps: Moisture effects and landscape implications for carbon release," *Forest Ecology and Management*, vol. 294, pp. 178 – 187, 2013. The Mega-fire reality.

[19] S. Cerulean and R. T. Engstrom, eds., *Ignition and burning characteristics of organic soils*, Tallahassee, FL., 1995.

[20] P. Thomas and R. McAlpine, *Fire in the Forest*. Cambridge University Press, 2010.

[21] V. Zanon, F. Viveiros, C. Silva, A. Hiplito, and T. Ferreira, "Impact of lightning on organic matter-rich soils: influence of soil grain size and organic matter content on underground fires," *Natural Hazards*, vol. 45, no. 1, pp. 19–31, 2008.

[22] C. M. Belcher, J. M. Yearsley, R. M. Hadden, J. C. McElwain, and G. Rein, "Baseline intrinsic flammability of Earths ecosystems estimated from paleoatmospheric oxygen over the past 350 million years," *Proceedings of the National Academy of Sciences*, vol. 107, no. 52, pp. 22448–22453, 2010.

[23] G. S. Campbell, J. D. Jungbauer, K. L. Bristow, and R. D. Hungerford, "Soil Temperature and Water Content Beneath A Surface Fire," *Soil Science*, vol. 159, no. 6, pp. 363–374, 1995.

[24] J. Valdivieso and J. D. Rivera, "Effect of wind on smoldering combustion limits of moist pine needle beds," *Fire Technology*, vol. 50, no. 6, pp. 1589–1605, 2014.

[25] C. Huggett, "Estimation of rate of heat release by means of oxygen consumption measurements," *Fire and Materials*, vol. 4, no. 2, pp. 61–65, 1980.

Chapter 7

Conclusions

7.1 Outcomes of the present research

In this thesis, smouldering combustion of peat in wildfire has been systematically studied for (i) the *zero-dimensional* (0D) thermal analysis of microgram-scale peat degradation (Chapters 1 and 4), (ii) the *one-dimensional* (1D) in-depth spread of peat fires (Chapters 2-5), and (iii) the *two-dimensional* (2D) surface fire spread in bench-scale peat samples (Chapter 6). Two controlling mechanisms, *heat loss* and *oxygen supply*, have been studied extensively in the ignition and extinction as well as in two dominating spread modes, *lateral* and *in-depth* spread.

The heterogeneous chemistry in smouldering combustion of peat plays an fundamental role in understanding and describing its thermochemical conversion and fire dynamics. Therefore, the smouldering kinetics has been first studied in Chapter 1. Based on the thermogravimetric analysis (TGA) of four types of peat soils, for the first time a 5-step kinetic scheme (including drying) is proposed for peat smouldering, and compared with other two reduced schemes. Then, genetic algorithm (GA) is applied, and successfully finds the best kinetic parameters matching all TG data. The interdependence among kinetic triplets (Z, E, and n) has been discussed, and it is emphasized there is no unique solutions in this heuristic optimization. With this 5-step kinetics, a 1D plug-flow model successfully describes reaction profiles in both lateral and in-depth spread modes, and particularly the drying sub-front is predicted for the first time in peat fire.

Such heterogeneous chemistry is further generalized for thermochemical conversion in smouldering combustion of most biomass and under various oxygen concentrations (X_{O_2}) in Chapter 4. Kinetic schemes with different complexities, 3-, 5-, and 9-step including 1-step drying, are proposed and compared. In addition, Kissinger's analytical approach is used to feed the GA (K-GA method) to more quickly optimize the kinetic parameters of two peat soils for TGA under several oxygen concentrations. For the first time, orders of oxidations in smouldering combustion are found, which are smaller than the widely assumed first order. Comparison shows that the 5-step kinetic scheme can predict all experiments in TGA and a bench-scale smouldering reactor under all oxygen

concentrations, much better than the simplest 3-step scheme while similar to the more complex 9-step scheme. Therefore, this 5-step kinetics shows an excellent capability to describe both peat fire and smouldering combustion of other biomass.

The ignition of smouldering peat fire has been studied in Chapters 2 and 4. Understanding which factors and how these factors affect the smouldering threshold are crucial to understand the fire risk of in peatlands. The influence of (i) heat loss due to peat moisture (Chapter 2), (ii) the oxygen supply by varying atmospheric oxygen concentration, and (iii) the interaction between them (Chapter 5) on ignition of peat fires are investigated numerically. A comprehensive 1-D model of a reactive porous media is developed in an open-source code, Gpyro. Modelling results first shows that (i) both moisture content (MC) and inert content (IC) of peat acts a heat sink, preventing the smouldering ignition, and (ii) there is a nonlinear compensation effect between the critical moisture content (MC^*) and inert content (IC^*). Such prediction corrects previously linear extrapolation of experimental data given by Frandsen, and show a better agreement with the experimental results for a wide range of soil types. In addition, the smouldering thresholds are found to (i) depend on the decomposition kinetics, physical properties, and ignition protocol, and (ii) reduce as the oxygen concentration increases. More importantly, compared to flaming fires, smouldering fires can be ignited in a higher fuel MC ($> 100\%$), and at a lower oxygen concentration ($\sim 12\%$), defining a much lower wildfire threshold.

The spread of smouldering peat fire has been studied in Chapters 3-5. Once ignited, smouldering peat fire will spread laterally along the free surface and vertically to peat layers in-depth, dominated by forward smouldering. Particularly, the in-depth spread controls the depth of burn (DOB), which can be used to estimate the carbon release from peatlands. Therefore, understanding the fire dynamics (e.g. the fire spread rate and extinction limit) related to the in-depth smouldering spread is essential to effectively manage peat fires, and estimate the impact of magefires in peatlands on the global green house gas emission and climate change. With the 1D model, heat loss due to peat moisture is studied with a tall heterogenous peat sample, and both MC^* and DOB are predicted (Chapter 3). It is found that the smouldering fire can spread over an extremely wet peat ($MC > 250\%$) if the top burnt layer is thick and the wet layer below is thin. The critical MC of extinction (MC^*_{ex}) is found to be very different from that of ignition (MC^*_{ig}) : much higher value, insensitive to ignition protocol, and no tendency to decrease in high density. The predicted DOBs agree with experiments of 18 natural peat samples in the literature.

On the other hand, oxygen supply by varying atmospheric oxygen concentration on smouldering spread is investigated in a short smouldering reactor (Chapter 4) and a tall peat column (Chapter 5). For the bench-scale smouldering reactor, the predicted mass-loss rates show a good agreements with those of experiments from the literature under both sub- and super-atmospheric oxygen concentration. The model accuracy and sensitivity to multiple physico-chemical properties and boundary conditions are explored with

a stochastic sensitivity analysis. For smouldering spread in the tall peat column, (i) there is a nonlinear critical curve between MC^* and $X^*_{O_2}$, which is higher than that for ignition; and (ii) the spread rate increases in a oxygen-richer atmosphere, while decreasing over a wetter fuel, both agreeing with flaming fires. The predicted spread rate of smouldering peat is on the order of 1 mm/min, much slower than flaming fires and in agreement with experiments in the literature.

In Chapter 6, the surface spread of smouldering peat fire has been experimental studied under various moisture and wind conditions. For the first time the overhang phenomenon, i.e. peat fire spreading below the free surface, is observed with bench-scale tests using homogeneous peat samples in the laboratory. In addition, the formation and collapse of overhang is observed in laboratorial experiments to be periodical, and the thickness of overhang is found to increase with both peat moisture and wind speed. The depth profile of lateral spread rate is successfully measured by visual and infrared imaging as well as by thermocouple array. Experimental results show that the lateral spread rate decreases with moisture content, while increases with wind speed. The proposed simple analysis on the heat loss and oxygen supply shows that the oxygen supply is the dominant mechanism for dry peat samples, so the spread rate decreases with depth. As the moisture content increases, the spread rate becomes less sensitive to the depth and the wind speed because peat MC becomes the dominant mechanism. The analysis further suggests that for surface peat fire spread, formation of overhang is caused by the spread rate difference between the top and lower peat layers.

7.2 Future work

Smouldering combustion of peat in wildfires is an emerging and fascinating multi-discipline topic in combustion, fire ecology and geoscience. It may be as complex as turbulence and flaming wildfires, but significantly few studies have been conducted in each of the related discipline. Many aspects are still not well understood and deserve significantly more research efforts. Some of the difficulties and potential research areas are briefly introduced.

Based on the effort of this thesis, the understanding of chemical kinetics and the optimization method for kinetic parameters in smouldering combustion have been significantly improved. However, the heat of reaction in multi-step kinetic model has not yet been determined, largely because of the lack of analysis methods as reliable as those for TG experiments in differential scanning calorimetry (DSC) or other effective measurements. Once the kinetics and heat of reaction are both determined, the understanding of degradation chemistry and fuel chemical composition in smouldering can be significantly improved.

The coupling among kinetics, thermo-physical properties, and transport processes in peat smouldering are still far from clear, considering the complexity in each term.

Even for a bench-scale pyrolysis process, the interactions among these factors are not well quantified due to lack of accurate input parameters for modelling and experimental measurements for comparison. It is recommended to study a simple case, for example the drying in a homogeneous sand sample. Since the drying process and moisture content play particularly important roles in peat fires, both experimental and numerical approaches would help understand their fire behaviours.

The interaction between flaming and smouldering wildfires is another interesting and important research topic. Smouldering can be initiated by the direct heating (convection and radiation) from flaming, or indirectly from firebrands. In turn, gaseous products from incomplete smouldering fires can also supply and enhance flaming fires. Moreover, smouldering can also go through a transition to flaming. Once the smouldering-to-flaming transition occurs on the ground, it can completely change the wildfire behaviour, and threat human life. There has been few experimental or computational studies on the coupling between flaming and smouldering, especially for wildfires.

Modelling of smouldering wildfires is still lacking and challenging, desiring more research effects and new scientific ideas. Moreover, the fundamental research on smouldering peat fires has many implications to other disciplines, and equally there can be more breakthroughs through multi-discipline collaborations. Some interesting research are suggested for future research:

1. Few modelling studies have been done to simulate real peat fire behaviours, for example using natural soils in the field, ignition by lighting, self-heating and hot particles, and suppression by rain and firefighting attempts. More insights can be learned by starting with some well-controlled bench-scale experiments in laboratory, and conducting corresponding computational studies for comparison.
2. There is little research conducting sophisticated 2D/3D model and providing more insides on high-dimensional and geometric effects. On the other hand, compared to flaming, smouldering is a much slower process (for days, weeks and months) because of a lower combustion temperature, while having equally large scales. Therefore, modelling of smouldering wildfires can be extremely time consuming, despite of using a simple model. Furthermore, little research has been done on the forecast of smouldering wildfires where long-term smouldering fires coupling with fast flaming fires need to be modelled and coupled in a mega-scale. In short, how to balance the complexity and accuracy of model and to scale up are emerging topics in wildfires.
3. The close collaboration with firefighters, forest service and fire ecology community can improve current wildfire management and inspire more new fundamental research topics. Much more effects need to put into transferring the newly found knowledge to other scientific communities and the education of new-generation researchers, firefighters, policymakers and the public.
4. Locally, there is still little knowledge on the emission from regional peat fires. The

quantity and composition of toxic gases and particle matters from the incomplete smouldering have not been identified, which can be very different from the high-temperature flaming. Their impacts on human health as well as the generation mechanism of haze phenomenon are still poorly understood. A better understanding on emission may provide a "fire signature", helping detect and monitor the risk, existence, location, and intensity of underground fires.

5. Globally, the greenhouse gas emission from both tropic and boreal peat fires plays important roles in global carbon cycle and climate change. Recent global warming dries the peatlands and increases the depth of below ground soil combustion, creating a positive feedback to the climate system. So far, there are large uncertainties in estimations of burning severity, area and duration in peat fire due to the lack of effective detection and modelling techniques. As those uncertain parameters are used in modelling and predictions, large uncertainty also exists in the corresponding estimation on carbon emission and the impact on climate.
6. Since the last decade, peat fires have caught much attention from the geoscience community. More researchers start to consider the largest, longest, and most persistent smouldering wildfires, particularly peat fires, as the dominating fire activity in geographic scale and geological timescale. The Earth fire activity is closely linked to the origin of life, evolution of biosphere and fossil fuel record, and these fascinating research topics need more talents and wisdom across disciplines.